AD-A130 767 USAF/SCEEE GRADUATE STUDENT SUMMER SUPPORT PROGRAM (1982) MANAGEMENT AND..(U) SOUTHEASTERN CENTER FOR ELECTRICAL ENGINEERING EDUCATION INC S..

1/5

UNCLASSIFIED W D PEELE ET AL. OCT 82 AFOSR-TR-83-0611 F/G 5/9 NL

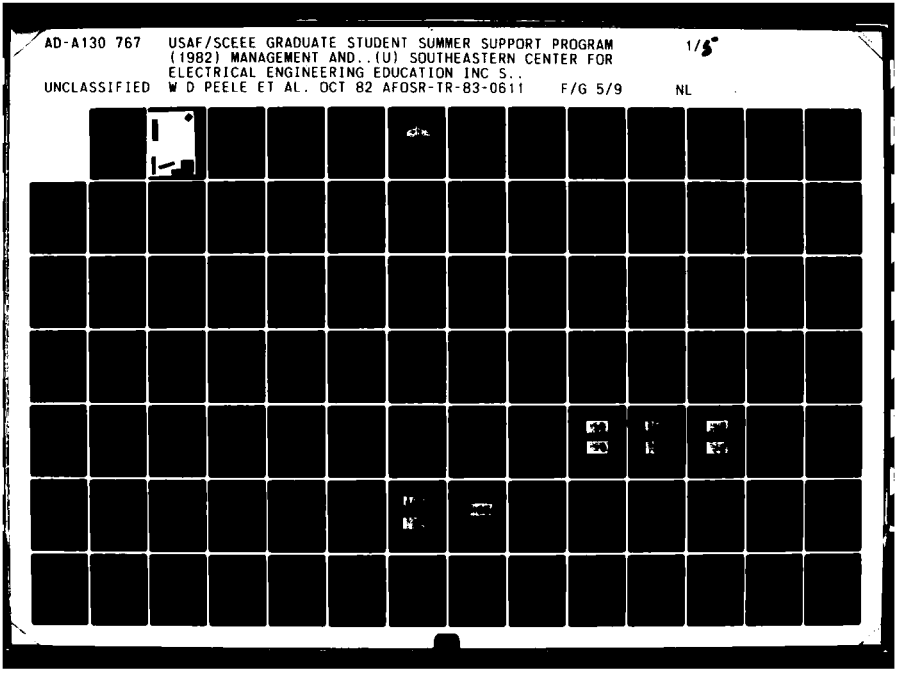

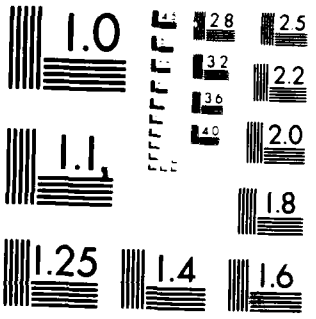

AIR FORCE OFFICE OF SCIENTIFIC RESEARCH

UNITED STATES AIR FORCE

GRADUATE STUDENT

1982

UNCLASSIFIED

SECURITY CLASSIFICATION OF THIS PAGE *(When Data Entered)*

REPORT DOCUMENTATION PAGE

READ INSTRUCTIONS BEFORE COMPLETING FORM

REPORT NUMBER	2. GOVT ACCESSION NO.	3. RECIPIENT'S CATALOG NUMBER
AFOSR-TR- 83-0611		

4. TITLE *(and Subtitle)*	5. TYPE OF REPORT & PERIOD COVERED
United States Air Force Graduate Student Summer Support Program	FINAL
	6. PERFORMING ORG. REPORT NUMBER

7. AUTHOR(s)	8. CONTRACT OR GRANT NUMBER(s)
Warren D. Peele Earl L. Steele	F49620-82-C-0035

9. PERFORMING ORGANIZATION NAME AND ADDRESS	10. PROGRAM ELEMENT, PROJECT, TASK AREA & WORK UNIT NUMBERS
Southeastern Center for Electrical Engineering Education 11th and Massachusetts Ave. St. Cloud, Florida 32769	61102F 2301/D5

11. CONTROLLING OFFICE NAME AND ADDRESS	12. REPORT DATE
AFOSR/XOT Building 410 Bolling AFB, DC 20332	October 1982
	13. NUMBER OF PAGES

14. MONITORING AGENCY NAME & ADDRESS *(if different from Controlling Office)*	15. SECURITY CLASS. *(of this report)*
	UNCLASSIFIED
	15a. DECLASSIFICATION/DOWNGRADING SCHEDULE

16. DISTRIBUTION STATEMENT *(of this Report)*

APPROVED FOR PUBLIC RELEASE· DISTRIBUTION UNLIMITED

17. DISTRIBUTION STATEMENT *(of the abstract entered in Block 20, if different from Report)*

18. SUPPLEMENTARY NOTES

19. KEY WORDS *(Continue on reverse side if necessary and identify by block number)*

20. ABSTRACT *(Continue on reverse side if necessary and identify by block number)*

A pilot program for graduate Student Summer Support via the AFOSR Summer Faculty Research Program (SFRP) was initiated by contract modification on 26 March 1982. The program was developed as an adjunct effort to the SFRP. Its purpose is to provide funds for selected graduate students to work at an appropriate Air Force Laboratory or Center with a supervising professor who holds a concurrent SFRP appointment. Although only 16 positions were budgeted, SCEEE appointed 17 graduate students who represented fifteen schools and ten disciplines in science and engineering.

DD FORM 1 JAN 73 1473 EDITION OF 1 NOV 65 IS OBSOLETE

UNCLASSIFIED

SECURITY CLASSIFICATION OF THIS PAGE *(When Data Entered)*

1982 USAF/SCEEE
GRADUATE STUDENT SUMMER SUPPORT PROGRAM

Conducted by

Southeastern Center for

Electrical Engineering Education

under

USAF Contract Number F49620-82-C-0035

MANAGEMENT AND TECHNICAL REPORT

Submitted to

Air Force Office of Scientific Research

Bolling Air Force Base

Washington D.C.

by

Southeastern Center for
Electrical Engineering Education

October 1982

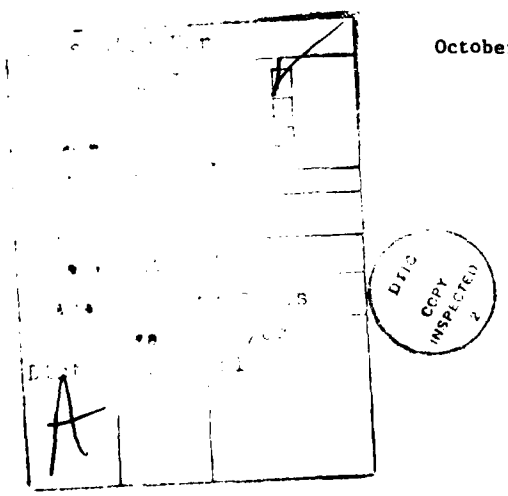

UNITED STATES AIR FORCE

GRADUATE STUDENT SUMMER SUPPORT PROGRAM

1982

PROGRAM MANAGEMENT AND TECHNICAL REPORT

SOUTHEASTERN CENTER FOR ELECTRICAL ENGINEERING EDUCATION

TABLE OF CONTENTS

INTRODUCTION & SUMMARY

A pilot program for Graduate Student Summer Support via the AFOSR Summer Faculty Research Program (SFRP) was initiated by contract modification on 26 March 1982. The program was developed as an adjunct effort to the SFRP. Its purpose is to provide funds for selected graduate students to work at an appropriate Air Force Laboratory or Center with a supervising professor who holds a concurrent SFRP appointment. Although only 16 positions were budgeted, SCEEE appointed 17 graduate students who represented fifteen (15) schools and ten (10) disciplines in science and engineering.

To be eligible, all candidates had to be currently registered in a graduate program. The graduate students were selected from the fields of engineering, computer science, mathematics, or the physical sciences and were supervised by a faculty member who held an appointment as a SCEEE Fellow for the summer of 1982 under the Summer Faculty Research Program. The students were U.S. citizens, working toward an appropriate graduate degree, and currently enrolled in the graduate school at their respective institutions.

The graduate student researchers in this program had the following specific obligations:

1) To participate in research under the direction of a Faculty Member at an Air Force Laboratory or Center;
2) To prepare a report at the end of the summer period describing the summer research accomplishments. This report will be approved by or co-authored with the supervising faculty member;
3) To complete an evaluation questionnaire on the Graduate Student Summer Support Program.

1982 GSSS Objectives were: (1) To provide a productive means for a graduate student to participate in research under the direction of a faculty member at an Air Force Laboratory or Center; (2) To stimulate continuing professional association among graduate students, their supervising professors, and professional peers in the Air Force; (3) To further the research objectives of the Air Force; (4) To enhance the research productivity and capabilities of engineering and science graduate students.

Prerequisities For Appointments: To qualify as a Graduate Researcher in the 1982 GSSS program, applicants must have been: (1) US citizens; (2) holders of a BS of MS degree in an appropriate technical specialty; (3) registered in a Graduate School working toward an appropriate graduate degree; (4) willing to pursue their summer research work under the direction of a supervising professor who holds an appointment under the SFRP for the summer of 1982.

Research Period: The period of the student appointments was for ten continuous weeks at the research site between May 15, 1982 and September 30, 1982. The students research period coincided with the appointment period of the supervising professor with whom the student worked.

Application Deadline: April 30, 1982

Financial Terms: The stipends for graduate student Researchers in this program depend upon the student's degree status. They are:

$55.00 per day ($275 per week) for B.S. degree holders
$65.00 per day ($325 per week) for M.S. degree holders

Travel expenses were reimbursed to the student for round trip travel between the Researcher's school location and the Air Force facility in accordance with SCEEE travel policy.

A living expense allowance of $25.00 per day was paid for each day the researcher spent at the Air Force Location.

SCEEE has received only positive responses regarding the concept of the GSSS Program. A few issues of implementation have been questioned, but they all relate to the late announcements of the program, the late appointment dates, or facility limitations.

Evaluations have been requested of the Laboratory Contacts and all have responded in writing or verbally. The common opinions among government laboratory scientists, faculty, and students are: that the program is a valuable addition to the Summer Faculty Research Program; that the program should be enlarged and continued; that students should be supervised by faculty researchers; that the students are highly motivated and contribute significantly to the research effort; that exposure to USAF R&D produces a positive student opinion of the USAF. This report contains detailed and summarized data relevant to the 1982 Graduate Student Summer Support Program.

The following are GSSS comments by Laboratory Representatives:

(1) We are profiting from the 1982 Graduate Student Summer Support Program. I highly encourage the continuation of this program in the future. The graduate student working for us was from a different university than our SFRP appointee this summer. I suspect that we would get the maximum benefit from the graduate student program in the future, if the student and professor were from the same organization or have a close tie. (For example, a professor from Harvard may know a student from MIT, or may have had the student as an undergraduate.) There may even be some consideration given to having a laboratory prioritize the professors

based on the availibility of graduate students to accompany him. There might be a way to indicate the availability of accompanying graduate students on the application blank for the 1983 AFOSR/SFRP.

(2) It would be desirable, during the SFRP selection process, to know which SFRP applicants wished to bring students to the laboratories. In this way the research topics to be addressed could be matched more closely to the professor/student combinations and the unique capabilities they would bring to the laboratories as a research team.

Graduate students thesis or dissertation topics oftimes require unique facilities which may not be available at their universities but which may be available at Government laboratories. The GSSSP could provide an opportunity for graduate students to use Government facilities during the summer months under the guidance of SFRP professors. To this end, however, it would be useful if the brochure for the SFRP/GSSSP included mention of unique or specialized research facilities available at laboratories along with research opportunities.

The laboratory experience thus far with the GSSSP is very favorable and we strongly encourage its continuation. The GSSSP provides graduate level students with exposure to AF research interests and also provides the AF with an excellent source for future recruitment.

(3) The newly initiated pilot program sponsored by AFOSR labeled "Graduate Student Summer Support Program" has proved quite beneficial in our Laboratory. The three advisors within the Materials Laboratory all enthusiastically support this program. They feel it is beneficial both to the student and the Laboratory and recommend that it be continued and at an increased level, if possible. One advisor stated a student may use work in this Laboratory as a possible thesis project. The key ingredient to a successful program seems to be a good mesh between the Summer Faculty Researcher and the Graduate Student.

(4) Our Laboratory has determined, through participation in the pilot program, that the AFOSR Graduate Student Summer Program is an excellent idea which has worked very well for us during the first year. This program makes sense with respect to supporting the natural professor/student relationship which is the basis of all of our university research efforts. Because of the professor/student relationship, the background of the student will be appropriate to the task of the research associate professor while the student gains valuable experience. It is possible that research conducted during the summer could lead to a possible thesis topic that may be of potential benefit to the AFOSR. In conclusion, it was suggested that it may be beneficial to the AFOSR to consider funding for Graduate Student Support on a project funded under the Mini-grant Program, especially if this is a follow-on to a Summer Faculty/Graduate Student effort. We are extremely pleased with this new program and are already anticipating the possibility of even more students next summer.

INFORMATION BROCHURE

for

GRADUATE STUDENT RESEARCHERS

on the

1982 USAF-SCEEE GRADUATE STUDENT SUMMER SUPPORT PROGRAM

May 1982

INFORMATION BROCHURE

for

GRADUATE STUDENT RESEARCHERS

Table of Contents

I. GRADUATE STUDENT RESEARCHER OBLIGATIONS

SCEEE is required by contract to impose certain obligations on you in your status as a Graduate Student Researcher. This section outlines those obligations, and you should read them thoroughly. You are required to sign and return the statement of understanding before the final processing of your appointment can be completed. The following is a list of these obligations:

1. Research Goals and Objectives: A statement of research objectives must be provided to SCEEE near the beginning of the Summer Research period. It should outline your goals and the approach you intend to follow in researching these goals. It should be submitted with your first invoice for payment. Neither travel expenses nor expense allowances will be reimbursed until after receipt of your statement of research objectives. The report should also clearly indicate the date of your first working day of the summer research period.

2. Final Report: At the end of your summer research effort, you are required to submit to SCEEE a completed, typewritten scientific report stating the objective of the research effort, the approach taken, results, and recommendations. Information on the required format is included in the "FINAL REPORT INFORMATION BULLETIN" enclosed with this packet. However, the final report must be approved by your SFRP Supervising Faculty Member and then transmitted so as to reach SCEEE by Monday September 20, 1982. Payment of "Compensation" for the final four weeks of your ten-week research period cannot be made until SCEEE has received and approved this report in the required format.

3. Program Critique: You will be asked to complete a critique form at the end of your research period regarding your impressions of the program. This critique form should be completed and returned to SCEEE by September 30, 1982. Return of this form is a program requirement.

4. U.S. Air Force-SCEEE Graduate Student Researcher Relationship: The U.S. Air Force and SCEEE understand and agree that the services to be delivered by the SCEEE Graduate Student Researcher under this contract will be non-personal services and the parties recognize and agree that no employer-employee or master-servant relationships will exist between the U.S. Air Force and the SCEEE Researcher. Non-personal services are defined as work performed by an individual who is responsible for an end item (such as a report), free of supervision of the U.S. Air Force and free of an employer-employee relationship.

As a SCEEE Graduate Student Researcher, you will not:

(a) Be placed in a position where you are appointed or employed by a Federal Officer or are under the supervision, direction, or evaluation of a Federal Officer, military or civilian.

(b) Be placed in a staff or policy-making position.

(c) Be placed in a position of command, supervision, administration, or control over Air Force military or civilian personnel or personnel of other contractors or become a part of the U. S. Air Force organization.

The services to be performed under the GSSS Program do not require SCEEE or the SCEEE Researcher to exercise personal judgement and discretion on behalf of the U.S. Air Force; rather, the SCEEE Researchers will act and exercise personal judgement and discretion in coordination with their SFRP Supervising Faculty Member on their research programs on the GSSS Program conducted by SCEEE.

The Air Force will have unrestricted use of and access to all data developed during the period of this appointment.

II. ALLOWABLE TRAVEL EXPENSES

The GSSS Program provides potential funding for one round trip between your home and your assigned research location. As soon as you have signed and returned your appointment letter along with the budget sheet, you will be authorized to receive reimbursement for travel expenses as described below.

As outlined in the SCEEE Graduate Student Researcher Obligations section in this brochure, you are authorized reimbursement for travel to your assigned research location at the start of your summer effort and a return trip at the end of the summer research period. You are expected to make your own arrangements for this travel; after each trip you may invoice SCEEE for reimbursement of allowable expenses in the format described in the Instructions for Invoicing for Compensation and Reimbursement section of this brochure. Closely coordinate your travel plans with your SFRP SUPERVISING FACULTY MEMBER.

All travel reimbursements under SCEEE GSSS appointments are made according to current SCEEE policy, and deviations from the approved budget are not authorized and will not be reimbursed. In light of these restrictions, you may choose either to travel by commercial airline at coach rates or less, by bus, by driving your private auto, or by a combination. (Please note that funding for rental cars is not allowed; SCEEE will not reimburse this expense. With any of these choices you may claim reimbursement up to the amount for the most direct routing, taking into the account the desirability of routing on interstate highways if you drive your private auto.

Reimbursement for direct route travel by commercial airline will thus be paid on your submission of an invoice to SCEEE following the invoicing instructions referenced above. In the view of the convenience of having a car at the research location, SCEEE strongly recommends that a private auto be used for travel when practical. Reimbursement for mileage when you drive your private auto is at the rate of 20¢ per mile within the routing restrictions mentioned above and will likewise be paid on submission of an invoice prepared according to the referenced instructions. These reimbursements cannot be extended to cover travel by your family if they accompany you.

During the ten week Summer Research period, you will be authorized to receive an expense allowance in lieu of a per diem payment. The rate of this allowance is $25 per day for a maximum of 70 days. To receive this allowance, you are required to invoice for it as described in the invoicing reference above.

These items above are the only reimbursable travel allowances authorized for the GSSS appointment. Please be advised that any additional travel expenses incurred during the appointment period will be your personal responsibility.

III. INSTRUCTIONS FOR INVOICING FOR COMPENSATION AND REIMBURSEMENT

Attached is a copy of the Invoice Format that you are required to use to obtain compensation or reimbursement from SCEEE. Note that all disbursements by SCEEE for compensation, travel, and/or other expenses are subject to audit approval, so you must submit receipts substantiating charges invoiced.

In addition, you must prepare and attached to each completed invoice a Brief Report of Effort.

A. PREPARATION OF BRIEF REPORT OF EFFORT

Whenever you submit an Invoice for reimbursement to SCEEE you must also include a brief report describing your activities for the invoice period. To meet this obligation, you must prepare, date, sign, and attach to your completed invoice a Brief Report of Effort describing the research accomplished on the appointment and explain any travel during the invoice period.

This report should include innovative techniques and designs or discoveries which may be disclosed as patents. Rights to any inventions or discoveries shall reside with SCEEE unless determined otherwise by the contracting agency.

The Brief report should never exceed one typewritten page and most often should be considerably shorter than one page.

The following is an example of such a report:

BRIEF REPORT OF EFFORT

Effort has been initiated on pole extraction methods. The modified ordinary least squares technique has been giving fair results. Work is presently being done on finding a better matrix inversion technique for the case when the coefficient matrix is ill-conditioned. Some problems have been encountered with conditioning when the data is filtered.

Travel invoice is for the trip to my research location.

_____June, 16, 1982

B. PREPARATION OF INVOICE FORMAT

Detailed instructions on properly completing your Invoice Format for reimbursement are provided below. Review them carefully.

(1) In the opening statement of the claim for remuneration on the invoice format, two dates are required. They are the date of your appointment letter from SCEEE (in the first blank) and the date you signed that letter accepting your appointment (in the second blank).

Other financial items required on the Invoice Format are for COMPENSATION, TRAVEL, EXPENSE ALLOWANCE. These are now explained individually with examples.

(2) COMPENSATION

(a) In the first blank to the right of COMPENSATION indicate the number of days you are claiming for compensation in this particular invoice.

(b) In the next blank enter your SCEEE Researcher daily appointment rate of $55.00 or $65.00 as noted in your appointment letter.

(c) Multiply the number of days times your appointment rate and enter the total dollar amount in the blank at the far right side. Note that the accumulated total number of days you claim on this appointment may not exceed the number authorized in your appointment letter. Some specific details on the compensation days must be provided in the next space.

(d) Under the heading Date, list the date of each of the days you are claiming for compensation, and opposite each date under the heading Place of Activity indicate where you worked on that date.

A sample entry of a correctly completed COMPENSATION item is shown below:

SAMPLE COMPENSATION ENTRY ON INVOICE

COMPENSATION: (10 days @ $65.00 per day)..... $ 650.00 (II)

Date (Specify exact dates)	Place of Activity
June 3,4 1982	AFAPL/POD High Power Lab
June 7-11, 1982 (inclusive)	WPAFB Computer Center
June 14, 15, 16, 1982	AFAPL/POD High Power Lab

(3) TRAVEL

(a) Under the heading Date indicate the date you departed on your trip and the date you arrived at your destination.

(b) Under the heading Departure/Arrival Time list the departure and arrival times for the corresponding days you listed under Date.

(c) List your destination under the heading Destination.

(d) Under the heading Mode, indicate your principal means of conveyance; i.e., commercial air, private auto, etc.

(e) Under the heading Amount, itemize these expenditures for travel reimbursement.

(f) Total these travel items and enter the total dollar amount to be reimbursed for travel in this particular submission on the line to the right of Total Travel Expense.

An example of a correctly completed TRAVEL entry is shown below.

TRAVEL EXAMPLE: TRAVEL TO RESEARCH LOCATION BY PRIVATE AUTO

TRAVEL: (Attach receipts for all Airline or Bus charges. Payment cannot be made without receipts attached to invoice.)

Date	Departure/Arrival Time	Destination	Mode	Amount
5/27-6/2/82	0630/1530	Wright-Patterson AFB, Ohio	Private Auto	$480.00

One-way trip from home in Eugene, Oregon to Wright-Patterson AFB, Ohio, (2400 mi x 20¢/mi= $480.00)
(mileage at start: 24162; at end: 26562)

Total Travel Expense ..... $ 480.00 (III)

Please note the following comments about the TRAVEL EXAMPLE:

i) Travel by your private auto in lieu of a commercial airline is authorized as a convenience to the traveler.

ii) Travel with use of a privately-owned vehicle will be reimbursed at the rate of 20¢ per mile provided mileage is listed with the start and end mileage on each separate use for all distances over 100 miles.

(4) EXPENSE ALLOWANCE

This item on the invoice will be used to claim the $25 per day for reimbursement of costs incurred at your assigned research location.

(a) In the first blank to the right of EXPENSE ALLOWANCE enter the number of days for which you are claiming reimbursement of the expense allowance for costs incurred at your assigned research location.

(b) Multiply this number by the daily allowance rate of $25.00 and enter this total dollar amount in the blank at the far right.

(c) Itemize the days for which you are claiming the Expense Allowance reimbursement. It can include weekend days and holidays as well as regular work days.

The following is a sample of a correctly completed EXPENSE ALLOWANCE item.

SAMPLE

EXPENSE ALLOWANCE: (14 days @ $25.00/day)..... $ 350.00 (IV)

Specific dates covered:
7/3/82 - 7/16/82 (inclusive)

(5) You may combine reimbursement requests for compensation, travel, and expense allowance in the same invoice. The total for all items invoiced should be indicated on the blank labeled "GRAND TOTAL FOR INVOICE" in the lower right hand side of line 5.

(6) IMPORTANT: Indicate in the space provided on each invoice the address to which you want the check mailed.

(7) You must sign and date your invoice in the lower right hand corner as "VENDOR" before it is submitted; you MUST also have your Summer Faculty Research Program (SFRP) Supervising Faculty Member countersign the invoice before it is mailed to SCEEE.

Invoices should be mailed to:

GSSS PROGRAM OFFICE
SCEEE Central Florida Facility
1101 Massachusetts Avenue
St. Cloud, Florida 32769

GRADUATE STUDENT SUMMER SUPPORT PROGRAM
INVOICE FORMAT

(Brief Report of Effort Attached)

1. I claim remuneration from SCEEE, Inc. via the terms and conditions of the agreement dated_____and accepted_____ as follows:

2. COMPENSATION: (_____days @ $_____ per day).....$_____(II)

Date (Specify exact dates) Place of Activity

3. TRAVEL: (Attach receipts for all Airline or Bus charges. Payment cannot be made without receipts attached to invoice.)

Date	Departure/Arrival Time	Destination	Mode	Amount

Total Travel Expense ..... $_____(III)

4. EXPENSE ALLOWANCE: (_____days @ $25.00/day..... $_____(IV)

Specific dates covered:

5. GRAND TOTAL FOR INVOICE (Sum of II, III, IV above)..... $_____(V)

6. Please send check to following address:

7. I certify that compensation invoice is not concurrent with compensation received from other Federal government projects, grants, contracts, or employment.

X_____
SFRP SUPERVISING FACULTY SIGNATURE

Location of Faculty_____

Telephone _____

Date _____

X_____
VENDOR SIGNATURE

Social Sec. No._____

Telephone_____

Date _____

GRADUATE STUDENT'S QUESTIONNAIRE & SUMMARY

1982 USAF/SCEEE GRADUATE STUDENT SUMMER SUPPORT PROGRAM
EVALUATION QUESTIONNAIRE
(TO BE COMPLETED BY GRADUATE STUDENT PARTICIPANT)

Name _____ Title _____
Dept. (at home) _____ Home Institution _____
Summer Supervising Professor _____
Research Colleague(s) _____
Laboratory Address of Colleague(s) _____
Brief Title of Research Topic _____

A. TECHNICAL ASPECTS

1. Was the offer of research assignment within your field of competency and/or interest? YES___ NO___.

2. Was the work challenging? YES___ NO___. If no, what would have make it so? _____
_____

3. Were your relations with your Supervising Professor and research colleague satisfactory from a technical point of view? YES___ NO___. If no, why? _____
_____

4. Suggestions for improvement of relationship(s). _____
_____
_____

5. Considering the circumstances of a summer program, were you afforded adequate facilities and support? YES___ NO___. If no, what did you need and why was it not provided? _____
_____

6. Considering the calendar "window" of ten weeks being limited by varying college and university schedules, please comment on the program length.
Did you accomplish: more than____, less than____, about what you expected____?

7. Do you feel the Graduate Student appointment should continue to require affiliation with a Summer Research Faculty Member? YES___ NO___.

8. Were you asked to present seminars on your work and/or your basic expertise? YES___ NO___. Please list number, dates, approximate attendance, length of seminars, title of presentations (use reverse side if necessary.)

GRADUATE STUDENT QUESTIONNAIRE (Page 2 of 3)

9. Were you asked to participate in regular meetings in your laboratory? YES___NO___.
If yes, approximately how often?_____

10. Other comments concerning any "extra" activities._____
_____
_____

11. On a scale of A to D, how would you rate this program? (A high, D low)

Technically challenging	A	B	C	D
Future research opportunity	A	B	C	D
Professional association	A	B	C	D
Enhancement of my academic qualifications	A	B	C	D
Enhancement of my research qualifications	A	B	C	D
Overall value	A	B	C	D

B. ADMINISTRATIVE ASPECTS

1. How did you first hear of this program?_____
_____

2. What aspect of the program was the most decisive in causing you to apply?_____
_____

3. How do you rate the stipend level? Meager___Adequate___Generous___.

4. Please give information on housing: Did you reside in VOQ___, apartment___,
other (specify)_____? Name and address of apartment complex and manager's name.
_____

5. Would you encourage or discourage expansion of the Student Program?_____
Why?_____

6. Considering the many-faceted aspects of administration of a program of this magnitude, how do you rate the overall conduct of this program?
Poor___Fair___Good___Excellent___. Please add any additional comments._____
_____
_____

GRADUATE STUDENT QUESTIONNAIRE (Page 3 of 3)

7. Please comment on what, in your opinion, are:

a. Strong points of the program: _____

_____

_____

b. Weak points of the program: _____

_____

_____

8. On balance, do you feel this has been a fruitful, worthwhile, constructive experience? YES___ NO___.

9. Other remarks: _____

_____

_____

_____

_____

_____

_____

_____

THANK YOU

QUESTIONNAIRE EVALUATION SUMMARY

A. TECHNICAL ASPECTS

1. Assignment in field of competency and/or interest? Yes - 17 No - 0

2. Work Challenging? Yes - 16 No - 1

3. Relations with Professor and Colleague satisfactory? Yes - 16 No - 1

   If no, why? Poor communication stemming from personality clash.

4. Suggestions for improvement? Professor and Graduate Student should be closely associated; a few more informal discussions with USAF people were needed; student needs to be more involved with USAF people; the Air Force was not aware of the guidelines of my status with SCEEE; better briefings are needed prior to beginning the research work; close association with professor is essential.

5. Afforded adequate facilities? Yes - 17 No - 0

6. Accomplishment in ten weeks? More than expected - 4 Less than expected - 6
   About what expected - 7

7. Should Graduate Student appointment continue to require affiliation with faculty member? Yes - 12 No - 5

8. Asked to present seminars? Yes - 2 No - 15

9. Asked to participate in meetings? Yes - 7 No - 10

10. Other comments on extra activities? It is helpful to talk to other chemists; had good opportunity to visit related USAF activities; several tours were organized to acquaint us with AFESC facilities; we were also able to attend lectures concerning current projects underway; the chance to observe other engineering techniques at the Avionics Lab was excellent; had the opportunity to meet several government scientists, needed travel funds to other AF locations, I was invited to attend siminars at RADC.

11.

Technically Challenging?	A - 10 B - 6 C - 1 D - 0
Future Research Opportunity?	A - 10 B - 4 C - 1 D - 2
Professional Association?	A - 10 B - 5 C - 1 D - 1
Enhancement of my academic qualifications?	A - 7 B - 8 C - 1 D - 1
Enhancement of my research qualifications?	A - 9 B - 8 C - 0 D - 0
Overall value?	A - 9 B - 7 C - 1 D - 0

B. ADMINISTRATIVE ASPECTS

1. First hear about program? Through local faculty; through faculty at the University of Dayton; Bulletin Board at Chemistry Department; from my advisor; from my supervising professor; by university faculty member; fellow student at Penn State; asked by research faculty member to join him; asked a university professor about some possible summer work so he informed me about this program.

2. Decisive aspect of application? Needed summer work; financial consideration; research experience gained; opportunity to work on topic of interest; opportunity to work at government research labs; working with my advisor on a real world problem; professor asked me to go so I went; to get engineering experience; the pay and the location; the fact that I was going to be at WPAFB whether I was a Graduate Fellow or not; opportunity to work with professionals and enhance my research skills; tough for student researchers to find work in their field - this was such a job; offered the opportunity to work full-time without the usual university interruptions and on a one-to-one basis with my advisor; monetary and future references; a chance to do some research and become familiar with the workings of the Air Force.

3. Stipend level? Meager - 1 Adequate - 9 Generous - 7

4. Housing information? VOQ - 4 Apartment - 3 Other - 10

5. Encourage or Discourage expansion of Student program? Encourage - 17 Discourage - 0

6. Program administration overall rating? Poor - 0 Fair - 2 Good - 9 Excellent - 6

7. A. Strong Points of Program? Good research experience for student as well as developing good relations with Air Force - I've become much more aware of the opportunities within the government; research opportunity in field of interest and good salary; 1) well organized 2) strong colleague interest and support 3) excellent laboratory assistance; experience in lab setting and monetary benefits are the strongest points - students need both; opportunity to dive head-long into a problem with the individual attention from a faculty member; the availabilty of Air Force resources; excellent alternative to teaching summer courses; freedom left to Graduate Student to research a topic worthwhile to himself and his colleagues; Graduate Student support makes SFRP more effective.

B. Weak Points of Program? Requiring faculty sponsorship; minimal connection of Graduate Student with faculty member and payment time lag between submitted invoice to check arrival; not enough time allowed; short length of program; lack of opportunity for continuation; excessive paper work, rules and regulations; conflicts arose with our Air Force research colleagues concerning the access of information, many valuable publications were not made available to us until the end of our 10 week stay; Graduate Students style is cramped by having to work for faculty; Graduate Student final report; not knowing in the beginning what living and working conditions would be; difficulty in surviving financially; It would be more convenient for Graduate Student to know what summer program they were involved with sooner.

8. Has this been a fruitful, worthwhile, constructive experience? Yes - 17 No - 0

APPENDIX I

1. Program Statistics

2. List of 1982 Graduate Students

3. Graduate Student Laboratory Assignments

1982 USAF/SCEEE GRADUATE STUDENT SUMMER SUPPORT PROGRAM

Conducted by
SOUTHEASTERN CENTER FOR ELECTRICAL ENGINEERING EDUCATION, INC.

PROGRAM STATISTICS

1. Number of Air Force Installations (Laboratories/Centers) - 10

2. Applications Received (First Choice as Follows) - 38

APL	(W-PAFB)	- 3	GL	(Hanscom)	- 1
AMRL	(W-PAFB)	- 7	HRL/FTD	(Williams)	- 1
AD	(Eglin)	- 1	LMC	(Gunter)	- 1
AL	(W-PAFB)	- 2	ML	(W-PAFB)	- 8
BRMC	(W-PAFB)	- 1	RADC	(Griffiss)	- 4
ESC	(Tyndall)	- 1	SAM	(Brooks)	- 2
FJSRL	(USAFA)	- 1	WL	(Kirtland)	- 4
		Unknown - 1			

3. Number of Participants - 17

Number holding Masters Degree - 1
Number holding Bachelors Degree - 16

4. Average Age of Participants - 24.4 years

5. Distribution of Participants Location

APL	(W-PAFB)	- 2	FJSRL	(USAFA)	- 1
AMRL	(W-PAFB)	- 3	GL	(Hanscom)	- 1
AD	(Eglin)	- 1	ML	(W-PAFB)	- 3
AL	(W-PAFB)	- 1	RADC	(Griffiss)	- 3
ESC	(Tyndall)	- 1	WL	(Kirtland)	- 1

6. Disciplines Represented - 9

Chemical Engineering	- 1	Industrial Engineering	- 2
Chemistry	- 2	Mathematics	- 1
Civil Engineering	- 1	Mechanical Engineering	- 1
Computer Science	- 1	Physics	- 4
Electrical Engineering	- 4		

PROGRAM STATISTICS - PAGE TWO

7. Number of Colleges/Universities Represented - 15

Boston University
Carnegie Mellon University
Colorado State University
Dayton, University of (2)
Florida, University of
Kansas, University of
Kent State University
Kentucky, University of
Missouri/Rolla, University of
New Mexico, University of
Oklahoma, University of
Pennsylvania State University (2)
South Florida, University of
Wright State Unviersity
Wittenberg University

8. Number of States/US Territories Represented - 11

Colorado
Florida
Indiana
Kansas
Kentucky
Massachusetts
Missouri
New Mexico
Ohio
Oklahoma
Pennsylvania

NAME/ADDRESS	DEGREE, SPECIALTY, LABORATORY ASSIGNED
Robin Archer University of Dayton Chemical Engineering Department Dayton, OH 45469 (513) 229-6227	Degree: B.S. in Chemical Engineering 1982 Specialty: Biomedical Engineering Assigned: APL
James Bogan Colorado State University Physics Department Ft. Collins, CO 80523 (303) 491-7723	Degree: B.S. in Physics, 1975 Specialty: Ring Laser & Dye Laser Amp. Assigned: FJSRL
Mary Doddy Univeristy of Dayton Mechanical Engineering Department Dayton, OH 45469 (513) 229-2238	Degree: B.E. in Mechanical Engineering, 1980 Specialty: Mechanical Engineering (Design & Materials) Assigned: AMRL
Brenda Evans Wright State University Chemistry Department Dayton, OH 45435 (513) 873-2855	Degree: B.S. Ed. Biology, Chemistry, Physical Science, 1981 Specialty: Organic and Polymer Chemistry Assigned: ML
Dorothy Fitzgerald Boston University College of Engineering Boston, MA 02215 (617) 353-2823	Degree: B.S. in Geology, 1977 Specialty: Computer Science Assigned: AD
Jeffery Harpster Penn State University Industrial Engineering Department University Park, PA 16802 (814) 865-7601	Degree: B.S. in Industrial Engineering, 1982 Specialty: Ergonomics Engineering Assigned: AMRL
David Israel University of Florida Civil Engineering Department Gainesville, FL 32601 (904) 392-0933	Degree: B.S. in Civil Engineering, 1982 Specialty: Geotechnical Engineering Assigned: ESC
Jeffrey Kallman Carnegie-Mellon University Electrical Engineering Department Pittsburgh, PA 15213 (412) 578-3030	Degree: M.S. in Electrical Engineering, 1981 Specialty: Biological Control Threory Assigned: AMRL

NAME/ADDRESS	DEGREE, SPECIALTY, LABORATORY ASSIGNED
James Kempton Wittenberg University Physics Department Springfield, OH 45504 (513) 323-6600	Degree: B.A. in Physics, 1982 Specialty: Solid State Physics Assigned: AL
Tim Krimm University of Kentucky Electrical Engineering Department Lexington, KY 40515 (606) 272-3802	Degree: B.S. in Electrical Engineering, 1982 Specialty: Electromechanics Assigned: APL
John Newman University of New Mexico Physical Chemistry Department Albuquerque, NM 87123 (505) 296-7674	Degree: B.S. in Chemistry Specialty: Physical Chemistry Assigned: WL
Craig A. Paul Kansas University Computer Science Department Lawrence, KS 66045 (913) 864-4832	Degree: B.S. in Computer Science, 1980 Specialty: Computer Science Assigned: RADC/Griffiss
Gregory Punkar Kent State University Physics Department Kent, OH 44242 (216) 672-2880	Degree: B.S. in Physics, 1981 Specialty: Physics Assigned: ML
Jeffrey Swindle University of Missouri-Rolla Electrical Engineering Department Rolla, MO 65401 (314) 364-4180	Degree: B.S. in Electrical Engineering, 1981 Specialty: Optics Assigned: RADC/Griffiss
Rodney Wetterskog University of Oklahoma Physics Department Norman, OK 73019 (405) 325-3961	Degree: B.S. in Physics, 1981 Specialty: Atomic and Molecular Physics Assigned: GL
Kevin Wilson University of South Florida Electrical Engineering Department Tampa, FL 33620 (813) 974-2582 ext. 285	Degree: B.S. in Engineering Specialty: Microelectronics-Experimental and Theoretical Assigned: RADC/Griffiss

NAME/ADDRESS	DEGREE, SPECIALTY, LABORATORY ASSIGNED
Brian Wood Pennsylvania State University Industrial Engineering Department State College, PA 16801 (814) 234-8168	Degree: B.S. in Industrial Engineering, 1982 Specialty: Industrial Engineering Assigned: ML

PARTICIPANT LABORATORY ASSIGNMENT

1982 USAF/SCEEE GRADUATE STUDENT SUMMER SUPPORT PROGRAM

AERO PROPULSION LABORATORY
(Wright-Patterson Air Force Base)
1. Ms. Robin Archer - University of Dayton
2. Mr. Tim Krimm - University of Kentucky

AEROSPACE MEDICAL RESEARCH LABORATORY
(Wright-Patterson Air Force Base)
1. Ms. Mary Doddy - University of Dayton
2. Mr. Jeffrey Harpster - Pennsylvania State University
3. Mr. Jeffrey Kallman - Carnegie-Mellon Unviversity

ARMAMENT DIVISION
(Eglin Air Force Base)
1. Ms. Dorothy Fitzgerald - Boston University

AVIONICS LABORATORY
(Wright-Patterson Air Force Base)
1. Mr. James Kempton - Wittenberg University

ENGINEERING & SERVICES CENTER
(Tyndall Air Force Base)
1. Mr. David Israel - University of Florida

FRANK J. SEILEER RESEARCH LABORATORY
(USAF Academy)
1. Mr. James Bogan - Colorado State University

GEOPHYSICS LABORATORY
(Hanscom Air Force Base)
1. Mr. Rodney Wetterskog - University of Oklahoma

MATERIALS LABORATORY
(Wright-Patterson Air Force Base)
1. Ms. Brenda Evans - Wright State University
2. Mr. Gregory Punkar - Kent State University
3. Mr. Brian Wood - Pennsylvania State University

ROME AIR DEVELOPMENT CENTER
(Griffiss Air Force Base)
1. Mr. Craig Paul - Kansas University
2. Mr. Jeffrey Swindle - University of Missouri/Rolla
3. Mr. Kevin Wilson - University of South Florida

WEAPONS LABORATORY
(Kirtland Air Force Base)
1. Mr. John Newman - University of New Mexico

APPENDIX II

1. Listing of Research Reports Submitted in the 1982 Summer Faculty Research Program

2. *Abstracts of the* 1982 Associate's Research Reports

RESEARCH REPORTS

1982 GRADUATE STUDENT SUMMER SUPPORT PROGRAM

Volume I Report Number	Title	Graduate Researcher
1	Conceptualization of the Dynamic Behavior of the Flow-Field in APL Combustor	Robin S. Archer
2	Technology Development for the Study of Laser Damage in Plastics	James R. Bogan
3	A Dynamic Model of Acceleration Stress Protection in the Human Aircrew Member	Mary Doddy
4	Synthesis of Acetylene Terminated Sulfone (ATS) Candidates	Brenda G. Evans
5	Improvement in the Numeric Solution of Aerodynamic Equations	Dorothy A. FitzGerald
6	Modeling of Active neuromusculature Response to Mechanical Stress	Jeffrey L. Harpster
7	Static and Dynamic Response of Aircraft Shelters	David L. Israel
8	Trials and Tribulations at the Helmet Mounted Oculomotor Facility	Jeffrey S. Kallman
9	Oxygen Implantation of Gallium Arsenide	James R. Kempton
10	Electrically Compensated Constant Speed Drive	Tim W. Krimm

Volume I Report Number	Title	Graduate Researcher
11	Photoionization of Iodine Molecules and Clusters in a Supersonic Molecular Beam	J. Kent Newman
12	A Simplified Users Guide for the ICSSM Communications Package	Craig A. Paul
13	A Model for Pulsed Laser Annealing of Silicon	Gregory D. Punkar
14	Analysis and Modeling of a Real-Time Holography System	Jeffrey M. Swindle
15	The Measurement of Ion-Molecule Reaction Rate Coefficients	Rodney E. Wetterskog
16	Analysis and Comments on the Theory of the Capacitance-Ratio Test	Kevin Wilson
17	The Manufacturing Control Language for Robotic Work Cell	Brian O. Wood

CONCEPTUALIZATION OF THE DYNAMIC BEHAVIOR OF THE FLOW-FIELD IN THE APL COMBUSTOR

by

Sarwan S. Sandhu and Robin S. Archer

ABSTRACT

Results of a brief investigation of the dynamic behavior of a bluff-body stabilized diffusion flame are presented for air and fuel flow rates of 1kg/s and 6kg/hr, respectively. A cine film, acquired at 4000 frames/s, of the reacting flow field near the bluff-body was analyzed with regard to time variant interaction between the annulus air stream and the flame stabilizing recirculation zone. Air vortices generated from the shear layer of the air stream appear to interact with the recirculating zone while growing as they move downstream. Estimated air vortex average axial and rotational velocities are 22.8 m/s and 548.9 rad/s, respectively. Estimated peripheral average angular velocity of reactive fluid recirculating zone is 506.5 rad/s. Fluid, made visible by dispersed reacting and emitting relatively "small" sized gaseous pockets, appears to move upstream in a core about the centerline towards the recirculating spatial region. Reacting fluid, made visible by light emission, appears to be peeled off the recirculating reactive zone in the form of cylindrical shells with irregular boundaries at quasi-periodic intervals. Ratio of air vortex to flame turbule frequency at an axial dimensionless location of 0.68 is about 2/1.

TECHNOLOGY DEVELOPMENT FOR THE STUDY OF LASER DAMAGE IN PLASTICS

by

James R. Bogan

Abstract

Certain transparent plastic materials have exhibited laser damage thresholds comparable to conventional optical materials such as glass. To ascertain the physical properties of these materials which enhance their resistance to pulsed laser beam damage, several experiments were initiated with laser pulses which will repeatably produce damage. Finally, the construction, alignment, and testing of a nitric oxide Raman cell wavelength shifter is described. This device is used in conjunction with a Q-switched Nd:Glass laser system, to derive high peak power infrared light pulses of wavelengths of 1.315 microns, as well as 1.06 microns for the study of laser damage in plastics.

A DYNAMIC MODEL OF ACCELERATION STRESS PROTECTION IN THE HUMAN AIRCREW MEMBER

by

Patrick J. Sweeney, Ph.D., P.E.

Mary Doddy, M.S.

ABSTRACT

This dynamic simulation computer model demonstrates the affects of G-forces upon the eyeball pressure of the aircrew member in various G-force environments. The stress relieving affects of G-suits and aircrew straining (M-1 and L-1 maneuvers) are dramatically depicted. The changes in the straining maneuver programs are evident in eyeball pressure and energy drain on the aircrew members. Further research in this area will undoubtedly result in improved aircrew performance in high and varying G-force environments.

SYNTHESIS OF ACETYLENE TERMINATED SULFONE (ATS) CANDIDATES

by

James J. Kane

and

Brenda G. Evans

ABSTRACT

Certain acetylene terminated sulfone (ATS) systems are of interest as possible replacements for epoxy resins. The beneficial feature which the ATS systems are expected to offer is their insensitivity to moisture. Reaction schemes for their synthesis are outlined and discussed. Finally, the synthesis of certain of the intermediates required for the ATS candidates are reported and discussed and recommendations for future work in this area are presented.

IMPROVEMENT IN THE NUMERIC SOLUTION OF AERODYNAMIC EQUATIONS

by

Dorothy A. FitzGerald
Luigi Morino

ABSTRACT

An improvement is made in the algorithm for the time-domain integration of the potential aerodynamic equations. The new method of solution is considerably faster than the old one (which is already about one order of magnitude faster than the only competitor) and the results indicate that considerable additional savings can be achieved, especially if parallel processing is utilized. It was noted that with the above changes, the solution of the steady state problem using a time domain transient analysis can be faster than by direct Gaussian elimination of the steady state equation. An attempt is made to extend the same idea to oscillatory flows.

MODELING OF ACTIVE NEUROMUSCULATURE RESPONSE TO MECHANICAL STRESS

by

Dr. Andris Freivalds

and

Mr. Jeffrey L. Harpster

ABSTRACT

The Articulated Total Body (ATB) Model, based on rigid-body dynamics with Euler equations of motion and Lagrange type constraints, was used to predict the forces and motions experienced by air crew personnel in typical flight operations. To provide a more realistic representation of human dynamics, an active neuromusculature was added to the ATB Model via the newly developed advanced harness system. The lumped three parameter muscle model included a contractile element, a damping element and a parallel elastic element.

Two validation studies were performed. The first simulated elbow flexion with one muscle/harness system representing the biceps brachii and the brachialis. The results indicated that the force velocity effects produced the greatest changes in force, with significant force changes due to the damping element and length tension relationship and no force changes due to the parallel-elastic element. The second study simulated the whole body response to a 2-G_y lateral force utilizing trunk musculature. Although the musculature did not completely prevent the lateral deflection of the body, the response is significantly delayed compared to a control response, with the head and neck maintaining the upright posture for a longer period of time.

Static and Dynamic Response

of Aircraft Shelters

by

David L. Israel

ABSTRACT

The feasibility of a fourth generation aircraft shelter is investigated. The development of mathematical models, simulating a double-radius cylindrical shelter are presented. The models are analyzed both statically and dynamically with the use of SAP IV (Structural Analysis Program).

Investigations of various loading conditions were performed to determine the effect of assumed threats on the structure. Structural response under each of the loading cases is studied in an attempt to determine which parts of the shelter will be subjected to the most severe stresses. Suggestions are offered as to which type of model and loading configuration would be the most representative and realsitic for any future development in this area.

TRIALS AND TRIBULATIONS AT THE HELMET MOUNTED OCULOMOTOR FACILITY

by

A. Terry Bahill & Jeffrey S. Kallman

ABSTRACT

We spent most of the summer debugging the Helmet Mounted Oculometer Facility (HMOF) equipment. On our last day we were finally able to gather data on human head and eye coordination. We brought this data back to Carnegie-Mellon University; we were able to put it on our computer system and analyze it with our programs.

OXYGEN IMPLANTATION OF GALLIUM ARSENIDE

by

James R. Kempton

ABSTRACT

The development of a stable semi-insulating layer in ion-implanted gallium arsenide is investigated. Analysis of samples, implanted with oxygen-18, by Rutherford backscattering and Capacitance-Voltage techniques discloses thick compensating layers with a low amount of damage after an 800°C anneal. Suggestions for further research on this material are offered.

ELECTRICALLY COMPENSATED CONSTANT SPEED DRIVE

by

Tim W. Krimm

and

Jimmie J. Cathey

ABSTRACT

The feasibility of designing a constant speed drive utilizing a mechanical differential in conjunction with a parallel electric drive speed compensation link is examined. Bidirectional power flow in the electric compensation link uses two high-speed, permanent-magnet, three-phase machines interconnected by a power conditioning network. One machine is operated as a brushless dc machine, while the other functions as a variable speed synchronous machine. Steady-state performance of two types of power conditioning are studied--a dc link inverter and a cycloconverter link.

The dc link inverter with bidirectional power flow is found to require excessive values of current to allow full range reverse power flow. A mode switch to synchronous inversion is necessary to reduce current values, but it adds the penalty of increase in power electronic devices and control complexity. The cycloconverter link is found to offer the better full range bidirectional power flow. In addition, a dc link system is examined for a method of operation with unidirectional power flow through the compensation link at the expense of increased size of electrical machines, but offering simpler controls.

Suggestions are made for further research on this system concept.

PHOTOIONIZATION OF IODINE MOLECULES AND CLUSTERS IN A SUPERSONIC MOLECULAR BEAM

by

Edward A. Walters

and

J. Kent Newman

ABSTRACT

In preparation for a study of the photoionization of I_2, I_3, I_4, etc. a photoionization mass spectrometer employing a supersonic molecular beam emerging from a small nozzle was relocated from Los Alamos National Laboratory. Much of the effort described here has to do with moving and critical alignment of the mass spectrometer. Also described are the results of a literature survey of the photoionization and photoelectron spectroscopy literature on the important iodine molecules and clusters. Design of a nozzle for the generation of I_3 is discussed. Work done in interfacing a PDP 11/23 computer to the mass spectrometer and initial results of software development for controlling the experiments are described.

A SIMPLIFIED USERS GUIDE FOR THE ICSSM COMMUNICATIONS PACKAGE

by

Craig A. Paul

ABSTRACT

The Interactive Communications System Simulation Model (ICSSM) was presented to RADC by Hazeltine Corporation on June 16, 1982. The accompanying users manual, while presenting some information for running the ICSSM package and programming to add simulation capabilities to ICSSM was far too detailed in some cases, lacked important information in other cases, and required too much knowledge of the internal workings of the package for the manual to make much sense to the user and potential programmer.

Hazeltine presented a half-day briefing for potential ICSSM users and left a users manual behind. After two and a half weeks of reading the users manual, some conversations with Hazeltine, and examination of the ICSSM FORTRAN coding I could implement my own ICSSM modules and explain to others via a seminar and a short users guide how to really use ICSSM to simulate communication systems

and install their own ICSSM modules into the package.

Included in this report is a half-page users guide and an ICSSM programmers guide. The programmers guide is intended as a supplement to be referred to concurrently while examining certain sections of the ICSSM users manual.

A MODEL FOR PULSED LASER ANNEALING OF SILICON

by

Gregory D. Punkar

ABSTRACT

In this paper we seek a solution of the thermal diffusion equation, which describes pulsed laser annealing of silicon. This equation is a non-linear differential equation with temperature-dependent parameters; functional forms are fitted to these parameters using empirical data. For the non-homogeneous case (including the incident laser source term), the equation is solved numerically, using an adiabatic approximation to incorporate the temperature dependences of thermal and optical properties. Melt depths and evaporation losses are also tabulated numerically using energy balance equations.

An analytical method for solving the homogeneous equation is introduced, applicable for certain functional forms of temperature-dependent thermal properties. This method is not incorporated into the above-mentioned model; however, we include it as it may be useful in other contexts.

ANALYSIS AND MODELING OF A REAL-TIME HOLOGRAPHY SYSTEM

by

Jerome Knopp

and

Jeffrey M. Swindle

ABSTRACT

The real-time holography system was studied in some detail using a generic model. It is shown that aberrations are introduced by wavelength rescaling. Further errors are generated by the very nature of phase recording a hologram plus the non-linearities in the recording media. Resolution requirements and MTF limitations show that present day phase recording devices are just barely adequate to correct low level turbulence.

A study of the system using dimensional analysis showed that the Fresnel approximation may be used to construct a scale model based on Arkadiew's Law.

THE MEASUREMENT OF ION-MOLECULE REACTION RATE COEFFICIENTS

by

Thomas M. Miller and *Rodney E. Wetterskog*

ABSTRACT

Rate coefficients have been measured for C^+, CO^+, and CO_2^+ reactions with O_2 over a temperature range of 90-450 K using a selected-ion flow-tube (SIFT) apparatus at the Air Force Geophysics Laboratory. Charge transfer is observed to take place for $CO^+ + O_2$ and $CO_2^+ + O_2$, but is not allowed energetically for $C^+ + O_2$. Instead, we observe $C^+ + O_2 \rightarrow O^+ + CO$ and $C^+ + O_2 \rightarrow CO^+ + O$ *occurring.* The $C^+ + O_2$ reaction is found to proceed at its gas kinetic rate of about 9×10^{-10} cm^3/s, independent of temperature for 90-450 K. The rate coefficients for both the $CO^+ + O_2$ and $CO_2^+ + O_2$ reactions are decreasing functions of temperature in this range. The ion flow velocity in the SIFT apparatus has been determined versus gas pressure and temperature using a time-of-flight technique. These results, combined with our helium flow measurements, have significant implications for low-temperature reaction experiments with flow-tube reactors.

ANALYSIS AND COMMENTS ON THE THEORY OF THE CAPACITANCE-RATIO TEST

BY

R. L. REMKE

K. WILSON

University of South Florida

ABSTRACT

A detailed analysis is given on the theory of the capacitance-ratio test used in the detection of moisture in hermetically sealed microelectronic packages. The model for the moisture-induced frequency-dependent capacitance observed between pins of an integrated circuit is developed. This model is then extended to describe its use in the capacitance-ratio test. Also included are some observations and comments concerning the implementation and use of the capacitance-ratio test.

THE MANUFACTURING CONTROL LANGUAGE FOR ROBOTIC WORK CELLS

by

Mark A. Fugelso and Brian O. Wood

ABSTRACT

Under contract F33615-78-C-5189 within the United States Air Force ICAM program, the McDonnell Douglas Corporation has developed the Manufacturing Control Language (MCL) for use with robotic work cells. An extension of the numerical control language APT, MCL contains control words for real time decision making and vision processing. These facilities, along with several other features, make this language a versatile off-line programming tool. This paper gives a basic overview of MCL's capabilities. Suggestions for further research in this area are offered.

APPENDIX III

1982 Graduate Student Final Reports

1982 USAF-SCEEE GRADUATE STUDENT SUMMER SUPPORT PROGRAM

Sponsored by the

AIR FORCE OFFICE OF SCIENTIFIC RESEARCH

Conducted by the

SOUTHEASTERN CENTER FOR ELECTRICAL ENGINEERING EDUCATION

FINAL REPORT

CONCEPTUALIZATION OF THE DYNAMIC BEHAVIOR OF THE FLOW-FIELD IN THE APL COMBUSTOR

Prepared by:	Robin S. Archer
Academic Department:	Chemical Engineering
University:	University of Dayton
Research Location:	Aero Propulsion Laboratory Wright Patterson Air Force Base
USAF Research Contact:	Dr. W. M. Roquemore
SFRP Supervising Faculty Member:	Dr. S. S. Sandhu Assistant Professor

Date:	July 23, 1982
Contract No:	F49620-82-C-0035

ACKNOWLEDGEMENTS

The author would like to thank the Air Force Office of Scientific Research, the Southeastern Center for Electrical Engineering Education, and the Aero Propulsion Laboratory, WPAFB for providing the opportunity of a worthwile summer experience. She would also like to thank Dr. W. M. Roquemore and Mr. Royce Bradley for helpful discussions. The supervision of Dr. S. Sandhu during the course of this investigation is acknowledged. The expert typing skill of Mrs. Mary Lu Kinzeler is appreciated.

CONCEPTUALIZATION OF THE DYNAMIC BEHAVIOR OF THE FLOW-FIELD IN THE APL COMBUSTOR

by

Sarwan S. Sandhu and Robin S. Archer

ABSTRACT

Results of a brief investigation of the dynamic behavior of a bluff-body stabilized diffusion flame are presented for air and fuel flow rates of 1kg/s and 6kg/hr, respectively. A cine film, acquired at 4000 frames/s, of the reacting flow field near the bluff-body was analyzed with regard to time variant interaction between the annulus air stream and the flame stabilizing recirculation zone. Air vortices generated from the shear layer of the air stream appear to interact with the recirculating zone while growing as they move downstream. Estimated air vortex average axial and rotational velocities are 22.8 m/s and 548.9 rad/s, respectively. Estimated peripheral average angular velocity of reactive fluid recirculating zone is 506.5 rad/s. Fluid, made visible by dispersed reacting and emitting relatively "small" sized gaseous pockets, appears to move upstream in a core about the centerline towards the recirculating spatial region. Reacting fluid, made visible by light emission, appears to be peeled off the recirculating reactive zone in the form of cylindrical shells with irregular boundaries at quasi-periodic intervals. Ratio of air vortex to flame turbule frequency at an axial dimensionless location of 0.68 is about 2/1.

CONCEPTUALIZATION OF THE DYNAMIC BEHAVIOR OF THE FLOW-FIELD IN THE APL COMBUSTOR

Objective and Introduction

The main objective of the effort expended in the ten week summer period was to clarify the dynamic behavior of the flow-field in the APL combustor in the "near bluff-body spatial region". Such clarification helps in gaining insight into the air and fuel mixing process resulting in reactant consuming exothermic combustion process. Unsteady flame behavior was observed and studied in terms of flame turbules in the APL combustor,[1,2,3] using cine photograpic and CH emission recording techniques. Later, high speed Mn-laser shadowgraphy and cine photography were employed to further shed some light on the dynamic behavior of the APL combustor. A cine film acquired at 4000 frames per second for air flow rate of 1kg/s and fuel flow rate of 6kg/hr indicated the dynamic behavior more clearly. Dynamic behavior of the flow field was investigated by analyzing the cine and high speed shadowgraphic films.

Methods of analyses to acquire various types of qualitative and quantitative information regarding the dynamic behavior of the flow field are described. Deduced dynamic flow field is approximately depicted as contour diagrams. Quantitative estimated results on air indentation (or vortex) axial velocity, its growth rate and frequency; flame turbule frequency and length for air flow rate of 1kg/s and fuel flow rate of 6kg/hr are briefly discussed. Estimated characteristic dimensions of the CO_2 jet for air flow rate of 1kg/s and CO_2 flow rate of 4kg/hr are also reported.

EXPERIMENTAL

Combustion Rig

A schematic diagram of the Aero Propulsion Laboratory (APL) combustion tunnel is shown in Figure 1. The centerbody is 79 cm. long and 14 cm. in diameter. Gaseous propane fuel is injected through a 4.8 mm diameter tube at the center of the centerbody. Air flows through the annular space between the outer duct and the centerbody. A 31.8 mm long square-cell honeycomb flow straightener with a cell size of 4.8 mm square and two number 16 mesh screens are mounted in the annulus. The 25.4 cm diameter duct has 30.5 x 7.6 cm viewing ports that provide both optical and conventional probe access to combusting regions. Additional information about the combustion tunnel is given in References 1 and 3.

QUALITATIVE CHARACTERIZATION OF FLOW FIELD

The qualitative characterization of the flow field of the bluff-body diffusion flame was obtained by examining shadowgraphic and cine films of the flame at an air flow rate of 1kg/s and fuel flow rates of 4 and 6kg/hr. The shadowgraphic films were shot at 6583 frames/s and the cine films at 4000 frames/s. Two hundred photographic stills were obtained from the cine films and used for closer examination. The viewing port did not facilitate the visualization of the entire flame so that the flame was assumed to be symmetrical and only half was investigated.

QUANTITATIVE DATA COLLECTION

The cine films, shadowgraphic films, and photographic stills were used to quantify certain aspects of the flow field. In all cases, the bluff-body image diameter was measured and a magnification factor obtained to facilitate the conversion of image measurements to real values. The cine films were used to determine air indentation or vortex

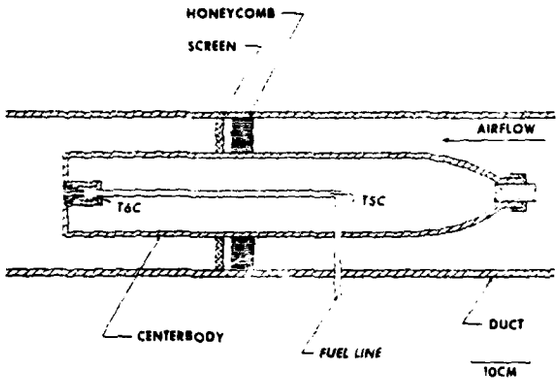

Figure 1. Combustion Rig

linear velocities, flame turbule and air vortex shedding frequencies, and recirculation zone rotational velocity. The photographic stills were used to measure flame turbule length and air vortex and recirculation zone rotational velocities. The shadowgraphic films were used to determine the cold jet dimensions for CO_2 flow rate of 4kg/hr and air flow rate of 1kg/s.

The presence of an air vortex was detected by observing the air-reaction zone interface. An indentation of the reactiong zone, caused by the vortexing air, indicated the presence of an air vortex. These indentations were used to measure air vortex shedding frequency and velocities. The presence of a flame turbule was indicated by the formation of a cylindrical shell of reacting and emitting fluid which moved downstream.

AIR VORTEX SHEDDING AND FLAME TURBULE FREQUENCIES

Two locations were chosen to measure air vortex shedding frequency; 5 and 9.5 cm downstream of the bluff-body face. Flame turbule frequency was determined at a location 9.5 cm downstream of the bluff-body face. The cine film was viewed at 2 frames/s to measure frequencies.

When measuring air vortex shedding frequency, the number of indentations that appeared in a set number of frames was counted; the number of indentations and number of frames were recorded. The frequency was obtained by dividing the number of indentations by the time equivalent of the number of frames. Ten and nine independent measurements were taken at the 5 and 9.5 cm locations, respectively. The arithmetic mean of the measurements was found to give an average air vortex shedding frequency at each location.

To measure flame turbule frequency, the number of reacting fluid shells which passed by the location in a set number of frames was recorded. Six independent measurements were made and those results were averaged to yield an average flame turbule frequency.

AIR VORTEX LINEAR VELOCITIES

For simplification of analyses, as well as to make the results more consistent and less subjective, each air vortex was assumed to be circular. The center and arc of the vortex were then traced through a series of frames, corresponding to a real time interval. The velocity in the Z-direction was determined by measuring the movement of the vortex center in the Z-direction. The velocity in the y-direction, the growth rate, and the flame velocity were determined in the following manner.

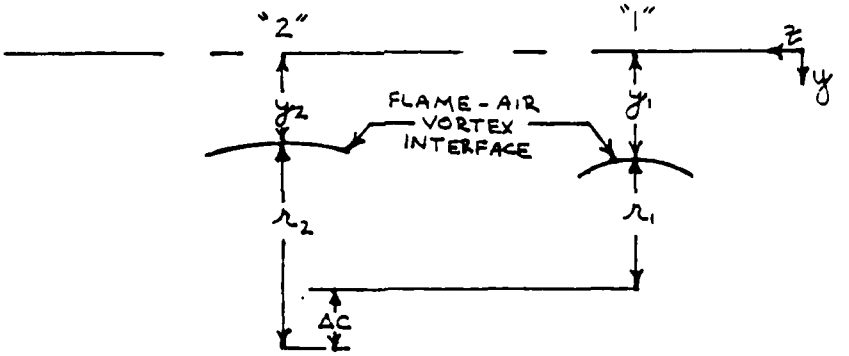

$$\therefore\ y_2 + r_2 - \Delta C = y_1 + r_1$$

$$y_2 - y_1 = \Delta C - (r_2 - r_1)$$

$$\therefore\ \frac{y_2 - y_1}{\Delta t} = \frac{\Delta C}{\Delta t} - \frac{2(r_2 - r_1)}{2\,\Delta t},$$

WHERE Δt IS THE TIME INTERVAL FROM "1" TO "2"

∴ (Air vortex-flame interface radial velocity) = (air vortex center radial velocity) - 1/2 (air vortex diametrical growth rate)

The flame-air vortex interface velocity was measured by drawing horizontal tangents to the vortex curves. Air vortex center velocity in the y-direction was measured by the movement of the vortex center in the y-direction. Growth rate was determined from twice the change in radii of the vortex curves.

RECIRCULATION ZONE ROTATIONAL VELOCITY

The recirculation zone rotational velocity was determined using photographic stills under the assumption that the air vortex was an identifiable object on the recirculation zone. The angle swept by the vortex in a set number of frames was recorded. The rotational velocity was determined by dividing the angle by the time equivalent of the frames. Such measurements were performed on five distinct air vortices.

FLAME TURBULE LENGTH

The flame turbule length was found by use of the photographic stills. Appropriate frames in which the turbule was apparent were found and the length was determined directly from the picture by the application of magnification factor. Figure 2 illustrates two such appropriate frames. Four independent measurements were made and the results were averaged to give an average flame turbule length.

AIR VORTEX ROTATIONAL VELOCITY

The photographic stills were used to measure air vortex rotational velocity. A series of frames were selected in which an identifiable eddy was present. Figure 3 shows one such series. The angle swept from one frame to the next was measured and from this the air vortex angular velocity was determined. Eleven independent measurements were made and the arithmetic mean was calculated to give an average air vortex

Air flow rate = 1kg/s
Fuel flow rate = 6kg/hr

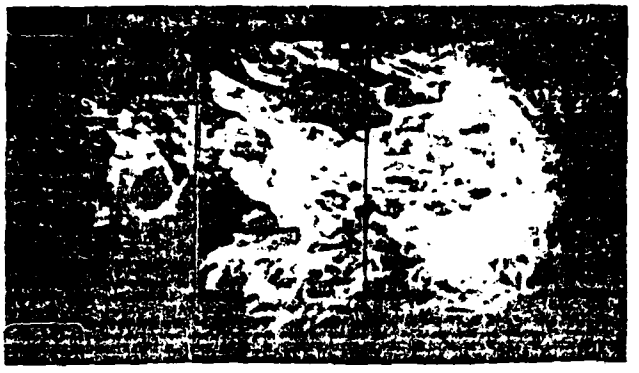

(1)

(2)

Figure 2. Photographic stills made from cine film (framing speed 4000/s) illustrating method of estimation of flame turbule length

Air flow rate = 1kg/s
Fuel flow rate = 0kg/hr

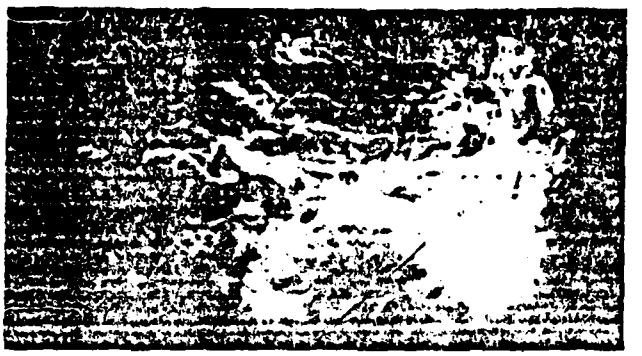

(1)

(2)

Figure 3. Photographic "stills" made from cine film (framing speed, 4000/s) illustrating method of estimation of air indentation rotational velocity.

(3)

(4)

Figure 3. (continued)

rotational velocity.

COLD JET DIMENSIONS

In the shadowgrapic film, the outline of the cold jet was visible. The jet consists of a linearly expanding portion, originating at the bluff-body. This conical portion terminates in a "mushroom" portion.

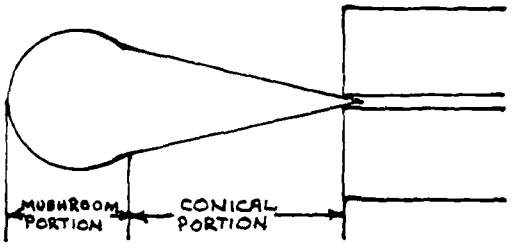

The diameter at the end of the conical portion of the jet and the axial position of this diameter, the maximum jet diameter and the axial position of this diameter, and the axial position of the end of the jet were measured and recorded. Six independent measurements of each dimension were taken and averaged to yield the average cold jet dimensions.

RESULTS AND DISCUSSIONS

A MODEL OF NEAR REGION REACTING FLOW FIELD IN THE WAKE OF THE BLUFF-BODY

Figure 4 depicts a model of near flow field deduced from cine and high speed shadowgraphic film analyses. A picture of the flow-field indicated is considered to be applicable for air flow rate of 1kg/s and fuel flow rate range up to 6kg/hr. Fuel jet, 1, spreads in a conical manner up to Z/D = 0.4 by entraining fluid from the surrounding environment. Fuel jet "mushroom" is apparent between Z/D = 0.4 to 0.7. Fuel jet "mushrooming" can be thought of as a resultant effect of backward flow, 2 , interaction against the forward flowing jet fuel, and inner, 3 and outer, 5 recirculation zones. Analyses of high speed shadowgraphic films indicate that fuel jet mushroom "wobbles" with time. The jet mushroom wobbling phenomenon may be explained in terms of fluid interactions and time varying turbulence structure of the jet-surrounding flow field. Jet fuel and hot backward flowing fluid, 2, are shown to mix as indicated by 4 . The hot fluid and jet fuel keep on mixing by turbulence and molecular diffusion processes while the mixed fluid moves upstream towards the face of the bluff-body, 9 . The mixed flow fluid stream, 4 splits into two portions. One becomes part of the inner recirculation zone,3, and the other part of the outer recirculation zone, 5. Structure and rotational orientation of the inner recirculation zone is indicated by 3. The jet fuel and the inner recirculation zone fluid mixing could occur via turbulent entrainment and molecular diffusion processes. Time varying structures of outer recirculation zone,5, and air indentation (or, air vortex), 6, are depicted in Fig. 4 a - e. Recirculation zone, 5 extends to almost Z/D

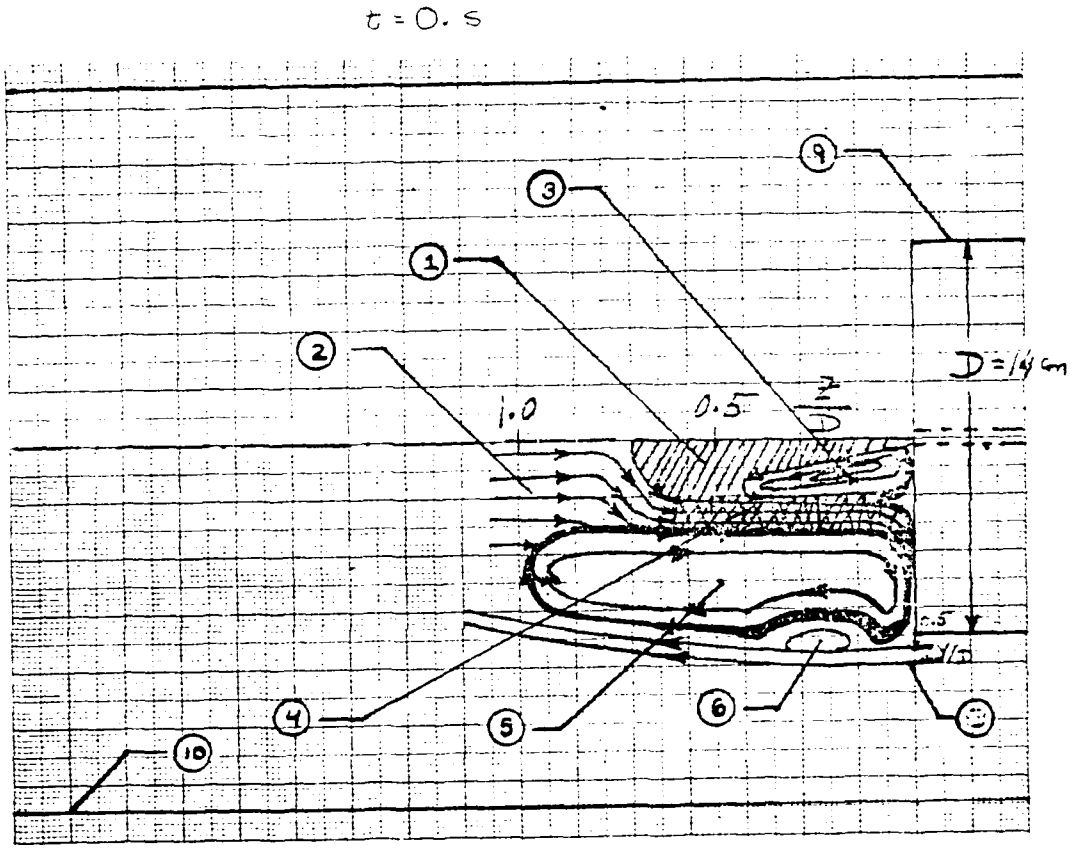

(cc)

Figure 4. A conceptual model of near region reacting flow field in the wake of the bluff-body in the APL combustor. Scale: 1/2 of full size.

LEGEND

Fuel jet, 1

"Backward Flow" 2

Inner recirculation zone, 3

"Mixed Upstream Flow" 4

"Outer Recirculation Zone" 5

Air Vortex, 6

Flame turbule fragment, 7

Annulus air stream, 8

Cylindrical bluff-body incorporating fuel injection tube, 9

Combustion duct, 10

Figure 4 (continued)

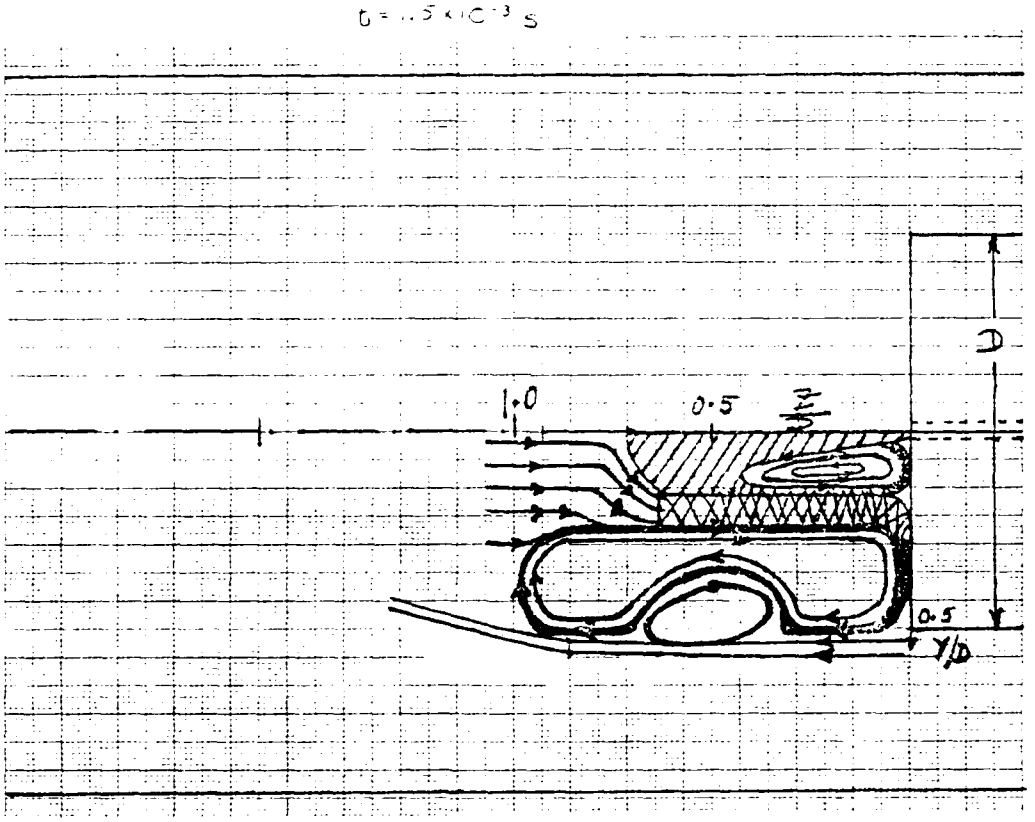

(b)

Figure 4. (continued)

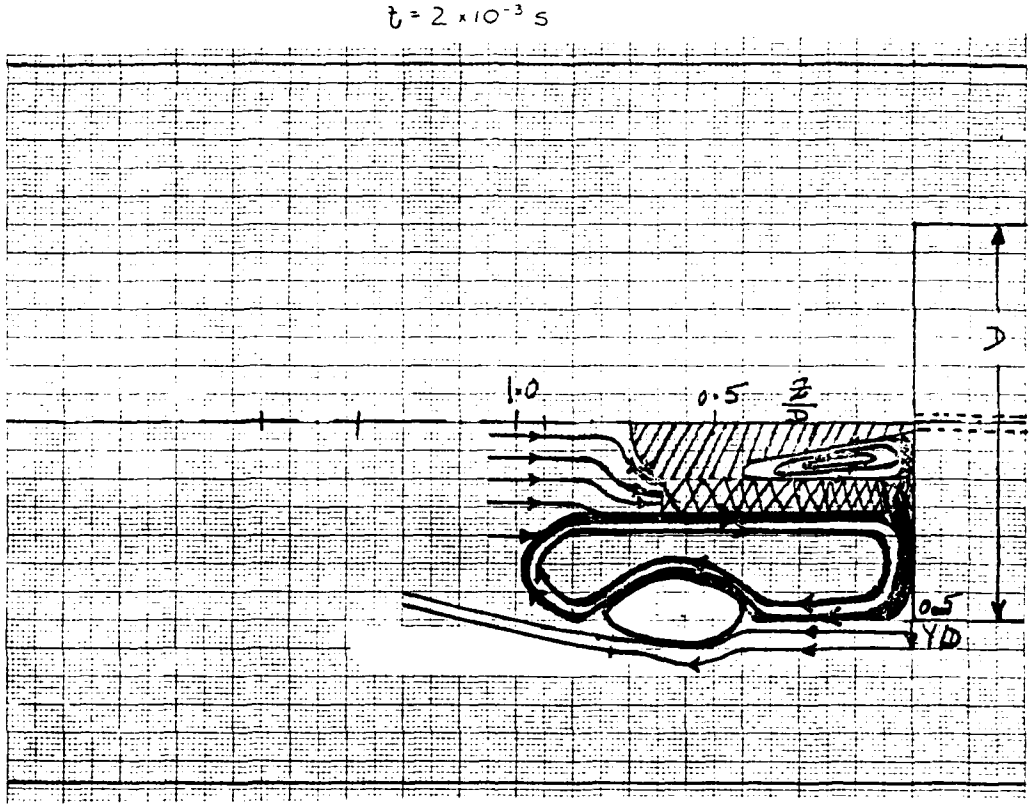

(c)

Figure 4. (continued)

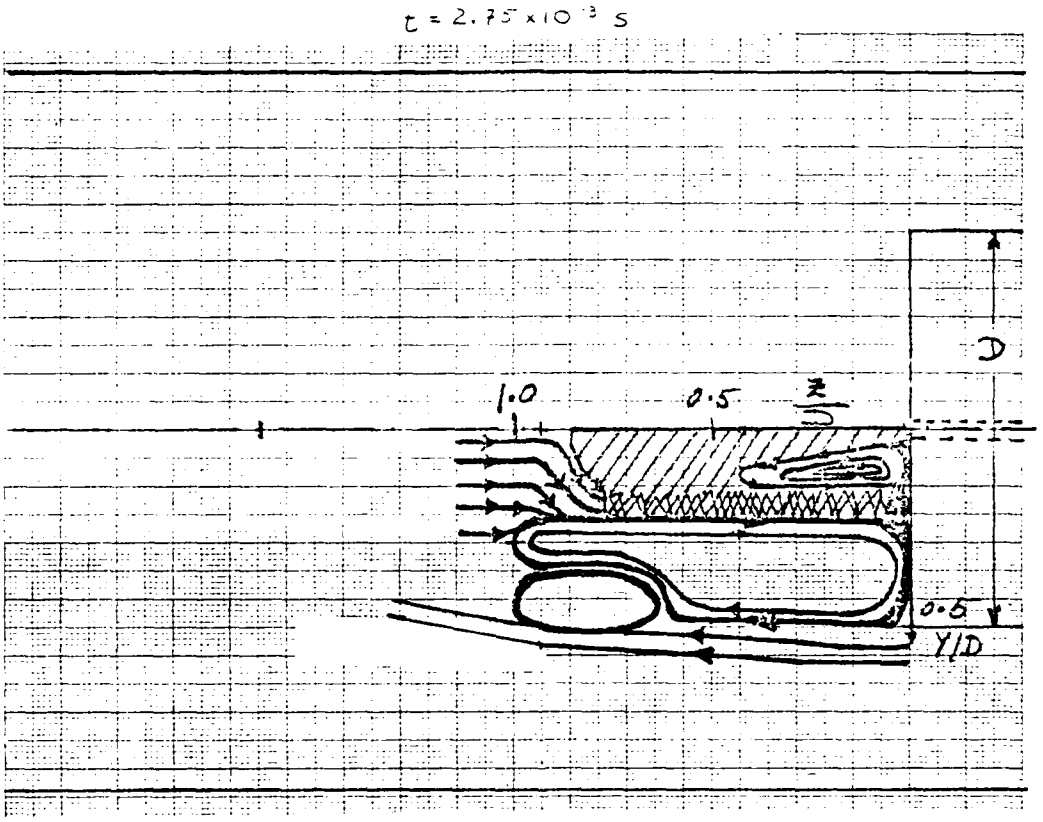

Figure 4. (continued)

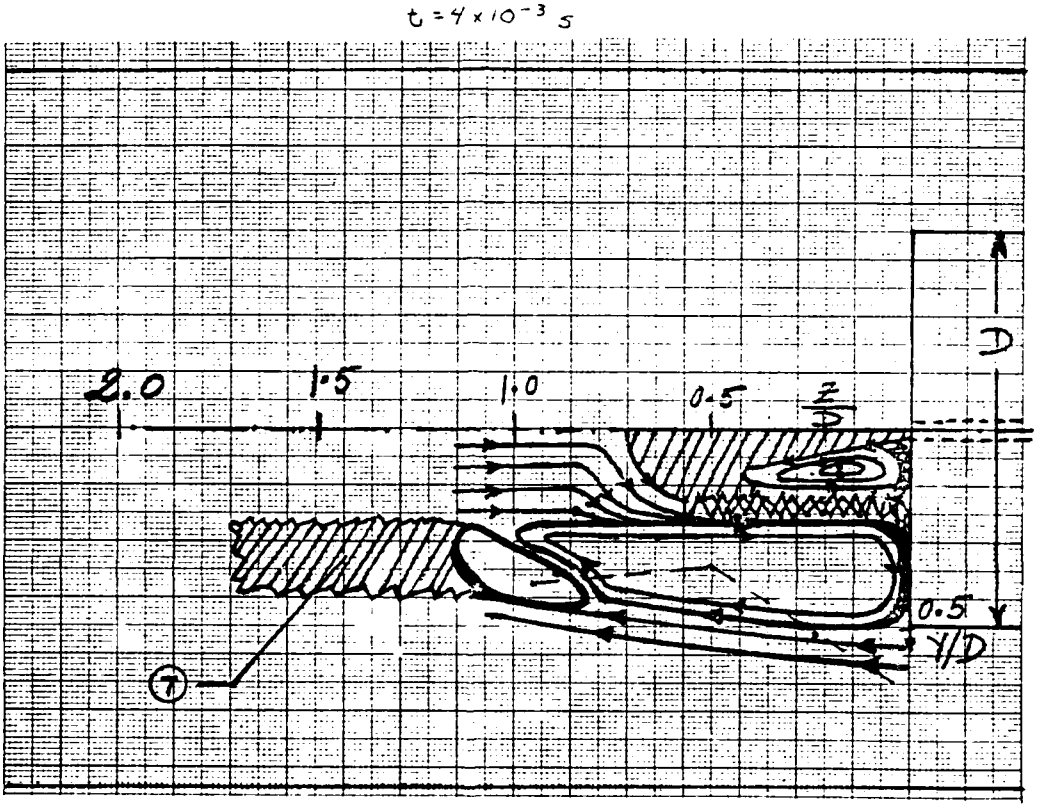

(e)

Figure 4. (continued)

Air flow rate = 1kg/s
Fuel flow rate = 6kg/hr

(1)

(2)

Figure 5. Photographic stills made from cine film (framing speed,4000/s)showing air indentation (vortex) growth.

(3)

Figure 5. (continued)

= 1.0, and Y/D ~ 0.5. It is pointed out here that the outer recirculation zone boundary may fluctuate around these size limits. Air indentation or vortex, 6, is made visible by interaction of annulus air against reacting and illuminating fluid in the outer recirculation zone. Air vortex appears to grow as indicated by Fig. 4 and photographic stills, Fig. 5. Air vortex moves downstream with average estimated axial velocity of about 22.8 m/s which is close to annulus air velocity of 23.3 m/s. Assuming air vortex as an identifiable object attached to the periphery of the outer recirculation zone, estimated peripheral angular velocity of the recirculation zone is 506.5 radians/s. Air turbule growth may be attributed to its fluid heating as it moves downstream by exchange of heat energy between the relatively hot reacting fluid in the recirculation zone and vortex fluid. Some dispersion of the reacting fluid of the outer recirculating zone into the air vortex is also indicated by cine film analyses. Quasi-periodic interaction of air turbules with the outer recirculation zone fluid can be thought to augment mixing of the jet fuel with the surrounding fluid. Fig. 4 e indicates an ideal situation of an air vortex arrival at the downstream end of the outer recirculation zone. Such a situation often coincides with "slipping" of an irregularly bounded cylindrical shell of reacting fluid in the downstream direction. It is interesting to note that the ratio of air vortex to flame turbule frequency determined at location of Z/D ~ 0.7 is about two to one, and average flame turbule length being about 9 cm determined at this location. These results are specifically valid for air flow rate of 1kg/s.

Fluid evacuation of the recirculation region in terms of frequency associated flame turbules may be speculated as a mechanism to maintain time average mass conservation of the recirculating fluid spatial

region. Just after the moment of "detachment" of a flame turbule, upstr am moving fluid appears to speed-up to undo the effect of fluid evacuation of the recirculation region. The upstream moving fluid is speculated to slow down as mass and thermal energy content of the recirculation region dynamically increases to a "saturation" point for an air and fuel flow rate combination. The moment the saturation point is reached, the recirculation zone is thought to be most unstable and ready to loose fluid in the form of irregularly surfaced cylindrical shells.

The view about the rotation of air indentation or vortex, 6, is as follows. Air vortices are generated from shear layer of annulus air stream in the vicinity of the bluff-body cylindrical surface. The probable rotational sense, clockwise, is in opposition to that of the outer recirculation zone, 5 . Rotational sense of the air vortex should not be necessarily taken as opposing the linear motion of fluid elements on the periphery of the outer recirculation zone. If one imagines that the downstream directional net of the downstream convection and tangential velocity of a point on the vortex periphery closest to the recirculation zone is greater or equal to the linear velocity of a fluid element on the periphery of the recirculation zone, rotating vortex does not oppose motion of the recirculation zone fluid. This explanation is in agreement with what has been observed in relevance to the dynamic behavior of the near flow field spatial region. Alternatives to the above explanation are: (a) no air vortex rotation, (b) a pair of two fluid vortices, one nearer to the air stream, rotating clockwise and the other nearer to the recirculation zone rotating counterclockwise. At the time of the writing of this report the explanation given prior to

the alternatives appears to be more appropriate. Vortex angular velocity estimated from photographic stills is 548.9 rad/s.

A comment concerning the relationship of the flow-field to the combustion process is as follows. Fuel combustion takes place in the spatial region consisting of inner and outer recirculation zones sandwiching a mixed upstream flowing fluid in between them in three dimensional space. Escape of the fuel from the near flow field region can be thought of in terms of irregularly surfaced cylindrical flame turbules slipping downstream of the flow-field region, at least, for fuel flow rates of less than 6kg/hr and air flow rate of 1kg/s.

Air Indentation (or vortex) Axial Velocity, Growth Rate, Frequency

Table 1 shows the air indentation estimated axial velocity component and growth rate data used to determine the average values. Arithmetic average values of axial velocity component and growth rate are 22.78 $\pm$ 11.4 (std. dev.) m/s, and 12.6 $\pm$ 8.96 (std. dev.) m/s, respectively. Data show the variation in axial velocity and growth rate as a function of the dimensionless axial distance, Z/D. Even at the same location respective parametric values differ for different air turbules. Variation in these parametric values could be explained in terms of spatial and temporal variations in chemical reaction rate resulting in heat release rate, and variation in fluid dynamic interaction process occurring at the interface between the reacting fluid in the recirculation zone and the relatively less hot surrounding air stream.

Table 2 shows air indentation (vortex) frequency determinations at two axial locations of Z/D = 0.36 and 0.68. Frequency at Z/D = 0.36 is 177.4 $\pm$ 8.8 (std. dev.) Hz as compared with that of 143.4 $\pm$ 9.8 (std.

TABLE 1

AIR INDENTATION OR VORTEX AXIAL VELOCITY COMPONENT
AND ITS GROWTH RATE

Air Flow Rate = 1kg/s
Fuel flow rate = 6kg/hr

Z/D, dimensionless axial distance	Axial velocity component, $V_{x,a}$ m/s	Growth rate, m/s
0.16	16.38	6.3
0.21	12.60	4.2
0.24	28.35	12.6
0.28	15.75	0
0.34	13.23	22.04
0.34	30.23	10.5
0.37	34.65	37.8
0.38	13.23	15.74
0.44	13.44	8.4
0.48	31.50	12.6
0.49	51.02	8.4
0.51	15.75	-
0.56	11.34	12.6
0.60	31.50	12.6
Average	22.78	12.6
±Std. Dev.	±11.4	±8.96

TABLE 2

AIR INDENTATION (OR VORTEX) FREQUENCIES

Frequency, Hz

Z, location
of frequency determination from face of the bluff-body

	Z = 5 cm	Z = 9.5 cm
	168.00	144.00
	176.00	160.00
	176.00	122.00
	164.06	144.93
	194.29	142.86
	186.33	140.19
	173.16	138.41
	181.82	151.72
	170.37	146.67
	184.33	
Average	177.44	143.42
± Std Dev	± 8.78	±9.73

dev.) Hz at Z/D = 0.68. This implies that for every ten air indentations at the upstream axial location only about eight identations make themselves identifiable at the downstream location. This is indicative of probable air indentation coalescing phenomenon. Occurrence of the phenomenon is, perhaps, due to variation in the dynamic behavior of air indentations as they move downstream. This view is supported by the data in Table 2.

Flame Turbule Frequency and Length

Table 3 shows flame turbule frequency and length determined at an axial location of Z/D = 9.5/14 = 0.68. Flame turbule frequency of 70.6 ± 4.0 (std. dev.) Hz is less in comparison with air turbule frequency of 143.4 ± 9.8 (std. dev.) Hz at the same axial location. This translates into one slipping of "an irregularly surfaced cylindrical reacting fluid region from the recirculating spatial region" for every two air indentations appearing. Average flame turbule length is 9.0 ± .6 (std. dev.) cm. This type of information is suggestive of development of empirical mathematical expressions to predict air vortex and flame turbule frequencies, and, flame turbule length for a given air/fuel flow rate combination in a bluff-body diffusion flame combustor of the APL type. The empirically developed mathematical expressions might then be utilized to develop a mathematical "flame turbule" combustion model to predict combustion performance of a given combustor of the above said type.

Cold Flow CO_2 Jet Characteristics, and, Air Vortex and Flame Interface Location and Radial Velocity

Table 4 shows the various dimensions of cold flow CO_2 jet issuing into the combustor space for an air/fuel flow rate combination of 1kg/s/ 4kg/hr. It is appropriate to mention that the dimensions reported were

TABLE 3

FLAME TURBULE FREQUENCY AND LENGTH AT AXIAL LOCATION OF 9.5 CM FROM THE FACE OF THE BLUFF-BODY

	Frequency (Hz)	Length (cm)
	67.80	8.40
	72.95	
	70.26	8.40
	68.89	9.28
	78.05	9.80
	65.57	
Average	70.59	8.97
±Std. Dev.	+4.02	± 0.60

TABLE 4

DIMENSIONS OF COLD FLOW CO_2 JET ISSUING INTO THE APL COMBUSTOR

CO_2 flow rate = 4kg/hr

Air flow rate = 1kg/s

Jet diameter at Z = 0 is 4.8mm

Set No.	Z_c,cm	d_c,cm	Z_{max},cm	d_{max},cm	Z_e,cm
1	6.24	1.9	6.51	4.61	9.77
2	5.70	2.44	7.60	5.43	10.31
3	5.97	2.71	7.60	5.43	10.31
4	5.70	2.71	7.60	4.89	9.23
5	5.97	2.99	7.60	5.19	10.04
6	5.70	2.17	7.60	5.43	10.59
Mean	5.88+.20	2.49	7.42	5.16±.31	9.99±.45
±Std. Dev.		±.37	±0.41		

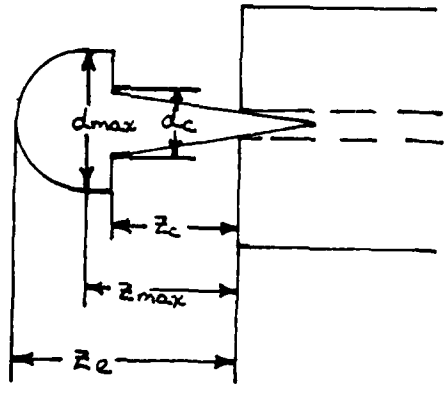

deduced from a shadowgraphic film recorded by means of Mn-laser with average firing frequency of 6563/s. CO_2 jet diameter spreads from 0.48 cm at Z/D = 0 to 2.49 cm at Z/D = 5.88/14 = 0.42 in a linear manner. Downstream of Z/D = 0.42, jet spreads in to "mushroom". Jet mushrooming phenomenon is explained in terms of the backward flow and the jet fluid interaction, and the influence of the dynamic behavior of the jet surrounding flow-field. Jet mushroom maximum diameter is 5.16 cm at Z = Z_{max} = 7.42 cm; cherefore, (jet mushroom maximum dia.)/(jet cone maximum dia.) is 2.0. Maximum jet length is about 10.0 cm. Such type of information regarding fuel jet is useful in developing predictive combustion model in light of involvement of the fuel jet surface and volume in reactant species mixing and combustion processes.

Table 5 shows the air vortex and flame interface location and radial velocity towards the combustor centerline. Variation in Yint/D as a function of Z/D may be envisioned as "flame surface wrinkling" of the reactive zone. Yint/D fluctuates within 0.31 ~ 0.48 for Z/D variation from 0.16 to 0.60. Variation in the interface radial velocity towards the centerline as function of Z/D is also observed.

TABLE 5

RADIAL VELOCITY COMPONENT, $V^{+}_{Y,T}$, INTERFACE BETWEEN THE OUTER RECIRCULATION ZONE REACTING FLUID AND AN AIR INDENTATION OR VORTEX

Air flow rate = 1kg/s
Fuel flow rate = 6kg/hr

Z/D	Yint/D	$V_{y,t}$, m/s
0.16	.48	0.00
0.21	.47	-1.68
0.24	.47	-6.93
0.28	.45	-7.56
0.34	.39	-0.63
0.34	.44	-5.88
0.37	.43	-4.41
0.38	.38	-5.04
0.44	.35	-6.72
0.48	.40	-10.71
0.49	.42	-2.10
0.51	.33	-3.78
0.56	.31	-8.19
0.60	.38	-1.26
Average		-4.64
$\pm$ Std. Dev.		$\pm$ 3.10

+ Movement of the interface along radius towards the centerline is considered negative

TABLE 6

Recirculation Zone Rotational

Velocity determination

Air flow rate = 1kg/s
Fuel flow rate = 6kg/hr

Vortex #	Rotational velocity (rad/s)
1	546.87
2	477.06
3	314.16
4	570.14
5	624.0
Average	506.45
Std. Dev.	$\pm$107.1

Summary of Main Conclusions

1. Dynamic behavior of the near-region combusting flow field in the wake of the bluff-body appears to be resulting from temporal and spatial interactions among the jet fuel, upstream moving fluid, and annular air stream. Such interactions lead to an interesting flow-field as shown in Figure 4 for air flow rate of 1kg/s and fuel flow rate of 6kg/hr or less.

2. "Outer recirculation zone" dimensionless size limits appear to extend to about 1.0 and 0.5 in axial and radial directions, respectively, for air flow rate of 1kg/s and fuel flow rate of 6kg/hr or less. Average peripheral rotational velocity of the recirculation zone is 506.5 rad/s.

3. Fuel escaping from combustion in the near flow field spatial region, in the wake of the bluff-body, can be thought of in terms of irregularly surfaced flame cylindrical shells that slip off the flow field region quasi-periodically.

4. Ratio of air vortex/flame turbule or shell frequency is about 2/1 for the flow rate combination investigated (Air flow = 1kg/s, fuel flow = 6kg/hr).

5. Air indentation or vortex interacting with the reacting, heat generating, and light emitting fluid has estimated average axial velocity of 22.8 m/s and rotational velocity of 548.9 rad/s.

6. The internal cold flow conical jet appears to spread linearly with the axial distance and then changes into instable "mushroom". The jet fluid appears to be pulled into the surrounding environment as partially indicated in Figure 4.

Recommendations

Although by means of the information generated from cine and high speed shadowgraphic photography it has been possible to develop a partial picture of the dynamic behavior of the near region flow field in the wake of the bluff-body in the APL combustor, more quantitative information regarding time variant system variables such as velocity and pressure throughout the entire flow field would be needed to complete the picture. Truly, one needs to know instantaneous values of the above mentioned variables simultaneously at a number of points in the spatial region in the wake of the bluff-body. Local instantaneous information in the entire flow field should be gathered as function of time for an isothermal cold flow under investigation. Because for a combusting flow dynamic behavior would be different, at least in magnitude of the values of behavior related parameters if not in gross trends, simultaneous spatial time variant quantitative information regarding velocity, pressure, and, for maximum usefulness of the generated data, additional information regarding temperature and species concentrations should be experimentally acquired. A comprehensive data acquisition scheme is suggested as follows. For each combination of air and fuel flow rates spatial region extending from Z/D = 0. to 1.5 and, Y/D = 0. to 0.7 is proposed for probing with 1/2 cm distance between adjacent points. For each of two air flow rate conditions of 1 and 2kg/s, fuel flow rate conditions to be investigated are 2,4,6 and 8,10,12 kg/hr. In addition, cine films for combusting flows and high speed shadowgraphic films for isothermal CO_2 and air jet combinations would be useful. After gathering such experimental information one would be in a better situation to gain deeper insight and develop a more sophisticated explanation of the dynamic behavior of the flow field, and, hence, of

the combustion process.

REFERENCES

1. Roquemore, W.M., Bradley, R.P., Stutrud, J.S., Reeves, C.M., and Krishnamurthy, L., "Preliminary Evaluation of a Combustor for Use in Modeling and Diagnostic Development," ASME Publication 80-GT-93, March, 1980.

2. Sandhu, S.S., "Study of Dynamic Behavior of a Bluff-body Diffusion Flame in the APL Combustion Tunnel Facility," 1981 USAF SCEE Summer Faculty Research Program, Final Report, Contract No. F49620-79-0038.

3. Roquemore, W.M., Britton, R.L., and Sandhu, S.S., "Investigation of the Dynamic Behavior of a Bluff-body Diffusion Flame Using Flame Emission," presented at the AIAA 20th Aerospace Sciences Meeting, January, 1982.

FLOW-FIELD VECTOR DIAGRAMS

In the final two weeks of the project, vector diagrams of the proposed flow-field were constructed. The hand drawn diagrams, the computer-generated plots, and the tabulated data are found in this Appendix. W is the magnitude of the vector and $\measuredangle$ is the angle the vector makes with the positive Z axis.

To generate the diagrams, first a model was used to obtain relative magnitudes of the vectors. Then known rotational velocities and dimensions were used to arrive at the actual vector magnitudes. Vector angles were obtained by using the contour diagrams as a guide.

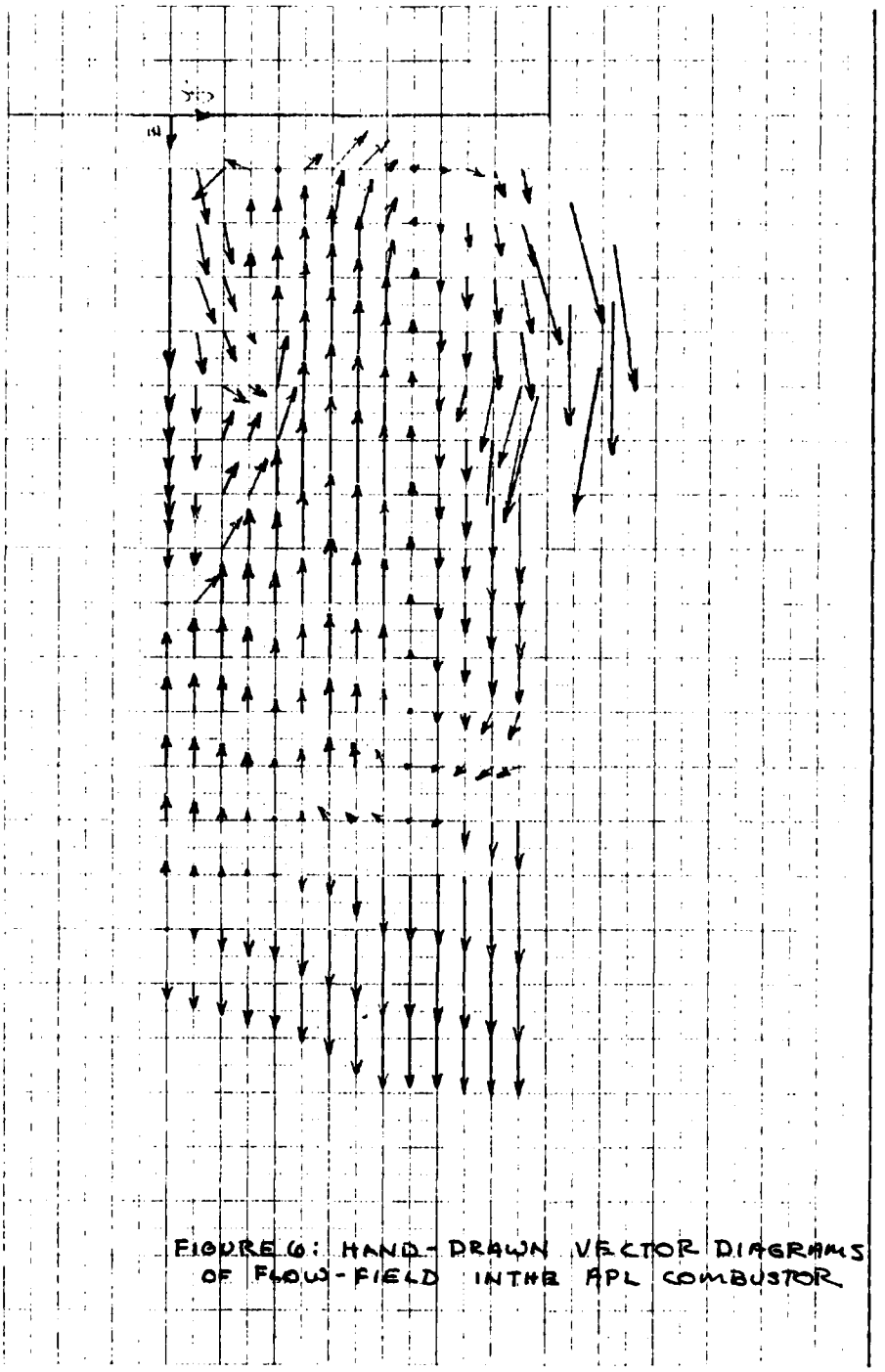

FIGURE 6: HAND-DRAWN VECTOR DIAGRAMS OF FLOW-FIELD IN THE APL COMBUSTOR

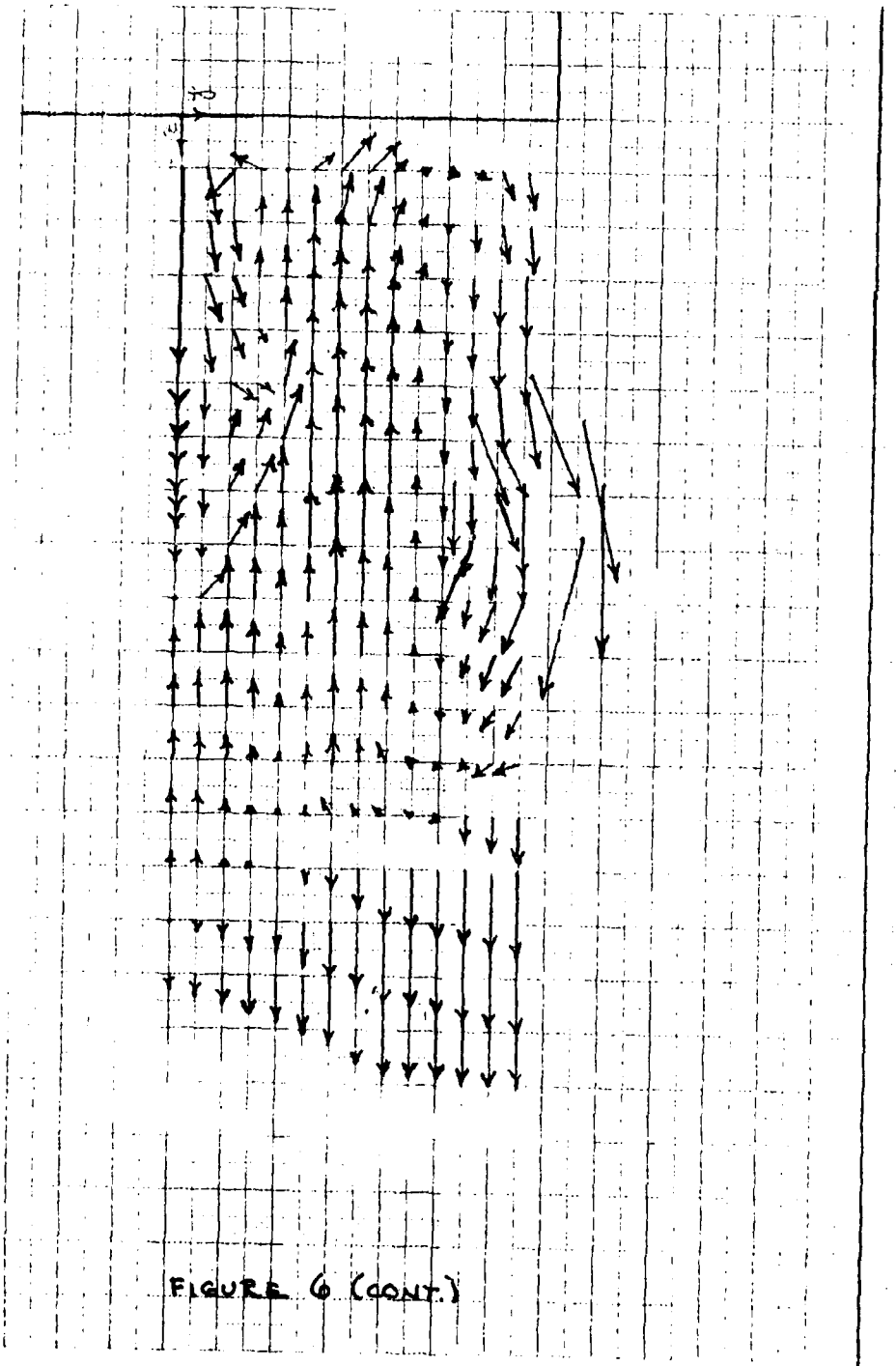

FIGURE 6 (CONT.)

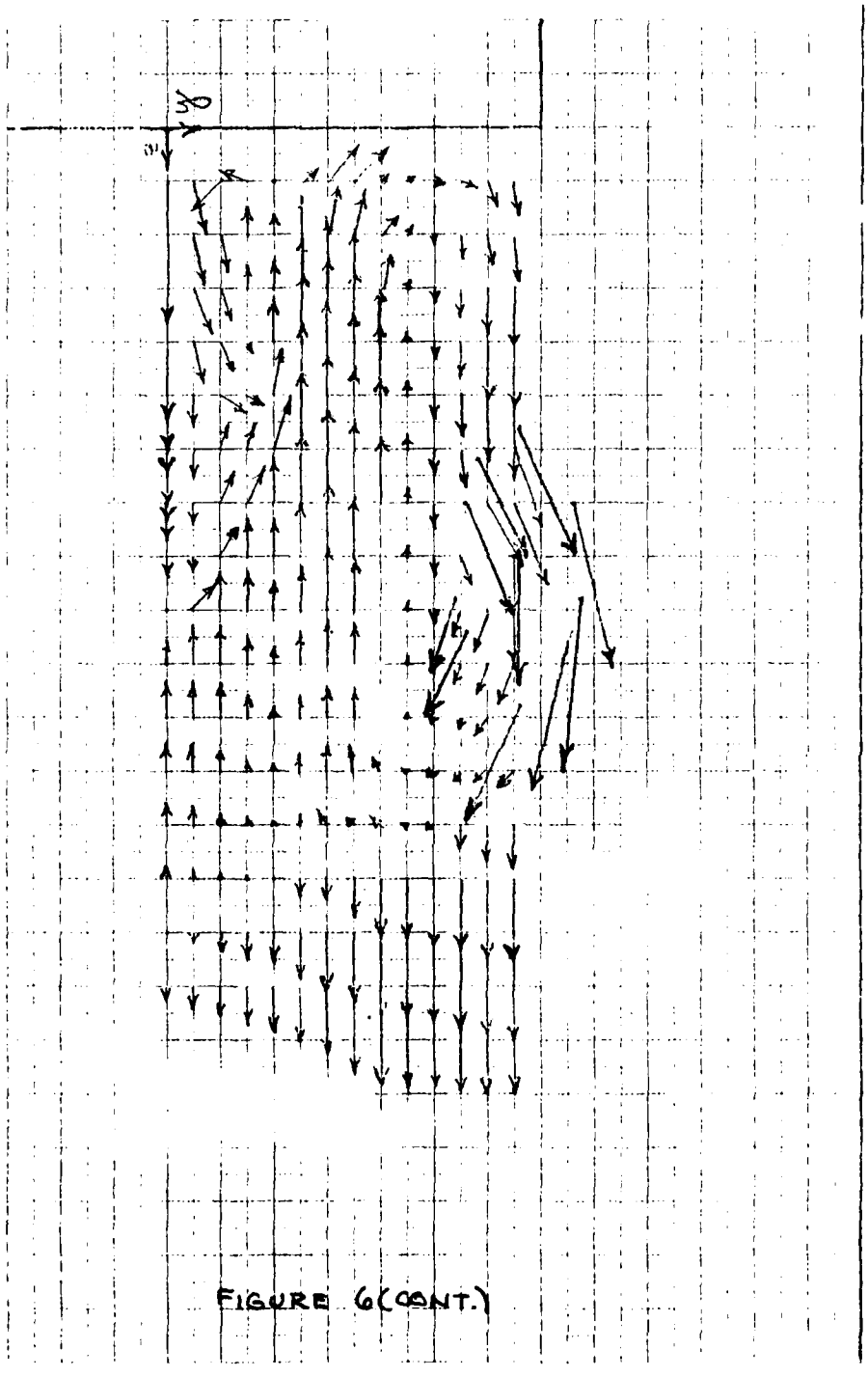

FIGURE 6(CONT.)

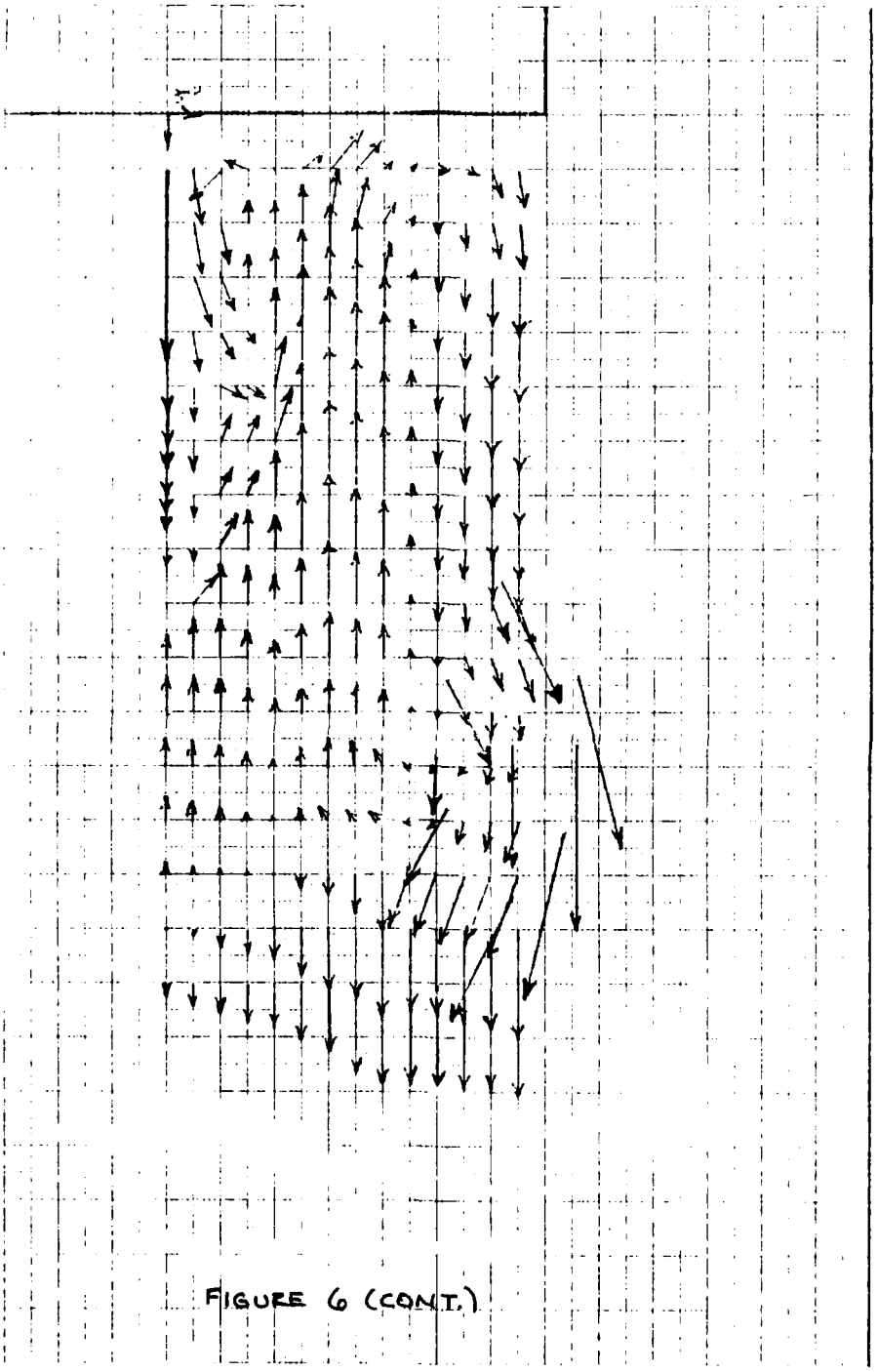

(d)

FIGURE 6 (CONT.)

AD-A130 767 USAF/SCEEE GRADUATE STUDENT SUMMER SUPPORT PROGRAM (1982) MANAGEMENT AND..(U) SOUTHEASTERN CENTER FOR ELECTRICAL ENGINEERING EDUCATION INC S..

UNCLASSIFIED W D PEELE ET AL. OCT 82 AFOSR-TR-83-0611 F/G 5/9 NL

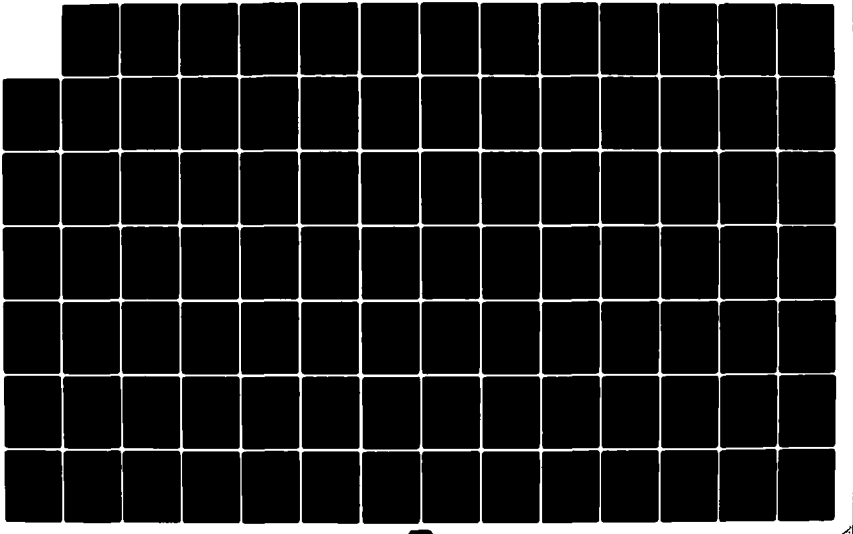

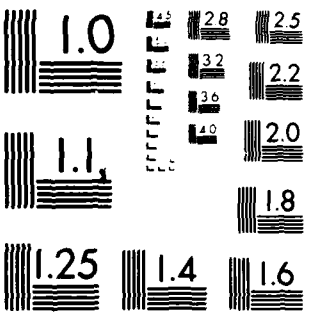

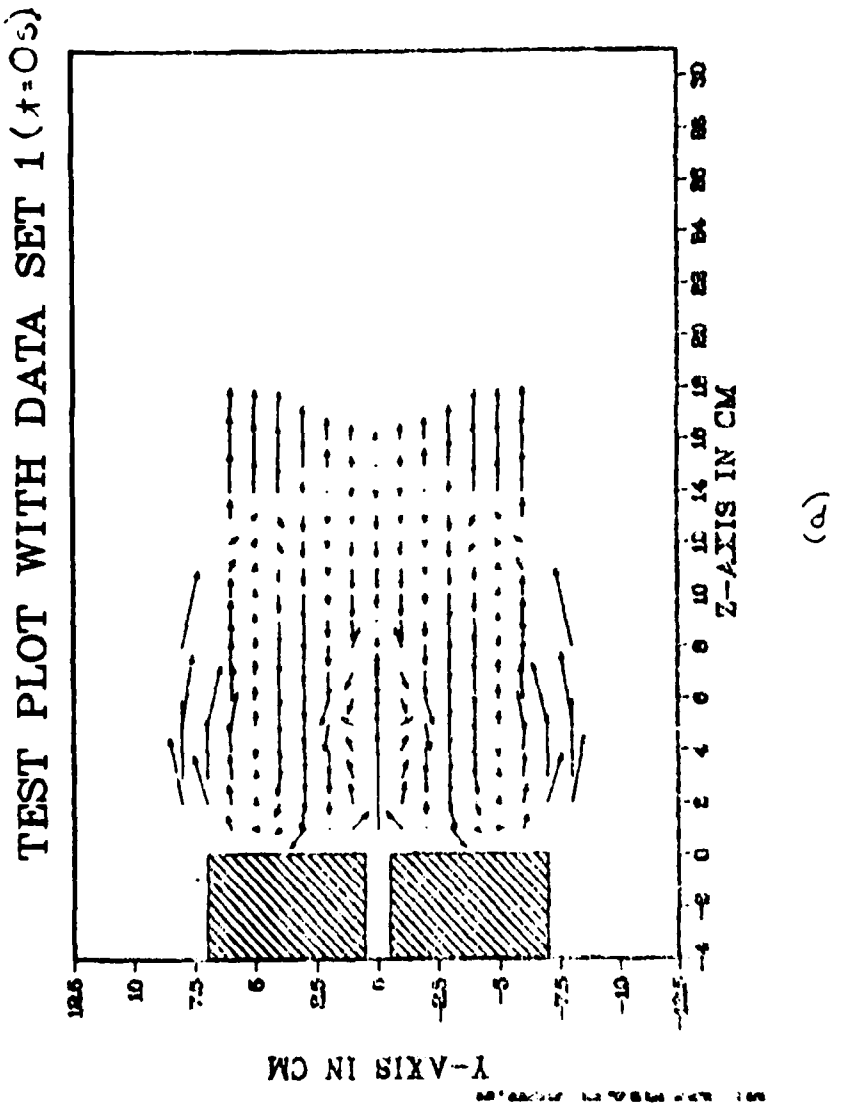

FIGURE 7: COMPUTER-GENERATED VECTOR DIAGRAMS OF FLOW-FIELD IN THE APL COMBUSTOR

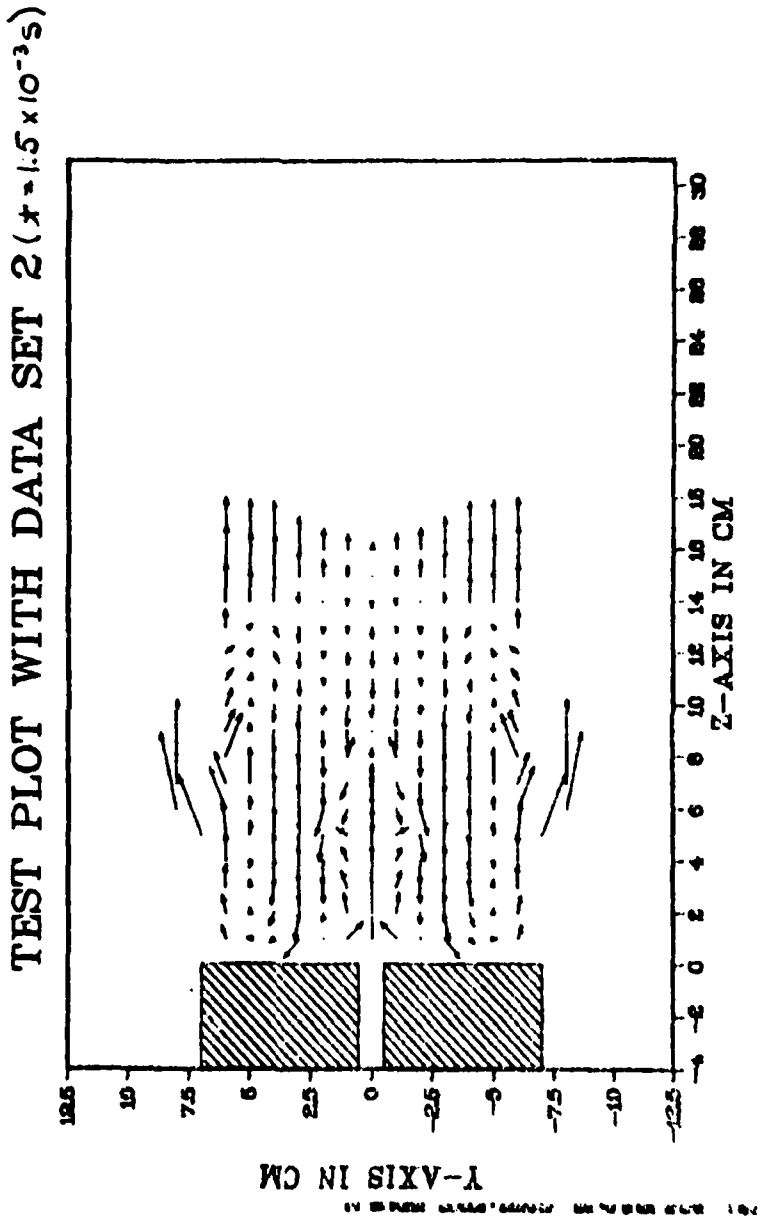

(c)

FIGURE 7 (CONT.)

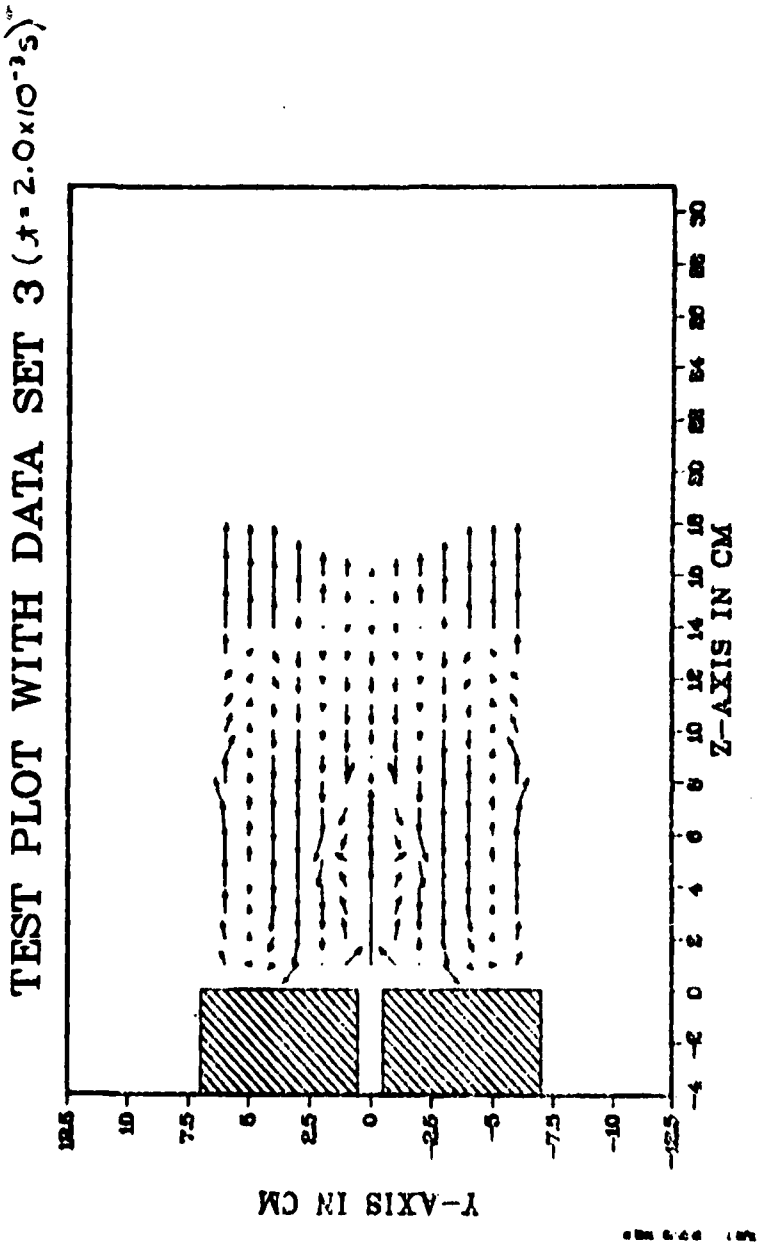

(c)

FIGURE 7 (CONT.)

Table 7 : Vector Diagram Data for t=0s.

Z(cm)	Y=0 W	Δ	Y=½ W	Δ	Y=1 W	Δ	Y=1½ W		Y=2 W	Δ	Y=2½ W	Δ	Y=3 W	Δ
1	36.35	0	10.21	-10	8.79	45	5.75	112	0	0	4.79	228	9.57	220
2	34.72	0	9.55	-10	7.51	-10	4.12	180	4.12	180	9.39	180	10.65	190
3	30.29	0	9.15	-20	6.35	-20	4.73	180	5.83	180	9.57	180	13.31	180
4	25.52	0	7.78	-10	5.77	-24	2.12	-25	8.62	180	12.08	180	15.55	180
5	20.97	0	6.82	0	5.23	-57	3.71	-60	9.79	190	13.77	180	17.75	180
6	13.98	0	5.58	0	5.58	200	5.58	200	10.48	198	14.12	180	17.75	180
7	6.99	0	4.12	0	6.59	205	7.92	205	8.85	180	13.30	180	17.75	180
8	3.12	0	2.01	0	7.75	210	7.75	180	6.99	180	10.15	180	13.31	180
9	0	0	7.65	221	7.75	180	7.57	180	5.83	180	8.45	180	11.07	180
10	4.66	180	7.45	180	7.55	180	5.72	180	3.30	180	6.08	180	8.87	180
11	6.99	180	6.99	180	6.99	180	4.59	180	2.19	180	4.14	180	6.09	180
12	5.83	180	5.01	180	4.19	180	2.87	180	1.54	180	3.36	180	5.18	180
13	4.66	180	3.44	180	2.21	180	1.53	180	0.85	180	2.00	180	3.07	150
14	2.33	180	1.75	180	1.17	180	0.62	180	0	0	2.37	0	3.55	0
15	0	0	1.75	0	3.50	0	4.74	0	5.97	0	8.52	0	10.12	0
16	2.33	0	4.08	0	5.83	0	7.02	0	8.21	0	10.08	0	12.82	0

Table 7 (cont.)

Z(cm)	Y=3½ W	Δ	Y=4 W	Δ	Y=4½ W	Δ	Y=5 W	Δ	Y=5½ W	Δ	Y=6 W	Δ	Y=6½ W	Δ
1	8.17	225	2.73	230	0.72	240	1.33	-85	3.24	-70	5.32	-20	6.44	-10
2	9.09	195	5.45	200	1.25	200	1.82	0	4.15	-4	6.83	-10	8.27	-15
3	11.36	180	7.13	190	1.73	191	2.38	0	5.15	0	8.46	-5	10.25	-10
4	13.27	180	10.02	180	2.33	180	3.54	0	6.35	0	10.44	-5	12.65	-10
5	15.15	180	13.14	180	3.00	180	4.38	0	7.61	14	12.50	10	15.14	15
6	15.15	180	13.14	180	3.00	180	4.38	0	7.61	0	12.50	5	15.14	10
7	15.15	180	12.87	180	2.94	180	4.29	0	7.56	0	12.39	0	15.01	0
8	11.36	180	9.60.	180	2.22	180	3.20	0	5.77	0	9.48	0	11.48	0
9	9.45	180	8.53	180	1.96	180	2.84	0	5.02	0	8.25	0	10.00	0
10	7.57	180	6.57	180	1.50	180	2.19	4	4.06	0	6.67	0	8.08	0
11	5.20	180	4.37	180	1.00	180	1.88	7	2.70	0	4.43	25	5.37	20
12	4.42	175	3.73	155	0.87	130	1.54	36	2.40	45	3.94	55	4.77	70
13	2.62	143	2.74	130	0.72	115	1.45	45	4.21	0	6.85	0	8.30	0
14	7.12	0	10.23	0	11.21	0	12.21	0	13.43	0	14.54	0	15.33	0
15	12.52	0	15.38	0	15.87	0	16.29	0	17.65	0	18.89	0	19.94	0
16	16.09	0	18.57	0	18.70	0	16.83	0	19.28	0	19.74	0	20.20	0

Z(cm)	Y(cm)	W	Δ
1.6	7.4	23.57	-14.85
2.4	8.2	27.38	-8.97
2.4	6.6	19.00	-18.00
3.4	8.2	28.82	0.00
3.4	7.4	22.78	0.00
4.6	8.0	27.38	8.97
5.2	6.8	23.57	14.85

Table 8 : Vector Diagram Data for $t = 1.5 \times 10^{-3}$ s.

Z(cm)	Y=0 W	Δ	Y=½ W	Δ	Y=1 W	Δ	Y=1½ W	Δ	Y=2 W	Δ	Y=2½ W	Δ	Y=3 W	Δ
1	36.35	0	10.21	-10	8.79	45	5.75	112	0	0	4.79	228	9.57	220
2	34.72	0	9.55	-10	7.51	-10	4.12	180	4.12	180	9.39	180	10.65	190
3	30.29	0	9.15	-20	6.35	-20	4.73	180	5.83	180	9.57	180	13.31	180
4	25.52	0	7.78	-10	5.77	-24	2.12	-25	8.62	180	12.08	180	15.55	180
5	20.97	0	6.82	0	5.23	-57	3.71	-60	9.79	190	13.77	180	17.75	180
6	13.98	0	5.58	0	5.58	200	5.58	200	10.48	198	14.12	180	17.75	180
7	6.99	0	4.12	0	6.59	205	7.92	205	8.85	180	13.30	180	17.75	180
8	3.12	0	2.01	0	7.75	210	7.75	180	6.99	180	10.15	180	13.31	180
9	0	0	7.65	221	7.75	180	7.57	180	5.83	180	8.45	180	11.07	180
10	4.66	180	7.45	180	7.55	180	5.72	180	3.30	180	6.08	180	8.87	180
11	6.99	180	6.99	180	6.99	180	4.59	180	2.19	180	4.14	180	6.09	180
12	5.83	180	5.01	180	4.19	180	2.87	180	1.54	180	3.36	180	5.18	180
13	4.66	180	3.44	180	2.21	180	1.53	180	0.85	180	2.00	180	3.07	150
14	2.33	180	1.75	180	1.17	180	0.62	180	0	0	2.37	0	3.55	0
15	0	0	1.75	0	3.50	0	4.74	0	5.97	0	8.52	0	10.12	0
16	2.33	0	4.08	0	5.83	0	7.02	0	8.21	0	10.08	0	12.82	0

Table 8 (cont.)

Z(cm)	Y=3½ W	Δ	Y=4 W	Δ	Y=4½ W	Δ	Y=5 W	Δ	Y=5½ W	Δ	Y=6 W	Δ	Y=6½ W	Δ
1	8.17	225	2.73	230	0.72	240	1.33	-85	3.24	-70	5.32	-20	6.45	-10
2	9.09	195	5.45	200	1.25	200	1.82	0	4.15	-4	6.83	-10	8.27	-5
3	11.36	180	7.13	190	1.73	191	2.38	0	5.15	0	8.46	0	10.25	0
4	13.27	180	10.02	180	2.33	180	3.54	0	6.35	0	10.44	0	12.65	0
5	15.15	180	13.14	180	3.00	180	4.38	0	7.61	-2	12.50	-5	15.15	-10
6	15.15	180	13.14	180	3.00	180	4.38	0	7.61	-5	12.50	-15	15.15	-5
7	15.15	180	12.87	180	2.94	180	4.29	0	7.54	-2	12.39	-20	15.01	0
8	11.36	180	9.60	180	2.22	180	3.20	0	5.77	15	9.48	5	11.48	0
9	9.45	180	8.53	180	1.96	180	2.84	0	5.02	10	8.25	20	10.00	20
10	7.57	180	6.57	180	1.50	180	2.19	4	4.06	15	6.67	20	8.08	25
11	5.20	180	4.37	180	1.00	180	1.88	7	2.70	15	4.43	35	5.37	25
12	4.42	175	3.73	155	0.87	130	1.54	36	2.40	45	3.94	55	4.77	70
13	2.62	143	2.74	130	0.72	115	1.45	45	4.21	0	6.85	0	8.30	0
14	7.12	0	10.23	0	11.21	0	12.21	0	13.43	0	14.54	0	15.35	0
15	12.52	0	15.38	0	15.87	0	16.29	0	17.65	0	18.89	0	19.94	0
16	16.09	0	18.57	0	18.70	0	18.83	0	19.28	0	19.74	0	20.20	0

Z	Y	W	Δ
4.8	6.6	24.62	-22.27
5.6	7.6	30.11	-12.66
5.6	5.6	17.47	-22.19
6.8	8.0	32.11	0
6.8	5.2	13.45	0
7.8	7.6	30.11	12.66
7.8	5.6	17.47	22.19

Table 9 : Vector Diagram Data for $t=2.0\times10^{-3}$s.

Z(cm)	Y=0 W	Δ	Y=½ W	Δ	Y=1 W	Δ	Y=1½ W	Δ	Y=2 W	Δ	Y=2½ W	Δ	Y=3 W	Δ
1	36.35	0	10.21	-10	8.79	45	5.75	112	0	0	4.79	228	9.57	220
2	34.72	0	9.55	-10	7.51	-10	4.12	180	4.12	180	9.39	180	10.65	190
3	30.29	0	9.15	-20	6.35	-20	4.73	180	5.83	180	9.57	180	13.31	180
4	25.52	0	7.78	-10	5.77	-24	2.12	-25	8.62	180	12.08	180	15.55	180
5	20.97	0	6.82	0	5.23	-57	3.71	-60	9.79	190	13.77	180	17.75	180
6	13.98	0	5.58	0	5.58	200	5.58	200	10.48	198	14.12	180	17.75	180
7	6.99	0	4.12	0	6.59	205	7.92	205	8.85	180	13.30	180	17.75	180
8	3.12	0	2.01	0	7.75	210	7.75	180	6.99	180	10.15	180	13.31	180
9	0	0	7.65	221	7.75	180	7.57	180	5.83	180	8.45	180	11.07	180
10	4.66	180	7.45	180	7.55	180	5.72	180	3.30	180	6.08	180	8.87	180
11	6.99	180	6.99	180	6.99	180	4.59	180	2.19	180	4.14	180	6.09	180
12	5.83	180	5.01	180	4.19	180	2.87	180	1.54	180	3.36	180	5.18	180
13	4.66	180	3.44	180	2.21	180	1.53	180	0.85	180	2.00	180	3.07	150
14	2.33	180	1.75	180	1.17	180	0.62	180	0	0	2.37	0	3.55	0
15	0	0	1.75	0	3.50	0	4.74	0	5.97	0	8.52	0	10.12	0
16	2.33	0	4.08	0	5.83	0	7.02	0	8.21	0	10.08	0	12.82	0

Table 9 (cont.)

Z(cm)	Y=3½ W	Δ	Y=4 W	Δ	Y=4½ W	Δ	Y=5 W	Δ	Y=5½ W	Δ	Y=6 W	Δ	Y=6½ W	Δ
1	8.17	225	2.73	230	0.72	240	1.33	-85	3.24	-70	5.32	-20	6.45	-10
2	9.09	195	5.45	200	1.25	200	1.82	0	4.15	-5	6.83	-10	8.27	-5
3	11.36	180	7.13	190	1.73	191	2.34	0	5.15	0	8.46	0	10.25	0
4	13.27	180	10.02	180	2.33	180	3.54	0	6.35	0	10.44	0	12.65	0
5	15.15	180	13.14	180	3.00	180	4.38	0	7.61	-2	12.50	0	15.15	0
6	15.15	180	13.14	180	3.00	180	4.38	0	7.69	-7	12.50	-25	15.14	-20
7	15.15	180	12.77	180	2.94	180	4.29	0	7.54	-20	12.39	-20	15.01	-20
8	11.36	180	9.60	180	2.22	180	3.20	0	5.77	-20	9.48	-10	11.48	0
9	9.45	180	8.53	180	1.96	180	2.84	0	5.02	17	8.25	20	10.00	0
10	7.57	180	6.57	180	1.50	180	2.19	4	4.06	20	6.67	20	8.08	20
11	5.20	180	4.37	180	1.00	180	1.88	20	2.70	20	4.43	35	5.37	25
12	4.42	175	3.73	155	0.87	130	1.54	45	2.40	45	3.94	40	4.77	45
13	2.62	143	2.74	130	0.72	115	1.45	45	4.21	0	6.85	0	8.30	0
14	7.12	0	10.23	0	11.21	0	12.21	0	13.43	0	14.54	0	15.35	0
15	12.52	0	15.38	0	15.87	0	16.29	0	17.65	0	18.89	0	19.94	0
16	16.09	0	18.57	0	18.70	0	18.83	0	19.28	0	19.74	0	20.20	0

Z	Y	W	Δ
5.6	6.6	25.05	-24.60
6.2	5.8	20.29	-27.24
7.0	7.6	31.05	-13.75
7.0	5.6	17.08	-25.60
8.2	6.6	22.78	0
8.8	7.8	32.86	5.63
8.8	5.4	14.30	19.36
9.4	7.6	31.05	13.75
9.4	5.6	17.07	25.60
10.8	6.6	25.05	24.60

Table 10: Vector Diagram Data for $t = 2.75 \times 10^{-3}$ s.

Z(cm)	Y=0 W	Δ	Y=½ W	Δ	Y=1 W	Δ	Y=1½ W	Δ	Y=2 W	Δ	Y=2½ W	Δ	Y=3 W	Δ
1	36.35	0	10.21	-10	8.79	45	5.75	112	0	0	4.79	228	9.57	220
2	34.72	0	9.55	-10	7.51	-10	4.12	180	4.12	180	9.39	180	10.65	190
3	30.29	0	9.15	-20	6.35	-20	4.73	180	5.83	180	9.57	180	13.31	180
4	25.52	0	7.78	-10	5.77	-24	2.12	-25	8.62	180	12.08	180	15.55	180
5	20.97	0	6.82	0	5.23	-57	3.71	-60	9.79	190	13.77	180	17.75	180
6	13.98	0	5.58	0	5.58	200	5.58	200	10.48	198	14.12	180	17.75	180
7	6.99	0	4.12	0	6.59	205	7.92	205	8.85	180	13.30	180	17.75	180
8	3.12	0	2.01	0	7.75	210	7.75	180	6.99	180	10.15	180	13.31	180
9	0	0	7.65	221	7.75	180	7.57	180	5.83	180	8.45	180	11.07	180
10	4.66	180	7.45	180	7.55	180	5.72	180	3.30	180	6.08	180	8.87	180
11	6.99	180	6.99	180	6.99	180	4.59	180	2.19	180	4.14	180	6.09	180
12	5.83	180	5.01	180	4.19	180	2.87	180	1.54	180	3.36	180	5.18	180
13	4.66	180	3.44	180	2.21	180	1.53	180	0.85	180	2.00	180	3.07	150
14	2.33	180	1.75	180	1.17	180	0.62	180	0	0	2.37	0	3.55	0
15	0	0	1.75	0	3.50	0	4.74	0	5.97	0	8.52	0	10.12	0
16	2.33	0	4.08	0	5.83	0	7.02	0	8.21	0	10.08	0	12.82	0

Table 10 (cont.)

	Y=3½		Y=4		Y=4½		Y=5		Y=5½		Y=6		Y=6½	
Z(cm)	W	Δ	W	Δ	W	Δ	W	Δ	W	Δ	W	Δ	W	Δ
1	8.17	225	2.73	230	0.72	240	1.33	-85	3.24	-70	5.32	-20	6.45	-10
2	9.09	195	5.45	200	1.25	200	1.82	0	4.15	-4	6.83	-10	8.27	-5
3	11.36	180	7.13	190	1.73	191	2.38	0	5.15	0	8.46	0	10.25	0
4	13.27	180	10.02	180	2.33	180	3.54	0	6.35	0	10.44	0	12.65	0
5	15.15	180	13.14	180	3.00	180	4.38	0	7.61	0	12.50	0	15.14	0
6	15.15	180	13.14	180	3.00	180	4.38	0	7.61	0	12.50	0	15.14	0
7	15.15	180	12.87	180	2.94	180	4.29	0	7.54	0	12.39	0	15.01	0
8	11.36	180	9.60	180	2.22	180	3.20	0	5.77	5	9.48	0	11.48	0
9	9.45	180	8.53	180	1.96	180	2.84	0	5.02	-5	8.25	-20	10.00	-20
10	7.57	180	6.57	180	1.50	180	2.19	4	4.06	-20	6.67	-20	8.08	-20
11	5.20	180	4.37	180	1.00	180	1.88	7	2.70	-20	4.43	0	5.37	-5
12	4.42	175	3.73	155	0.87	130	1.54	36	2.40	35	3.94	35	4.77	50
13	2.62	143	2.74	130	0.72	85	1.45	45	4.21	15	6.85	10	8.30	20
14	7.12	0	10.23	0	11.21	20	12.21	20	13.43	20	14.54	20	15.35	20
15	12.52	0	15.38	0	15.87	0	16.29	0	17.65	0	18.89	0	19.94	0
16	16.08	0	18.57	0	18.70	0	18.83	0	19.28	0	19.74	0	20.20	0

Z	Y	W	Δ
8.6	6.2	24.90	-27.53
10.4	7.6	32.00	-14.76
10.4	5.2	16.75	-29.12
11.6	7.6	34.31	0
11.6	6.4	22.78	0
11.8	5.0	11.29	3.55
12.8	5.2	16.75	29.12
13.2	7.4	32.34	13.67
14.4	6.4	25.53	26.85

1982 USAF-SCEEE GRADUATE STUDENT SUMMER SUPPORT PROGRAM

Sponsored by the

AIR FORCE OFFICE OF SCIENTIFIC RESEARCH

Conducted by the

SOUTHEASTERN CENTER FOR ELECTRICAL ENGINEERING EDUCATION

FINAL REPORT

TECHNOLOGY DEVELOPMENT FOR THE STUDY OF LASER DAMAGE IN PLASTICS

Prepared by:	James R. Bogan
Academic Department:	Physics
University:	Colorado State University
Research Location:	Frank J. Seiler Research Laboratory USAF Academy, Colorado 80840
USAF Research Contact:	Lt Colonel Theodore T. Saito
SFRP Supervising Faculty Member:	Dr. Thomas Wiggins, Professor of Physics, Pennsylvania State University
Date:	August 24, 1982
Contract No:	

Acknowledgements

The author would like to thank the Air Force Systems Command, the Air Force Office of Scientific Research, the Southeastern Center for Electrical Engineering Education, Professor I.L. Hall, and Lt Col T.T. Saito for providing him with the opportunity to spend a very worthwhile and interesting summer at the Frank J. Seiler Research Laboratory, USAF Academy, Colorado. In particular, he would like to thank Major Barry Crane, Captain Steve Snyder, and Mr. Phillip Chapnick for their hospitality and many stimulating discussions.

TECHNOLOGY DEVELOPMENT FOR THE STUDY OF LASER DAMAGE IN PLASTICS

by

James R. Bogan

Abstract

Certain transparent plastic materials have exhibited laser damage thresholds comparable to conventional optical materials such as glass. To ascertain the physical properties of these materials which enhance their resistance to pulsed laser beam damage, several experiments were initiated with laser pulses which will repeatably produce damage. Finally, the construction, alignment, and testing of a nitric oxide Raman cell wavelength shifter is described. This device is used in conjunction with a Q-switched Nd:Glass laser system, to derive high peak power infrared light pulses of wavelengths of 1.315 microns, as well as 1.06 microns for the study of laser damage in plastics.

I. Introduction

In 1981, a symposium on laser damage in optical materials was held in Boulder, Colorado. There, Lt Col Ted Saito of the Frank J. Seiler Research Laboratory noted that the visiting Soviet group of Manenkov, et al, of the Lebedev Physics Institute, Moscow, USSR,[1] reported the use of a 1.06 micron laser beam with a pulse width of 10-20 nanoseconds which induced damage in polymethylmethacaylate (PMMA) only at intensities exceeding 110 gigawatts per square centimeter. This is to be compared with the damage threshold of approximately eight gigawatts per square centimeter in Lithium Niobate,[2] a typical laser Q-switch optical material, when irradiated with a similar laser pulse.

Moreover, Manenkov *et al* reported that an enhancement of the damage threshold in PMMA was obtained by filtering the materials before polymerization and including additives to improve the viscoelastic properties of PMMA.

Such an improvement in optical materials would allow one to embed a dye in the plastic, and thereby obtain an inert and passive Q-switch for high power pulsed lasers or a wavelength selector for dye lasers.

Since the personnel of the Frank J. Seiler Research Laboratory and the Physics and Electrical Engineering Departments of the United States Air Force Academy (USAFA) possess a broad base of experience in the relevant technologies of laser damage, it is clear that such a study has an excellent chance of producing first-rate research in this field.

Assisting the USAFA staff in this research were Professor Thomas Wiggins of Pennsylvania State University and myself.

II. Objectives

The primary objective of this research is to develop the technology necessary to improve the laser damage resistance of plastics in order to use them for optical materials in Air Force laser systems. The Modus Operandi for achieving the primary goal is best summarized as follows:

a. Characterize the infrared pulses of our Nd:YAG and Nd:Glass lasers to be utilized in the damage testing.

b. Irradiate commercial and 'in-house' developed plastic materials to determine their damage thresholds.

c. Evaluate the laser damage morphology.

III. Laser Systems

At present, the Frank J. Seiler Research Laboratory is utilizing two pulsed, infrared laser systems for laser damage studies: an 'in-house' built Nd:YAG laser; and a commercial 'Space-Rays' Nd:Glass laser. The former operates at about one megawatt, and the latter at about 50 megawatts, each at 1.06 microns wavelength.

Initial damage studies were performed using the smaller Nd:YAG laser in the optical configuration sketched in Figure 1.

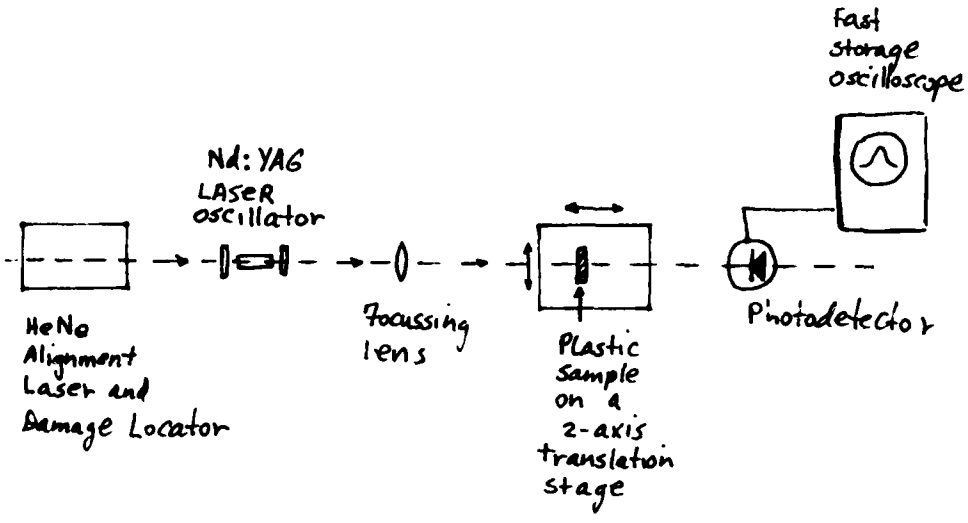

Figure 1.

Commercial plastic samples, such as lexan and acrylate were irradiated with single pulses from the Nd:YAG laser, and then visual inspection of the helium-neon (HeNe) illuminated site was performed. It was found that induced damage, in situ, could be visually detected with the naked eye, by observing the 90^{o} scattering of the HeNe light produced by the damaged site. This method, although qualitative, worked consistently whether or not the damage was localized on the surface or in the bulk volume of the sample. Indeed, definite HeNe scattering was almost always correlated with the subsequent observation under an optical microscope of laser induced damage.

However, to simulate the pulse parameters that Manenkov et al has achieved requires the use of a more powerful laser, namely the Nd:Glass system. It produces a $1/e^2$ beam diameter of approximately two centimeters incident on the focusing lens, which if one picks to be of 20 centimeters focal length produces an intensity of:

$$I = \frac{P_o}{\pi\left(\frac{f\lambda}{\omega\pi}\right)^2} = \frac{\pi\, 10^7 \text{ watts}}{400 \text{ cm}^2 10^{-8} \text{cm}^2} (1 \text{ cm})^2 \quad (1)$$

$$= .8 \times 10^{7+6}$$

$$= 8 \times 10^{12} \text{ watts/cm}^2$$

approximately an order of magnitude more than necessary to replicate Manenkov's experiments with PMMA.

In order to irradiate a large number of samples, it is desirable to not have to wait five minutes in between shots to allow the Nd:Glass rod to cool prior to firing. Hence, Dr. Wiggins has implemented a technique in which the Nd:Glass laser pulse impinges upon a fine metal mesh screen producing a large number of diffracted beams which are intense enough to damage a copper mirror. Thus, one may expose a plastics sample to N beams per shot and thereby obtain a larger data base in a given time period.

Much of our work this summer has been concentrated on readying a Raman wavelength shifter cell, which is presently charged with approximately 450 torr of NO gas. The Air Force is interested in conducting some of the damage studies at 1.315 microns, the principal wavelength of the atomic iodine laser. The iodine laser at the Frank J. Seiler Lab is not yet on-line. It has been calculated that

stimulated Raman scattering in NO gas should produce a .255 micron wavelength shift in the Nd:Glass laser wavelength to produce a high power beam at 1.315 microns. We have made many attempts to obtain such a wavelength conversion. Our primary efforts have included construction of a cavity resonant at 1.315 microns, and focussing the exciting 1.06 micron radiation in the center of the cell with a 50 centimeter focussing lens. All such efforts to date have not succeeded. Suspect in this failure is the inherently broad laser line of the Nd:Glass laser ($\sim$ 200 cm^{-1}). Since the gain of a stimulated process is inversely proportional to the line width, it is clear that the gain is attenuated <u>apriori</u> by at least a factor of 5×10^{-3}.

IV. Laser Damage

Optical microscopy has been employed to assess the morphology of laser induced damage in commercial plastics. What we have found primarily is that regardless of whether the laser beam traverses the short or long dimension of the sample, damage occurs when an impurity in the sample absorbs a fraction of the beam energy, and as a result, deforms the plastic in its neighborhood, thereby radically changing the scattering or the local index of refraction of the sample and rendering it visible. Indeed, the impurity need not even lie directly in the beam path to absorb enough energy to damage the sample; local proximity is all that is required. This corroborates the findings of Manenkov et al that a material has a laser damage threshold is inversely proportional to the sample's purity.

V. Recommendations

Overall, this research project is proceeding on a proper course, yet to accomplish the objectives outlined will require much more work.

In order to use the Raman-shifted Nd:Glass laser at 1.315 microns, a method will have to be found to narrow the linewidths of the 1.06 micron incident beam. A frequency selective etalon of the proper thickness might suffice to do the job.

Finally, an attempt should be made to assess the potential of the particular plastic(s) employed in the cladding of optical communication fibers for high damage threshold optics, since such materials are known to possess a low attenuation at near IR wavelengths.

JAMES R. BOGAN

THOMAS WIGGINS

References

1. A.A. Manenkov, K.M. Dyumasev, A.P. Maslyukov, C.A. Matyushin, V.S. Nechitailo, A.M. Prokorhov, "Transparent Polymers as a New Class of Optical Materials for Lasers," Invited Paper, Boulder Damage Symposium, 17-18 November 1981, to be published by the National Bureau of Standards, Department of Commerce.

2. S.C. Seitel, J.B. Franck, and G.D. Williams, "Selective and Uniform Laser-Induced Failure of Antireflection-coated $LiNbO_3$ Surfaces," Boulder Damage Symposium, 17-18 November 1981, to be published by the National Bureau of Standards, Department of Commerce.

1982 USAF-SCEEE SUMMER FACULTY RESEARCH PROGRAM

Sponsored by the

AIR FORCE OFFICE OF SCIENTIFIC RESEARCH

Conducted by the

SOUTHEASTERN CENTER FOR ELECTRICAL ENGINEERING EDUCATION

FINAL REPORT

A DYNAMIC MODEL OF ACCELERATION STRESS PROTECTION IN THE HUMAN AIRCREW MEMBER

Prepared by:	Patrick J. Sweeney, Ph.D., PE
Academic Rank:	Associate Professor
Department and University:	University of Dayton
	and
Prepared by:	Mary A. Doddy, M.S.
Academic Rank:	Graduate Student
Department and University:	University of Dayton
Research Location:	Air Force Aero Medical Research Laboratory Wright-Patterson AFB, Ohio
USAF Research Colleague:	Dr. Dana B. Rogers, Ph.D.
Date:	23 July 1982
Contract No.:	F49620-82-C-0035

ACKNOWLEDGMENTS

The authors wish to acknowledge the excellent and professional support of the entire Aero Medical Research Laboratory for their contribution in this effort.

Col. Mohr, AMRL Commander, very graciously explained the AMRL role in DOD activities and our part in this important mission. Ms. Patricia Lewandowski provided all of the necessary administrative support. Dr. Dana Rogers provided the authors with all the necessary data, background, and expertise for this report. He encouraged academic freedom and mission accomplishment during all of our many interactions. His study referenced in Section III was the major support study for this report.

The SCEEE staff and in particular Professor Peck and Dr. Steele were professional and supportive throughout this entire effort.

We thank all of these people, for without them the study could not have been accomplished.

A DYNAMIC MODEL OF ACCELERATION STRESS PROTECTION IN THE HUMAN AIRCREW MEMBER

by

Patrick J. Sweeney, Ph.D., P.E.

Mary Doddy, M.S.

ABSTRACT

This dynamic simulation computer model demonstrates the affects of G-forces upon the eyeball pressure of the aircrew member in various G-force environments. The stress relieving affects of G-suits and aircrew straining (M-1 and L-1 maneuvers) are dramatically depicted. The changes in the straining maneuver programs are evident in eyeball pressure and energy drain on the aircrew members. Further research in this area will undoubtedly result in improved aircrew performance in high and varying G-force environments.

A DYNAMIC MODEL OF ACCELERATION STRESS PROTECTION IN THE HUMAN AIRCREW MEMBER

I. INTRODUCTION:

Increased gravitational force results in a number of physiologic changes in the human exposed to such an acceleration. Classical methods of measuring these effects have led to an ever-increasing knowledge of the stressed physiologic systems. The two systems which have classically provided the defining limits in the stressed condition are vision and fatigue which then impinge on the performance capabilities of the human. Various performance measures have also been used to develop a greater knowledge of the acceleration environment. A multitude of model structures have arisen to describe the changes in oxygen levels, blood pressure, and in visual capability in hope of providing better descriptions and directions for advanced research. The model in this report has been developed from an alternative standpoint. The supposition is that there are competing systems within the human physiology which require oxygen in order to function at an acceptable level. The vision system requires a continuous flow of oxygen to the retinal layer to maintain function. The muscle system requires oxygen for replenishment of anaerobic activity and supply for aerobic activity. The central nervous system requires the same oxygen for its sustained higher level activity. The model in this development then becomes a model related to oxygen transport and competing energy used in the stressed physiologic system.

The total system of physiologic models was developed into a dynamic model according to the principles of system dynamics. System dynamics focuses on the structure and behavior of systems composed of interacting feedback loops. The resulting model integration allows investigation of the model in terms of an optimally controlled system. For example, varying acceleration time profiles can be run on the model resulting in unique physiologic response patterns for each profile. Performance is included through the pattern analysis inherent in the visual modulation transfer function and the cerebral oxygenation

prediction. The system model provides the basis for redefinition and extension of acceleration research into familiar areas with new intent.

II. OBJECTIVES:

The main objective of this project was to dynamically model the acceleration stress protection in the human. This involved refining past models and submodels which were based largely on the experimental data available in the literature. The difficulties with the previous models are in the assumptions that each of the submodels is a linear system and does not have a cross-coupling affect with the other subsystems. By refining these models it was hoped that these linkages and couplings could be closely studied. The ultimate goal in refining these models was to arrive at a model that could be used as an optimal protection model.

III. MODEL:

A. Previously Developed Physiologic Models. Increased gravitational force stresses the human physiology in a manner that causes detrimental changes in the human's capability to maintain acceptable performance levels. A set of physiologic models which dynamically describe acceleration stress responses have been developed previously. Each model represents a major physiologic system or acceleration protection mechanism. The submodels are assembled as a larger system using natural linkage variables from one subsystem to the next. The major subsystems are the visual system, cardiovascular subsystem, G-suit system, and the energy cost system. The integrated system model links all the subsystems as shown in Figure 1.

Human tolerance to long-term $+G_z$ acceleration is normally measured in terms of visual loss (blackout) and unconsciousness. Both of these tolerance end points are related to the ability of the cardiovascular system to deliver oxygenated blood at adequate pressure to the retinal and cerebral regions. The acceleration causes a changing blood pressure profile in the human such that the effective pressure vertically above the heart level is decreased and the pressure below the heart level is increased. There is therefore a lower perfusion pressure at

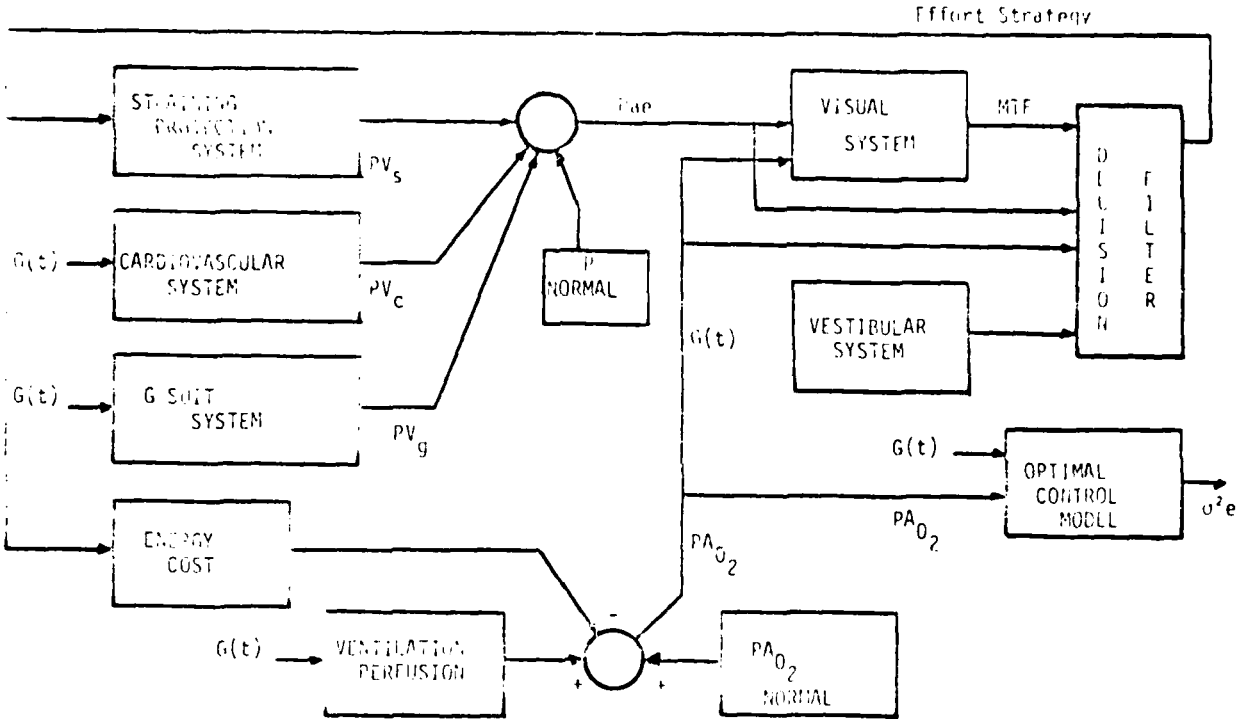

LEGEND

E(t) = Effort Strategy
G(t) = Acceleration Vector
PVs = Protection Value of Straining
PVc = Protection Value of Cardiovascular
PVg = Protection Value of G Suit
Pae = Arterial Pressure at eye level
PA_{O_2} = Arterial Oxygen Saturation in %
$\sigma^2 e$ = General Performance Metric
MTF = Modulation Transfer Function

Figure 1. Integrated System Model (Notes from Rogers' Study)

eye level. The distribution of the blood in the body also changes as the acceleration pools blood in the lower part of the body and lungs. There is therefore less available blood to circulate and a lower oxygen content because the lungs do not operate as efficiently. The cardiovascular response model output provides a dynamically responding signal which is equivalent to nominal eye level blood pressure values for an unprotected human undergoing the equivalent acceleration.

The effect that acceleration has on the visual apparatus is observed in terms of tunnel vision, greyout, and blackout. During the periods of greyout there are also decreases in visual acuity and brightness contrast detection ability. Although there are multiple factors related to the anatomy, psychology, and physiology of the human which are responsible for these changes in visual perception.

The structure of the eye is a primary factor and provides the basis for a usable model. When the blood pressure supply drops below a critical point the retinal supply vessels no longer remain open to blood flow. The changing pressure levels which are postulated across the eye serve as a partial explanation and a functional model for the prediction of field changes other than total blackout. The dynamic visual field model reacts to G level inputs from an external source and provides a dynamically responsive signal which predicts the expected visual field of a pilot undergoing the identical G profile.

The G suit model provides the parameters which describe the [illegible] and the garment used to increase the individual's tolerance to $-G_z$. The suit uses pressurized bladders to press against the legs and lower [illegible]. The external pressure inhibits pooling of the blood [illegible] the lower extremities thus forcing a better blood supply to the heart during acceleration. The suit [illegible] activated by the [illegible] predetermined level for the suit to be effective. The [illegible] accounts for the [illegible] pressure level [illegible] the suit to provide the necessary [illegible]. The suit pressure is [illegible] by the [illegible].

The ventilation perfusion model allows the effects of reduced [illegible] to be [illegible]. Acceleration induced shifts in the

pulmonary blood supply reduce the amount of oxygen transport across the alvedlar surface and thus reduce the oxygen supply.

The straining system model accounts for the G tolerance enhancement which is afforded by a properly executed M-1 or L-1 maneuver. The purpose of these straining maneuvers is to increase the blood pressure delivered to the eye. Proper performance of the maneuvers requires that the abdominal and upper torso muscles be tensed isometrically and that expirations should be made against a partially closed or closed glottis. The result is an increased intrathoracic pressure and increased blood pressure at the eye.

The energy stores/oxygen model is an energy balance system in which oxygen is proficed through the pulmonary system. The oxygen is utilized with the metabolic fuels in the straining system with the resultant higher blood pressure through the straining. Other oxygen is utilized in normal metabolic maintenance and the oxygen reserves are depleted. The energy expenditure model is simply an integrator which integrates the energy effort and translates this to a depletion of the oxygen stores in terms of a decreased percent of oxygen.

B. The Computer Model. The computer simulation model was based upon the 1979 study entitled "A Model for the Energetic Cost of Acceleration Stress Protection in the Human" by Dr. Dana B. Rogers. This report concluded by stating that "the use of dynamic models . . . allows for a variety of speculative studies." This report is a dynamic model that provides the vehicle necessary to evaluate the effects of varying acceleration loads on aircrew members.

The simulation language used in this study was developed by Dr. Jay Forrester of MIT. The language is DYNAMO and is based upon feedback interactions. Important variables are measured as levels (L on the right-hand margin in the model). The change factors are rates (R) and affect the inflow and outflow to the levels. These rates are affected by auxiliary (A) equations, constants (C), and initial conditions (N). In addition, table functions (T) are included when the input is a function of a specific variable.

```
0. L  PAE.K=MIN(80,PAE.J+DT(ETRO.JK+PVG.JK-PVC.JK))
0. N  PAE=79
2. *   PAE=PRESSURE AT THE EYEBALL
3. *   PVG=PRESSURE INCREASE DUE TO G SUIT
4. *   ETRO=ENERGY DRAIN
5. *   PVC=PRESSURE DUE TO G FORCES ALONE
6. R  PVC.KL=(CVS.K*FAC)
7. *   FAC=CONSTANT FOR CVS
8. *   CVS=G FORCE SLOPE (RATE OF CHANGE)
9. C   FAC=5
```

Equation 1 is a level equation that measures the blood pressure at the eyeball. Lower pressures reduce initially peripheral vision and at higher G-forces reduces visual to "tunnel vision" and subsequently to blackout. This eyeball pressure (PAE) is affected by the energy level (ETRO) of the aircrew members, the G-suit effects (PVG) and the G-forces encountered by the aircrewmen (PVC).

CVS is the actual G-force rate of change pattern on the crew member and the rate of change in G-force in PVC. For scaling and dimensional purity, FAC is included as a constant in the PVC equation.

```
10. A  CVS.K=TABHL(CVST,TIME.K,0,292.5,.5)
11. T  CVST=0,1,1,1,1,
12. X  0,0,0,0,0,0,0,0,0,0,0,0,0,0,0,0,0,0,0,0,
13. X  1,1,1,1,1,1,1,1,1,
14. X  0,0,0,0,0,0,0,0,0,0,
15. X  -1,-1,-1,-1,-1,
16. X  0,0,0,0,0,0,0,0,0,0,0,0,0,0,0,0,
17. X  -1,-1,-1,
18. X  0,0,0,0,0,0,0,0,0,0,
19. X  1,1,1,1,
20. X  0,0,0,0,0,0,0,0,0,0,
21. X  -1,-1,
22. X  0,0,0,0,0,0,0,0,0,0,
23. X  1,1,1,1,1,1,1,
24. X  0,0,0,0,0,0,0,0,0,0,
25. X  -1,-1,-1,-1,-1,-1,-1,-1,-1,
26. X  0,0,0,0,0,
27. X  1,1,1,1,1,1,
28. X  0,0,0,0,0,0,0,0,0,0,
29. X  -1,-1,-1,-1,-1,-1,-1,-1,-1,-1,
30. X  1,1,1,1,1,
31. X  0,0,0,0,0,0,0,0,0,0,0,0,0,0,0,0,0,0,0,0,
32. X  0,1,1,1,1,1,1,1,1,
33. X  0,0,0,0,0,0,0,0,0,0,
34. X  -1,-1,-1,-1,-1,
```

```
35. X  0,0,0,0,0,0,0,0,0,0,0,0,0,0,0,0,0,
36. X  -1,-1,-1,
37. X  0,0,0,0,0,0,0,0,0,0,
38. X  1,1,1,1,
39. X  0,0,0,0,0,0,0,0,0,0,
40. X  -1,-1,
41. X  0,0,0,0,0,0,0,0,0,0,
42. X  1,1,1,1,1,1,
43. X  0,0,0,0,0,0,0,0,0,0,
44. X  -1,-1,-1,-1,-1,-1,-1,-1,-1,
45. X  0,0,0,0,0,
46. X  1,1,1,1,1,1,
47. X  0,0,0,0,0,0,0,0,0,0,
48. X  -1,-1,-1,-1,-1,-1,-1,-1,-1,-1,
49. X  1,1,1,1,1,
50. X  0,0,0,0,0,0,0,0,0,0,0,0,0,0,0,0,0,0,0,0,
51. X  0,1,1,1,1,1,1,1,1,
52. X  0,0,0,0,0,0,0,0,0,0,
53. X  -1,-1,-1,-1,-1,
54. X  0,0,0,0,0,0,0,0,0,0,0,0,0,0,0,
55. X  -1,-1,-1,
56. X  0,0,0,0,0,0,0,0,0,0,
57. X  1,1,1,1,
58. X  0,0,0,0,0,0,0,0,0,0,
59. X  -1,-1,
60. X  0,0,0,0,0,0,0,0,0,0,
61. X  1,1,1,1,1,1,
62. X  0,0,0,0,0,0,0,0,0,0,
63. X  -1,-1,-1,-1,-1,-1,-1,-1,-1,
64. X  0,0,0,0,0,
65. X  1,1,1,1,1,1,
66. X  0,0,0,0,0,0,0,0,0,0,
67. X  -1,-1,-1,-1,-1,-1,-1,-1,-1,-1,
68. X  1,1,1,1,1,
69. X  0,0,0,0,0,0,0,0,0,0,0,0,0,0,0,0,0,0,0,0,
70. X  0,1,1,1,1,1,1,1,1,
71. X  0,0,0,0,0,0,0,0,0,0,
72. X  -1,-1,-1,-1,-1,
73. X  0,0,0,0,0,0,0,0,0,0,0,0,0,0,0,
74. X  -1,-1,-1,
75. X  0,0,0,0,0,0,0,0,0,0,
76. X  1,1,1,1,
77. X  0,0,0,0,0,0,0,0,0,0,
78. X  -1,-1,
79. X  0,0,0,0,0,0,0,0,0,0,
80. X  1,1,1,1,1,1,
81. X  0,0,0,0,0,0,0,0,0,0,
82. X  -1,-1,-1,-1,-1,-1,-1,-1,
```

```
 83. X  0,0,0,0,0,
 84. X  1,1,1,1,1,1,
 85. X  0,0,0,0,0,0,0,0,0,0,
 86. X  -1,-1,-1,-1,-1,-1,-1,-1,-1,-1,
 87. X  1,1,1,1,1,
 88. X  0,0,0,0,0,0,0,0,0,0,0,0,0,0,0,0,0,0,0,0,
 89. X  0,1,1,1,1,1,1,1,1,
 90. X  0,0,0,0,0,0,0,0,0,0,0,
 91. X  -1,-1,-1,-1,-1,
 92. X  0,0,0,0,0,0,0,0,0,0,0,0,0,0,0,
 93. X  -1,-1,-1,
 94. X  0,0,0,0,0,0,0,0,0,0,
 95. X  1,1,1,1,
 96. X  0,0,0,0,0,0,0,0,0,0,
 97. X  -1,-1,
 98. X  0,0,0,0,0,0,0,0,0,0,
 99. X  1,1,1,1,1,1,
100. X  0,0,0,0,0,0,0,0,0,0,
101. X  -1,-1,-1,-1,-1,-1,-1,-1,
102. X  0,0,0,0,0,
103. X  1,1,1,1,1,1,1,
104. X  0,0,0,0,0,0,0,0,0,0,
105. X  -1,-1,-1,-1,-1,-1,-1,-1,-1,-1,
```

As stated previously, CVS is the actual G-force rate of change exerted on the aircrewman. This G-profile has been provided by AMRL and was replicated five times to reflect a 400 second G-pattern. This force is depicted as the derivative of the actual G-force, because of the cumulative nature of the level equation, PAE, and the appropriate rate, PVC.

```
106. A  PVGD.K=DELAY1(CVR.K*FAC1,1)
107. *   PVGD=G SUIT PRESSURE DELAY FUNCTION
108. *   CVR=G SUIT-G FORCE FACTOR
109. *   FAC1=G SUIT-G FORCE CORRECTION FACTOR
110. *   FAC1=0.5
```

PVGD is an auxiliary equation that accounts for the effects of the programmed G-program and the G-suit system delay. G-suits increase the pressure to the eyeball but are affected by mechanical system operational delays. The delay is a single period (0.1 second delay) and is represented by a 1 in equation 106. FAC1 is a sizing and dimensional constant.

```
111. A  CVR.K=CVS.K*FACX
112. *   FACX=CVS TO CVR CORRECTION FACTOR
113. C  FACX=1
114. R  CVX.KL=CVR.K
115. *   CVX=G SUIT-G FORCE RATE FACTOR
116. L  CXX.K=CXX.J+DT(CVX.JK)
117. *   CXX=APPLIED G FORCE
118. N  CXX=1
```

CVR is a correction factor used to convert CVS to usable form in equation 106. FACX is the dimensional constant.

CVX is the equation used to convert CVR to a rate.

CXX is a level equation that is used to show the actual G-force on the aircrewman. This along with PAE, ET, and other important factors are plotted in the ensuing figure.

```
119. L  ACXX.K=ACXX.J+(DT/AT)(CXX.J-ACXX.J)
120. *   ACXX=AVERAGE APPLIED G FORCE
121. *   AT=AVERAGING DELAY FUNCTION
122. N  ACXX=0
123. C  AT=10
```

ACXX is the G-force averaged over the previous 10 periods. ACXX is initialized at 0, see line 122. AT is the averaging period of 10.

```
124. R  PVG.KL=MAX(CLIP(PVGD.K,0,80,PAE.K),0)*FACET
125. *   PVG=PRESSURE INCREASE DUE TO G SUIT
126. C  FACET=2
127. *   ENERGY LEVEL - G-SUIT PRESSURE LEVEL CONSTANT
```

PVG is the G-suit effect. Increasing G-forces will affect the G-suit input delayed by the system capabilities.

```
128. I  ET.K=ET.J+DT(ETRI.JK-ETRO.JK)*FAC10
129. C  FAC10=2
130. N  ET=100
131. R  ETRI.KL=ETRIC
132. C  ETRIC=0
133. R  ETRO.KL=CLIP(ETD.K/FAC2,0,80,PAE.K)*FAC8
134. C  FAC8=.5
```

```
135. C  FAC2=10
136. *   ET=ENERGY LEVEL OF THE AIRCREWMAN
137. *   ETRO=ENERGY OUTPUT RATE
138. *   ETRO=ENERGY INPUT RATE
139. *   ETRIC=ENERGY INPUT RATE CONSTANT
140. *   ETD=PILOT ENERGY EXPENDITURE PROGRAM
141. *   FAC2=ENERGY EXPENDITURE CONSTANT
```

ET is the energy level of the aircrew member. As energy is expended (ETRO) the energy level decreases from 100 percent. This would be restored to 100 percent when the G-forces were reduced to 1 over an extended period of time; however, in this model ETRI (Energy input rate is equal to years), since the G-program extends for 400 seconds. Both FAC10 and FAC8 are dimensional constants.

```
142. A  ETD.K=TABHL(ETDT,TIME.K,0,400,5)
143. T  ETDT=0,5,5,0,0,5,5,0,0,5,5,0,0,5,5,0,0,5,5,0,0,5,5,0,
144. X  0,5,5,0,0,5,5,0,0,5,5,0,0,5,5,0,0,5,5,0,0,5,5,0,0,5,5,0,
145. X  0,5,5,0,0,5,5,0,0,5,5,0,0,5,5,0,0,5,5,0,0,5,5,0,0,5,5,0,0
```

ETD is a table function that reflects the M-1 or L-1 maneuver and the quantity of energy expended by the aircrew member. The 400 and 5 in equation 142 shows that in equations 143-145 the effort extends for 400 seconds and the values are 5 seconds apart.

```
146. A  PAO2.K=(A*ACXX.K-B*CXX.K*CXX.K)(D-EXP((E*TIME.K)*LOGN(F)))+G
147. *   PAO2=PERCENT OXYGEN SATURATION
148. C  A=.5
149. C  B=.4
150. C  D=1
151. C  E=-.05
152. C  F=2.71828
153. C  G=98
154. *  A=CONSTANT
155. *  B=CONSTANT
156. *  D=CONSTANT
157. *  E=CONSTANT
158. *  F=EXPONENTIAL(E)
159. *  G=INITIAL PAO2 SATURATION
```

PAO2 is the percent oxygen saturation of the aircrewman. This equation was taken directly from the Rogers study and mathematically is:

$$PAO2 = H(.5g-.4g^2) \times (1-e^{-.05t}) + 98$$

Constants A-G are noted in equations 148-153.

```
160. A  EVP.K=ET.K*PAO2.K*H
161. C  H=.0001
162. A  VS.K=PAE.K*EVP.K*S/R
163. C  R=79
164. C  S=1
165. *   EVP=ENERGY OXYGEN FUNCTION
166. *   H=CONSTANT
167. *   VS=EYEBALL PRESSURE AND ENERGY-OXYGEN FUNCTION
168. *   R=CONSTANT
169. *   S=CONSTANT
```

EVP is the energy-oxygen relationship and reflects that energy is depleted faster when the oxygen supply is reduced. H is the dimensional constant.

VS is a measure of available field of vision as a function of eyeball pressure and the energy-oxygen function. R and S are dimensional constants. Note: Since some argument does exist concerning visual field and decision-making capability this factor was deemed beyond the scope of this ten-week study.

```
170. C  PRIPER=0
171. PRINT PAE,CVS,PVC,PVG,ETRO,CXX,ET
172. C  DT=.1
173. C  LENGTH=400
174. C  PLTPER=5
175. PLOT PAE=P/PVC=V/ETRO=E/PVG=G/CXX=X/ET=%/PAO2=*VS=S
```

The above functions control the operation of the model and the output. PRIPER is the printer period and controls how often a PRINT item is printed. PRINT controls what is printed. DT is the rate at which the DYNAMO compiler computes. LENGTH is the length of the printout. PLTPER defines how often the PLOT items are plotted. PLOT determines what is plotted.

IV. RESULTS AND CONCLUSIONS:

The model reflects the affects of varying G-forces on an aircrewman in changes in eyeball pressure, oxygen level, and energy level. The cumulative affects of these variables alter visual acuity and subsequently the aircrew member's ability to make decisions and accomplish his immediate mission.

Throughout the model constant factors have been included so as to facilitate easy value changes for future work. However, as the model is currently structured reasonable results are created. In Figure 2, Model Output--Basic Run, the following variables are plotted:

PAE(P) - Pressure at the Eyeball
PVC(V) - Pressure due to G-force
ETRO(E) - Energy Drain in Pressure
PVG(G) - Pressure Increase Due to G-Suit
CXX(X) - Actual G-Force on the Aircrewman
ET(%) - Energy Level of the Aircrewman
PAO2(*) - Percent Oxygen Saturation
VS(S) - Eyeball Pressure and Oxygen Function

As G-forces increase PAE, PVC, ETRO, ET, PAO2, and VS, all respond in the proper directions and at what the authors believe to be in a reasonable range. As the G-pattern continues and the aircrewmember executes either M-1 and L-1 maneuvers he eventually depletes his energy level, ET, and is unable to continue with the pressure reducing maneuvers. He subsequently blacks out. The G-suit has a similar but opposite affect upon the model.

The sensitivity analysis shows the affects of variable constants and M-1 or L-1 maneuver patterns. As the aircrewman alters his maneuvering pressure level and/or pattern, the affects of those maneuvers upon his eyeball pressure and oxygen supply levels vary. The model shows little difference when the aircrewman holds the M-1 or L-1 for "long periods" or whether he executes a large number by not holding for long periods on each individual maneuver.

The actual runs are not included due to the required limited brevity of this report.

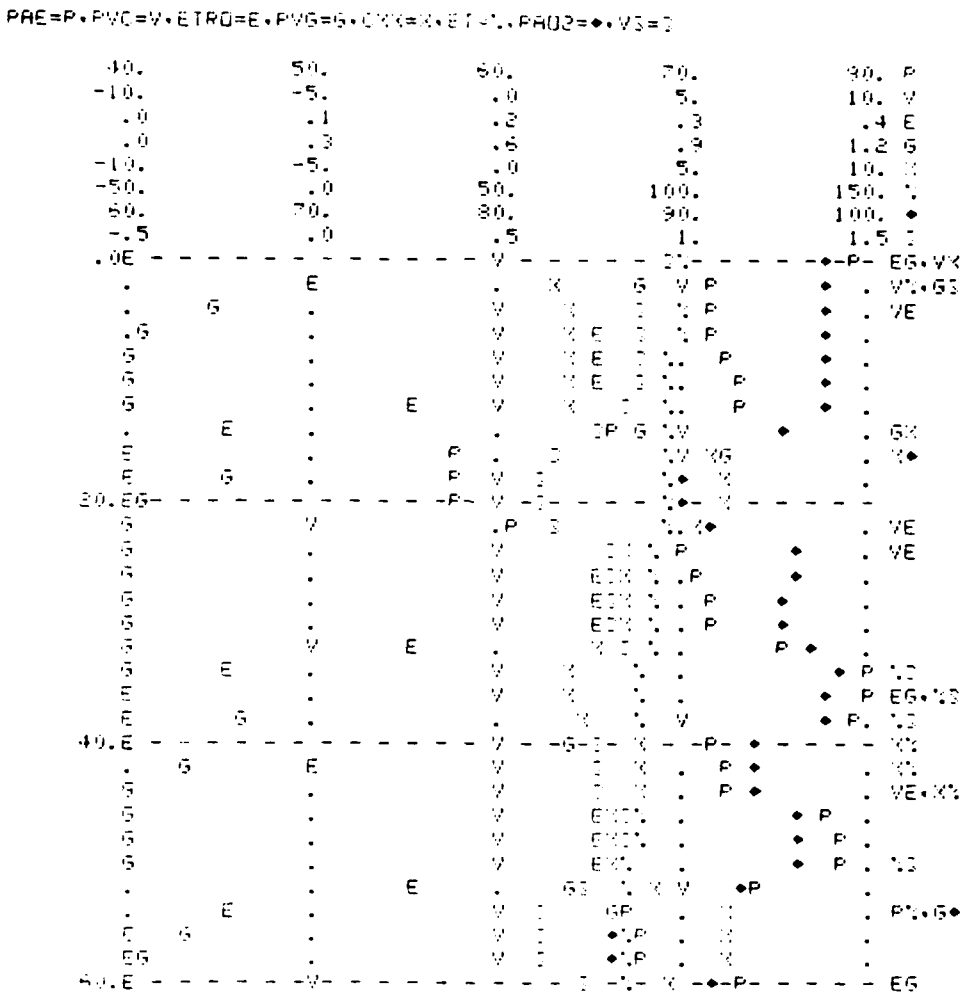

Figure 2. Model Output--Basic Run

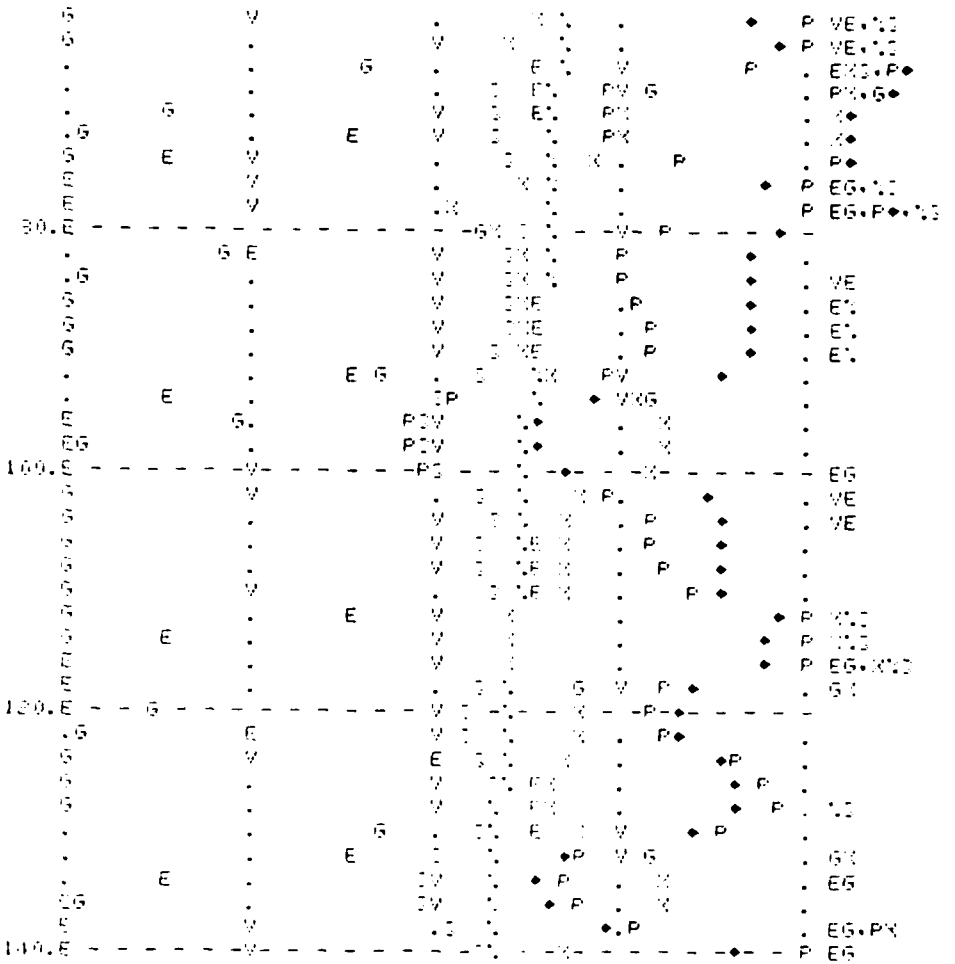

Figure 2--Continued

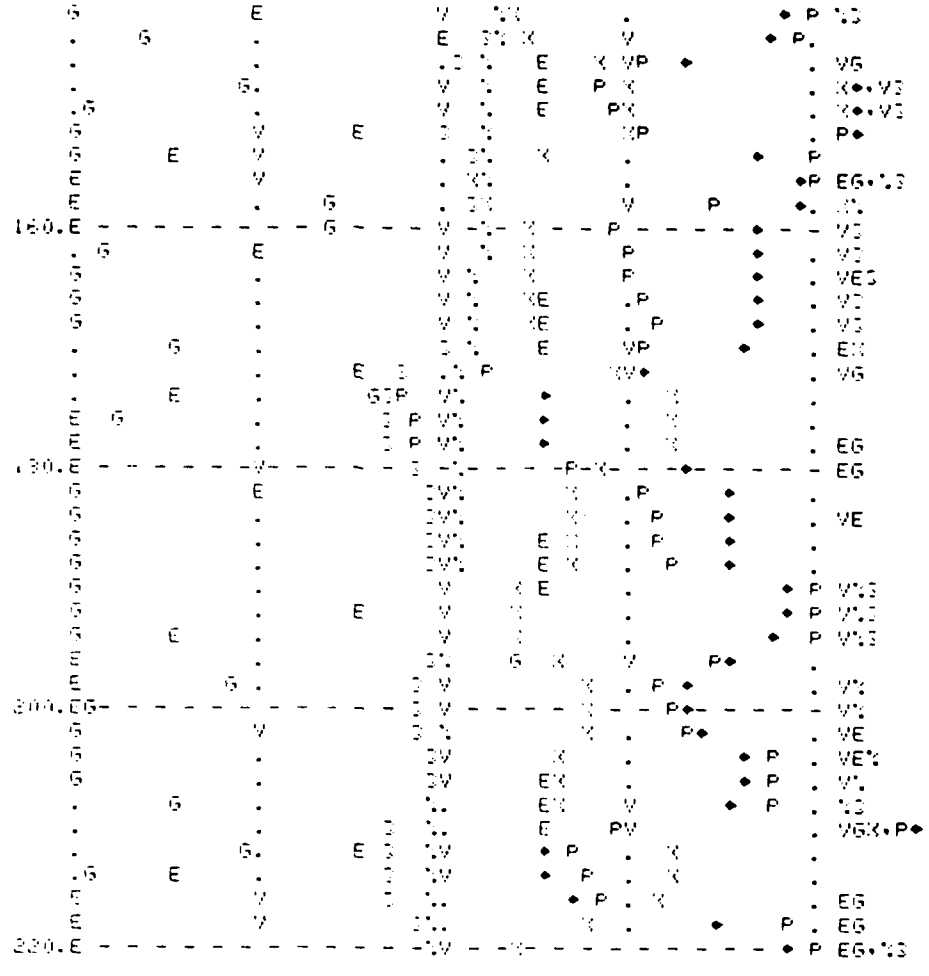

Figure 2--Continued

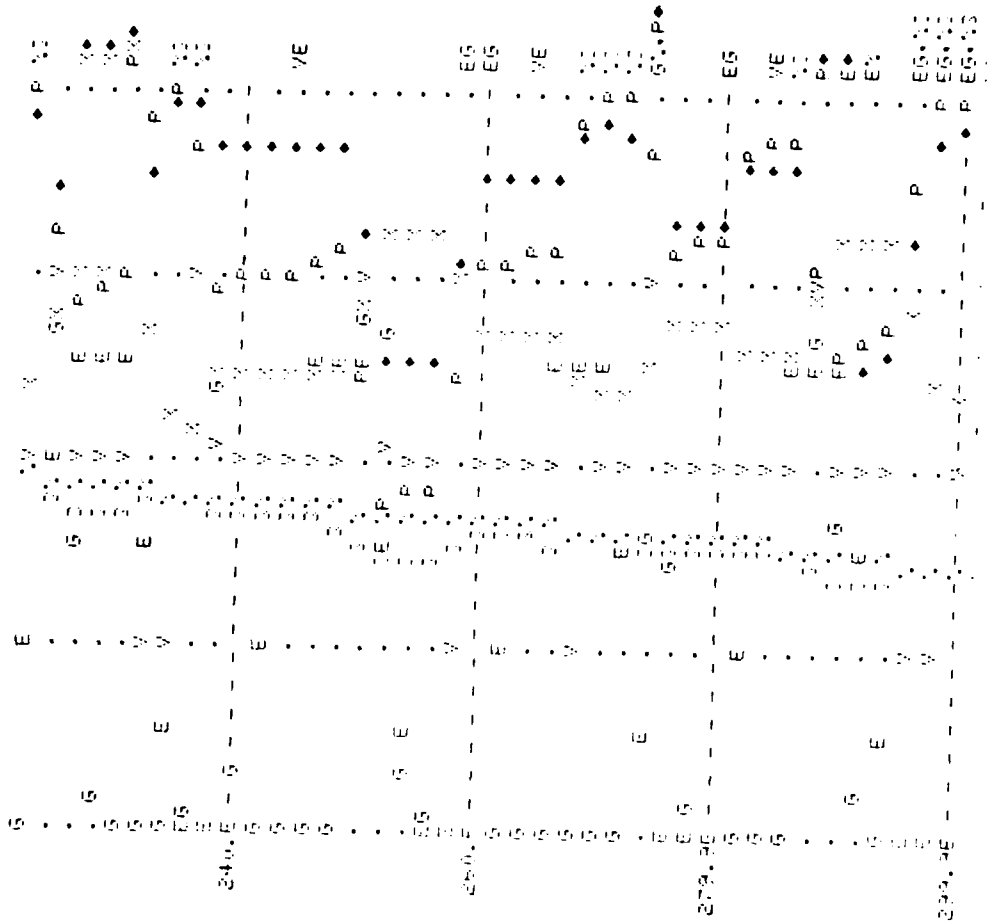

Figure 2–Continued

V. Recommendations

This type of study has great promise, for like the aircraft simulator, this model has the potential of testing without flying. The authors will apply for a mini-grant due to the high value potential of this work.

The authors suggest that the model be validated with actual test data. Modifications can be easily made since the model has captured the essence of the problem.

With the validated model the analyst can create enough scenarios and test them so as to develop the best M-1 or L-1 maneuver program based on the projected mission profile.

The authors believe that since each mission is plagued with its own unique G-pattern that the aircrewman should be provided with a suggested M-1 or L-1 program based upon the anticipated short and long term G-patterns of the mission.

1982 USAF-SCEEE GRADUATE STUDENT SUMMER SUPPORT PROGRAM

Sponsored by the

AIR FORCE OFFICE OF SCIENTIFIC RESEARCH

Conducted by the

SOUTHEASTERN CENTER FOR ELECTRICAL ENGINEERING EDUCATION

FINAL REPORT

SYNTHESIS OF ACETYLENE TERMINATED SULFONE (ATS) CANDIDATES

Prepared by:	Brenda G. Evans
Academic Department:	Chemistry
University:	Wright State University
Research Location:	Air Force Wright Aeronautical Laboratories Materials Laboratory, Polymer Branch Wright Patterson Air Force Base, Ohio
USAF Research Colleague:	Dr. Fred E. Arnold
SFRP Supervising Faculty Member:	Dr. James J. Kane
Date:	August 20, 1982
Contract No.	F49620-82-C-0035

Acknowledgement

The authors would like to express their sincere appreciation to the Air Force Systems Command, the Air Force Office of Scientific Research and the Southeastern Center for Electrical Engineering Education for their support and for the opportunity to spend a rewarding and interesting summer at the Air Force Materials Laboratory, Wright Patterson Air Force Base, Ohio. We would like to thank the people of the Polymer Branch in particular for their friendliness and their generosity in sharing their space, equipment, facilities and ideas so openly.

Finally, we would like to thank Dr. Fred E. Arnold for suggesting this area of research and for his helpful collaboration and guidance, and we would like to acknowledge the helpful discussions with Dr. Fred Hedberg, Lt. Patricia Lindley and Mr. Bruce Reinhardt.

SYNTHESIS OF ACETYLENE TERMINATED SULFONE (ATS) CANDIDATES

by

James J. Kane

and

Brenda G. Evans

ABSTRACT

Certain acetylene terminated sulfone (ATS) systems are of interest as possible replacements for epoxy resins. The beneficial feature which the ATS systems are expected to offer is their insensitivity to moisture. Reaction schemes for their synthesis are outlined and discussed. Finally, the synthesis of certain of the intermediates required for the ATS candidates are reported and discussed and recommendations for future work in this area are presented.

I. INTRODUCTION

Previous workers[1,2,3] in the Materials Laboratory synthesized and characterized acetylene terminated (AT) oligomers for use as addition curable, moisture resistant, thermoset systems. The cure process of the tetrafunctional AT system has been shown by kinetic studies[4] to involve a thermally induced free-radical chain mechanism resulting in a cross-linked conjugated polyene network. Subsequent higher temperature reactions are believed to occur by cyclization reactions which convert the polyene system to a variety of aromatic structures.

Early workers[1,2] demonstrated that acetylene terminated phenylquinoxaline (ATQ) oligomers exhibit excellent properties for application as adhesives[5] and fiber reinforced composites.[6]

More recent[3] work was directed toward application of the AT chemistry to overcome the problem of moisture sensitivity common to epoxy matrix systems. Thus it was expected that certain AT resins would provide an epoxy substitute having all of the processing, handling and performance characteristics of epoxies combined with the characteristic moisture insensitivity of AT systems. This work resulted in the synthesis of the first AT system which incorporates a phenylsulfone. This compound, 4,4'-di-(3-ethynylphenoxy)-diphenylsulfone (ATS) (I) has

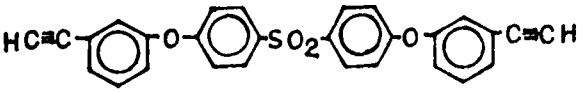

I

thermal properties (after cure) described as quite good. Further, it met all the processing criteria for a 350°F matrix material. Composites retained their strength properties after being saturated with moisture at 165°F.[7] However, the values for elongation to break and energy to fracture were marginal.[8] Thus it was considered desirable to introduce structural modifications into the ATS system which would be expected to improve these marginal properties and provide a more flexible material.

Cross-link density is one of the structural features in a cured material which contributes to brittleness. Thus the decision was made to synthesize ATS systems expected to have modified or decreased cross-link densities after cure. A straightforward route to this end is to synthesize ATS oligomers with greater distance between the reactive end groups than in the original ATS (I). Two compounds chosen for evaluation of this approach are the ATS systems II and III which incorporate in their backbone the rigid 4,4'-diphenyl and 1,4-phenylene segments respectively.

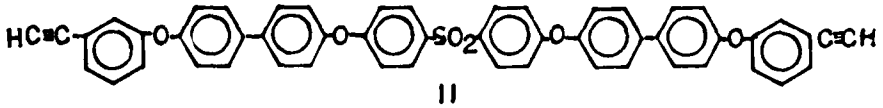

II

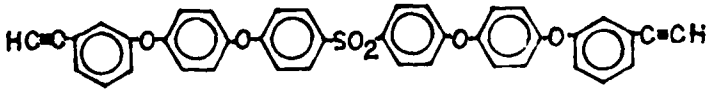

III

II. OBJECTIVES

The objective of this project was to synthesize compounds II and III. The general synthetic routes are based on the bis-phenols (hydroquinone and p,p'-biphenol), m-dibromobenzene and 4,4'-dichlorodiphenylsulone, all readily available materials.

A series of reaction schemes are outlined below (Reactions 1-12). It is appropriate at this point to comment on some specific aspects of certain of these reactions.

III. DISCUSSION OF REACTIONS

Three reaction types are proposed in these syntheses. All involve displacement of aromatic halides. In those reactions where nucleophilic aromatic substitution is involved, (Reactions 1, 6, 10) it is first necessary to convert the bisphenol to its potassium salt with KOH. The resulting water is then removed by azeotropic distillation with benzene before reaction of the phenoxide with dichlorodiphenylsulfone in sulfolane. The other ether forming reactions (Reactions 2, 5, 7, 8, 12) are of the classical Ullman ether synthesis type. The mechanism of this reaction is still the subject of study.[9] The active catalyst appears to be Cu^{+1} and it is necessary to do the reaction in inert atmosphere to avoid oxidation to Cu^{++}. However, it has been reported[10] that aryl halides react with cuprous ion to reduce the halide and form cupric ion.

The final displacement reaction was recently developed[11] and is effective for displacement of aromatic and vinylic bromides and iodides with an acetylene using the catalyst combination of cuprous iodide and bis-triphenylphosphine palladium dichloride in a tertiary amine solvent (Reaction 3). In a final step, the protective group is removed from the

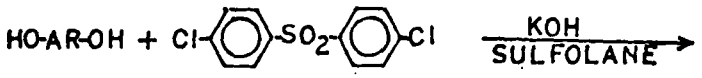

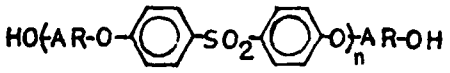

IV

REACTION 1

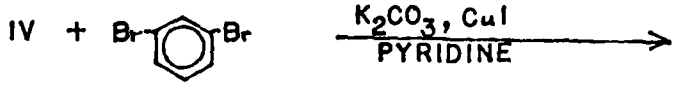

REACTION 2

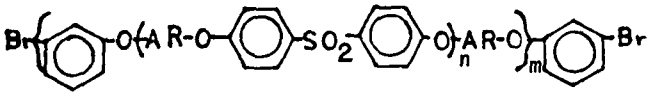

V

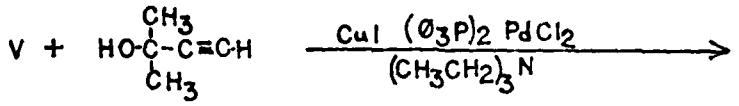

REACTION 3

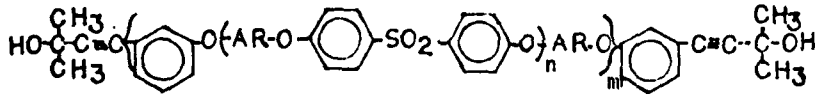

VI

VI + KOH ⟶

REACTION 4

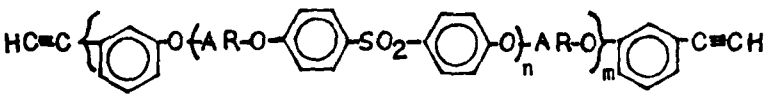

VII

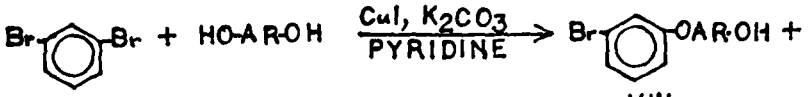

VIII

REACTION 5

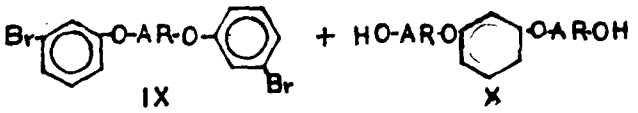

IX X

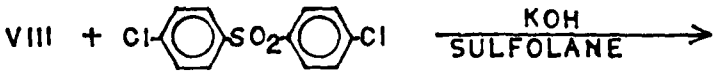

REACTION 6

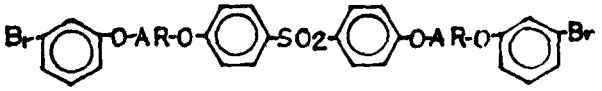

V(n=1)

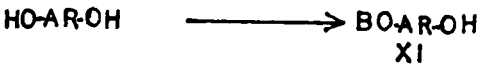

REACTION 7

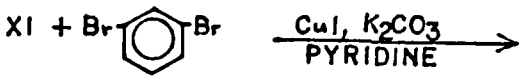

REACTION 8

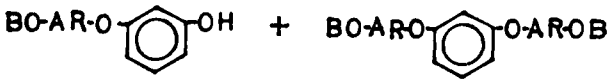

XII XIII

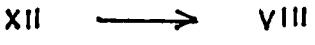

REACTION 9

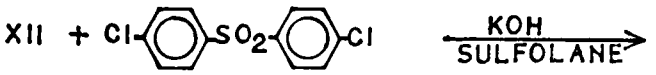

REACTION 10

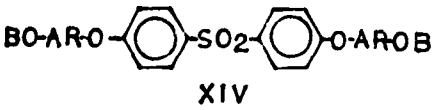

REACTION 11

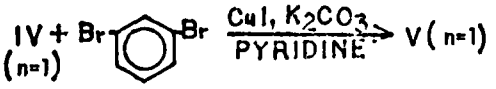

REACTION 12

terminal butynol functions by base catalyzed reversed addition to produce the AT product (Reaction 4).

Those condensation reactions in which the reactants are difunctional can lead to an array of oligomeric products. Use of an excess of bisphenol in Reaction I assures hydroxyl end-capping. However, the distribution of oligomers (Compound IV, values of n) is related to the relative rates of the competing reactions. Similarly Reaction 2 produces oligomers. In this case an excess of m-dibromobenzene assures m-bromophenyl end-caps and, as above, the distribution of oligomers (Compound V, values of m) is related to competing reaction rates.

Production of higher molecular weight oligomers may be useful to the overall goal of this project since values of n and/or m greater than one puts even greater distance between functional end groups. Alternatively, a reaction scheme assuring formation of oligomer in which the values of n and m are one is shown in Reaction 5. This reaction yields, among other products, the "half-product," VIII which when reacted with dichlorodiphenylsulfone yields V. Carrying V through the sequence of Reactions 3 and 4 yields compounds II and III as the lowest molecular weight oligomers (n=1, m=1).

Reaction 5 is complicated since the desired product, VIII, will react with starting materials to yield IX and X. IX and X can then go on to higher molecular weight products. Consideration of the various competing reactions suggests that an excess of m-dibromobenzene should suppress formation of X and higher molecular weight products while favoring formation of "half-product" VIII and "di-product" IX. It would be necessary to do an optimization study to determine the factors which favor

production of "half-product" VIII over "di-product," IX.

An alternate approach which might be expected to provide over-all high yields of "half-product" VIII involves blocking or protection of one of the phenol functions (Reaction 7) before its condensation with an excess of m-dibromobenzene to yield XII (Reaction 8) which after removal of the protecting groups provides "half-product" VIII.

Examples of protecting groups are methyl ether, dihydropyran and esters. All of these groups are relatively easily removed. However, of the three, an ester function would be least likely to survive the basic conditions of the Ullman ether synthesis.

IV. RESULTS

The synthetic sequences outlined in Section II represent a long range synthetic undertaking. During the term of this project a relatively small number of the reactions were accomplished. In some cases a sufficient quantity of a desired intermediate was prepared for future workers to carry on to the next step. In other cases, only small quantities were isolated and the reaction was evaluated and described for future workers to repeat and prepare sufficient quantities for subsequent synthetic steps.

In the following paragraphs the results of these synthetic experiments are reported.

A. Compound VIIIa (Ar = p,p'-biphenylene)

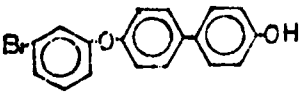

This compound was prepared in 26 percent yield by the Ullman ether synthesis (Reaction 5) using 4,4'-dihydroxybiphenyl and m-dibromobenzene. The reaction was repeated a number of times and the yields were found to be not reproducible although a total of 10 grams was prepared.

B. Compound IVa (Ar = p,p'-biphenylene)

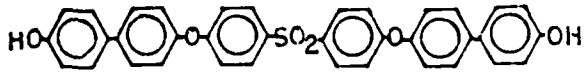

This oligomeric material was prepared in 88 percent yield by reaction of 4,4'-dihydroxybiphenyl with 4,4'-dichlorodiphenylsulfone (Reaction 1).

The lower molecular weight oligomers were separated from the mixture by base extraction.

C. Compound VIIIb (Ar = p-phenylene)

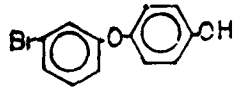

This "half-product" was prepared in very poor yield (traces only) by reaction of hydroquinone and m-dibromobenzene (Reaction 5). The appearance of the reaction mixture suggested extensive oxidation of the hydroquinone occurred despite the inert reaction atmosphere. Presumably the oxidizing agent is cupric ion which results from interaction of m-dibromobenzene and cuprous ion.[10]

Compound VIIIb was more successfully prepared by a two step sequence involving first the preparation of Compound XIIb (Ar = p-phenylene; B= CH_3), 4-methoxy-4'-bromodiphenylether. XIIb was made in 43 percent yield by Reaction 8 with hydroquinone monomethyl ether and m-dibromobenzene. Cleavage of the methyl group with refluxing aqueous HBr gave the desired product, 4-hydroxy-4'bromodiphenylether (VIIIb). Although the yield of this step was under 10 percent, it was observed that a large amount of the methyl ether (XIIb) was unreacted. This observation suggests that another reagent (e.g. pyridine hydrochloride see paragraph D below) would be expected to cleave the ether more efficiently.

D. Compound IVb (Ar = p-phenylene, n=1)

Compound IVb was prepared by a two-step synthesis involving first the reaction of hydroquinone monomethyl ether with 4,4-dichlorodiphenylsulfone (Reaction 10). The resulting dimethyl ether, XIVb (Ar = p-phenylene; B=CH_3) was obtained in 68 percent yield. Cleavage of the methylether functions was done with pyridine hydrochloride and gave the desired bisphenol, IVb, in 46 percent yield.

E. Compound Vb (Ar = p-phenylene; n=1)

Compound Vb was prepared in 80 percent yield by reaction of the bisphenol IVb with m-dibromobenzene. The product obtained was a viscous clear material which is probably oligomeric (m>1).

V. RECOMMENDATIONS

The synthetic sequences outlined in Section II offer several areas for concentration of effort. These may be classified into two categories. The one leads to ATS products which are monomeric (n=1, m=1) and the other leads to ATS products which are oligomeric.

On the basis of initial experimental work carried out in the term of this project, it appears that synthetic yields obtained with the Ullman ether synthesis are not reproducible. When applied to reactions which form oligomeric products, it will be extremely difficult to obtain product with similar molecular weight distribution from batch to batch. Thus post cure properties of such oligomeric products will be difficult to evaluate and to reproduce. It would probably be necessary to determine the factors necessary for better control of the Ullman ether synthesis before this problem could be simplified.

On the other hand, synthesis of the monomeric products II and III would provide, after cure, materials which would be of use in evaluating the effect of decreasing cross-link density by curing ATS materials of known structure. It is recommended that initial effort go into synthesis of the monomeric compounds.

The "half-product" VIIIa, 4-hydroxy-4'-(3-bromophenoxy)biphenyl was prepared in a sufficient quantity to take on through the next steps (Reactions 6, 3 and 4) to provide the required amount of the desired compound II. It is suggested that this be the first synthesis to be carried out. However, for future synthesis of this compound, it is strongly suggested that "half-product" be synthesized by first protecting one of the hydroxyl functions of the bis-phenol with either a methyl or a tetrahydropyranyl group (Reaction 7, Compound XI, Ar = p,p'-biphenylene; B=CH_3[1] or THP[2]) as discussed in Section III.

The synthesis of the ATS III should be approached in the same general way using the reactions reported in this project for synthesis of 4-methoxy-4'-bromodiphenyl ether, and its subsequent cleavage with

pyridine-hydrochloride to form the "half-product" 4-hydrooxy-4'-bromo-diphenyl ether.

REFERENCES

1. R. F. Kovar, G. F. L. Ehlers and F. E. Arnold, J. of Polymer Sci., Poly. Chem. Ed., 15, 1081 (1977).

2. F. L. Hedberg and F. E. Arnold, J. of Appl. Poly. Sci., 24 (3), 763 (1979).

3. G. A. Laughran and F. E. Arnold, Polymer Preprints, 21 (1), 199 (1980).

4. J. M. Pickard, E. G. Jones and I. J. Goldfarb, Macromolecules, 12 (5), 895 (1979).

5. M. G. Maximovitch, S. C. Lockerby, R. F. Kovar and F. E. Arnold, Adhesive Age, 40 (1977).

6. M. G. Maximovitch, S. C. Lockergy, R. F. Kovar and F. E. Arnold, Soc. Adv. Mat'rs. and Process Eng., 22, 713 (1977)

7. M. G. Maximovitch, S. C. Lockerby, G. A. Laughran and F. E. Arnold, Soc. Adv. Mat'rs. and Process Eng., 23, 490 (1978)

8. F. E. Arnold, Non-Metallic Materials Division, Air Force Materials Laboratory, Wright Patterson Air Force Base, Ohio 45433. Private Communication.

9. A. A. Moroz and M. S. Shvartsberg, Russ. Chem. Rev., 43, 679 (1974).

10. R. G. R. Bacon and O. J. Stewart, J. Chem. Soc., 4953 (1965).

11. E. T. Sabourin, Petroleum Chem. Preprints, 20 (1), 233 (1979).

12. O. T. Schmidt, E. Komarek, and H. Rentel, Ann 602, 50 (1957). Chem. Abstr. 51, 12041i.

1982 USAF-SCEEE GRADUATE STUDENT SUMMER SUPPORT PROGRAM

Sponsored by the

AIR FORCE OFFICE OF SCIENTIFIC RESEARCH

Conducted by the

SOUTHEASTERN CENTER FOR ELECTRICAL ENGINEERING EDUCATION

FINAL REPORT

ILL-POSEDNESS IN THE NUMERIC SOLUTION OF HYPERBOLIC EQUATIONS

Prepared By: Dorothy A. FitzGerald

Academic Department: Department of Mathematics

University: Boston University

Research Location: Air Force Armament Laboratory, Munitions Division, Compatibility Branch, Structural Dynamics Section

USAF Research Contact: Robert L. Lantor

SFRP Supervising Faculty Member: Dr. Luigi Perino, Professor

Date: September 14, 1982

Contract No: F49620-82-C-0035

ACKNOWLEDGEMENTS

The authors would like to thank the Air Force Systems Command, the Air Force Office of Scientific Research and the Southeastern Center for Electrical Engineering Education for providing them with the opportunity to spend an extremely productive and enjoyable summer at the Air Force Armament Laboratory, Eglin AFB, Florida. They would like to acknowledge the Laboratory, and in particular the Compatibility Branch, for its support throughout the research period.

The authors would like to extend special thanks to the Structural Dynamics Section, including Wiley J. Robinson, Robert Bunton, Dave Belk, William Miller, Ed Martin, Chuck Denegri, Marion Barber and Doug Chojecki, for all of their help and for making us feel welcome both during work and after.

IMPROVEMENT IN THE NUMERIC SOLUTION OF AERODYNAMIC EQUATIONS

by

Dorothy A. FitzGerald
Luigi Morino

ABSTRACT

An improvement is made in the algorithm for the time-domain integration of the potential aerodynamic equations. The new method of solution is considerably faster than the old one (which is already about one order of magnitude faster than the only competitor) and the results indicate that considerable additional savings can be achieved, especially if parallel processing is utilized. It was noted that with the above changes, the solution of the steady state problem using a time domain transient analysis can be faster than by direct Gaussian elimination of the steady state equation. An attempt is made to extend the same idea to oscillatory flows.

I. *INTRODUCTION:*

The field of unsteady potential aerodynamics is governed by

$$\nabla^2 \varphi - \frac{1}{a_\infty^2}\left(\frac{\partial}{\partial t} + U_\infty \frac{\partial}{\partial x}\right)^2 \varphi = \chi \qquad (1)$$

where χ includes all the nonlinear terms.

Using the Greens's function method, this equation can be transformed into an integral differential delay equation (Ref. 1)

$$\begin{aligned} E_\varphi \varphi_\varphi = &- \iint_{\mathcal{L}_B} \left[\psi \frac{1}{4\pi r} - \varphi \frac{\partial}{\partial n}\frac{1}{4\pi r} + \dot{\varphi}\frac{1}{4\pi r}\frac{\partial \hat{\theta}}{\partial n}\right]^\theta d\mathcal{L} \\ &+ \iint_{\mathcal{L}_w} \left[\Delta\varphi \frac{\partial}{\partial n}\frac{1}{4\pi r} - \Delta\dot{\varphi}\frac{1}{4\pi r}\frac{\partial\theta}{\partial n}\right]^\theta d\mathcal{L} \\ &- \iiint_{V_\varphi} [\chi]^\theta \frac{1}{4\pi r}\, dV \end{aligned} \qquad (2)$$

where all expressions are in the Prandtl-Glauert space, $\mathcal{L}_B$ is the surface of the body, $\mathcal{L}_w$ is the surface of the wake, V_φ is the volume of the field, $\psi = \frac{\partial \varphi}{\partial n}$, $\Delta x = x - x_\varphi$, $\theta = (M\Delta x + r)\frac{M}{\beta^2}$, $\hat{\theta} = (-M\Delta x + r)\frac{M}{\beta}$

and $E_\varphi = 0$ for P_φ inside surface

$= \frac{1}{2}$ for P_φ on surface

$= 1$ for P_φ outside surface.

The boundary condition on the wake is $\Delta p = 0$ or, using Bernoulli's theorem and integrating, $\Delta\varphi$ = constant following a point of the wake or,

$$\Delta\varphi(\bar{P}_w, t) = \Delta\varphi(\bar{P}_{TE}, t-\tau)$$

where τ is the convection time from P_{TE} to P_w.

Using the finite element method (e.g. for nodes on the body setting $\varphi(P, t-\theta) = \sum \varphi_K(T-\theta_K) M_K(P)$) one obtains the differential-delay equation (Ref. 2)

$$\phi_n(T) = \sum B_{nK}\,\psi_K(T-\theta_{nK}) + \sum C_{nK}\,\phi_K(T-\theta_{nK}) + \sum D_{nK}\,\dot{\phi}_K(T-\theta_{nK}) + \sum F_{nm}\,\Delta\phi_m(T-\theta_{nm}) + \sum G_{nm}\,\Delta\dot{\phi}_m(T-\theta_{nm}) + \sum H_{np}\,\gamma_p(T-\theta_{np}) \qquad (3)$$

with $\Delta\phi_n(T) = \Delta\phi_n^{*}(T-\pi_n)$ where π is the convection time from the trailing edge to the point P_n, the index k ranges over the nodes of the body, the index n ranges over the nodes of the wake, the index p ranges over the nodes of the field and the index h ranges over the control points on the body (which do not necessarily coincide with the body nodes).

The current method of solution (Ref. 2) approximates the delay and the derivative with difference equations, namely, if $\theta_{nK} = (m_{nK} + \alpha_{nK})\Delta t$ where m_{nK} is an integer and $0 \le \alpha_{nK} < 1$ then $\phi_K(T-\theta_{nK}) = (1-\alpha_{nK})\,\phi_K^{(m_{nK})} + \alpha_{nK}\,\phi_K^{(m_{nK}-1)}$
and $\dot{\phi}_K(T-\theta_{nK}) = (\phi_K^{(m_{nK})} - \phi_K^{(m_{nK}-1)}) / \Delta t$
where $\phi_K^{(m_{nK})} = \phi_K(T - m_{nK}\Delta t)$.

Letting

$$B_{nK}^{(1)} = (1-\alpha_{nK})\,B_{nK}$$

$$B_{nK}^{(2)} = \alpha_{nK}\,B_{nK}$$

$$C_{nK}^{(1)} = (1-\alpha_{nK})\,C_{nK} + \frac{1}{\Delta t}\,D_{nK} \quad \text{if } m_{nK} = 0$$
$$= 0 \quad \text{if } m_{nK} \neq 0$$

$$C_{nK}^{(2)} = (1-\alpha_{nK})\,C_{nK} + \frac{1}{\Delta t}\,D_{nK} \quad \text{if } m_{nK} \neq 0$$
$$= 0 \quad \text{if } m_{nK} = 0$$

$$C_{nK}^{(3)} = \alpha_{nK}\,C_{nK} - \frac{1}{\Delta t}\,D_{nK}$$

$$F_{nm}^{(1)} = (1-\alpha_{nm})\,F_{nm} + \frac{1}{\Delta t}\,G_{nm} \quad \text{if } m_{nm} = 0$$
$$= 0 \quad \text{if } m_{nm} \neq 0$$

$$
\begin{aligned}
F_{hn}^{(1)} &= (1-\alpha_{hn})\,F_{hn} + \tfrac{1}{\Delta t}\,G_{hn} && \text{if } m_{hn} \neq 0\\
&= 0 && \text{if } m_{hn} = 0\\
F_{hn}^{(2)} &= \alpha_{hn}\,F_{hn} - \tfrac{1}{\Delta t}\,G_{hn}\\
H_{hp}^{(0)} &= (1-\alpha_{hp})\,H_{hp} && \text{if } m_{hp} = 0\\
&= 0 && \text{if } m_{hp} \neq 0\\
H_{hp}^{(1)} &= (1-\alpha_{hp})\,H_{hp} && \text{if } m_{hp} \neq 0\\
&= 0 && \text{if } m_{hp} = 0\\
H_{hp}^{(2)} &= \alpha_{hp}\,H_{hp}
\end{aligned}
$$

and noting that $\Delta\phi_h = \Delta\phi_n^{TE}(\tau-\tau_n)$ where τ_n=nondimensional ζ_n and

$$\Delta\phi_n^{TE} = \phi_{kU} - \phi_{kL} = \sum_K S_{nK}\,\phi_K$$

where S_{nK}= 1 if $P_K = P_n^{TE}$ is on the upper side of $\mathcal{E}_\beta$

S_{nK}= -1 if $P_K = P_n^{TE}$ is on the lower side of $\mathcal{E}_\beta$

S_{nK}= 0 otherwise,

Eq. 3 may be rewritten as

$$
\begin{aligned}
&\sum_K \left(\delta_{hK} - C_{hK}^{(0)} - \sum_n F_{hn}^{(0)}\,S_{nK}\right)\phi_K^{(m)} - \sum_p H_{hp}^{(0)}\,\chi_p^{(m)}\\
&\quad = \sum_K \left(B_{hK}^{(1)}\,\psi_K^{(m_{hK})} + B_{hK}^{(2)}\,\psi_K^{(m_{hK}+1)}\right)\\
&\quad + \sum_K \left(C_{hK}^{(1)}\,\phi_K^{(m_{hK})} + C_{hK}^{(2)}\,\phi_K^{(m_{hK}+1)}\right)\\
&\quad + \sum_n \left(F_{hn}^{(1)}\,\Delta\phi_n^{(m_{hn})} + F_{hn}^{(2)}\,\Delta\phi_n^{(m_{hn}+1)}\right)\\
&\quad + \sum_p \left(H_{hp}^{(1)}\,\chi_p^{(m_{hp})} + H_{hp}^{(2)}\,\chi_p^{(m_{hp}+1)}\right)
\end{aligned}
\qquad (4)
$$

or, combining the right-hand-side terms,

$$\sum_K \left(\delta_{hK} - C_{hK}^{(0)} - \sum_n F_{hn}^{(0)}\,S_{nK}\right)\phi_K^{(m)} - \sum_p H_{hp}^{(0)}\,\chi_p^{(m)} = RHS \qquad (5)$$

Note that for subsonic flows the nonlinear terms χ_p can be neglected, giving

$$\sum_K \left(\delta_{hK} - C_{hK}^{(0)} - \sum_n F_{hn}^{(0)}\,S_{nK}\right)\phi_K^{(m)} = RHS \qquad (6)$$

Any solution of the transonic equation (Eq. 5) requires two basic macro-operations:

1. Matrix products of the type

$$\sum M_{hK}\,f_K^{(hK)}$$

2. Solution of equations of the type

$$\Sigma A_{nk} x_k = f_n$$

where f_n is a nonlinear function of x_k for the transonic case and constant for the subsonic case.

The above algorithm has been recently developed and implemented in a computer program (SUSAN, Ref. 3) for the purpose of algorithm validation (the subsonic algorithm is implemented in the program SOUSSA, Ref. 2). The results obtained are in excellent agreement with existing experimental and theoretical results. However, in the process of validating the algorithm no emphasis was placed on the efficiency in terms of memory and time.

The methods used to perform the macro-operations were very straight-forward. The matrix multiplication was obtained by first calculating the vector on the right-hand-side and then performing the matrix-vector multiplication. For the second macro-operation the approach taken was to use the equation

$$\phi = (I - C - FS)^{-1} [RHS] \tag{7}$$

The system solution was obtained through Gaussian elimination followed by straight-forward matrix-vector multiplication at each time step.

II. OBJECTIVES:

The objective of this research is to improve the method of solution of the differential-delay equations (Eq. 5) which result from the application of Green's function method

to the aerodynamic partial differential equations. In particular, the goal is to speed up the computer program SUSAN by developing more efficient algorithms which take advantage of the inherent parallelism in the solution. The subsonic version of the program, SOUSSA, will be studied initially.

Because of the very high cost of computer time, it is necessary to develop faster solutions to the aerodynamic problems in order to handle more complex problems than have previously been attempted (e.g. viscous unsteady three-dimensional transonic flows over wing-fuselage-tail configurations). Maximum efficiency can only be obtained by utilizing the full capabilities of the latest computer architectures. Parallel processors such as the ILLIAC IV, Cray-1 and CYBER 205 are currently being used, and new generations of supercomputers, with speeds at least one order of magnitude higher than current supercomputers, are being developed specifically for the field of computational fluid dynamics.

Although the algorithm used in the computer program SUSAN is already about one or two orders of magnitude faster than its only competitor (LTPAN3, based on the finite difference method), the time solution is still the limiting factor. Thus, the development of more efficient algorithms for the time-domain integration of the aerodynamic equations which facilitate the use of parallel computations is essential in order to practically obtain results for more complex

aircraft configurations.

The proposed changes in the algorithm are described in Section III. It was noted that after these changes the solution of a steady-state problem becomes easier using a time-domain transient analysis than by direct matrix inversion (this issue is examined in Section IV). Finally an attempt to extend the same idea to oscillatory flows is presented in Section V.

III. TIME DOMAIN SOLUTION:

In order to facilitate the implementation of new algorithms it was decided to rewrite *SCUSSA*, structured in such a way that experimentation with different algorithms would be easier. Thus, a considerable amount of time was spent on the development of this new code (called UTSA, for Unsteady Transonic and Subsonic Aerodynamics). For the sake of simplicity during algorithm development, the code currently handles subsonic only (see Eq. 6), although the major motivation for this work is the transonic field in which computer costs are extremely high.

The program UTSA is comprised of six totally independent modules, or "segments", which are called by the main program. The program was written such that each segment could be replaced by another segment which performs the same operation, possibly using a different algorithm, without affecting the other segments. Each segment is briefly explained below:

1. Generates the body geometry

2. Generates the boundary condition modes and the generalized-force modes

3. Evaluates the frequency-domain coefficients (i.e. matrices D, C, and F, see Eq. 3)

4. Evaluates coefficients relating the generalized coordinates to ψ and the generalized forces to ϕ

5. Evaluates the time domain coefficients from the frequency domain coefficients (i.e. generates matrices RHS, $C^{(n)}$ and $F^{(n)}$, see Eq. 6)

6. Performs the time solution. More precisely at each time step, it calulates

   a) Lagrangian generalized coordinates and their time derivatives (q_n and $\dot{q}_n$)

   b) Normalwash ψ_n from q_n and $\dot{q}_n$

   c) Potential ϕ_n and potential discontinuity $\Delta\phi_n$ (i.e., solution of Eq. 6) from ψ_n

   d) Generalized forces from ϕ_n

The last segment, and in particular the calculation of the potential ϕ, is the most critical in terms of computer memory and time and is therefore the subject of this research on algorithm efficiency.

As discussed in Section I, the approach taken in SOUSSA to solve for ϕ was to solve Eq. 7 using Gaussian elimination followed by a matrix-vector multiplication. This can be shown to take $(\alpha_1 n^3 + \alpha_2 n^2) * n_{TS}$ operations, where n is the size of the matrix and n_{TS} is the number of time steps (Ref. 4).

A new algorithm is used in UTSI which uses iteration. Eq. 6 is written as $\phi^{(k)} = RHS + (C + FS)\phi^{(k-1)}$ (7) and the potential ϕ is calculated by iteration (the initial value is that at the preceding time step). This method of solution takes $(\alpha_3 n n_I + \alpha_2 n^2) n_{IS}$ operations, where n_I is the number of iterations. Since this iterative solution of Eq. 6 must be repeated at every time step, this algorithm is much more suited for parallel processing than either the finite-difference or finite-element methods.

The initial effort was to implement SOURSA at the research facility (Cyber 205), study its method of solution, and then experiment with different known algorithms for performing the basic macro-operations. SOURSA was successfully converted from FORTRAN IV to FORTRAN V at the Cyber computing facilities, and results obtained correlated exactly with those obtained previously at Boston University. This was done in order to be able to validate the results from UTSI.

IV. STEADY STATE SOLUTION:

It should be noted that for high subsonic flows, the matrix C is highly sparse. Therefore the number of operations, n_1, required for the solution of the system of equations at each time step is $n_1 < n_e n_s n_I$ where n_e is the number of equations and n_s is the largest number of nonzero entries in the rows of $C^{(0)}$(S stands for sparseness). The number of operations required at each time step to evaluate the right hand side is (note that C^1 and C^2 are treated as

fully populated) $n_2 = 2n_E^2$. Therefore the total number of operations required for the solution, n_{SOL}, is

$$n_{SOL}^{TO} < (2n_E^2 + n_E n_s n_I) n_{TS} \qquad (9)$$

As noted by Tseng (Ref. 3), if $\Delta t \to \infty$ and E^1, C', and C^1 go to zero, Eq. 6 reduces to the steady state equation

$$Y = B\Psi + C Y$$

This implies that, as our experience indicates, the integration scheme is stable even for very large Δt. On the other hand as $\Delta t \to \infty$ the matrix $C^{(n)}$ becomes fully populated ($n_s \to n_E$), thereby decreasing the advantage of Gauss-Seidel iteration over Gaussian elimination; even convergence of the iteration scheme becomes questionable. Hence the best value of Δt is a trade-off between reducing the number of time steps and decreasing the number of operations per time step. Our results indicate that converged results can be obtained with $n_{TS} \sim 10$, $n_s \sim 10$ and $n_I \sim 5$, which yields

$$n_{SOL}^{TO} < 20 n_E^2 + 500 n_E \qquad (10)$$

Comparing this with the operations required to solve the system by Gaussian elimination (Ref. 4, p. 36, eq. 9)

$$n_{SOL}^{GE} = \frac{1}{3} n_E^3 + n_E^2 - \frac{1}{3} n_E$$

one can see that for a large number of equations the time domain solution is faster than the Gaussian elimination solution. For instance for n = 100,

$n_{SOL}^{TO} = 250{,}000$ whereas $n_{SOL}^{GE} = 343{,}300$.

V. OSCILLATORY SOLUTION:

Section IV dealt with the problem of steady state

flows. In this section oscillatory flows are considered. Such a flow occurs when the normalwash is given by

$$\Psi_K(T) = \tilde{\Psi}_K e^{i\Omega T} + \tilde{\Psi}_K^* e^{-i\Omega T} \tag{11}$$

where $\tilde{\Psi}_K$ are complex constants and * indicates complex-conjugate value. (These oscillatory boundary conditions are combined with the steady-state boundary conditions. However, the problem is linear and therefore the two solutions are decoupled and can be dealt with independently).

For the sake of clarity only a linear problem without wake (i.e. $\Gamma_{hm} = G_{hm} = H_{hp} = 0$) is considered here. In this case, a solution to Eq. 3 with boundary conditions given by Eq. 11 is of the type $\Phi_k(T) = \tilde{\Phi}_k e^{i\Omega T} + \tilde{\Phi}_K^* e^{-i\Omega T}$ (12) where $\tilde{\Phi}_K$ are constant. Combining this equation with Eq. 3 (with $\Gamma_{hm} = H_{hp} = 0$) yields

$$\tilde{\Phi}_h = \sum B_{hK} e^{-i\Omega\Theta_{hK}} \tilde{\Psi}_K + \sum (C_{hK} + i\Omega D_{hK}) e^{-i\Omega\Theta_{hK}} \tilde{\Phi}_K \tag{13}$$

or

$$\left[\delta_{hK} - (C_{hK} + i\Omega D_{hK}) e^{-i\Omega\Theta_{hK}}\right] \{\tilde{\Phi}_K\} = \left[B_{hK} e^{-i\Omega\Theta_{hK}}\right] \{\tilde{\Psi}_K\} \tag{14}$$

The above equation is the basis for oscillatory aerodynamics.

The analysis of Section IV indicates that obtaining a steady-state solution through a time-domain analysis may require less operations (see Eq. 9) than obtaining the same solution by Gaussian elimination (see Eq. 10).

A question that immediately arises is whether it is possible to accomplish similar results for oscillatory

flows. A method to accomplish this is proposed here. Advantages and disadvantages are discussed. Ultimately the algorithm should be validated by writing a computer program and comparing the results with those obtained with the frequency domain code.

The method proposed here is based on the idea of replacing the function $\Phi_k(T)$ with the amplitude of the envelope of the oscillatory solution. More precisely, set

$$\Phi_k(T) = \tilde{\Phi}_k(T)\, e^{i\Omega T} + \tilde{\Phi}_k^*(T)\, e^{-i\Omega T} \tag{15}$$

Note that this equation differs from Eq. 12 because $\tilde{\Phi}_k$ is not a complex constant but a complex function of time. Note also that $\tilde{\Phi}_k(T)$ is not uniquely defined by the above equation (in other words a given $\tilde{\Phi}(T)$ yields a unique value for $\bar{\Phi}(T)$, but the reverse is not true).

Combining Eqs. 11 and 12 with Eq. 6 (with $F_{hm} = 0$) yields

$$\begin{aligned}
&\dot{\tilde{\Phi}}_k(T)\, e^{i\Omega T} + \dot{\tilde{\Phi}}_k^*(T)\, e^{-i\Omega T} \\
&\quad = \sum B_{hk}\left[\tilde{\Phi}_k\, e^{i\Omega(T-\Theta_{hk})} + \tilde{\Phi}_k^*\, e^{-i\Omega(T-\Theta_{hk})}\right] \\
&\quad + \sum C_{hk}\left[\tilde{\Phi}_k(T-\Theta_{hk})\, e^{i\Omega(T-\Theta_{hk})} + \tilde{\Phi}_k^*(T-\Theta_{hk})\, e^{-i\Omega(T-\Theta_{hk})}\right] \\
&\quad + \sum D_{hk}\left[\dot{\tilde{\Phi}}_k(T-\Theta_{hk})\, e^{i\Omega(T-\Theta_{hk})} + \dot{\tilde{\Phi}}_k^*(T-\Theta_{hk})\, e^{-i\Omega(T-\Theta_{hk})}\right. \\
&\qquad \left. + i\Omega\,\tilde{\Phi}_k(T-\Theta_{hk})\, e^{i\Omega(T-\Theta_{hk})} - i\Omega\,\tilde{\Phi}_k^*(T-\Theta_{hk})\, e^{-i\Omega(T-\Theta_{hk})}\right]
\end{aligned} \tag{16}$$

Finally, by equating the coefficients of $e^{i\Omega T}$ and $e^{-i\Omega T}$, one obtains

$$\begin{aligned}
\dot{\tilde{\Phi}}_h(T) &= \sum B_{hk}\, e^{-i\Omega\Theta_{hk}}\,\tilde{\Phi}_k \\
&\quad + \sum (C_{hk} + i\Omega D_{hk})\, e^{-i\Omega\Theta_{hk}}\,\tilde{\Phi}_h(T-\Theta_{hk}) \\
&\quad + \sum D_{hk}\, e^{-i\Omega\Theta_{hk}}\,\dot{\tilde{\Phi}}_h(T-\Theta_{hk})
\end{aligned} \tag{17}$$

and its complex conjugate. (Note that having equated the coefficients of $e^{i\Omega T}$ and $e^{-i\Omega T}$ independently, the functions $\tilde{\Phi}_h$

and $\tilde{\Phi}_h^*$ are now completely defined). The above equation can be solved approximately in the time domain using the same approach used for the solution of Eq. 3 (i.e., approximating Eq. 3 with Eq. 6). If the solution $\tilde{\Phi}_h(T)$ reaches a steady state, then

$$\tilde{\Phi}_h^{(\infty)} = \lim_{T\to\infty} \tilde{\Phi}_h(T) \tag{18}$$

is the desired solution for Eq. 13.

In order to appreciate and understand the subtleties of the method of solution introduced above let us apply it to a simpler problem, such as

$$\begin{aligned} &\dot{x} + \alpha x = A e^{i\Omega t} + A^* e^{-i\Omega t} \\ &x(0) = B \end{aligned} \tag{19}$$

The solution of the above equation is

$$x = \frac{A}{\alpha + i\Omega} e^{i\Omega t} + \frac{A^*}{\alpha - i\Omega} A^* e^{-i\Omega t} + C e^{-\alpha t} \tag{20}$$

where C is determined by the initial condition, which yields

$$C = B - \frac{A}{\alpha + i\Omega} - \frac{A^*}{\alpha - i\Omega} \tag{21}$$

If $\alpha > 0$, as t goes to infinity, the last term in the above equation goes to zero and one obtains

$$x_\infty(t) = \frac{1}{\alpha + i\Omega} A e^{i\Omega t} + \frac{1}{\alpha - i\Omega} A^* e^{-i\Omega t} \tag{22}$$

Next consider the method introduced above: set

$$x(t) = \tilde{X}(t) e^{i\Omega t} + \tilde{X}^*(t) e^{-i\Omega t} \tag{23}$$

and combine with Eq. 19 to obtain

$$\begin{aligned} &\dot{\tilde{X}} + (i\Omega + \alpha)\tilde{X} = A \\ &\tilde{X}(0) = B/2 \end{aligned} \tag{24}$$

and its complex conjugate. The solution to the above equation is

$$\tilde{X} = \frac{A}{\alpha + i\Omega} + D e^{-(\alpha + i\Omega)t} \tag{25}$$

where

$$D = \frac{B}{2} - \frac{A}{\alpha + i\Omega} \tag{26}$$

Combining Eqs. 23 and 25 yields

$$x(t) = \frac{A}{\alpha + i\Omega} e^{i\Omega t} + \frac{A^*}{\alpha - i\Omega} e^{-i\Omega t} + (D + D^*) e^{-\alpha t} \tag{27}$$

(with $D + D^* = C$) in agreement with Eq. 20.

The main advantage of using Eq. 24 over Eq. 19 is that if only the steady-state (oscillatory) solution is desired, then using a numerical integration scheme yields this solution even with very large time steps (larger for instance than the period $T = 2\pi/\Omega$ of the steady state solution): the evaluation of $De^{-(\alpha + i\Omega)t}$ deteriorates as Δt increases, but, as long as this term goes to zero, our objective is attained. On the contrary the use of Eq. 19 requires the use of a small time step (typically many per cycle of oscillation) in order for the solution to be accurate.

VI. RECOMMENDATIONS:

The following recommendations are made for the continuation of this research:

1. Validation of the work done on the oscillatory solution through the development of an oscillatory version of the program UTSA
2. Extension to nonlinear problems, where the issue is that higher-frequency components are present
3. Extension to aeroelastic problems, where the issue is that the frequency is not known a priori
4. Vectorization of the program UTSA, from which the $\alpha_1 n^3$ term in the calculation of the number of necessary operations can be reduced

REFERENCES

1. Morino, L. "A General Theory of Unsteady Compressible Potential Aerodynamics," NASA CR-2464, 1974.

2. Tseng, K. and Morino, L. "Nonlinear Green's Function Method for Unsteady Transonic Flows," in Transonic Aerodynamics, David Nixon (ed.), American Institute of Aeronautics and Astronautics, 1981.

3. Tseng, K. Doctoral Dissertation, Boston University, Department of Mathematics, in preparation.

4. Isaacson, E. and Keller, H. Analysis of Numerical Methods. John Wiley and Sons, Inc., New York, 1966.

1982 USAF-SCEEE SUMMER FACULTY RESEARCH PROGRAM

Sponsored by the

AIR FORCE OFFICE OF SCIENTIFIC RESEARCH

Conducted by the

SOUTHEASTERN CENTER FOR ELECTRICAL ENGINEERING EDUCATION

FINAL REPORT

MODELING OF ACTIVE NEUROMUSCULATURE RESPONSE TO MECHANICAL STRESS

Prepared by:	Dr. Andris Freivalds and Mr. Jeffrey L. Harpster
Academic Rank:	Asst. Professor, Industrial Engineering Graduate Student
Department and University:	Dept. of Industrial & Management Systems Engineering The Pennsylvania State University
Research Location:	Air Force Aerospace Medical Research Laboratory, Biodynamics & Bioengineering Division, Modeling & Analysis Branch (AFAMRL/BBM)
USAF Research Colleague:	Dr. Imts Kaleps
Date:	August 13, 1982
Contract No:	F49620-82-C-0035

ACKNOWLEDGMENTS

The work described in this report was performed under the Air Force Office of Scientific Research and the Southeastern Center for Electrical Engineering Education Summer Faculty Research Program at the Air Force Aerospace Medical Research Laboratory, Wright-Patterson Air Force Base, Ohio. The authors express their sincere thanks to these organizations for a very productive and enjoyable summer research program and to the Modeling and Analysis Branch of the Biodynamics and Bioengineering Division for supporting this project.

The authors would also like to thank Dr. Ints Kaleps, Chief, Modeling and Analysis Branch, for suggesting this interesting topic and encouraging further challenging pursuits, Dr. Eberhardt Privitzer, Mr. Ric Rasmussen and Mr. Mark Hoffman for their assistance, Mrs. Elizabeth Alder and Ms. Brenda Martin for their typing and Lt. Thomas Gardner for his patient assistance and the many miles run together.

This research was sponsored by the Air Force Office of Scientific Research under Contract F49620-82-C-0035.

MODELING OF ACTIVE NEUROMUSCULATURE RESPONSE TO MECHANICAL STRESS

by

Dr. Andris Freivalds

and

Mr. Jeffrey L. Harpster

ABSTRACT

The Articulated Total Body (ATB) Model, based on rigid-body dynamics with Euler equations of motion and Lagrange type constraints, was used to predict the forces and motions experienced by air crew personnel in typical flight operations. To provide a more realistic representation of human dynamics, an active neuromusculature was added to the ATB Model via the newly developed advanced harness system. The lumped three parameter muscle model included a contractile element, a damping element and a parallel elastic element.

Two validation studies were performed. The first simulated elbow flexion with one muscle/harness system representing the biceps brachii and the brachialis. The results indicated that the force velocity effects produced the greatest changes in force, with significant force changes due to the damping element and length tension relationship and no force changes due to the parallel-elastic element. The second study simulated the whole body response to a 2-G_y lateral force utilizing trunk musculature. Although the musculature did not completely prevent the lateral deflection of the body, the response is significantly delayed compared to a control response, with the head and neck maintaining the initial posture for a longer period of time.

I. INTRODUCTION:

The use of biodynamic computer-based models for the prediction of human body response to mechanical stress has become an extremely useful and cost-effective research and developmental tool, especially as an alternative to direct experimentation with humans and animals. These models attempt to simulate or predict the forces and motions experienced by a body in high-acceleration events such as impacts or from sudden forces such as wind shear. In particular, the Air Force is interested in the reactions of aircrew personnel to such forces typically encountered in various phases of flight operations, including emergency ejections from high-speed aircraft. Such a hazardous environment is well suited to computer modeling, and with proper execution considerable insight of body motion and stresses developed in the body can be gained.

The Modeling and Analysis Branch of the Air Force Aerospace Medical Research Laboratory (AFAMRL) has been using a human body modeling program known as the Articulated Total Body (ATB) Model for several years. The model is based on rigid-body dynamics using Euler equations of motion with Lagrange-type constraints. The specific configuration uses 15 body segments (head, neck, upper torso, center torso, upper arms, lower arms, upper legs, lower legs, and feet) and 14 joints between the segments. Although it was originally developed by the Calspan Corporation for the study of human-body and anthropometric-dummy dynamics during automobile crashes for the United States Department of Transportation (Fleck et. al., 1974; Fleck, 1975), the ATB Model was sufficiently general to allow simulation of whole-body articulated motion resulting from various impacts or abrupt accelerations applied to the body. Furthermore, modifications involving special joint forces, aerodynamic forces and a complex harness system were added to accommodate specific Air Force applications (Fleck and Butler, 1975).

The ATB Model, although realistically reflecting human body structure, mass distribution and tissue material properties, presently has the serious limitation of only simulating events with passive internal responses. The gross, whole-body motion is no different for human aircrew personnel data than for anthropometric dummy or cadaver data. What is needed is the implementation of an active neuromusculature to simulate both voluntary and

reflex responses of the human subject to externally imposed forces.

II. OBJECTIVES:

The objective of this Summer Faculty Research Project has been to define and formulate methodologies for implementing active muscle effects such as body pretensing and time varying forces into the present ATB Model. Several considerations were involved: (1) the present model was not to be altered, (2) basic muscle phenomena such as the length-tension and force-velocity relationships and passive viscoelastic properties were to be included, and (3) particular emphasis was to be placed on muscles acting in the torso and neck region which affect flexion, extension and lateral motion of the trunk.

The objective was approached as follows: (1) A detailed literature search on muscle functions and current techniques used was performed. (2) Based on the results from the literature and theoretical principles, muscle models were formulated. (3) The new muscle models were implemented into the existing ATB model structure. (4) Simulation of available experimental results were performed.

This final report follows the approach used in fulfilling the objectives and therefore will be organized in a similar fashion.

III. BACKGROUND:

Skeletal Muscle - Skeletal muscles usually originate on the skeleton, span one or more joints and insert into a part of the skeleton again. Each muscle is enclosed in a connective tissue sheath called the epimysium and is held in its correct position in the body by layers of fascia. The muscle is attached to the bones via tendons, while the interior is compartmentalized into longitudinal sections called the fasciculi, each containing many individual muscle fibers. The fibers are enveloped by a connective tissue called the endomysium, which transmits the force of the muscle contraction from individual fibers to the tendons (Tome, 1981).

The muscle fibers do not always run parallel to the force transmitting tendons, as they do in fusiform muscles. They can be arranged in unipennate, bipennate or multipennate form, thus altering the force transmitting charac-

teristics (Fig. 1).

The muscle fiber, although the basic structural unit, with a diameter of 10-60 μ and length from several millimeters to several centimeters, can be subdivided further into myofibrils of 1μ diameter. These myofibrils comprise the hexagonal array of protein filaments that are directly responsible for the contractile process and give rise, with appropriate stains to the peculiar striations that are characteristic of skeletal muscle (Fig. 2). A repeating unit known as the sarcomere is defined by the vertical z-disk. Two types of protein filaments are distinguishable in each sarcomere, thin ones about 5μ in diameter and thicker ones about 12μ across. The thin filaments contain actin, globular molecules in a triple helix, while the thick filaments contain myosin, long molecules with globular heads. The thin filaments are each attached at one end to a z-disk and are free at the other to interlace with the thick filaments. The A-band is the region of overlap between thick and thin filaments, the I-band contains solely the thin filaments, while the H-band is the middle region of the A-band into which the actin filaments have not penetrated (Fung, 1981).

The actual contractile process takes place at the junctions between the myosin and actin in a process known as the sliding filament theory first presented by H.E. Huxley (1953). The myosin molecules consist of a long tail piece and a "head". The tails lie parallel in a bundle to form the core of the thick filament while the heads project laterally from the filament in pairs, rotated with respect to its neighbors to form a spiral pattern along the filament. These heads seem to be able to nod; they lie close to their parent filament in relaxation, but stick out to actin filaments when excited. Thus, during muscle contraction the muscle fiber shortens as the filaments slide over each other, forming, breaking and reforming chemical bonds between the myosin heads and the globular actin molecules.

IV. STRUCTURAL MODEL OF SKELETAL MUSCLE

If a muscle is not stimulated neurally, its tension, due to the contractile process, is extremely small. Practically all the tension observed when stretching the resting muscle will be due to elastic

structures which lie in parallel to the force-producing sarcomeres: the sarcolemna (sheath) of the individual fiber and all outer connective tissue sheaths (fascia, endomysia, perimysia). Thus, a set of parallel elastic elements (PEs) some of which are to be considered in parallel with each sarcomere of each fiber and others only in parallel with the whole muscle. Because these tissues move in fluid, appropriate damping elements (DE) also need to be included when stimulation takes place. The contractile proteins produce tension which, via elastic components such as tendons, is transferred to the end points of the muscle. These components are termed series elastic elements (SEs) Hatze, 1981).

Thus the following model based on Hatze (1981) can be constructed (Fig. 3). At both ends of each fiber are lightly damped SEs representing the tendinous parts of the fiber, and for each sarcomere two lightly damped SEs representing the elastic structures within the cross bridges (BE_i) and the z-disk (SE_i). The parallel elastic elements for each sarcomere (PS_i) do not individually contain the damping components, since the sarcolemna attached to the z-discs does not allow appreciable movement. The damping element is contained in the fiber external structure and is thus placed parallel to the entire fiber. The DE_i represent the purely contractile elements of the protein. Any mass of the sarcomeres is disregarded, especially when compared to the much larger external mass that the muscle contraction must move (Hatze, 1981).

Obviously such a distributed model for a complete muscle would be much too complicated to use in a multilink system of the human body such as the AIB model. Thus, a transition from the distributed system to a simpler lumped system must be made. One justifiable assumption is that all the sarcomeres in a fiber are more or less identical and activated at approximately the same time. It follows then that all the SE_is for one fiber can be replaced by an equivalent single element SE of length λs_i, the same procedure can be applied to the elements CE_i, BE_i and PS_i, resulting in equivalent lumped elements.

A similar process is applied in lumping fibers into motor units. The nervous system does not control single muscle fibers, but rather groups of fibers in the form of a functional unit, the motor unit. Each motor unit consists of the motor neuron producing the neural input signal to the unit, and all

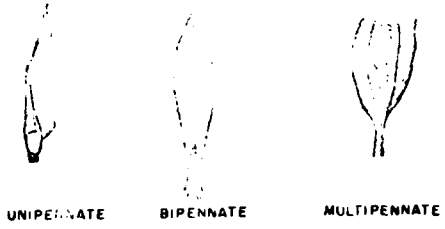

Fig. 1 Schematic representation of skeletal muscle fibre arrangement.

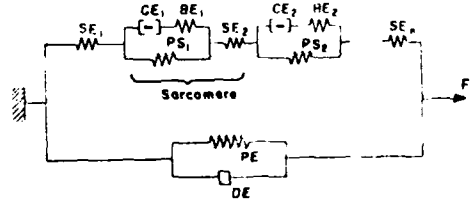

Fig. 3 Distributed model of skeletal muscle

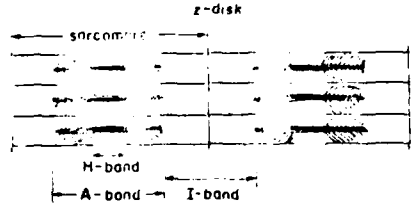

Fig. 2 Molecular substructure of mammalian skeletal muscle.

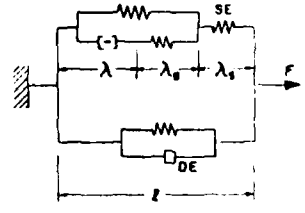

Fig. 4 Lumped model of skeletal muscle.

of the fibers that are innervated by branches of the motor neuron. In general, the motor unit fibers are distributed randomly over a certain volume of the muscle and all have similar morphological contractile and histochemical profiles (Close, 1972). Also, assuming BE to be very stiff, as suggested by Hatze (1981, p. 66), results in the final lumped model (Fig. 4).

For the parallel elastic element, extensive tests on the tensile properties of resting skeletal muscle carried out by Yamada (1970) indicate an exponential force-straint function:

$$f_{PE} = \alpha e^{\beta(\varepsilon-1)} - 1 \tag{1}$$

where f_{PE} is the force developed by the PE normalized with respect to maximum isometric tension in the muscle, α and β are constants and is the strain:

$$\varepsilon = \frac{l - l_o}{l_o} \tag{2}$$

where l is the instananeous muscle length and l_o is the resting length. Fitting Eq. 1 to the data of human sartorius muscle from Yamada (1970, p. 95) yields values of α = .0016296 and β = 7.6616. This typical force-strain curve is shown in Fig. 5. The SE and PS elements exhibit force-strain functions similar to the PE (Hatze, 1981) and will be discussed in more detail later.

The velocity dependence of the damping element (DE) can be expressed as for a simple mechanical dashpot:

$$f_{DE} = B\dot{\varepsilon} \tag{3}$$

where f_{DE} is the normalized force and B is the viscous damping coefficient. For the plantaris muscle of the cat, Rack et.al. (1976) have determined B = 6.4 g sec/mm which if normalized to the plantaris resting length (l_o = 50 mm) and maximum isometric tension (F_{MAX} = 1000 gr) yields B = .32 sec. (Fig. 6).

The contractile element is the only active component in the model. Its behavior is usually described by [illegible] contractile length, contractive history, velocity of movement, the degree of stimulation and its temperature. However, for practical purposes and as discussed later, only the [illegible] will be considered: the length-tension relationship and the force-velocity relationship.

The length-tension relationship is determined by the number of active cross links or filamentary overlap and can be adequately expressed from the data of Gordon et.al. (1966) by the function suggested by Hatze (1981, p. 42):

$$f_L(\xi) = .32 + .71e^{-1.112\ (\xi-1)}\ \sin\ (3.722\ (\xi-.656)) \qquad (4)$$

here $f_L(\xi)$ is the normalized force due to length-tension relationships and $\xi = \lambda/\bar{\lambda}$ with $.58 \leq \xi \leq 1.8$, where λ is the instantaneous length of CE and $\bar{\lambda}$ is the resting length of CE. This function is shown in Fig. 7.

The force-velocity relationship is determined by the rate of breaking and reforming the cross bridges with higher rates producing less effective bonds. To account for the whole range of negative velocities (shortening or concentric contractions) as well as positive velocities (lengthening or eccentric contractions) Hatze (1981, p. 44) has defined the following expression:

$$f_v(\dot{\eta}) = .1433\ \{.1074 + e^{-1.409\ \sinh\ (3.2\dot{\eta} + 1.6)}\}^{-1} \qquad (5)$$

where $f_v(\dot{\eta})$ is the normalized force due to the force-velocity relationship and

$$\dot{\eta} = \dot{\epsilon}/V_{MAX} \qquad (6)$$

where V_{MAX} is the maximum concentric velocity in muscle lengths/sec. and $\dot{\epsilon}$ is the velocity again in muscle lengths/sec. This relationship is shown in Fig. 8.

Scrutinizing Figs. 5-8, several important conclusions can be drawn. The passive force-strain property (Fig. 5) shows an exponential increase with very small values (compared to the maximum isometric tension or maximum voluntary contraction (MVC)) for strains less than 50% and very large values for strains greater than 50%. However, strain values of 50% would not be reached during normal movements and thus the passive force-strain effect should be negligible in the normal neuromuscular response.

The passive viscous damping forces (Fig. 6) show a linear increase with strain rate ($\dot{\epsilon}$). Force values equal to MVC are obtained for $\dot{\epsilon}$ = 3.125/sec. Since the maximum velocity for slow fibers is 2.9 muscle lengths/sec (Hatze, 1981) fairly substantial viscous damaging forces can be obtained.

The active length tension relationship (Fig. 7) shows a fairly peaked

Fig 5 PASSIVE MUSCLE FORCE - STRAIN FUNCTION

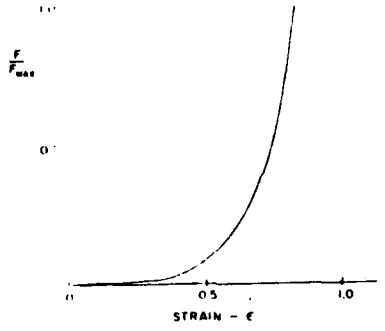

Fig 6 PASSIVE MUSCLE VISCOUS DAMPING FORCES

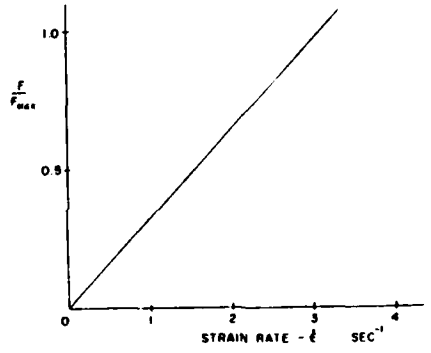

Fig 7 MUSCLE LENGTH TENSION RELATIONSHIP

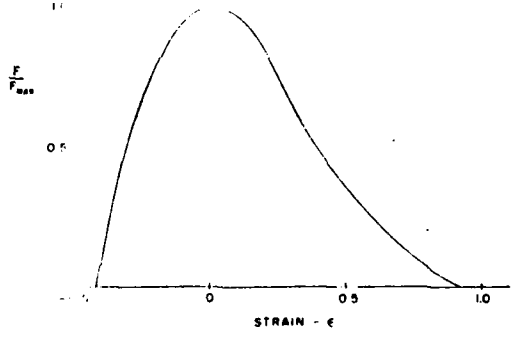

Fig 8 MUSCLE FORCE-VELOCITY RELATIONSHIP

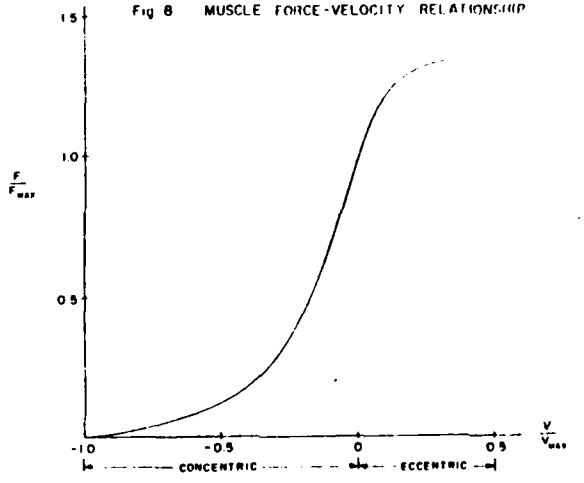

response with a 20% reduction in force for $\varepsilon = \pm$ 20%. Therefore, the length tension relationship shows a significant effect that should be accounted for.

The active force-velocity relationship (Fig. 8) shows a rapid increase up to an asymptotic value 34% greater than the MVC for eccentric contractions and a very rapid decrease in force (down to zero) for concentric contractions. Therefore, the force-velocity relationship should have a very significant effect in normal human movements.

Now, combining the model in Fig. 4 with the above-derived Equations 1-6 yield the following overall force equations

$$f_{SE} = f_{CE} + f_{PS} \tag{7}$$

$$f = f_{SE} + f_{PE} + f_{DE} \tag{8}$$

V. INCORPORATION OF THE MUSCLE MODEL INTO THE ATB MODEL:

With the consideration that existing features of the ATB model were to be used for the incorporation of muscle elements, two possibilities arose: (1) to use the spring-damper routine or (2) to use the advanced restraint system of harness and belts. The spring damper routine was quickly discounted because, as the name implies, only a direct spring force proportional to displacement were available. Other functions such as the length-tension or force-velocity relationships could not be accounted for. Furthermore, the spring-damper functions were limited to second power polynomials, which would be insufficient to fit the required forms of the muscle properties.

The harness routines provided a much better alternative. First of all, the functional form of the harness forces allowed the use of four terms:

$$NF(\varepsilon,\dot{\varepsilon}) = NF_1(\varepsilon) + NF_2(\varepsilon)NF_3(\dot{\varepsilon}) + NF_4(\dot{\varepsilon}) \tag{9}$$

where ε = strain, $\dot{\varepsilon}$ = strain rate and NF = functional form of force. Secondly, each of the terms could be expressed either as a fifth order polynomial or as a tabular function for more complex simulations.

On the other hand, there are still limitations within the harness routine that restrict the effectiveness of the muscle model. Obviously, from the functional form of Eq. 9 only three elements can be modeled

adequately. Furthermore, all three of these have to be in parallel, since forces add directly only in parallel. Series elements would require complex integro-differential equations in NF which can not be replicated with Eq. 9. Thus, the series elastic element (SE) needed to be eliminated.

The elimination of SE can be rationalized by considering SE to be a very stiff spring which is supported by Bawa et.al. (1976) who found K_{SE} = 380 g/mm as opposed to K_{PE} = 103 g/mm. Eliminating SE yields four elements in parallel, two of which are parallel elastic elements. This can be combined into one parallel elastic element, yielding the final simplified model in Fig. 9. The functional forms for each of these elements have been given previously in Eq. 1,3,4, and 5.

Simulation of Elbow Flexion - The simulation of elbow flexion (Fig. 10) consisted of three segments: the upper arm, the lower arm including the hand and a mass held at the center of gravity of the hand; and three joints: the shoulder which is fixed to an inertial reference frame, the elbow modeled as a hinge joint and an unconstrained joint acting as the attachment between the hand and the mass. One muscle was attached to act as the combination of elbow flexors, the biceps brachii and the brachialis. Anthropometric values for the segments and centers of gravity were taken from the data of Dempster (1955). The origin of the elbow flexor was put at the shoulder joint since the long head of the biceps even crosses the shoulder joint (McMinn and Hutchings, 1977). The insertion was set at 1.8 inches from the elbow corresponding to the biceps data of Wilkie (1950).

The maximum isometric tension of the elbow flexor was calculated from the data of Wilkie (1950). His subjects maintained a 10kg weight at the wrist with a lever ratio between muscle insertion distance and the moment arm of the weight of .15, yielding a maximum isometric tension of 133.3kg or 293 lbs. This result is confirmed using cross-sectional areas of 4.6 cm^2 and 7.0 cm^2, respectively, for the biceps and brachialis (An et.al., 1981) multiplied by the maximum muscle force of 10 kg/cm^2 (Hatze, 1981) to yield 255 lbs. This value is remarkably close to the more direct value, considering [illegible] for. As a result, a value of 300 lbs. was selected as the maximum isometric tension for the elbow flexors.

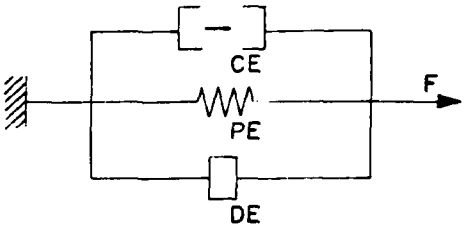

Fig. 9 Simplified muscle model.

Fig. 10 ANATOMY OF THE ELBOW FLEXORS

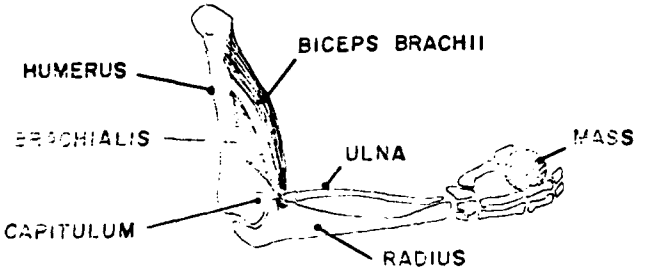

Special modifications needed to fit the four muscle functions to the ATB model included the following. At present, the ATB model doesn't allow negative strain which does occur during a concentric contraction, it was necessary to pretighten both the length-tension function and the muscle-spring function so that under extreme concentric contractions, the calculated strain would still be positive. Strain under pretensioning is calculated as follows:

$$\varepsilon' = \frac{1}{l_o + s} - 1 \tag{10}$$

where s = slack (negative if pretensioned). During a resting state when normal strain $\varepsilon = 0$ a pretensioning of $s = l_o/2$ yields $\varepsilon' = 1$. Then ε and ε' are related by:

$$\varepsilon' = 2\varepsilon + 1 \tag{11}$$

Thus for normal strain (ε) ranging from -.4 to .8, pretensioned strain (ε') would range from .2 to 2.6.

The velocity dependent functions are calculated based on strain rates. Thus a strain rate of 1 sec. would be equivalent to a muscle velocity of one muscle lenth per second. For slow twitch fibers, as typically found in the trunk musculature, the maximum velocity is approximately 2.9 muscle lengths/sec (Hatze, 1981). Thus Eq. 6 can be used to define $\dot{\eta}$ needed for the force-velocity function in Eq. 5.

The elbow flexor simulations utilized a fixed upper arm, a freely pivoting elbow joint (i.e. ,in joint) a fixed wrist joint and a mass held in the hand. The upper arm is fixed vertically while the lower arm starts out horizontally (i.e. elbow angle = 90°). The mass in the hand is varied and the lower arm is allowed to move under the combined effects of gravity and the elbow flexor forces. For a large mass, the torque created by the mass exceeds the maximum voluntary torque produced by the elbow flexors and the lower arm pivots down, lowering the mass. For a small mass, the torque produced by the mass is less than the maximally produced torque and the arm pivots up lifting the mass.

Muscle forces as a function of time for various masses and conditions are shown in Figs. 11-15. Figs. 11-14 show the effects of isolated muscle

Fig. 11 FORCE vs TIME FOR ISOLATED MUSCLE SPRING FUNCTION

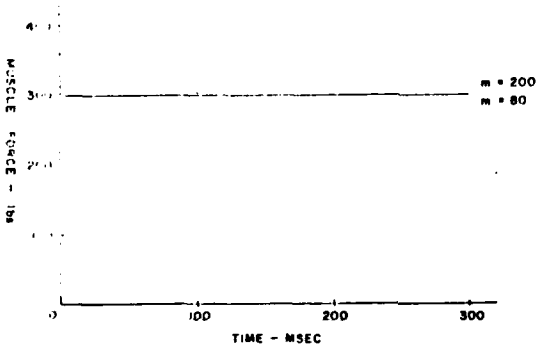

Fig. 12 FORCE vs TIME FOR ISOLATED MUSCLE DAMPER

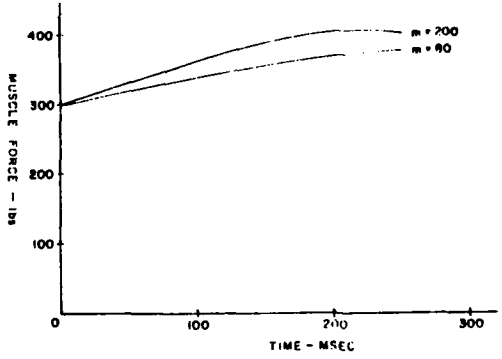

Fig. 13 FORCE vs TIME FOR ISOLATED MUSCLE LENGTH FUNCTION

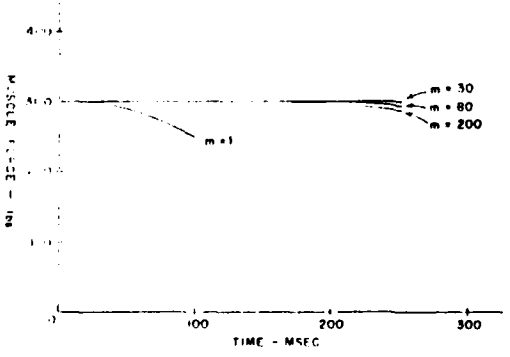

Fig. 14 FORCE vs TIME FOR ISOLATED MUSCLE VELOCITY FUNCTION

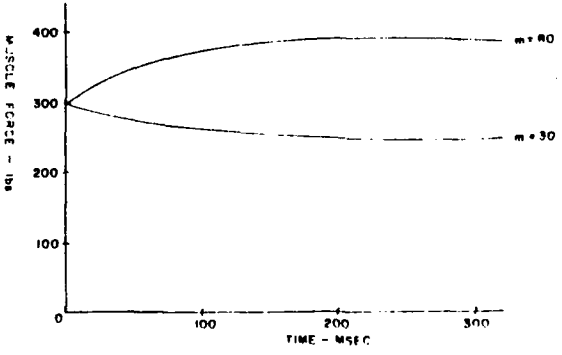

function (the other functions are replaced by dummy variables) while Fig. 15 shows the effects using the complete elbow flexor. More complete results including the angular displacement and strain at 256 msec, and the maximum linear muscle velocity and resulting $\dot{n}$ for the various conditions are summarized in Table 1.

The conclusions drawn in Section IV from theoretical muscle function relationships are definitely supported by these simulations. For example, Fig. 11 shows a constant muscle force over time for the isolated muscle-spring function for two different masses (m = 80 and m = 200). In both cases the lower arm pivots down (39° and 43° respectively) but the resulting muscle strain is too small to produce any significant increase in muscle force. In fact for a completely extended forearm, the resulting strain of 13.9% is insufficient to produce a significant muscle-spring force. On the other hand, the forces produced by the passive damper amount to a significant 30% increase above the maximum isometric tension (Fig. 12), which results in a substantial slowed descent and reduced angular displacement (Table 1).

The reduction in muscle force due to the length tension relationship amounts to approximately 16% of the maximum isometric tension at full flexion as shown for condition m=1 at time = 100 msec in Fig. 13. Full extension would result in a 10% decrease in force. Since these are the maximum decrements possible, the length-tension relationship seems less important than the passive damper effect. This, however, is slightly misleading in that the present case is not a completely realistic simulation of elbow flexion. Nearing full extension of the elbow, the biceps tendon tends to be distended by the capitulum of the humerus (Fig. 10) accentuating the length-tension relationship.

The active force-velocity relationship produces a 50% increase in force for a eccentric contraction (m=80) and a 16% reduction for a concentric contraction with mass = 30 lbs. However, a smaller mass would have resulted in a much faster contraction and consequently greater force reduction as shown more clearly in Fig. 15 for the force histories for the complete elbow flexor. A concentric contraction with mass = 1 lb. at maximum velocity results in a 24% reduction in muscle force. This predominant dependence of the muscle force on the velocity of contraction is shown even more distinctly in Fig. 16 in which the time plots of force strain and strain rate are

TABLE 1 - SUMMARY OF ELBOW FLEXION SIMULATIONS

	Mass (lbs)	Parameter	Spring	Damper	Length	Velocity	Complete Muscle
CONCENTRIC	1	Angular Disp. (^{o})			-90.0		-79.0
		Strain			-.162		-.159
		Muscle Velocity $\frac{in}{sec}$			-27.8		-8.65
		Strain Rate			-.805		-.250
	30	Angular Disp. (^{o})			-12.0	-6.0	-5.9
		Strain			-.031	-.016	-.015
		Muscle Velocity $\frac{in}{sec}$			-3.04	-1.05	-1.04
		Strain Rate			-.088	-.03	-.03
ECCENTRIC	40	Angular Disp. (^{o})					1.8
		Strain					.005
		Muscle Velocity $\frac{in}{sec}$					.330
		Strain Rate					.010
	80	Angular Disp. (^{o})	39.0	26.0	28.4	24.0	20.9
		Strain	.090	.063	.069	.059	.052
		Muscle Velocity $\frac{in}{sec}$	6.08	5.39	6.08	4.99	4.36
		Strain Rate	.176	.156	.176	.144	.126
	100	Angular Disp. (^{o})	43.0	41.0	43.0		39.0
		Strain	.097	.0935	.097		.090
		Muscle Velocity $\frac{in}{sec}$	7.65	7.39	7.65		7.12
		Strain Rate	.221	.213	.221		.206

Fig 15 FORCE vs TIME FOR COMPLETE ELBOW FLEXOR

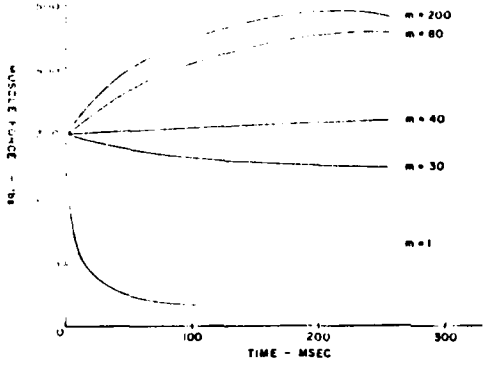

Fig 16 FORCE, STRAIN AND STRAIN RATE vs TIME FOR COMPLETE ELBOW FLEXOR

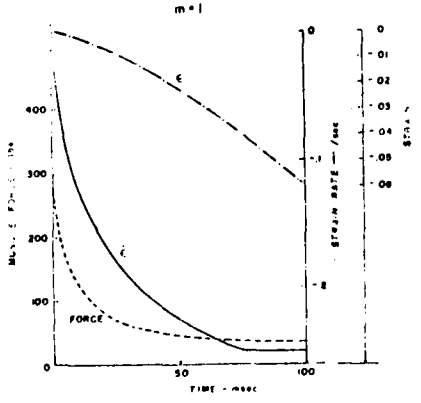

Fig 17 ANATOMY OF THE TRUNK AND NECK MUSCULATURE (POSTERIOR VIEW)

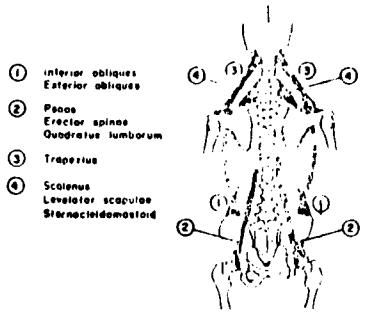

Fig 19 ANGULAR DISPLACEMENT (ROLL) OF UPPER TRUNK DUE TO LATERAL G-FORCES

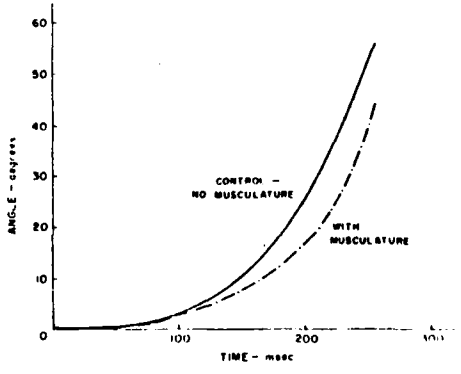

superimposed. Force and strain rate follow almost identical curves as compared to the strain function. Thus, for the present simulations, muscle force is determined primarily by the strain rate functions.

Simulation of Trunk Musculature - Simulation of the trunk musculature is a much more difficult undertaking than simulation of the elbow flexors. First of all, there are many more muscles involved, close to 20 for the lower back and trunk and equally many for the neck region. Secondly, some of the muscles, such as the erector spinae, have many attachment sites betwen the different vertebrae. Thirdly, the lines of action of the muscle forces are not always in straight line, e.g., the interior and exterior obliques. Fourthly, the vertebral joints are complicated by the ligaments and their additional force-bearing capabilities. Another restricting factor was the limit of five muscle harness systems for the recently added feature on the ATB model (Butler and Fleck, 1980). Therefore, for the present effort most of the above complications were avoided and a very simple model of the trunk musculature was constructed.

The model as shown in Fig. 17 consisted of four muscle-harness systems representing the major lateral bending muscles. One harness system was used to restrain the seated operator and since only lateral forces were of concern, all four muscle-harness systems were placed on the same side as the force being applied. The four major muscle groups used - two for the trunk, two for the neck - were as follows:

1) Interior and exterior obliques - which tend to curve around the trunk at the abdomen but act over a fairly short distance vertically.
2) Psoas, erector spinae, quadratus lumborum - which tend to be longer, originating in the pelvic area and inserting in the thoracic area.
3) Trapezius - originating laterally on the shoulders and inserting on the skull.
4) Scalenus, levator scapulae, sternocleidomastoid - which originate closer to the midline than trapezius and insert at various levels of the vertebral [illegible].

A procedure similar to the elbow flexor simulation was followed using cross-sectional areas from Takashima et.al. (1979) to determine maximum isometric tension for the neck muscle groups, maximum lateral bending forces

(225 lbs) from McNeil et.al. (1980) proportioned between the two trunk muscle groups according to Rab (1979) (which is more accurate than using the first technique) and finding insertions and origins in Takashima et.al. (1979), Williams and Belytschko (1981) and Rab et.al. (1977). This information is summarized in Table 2.

The study of trunk musculature simulated the conditions experience by a 95% male air crew personnel in a series of tests run in the Dynamic Environment Simulator at Wright-Patterson AFB, OH. The full ATB Model with 15 body segments and 14 joints was used along with the addition of the four muscle groups described previously. The body segments were arranged in the semi-reclining posture maintained by air crew personnel in the cockpit (Fig. 18). The lower trunk was restrained by a lap belt; any other restraints, such as shoulder pads or hands placed on controls, were eliminated. A 2 Gy lateral force was applied to the body and the acceleration; velocity and displacement of various body segments was recorded.

A graphical display of the whole body response to the lateral force over time is shown in Fig. 18b. For comparison purposes, the response to identical conditions except for the lack of musculature is given in Fig. 18a. Although the musculature does not completely prevent the lateral deflection of the body the response is significantly delayed with the head and neck maintaining the upright position for a longer period of time. This result is better observed in Fig. 19 which plots the angular displacement of the upper trunk for both conditions. At the end of 256 msec the angular displacement is reduced by 12° with the use of musculature. Based on the time history, the response with the musculature lags up to 30 msec behind the control response.

VI. RECOMMENDATIONS:

These two series of simulations validate the use of a simple muscle function to model an active neuromuscular response to dynamic mechanical stresses. However, for a more accurate simulation three modifications are recommended:

1) To satisfactorily [illegible] than 5 harness (muscle) systems need to be permitted by the current version of the ATB. A minimum number required for the torso and neck would be 20, with an additional 20 needed for the limbs.

AD-A130 767 USAF/SCEEE GRADUATE STUDENT SUMMER SUPPORT PROGRAM (1982) MANAGEMENT AND..(U) SOUTHEASTERN CENTER FOR ELECTRICAL ENGINEERING EDUCATION INC S..

3/3

UNCLASSIFIED W D PEELE ET AL. OCT 82 AFOSR-TR-83-0611 F/G 5/9 NL

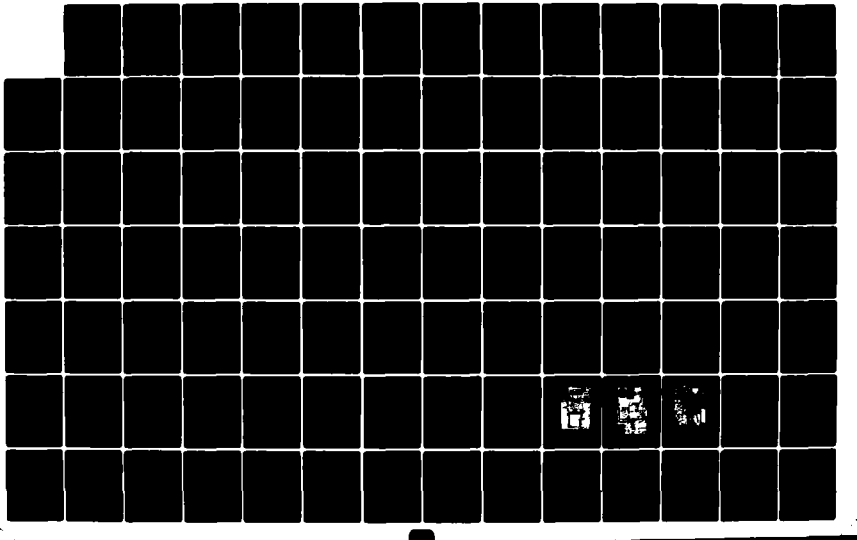

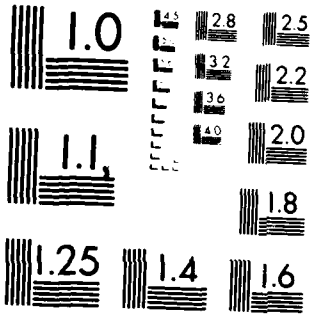

Fig. 1 - Graphical Display of Whole Body Response to Lateral G-Forces
a) Control b) Neuromusculature

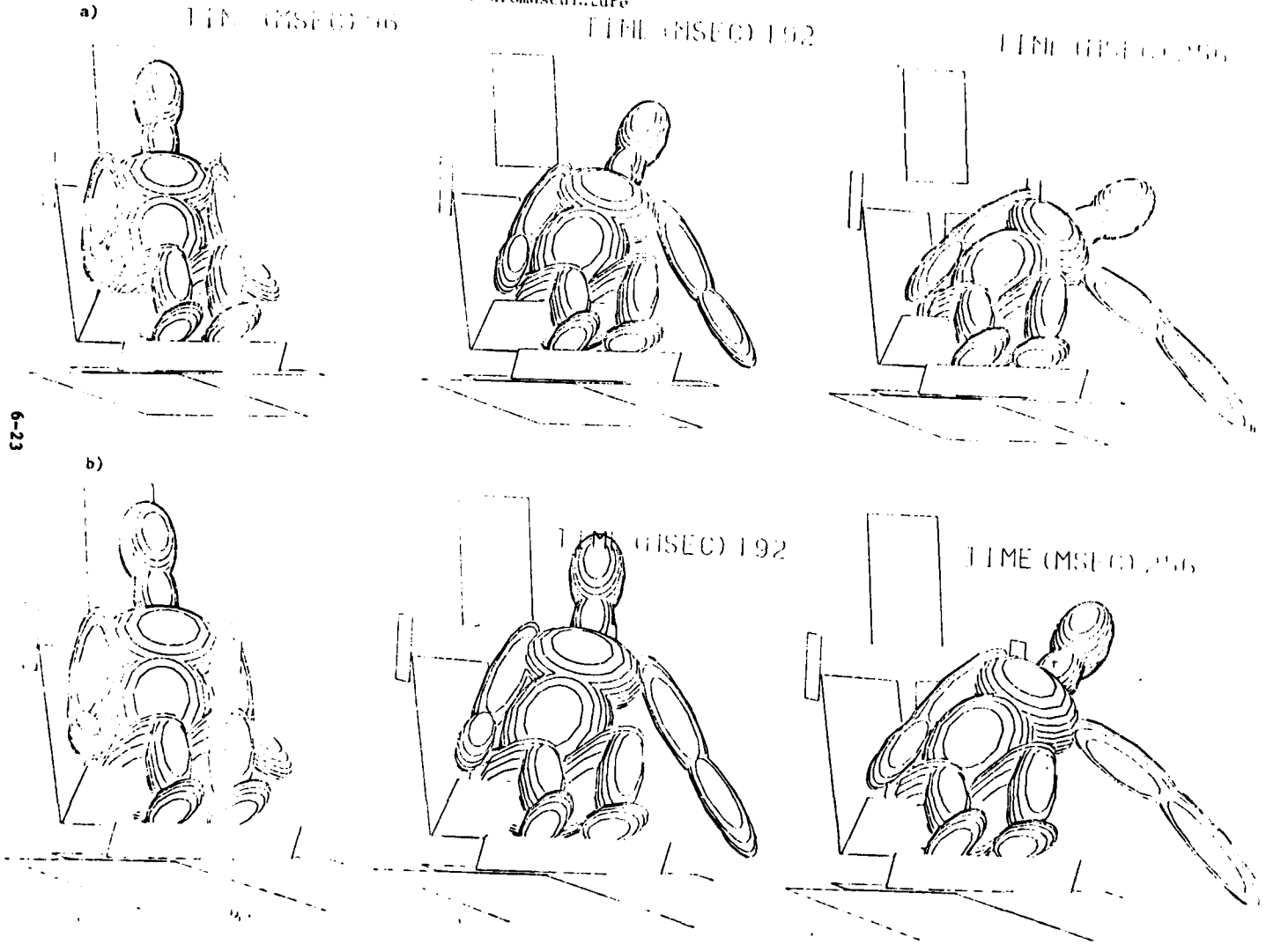

2) To more accurately describe the muscle performance, features such as the active state function, force build-up time, delineation of slow and fast twitch fibers, orderly recruitment patterns, fatigue effects and reflexes could be eventually included into the muscle model.

3) To account for the irregularities of the human body, a more detailed modeling of joint biomechanics, range of motion of limbs, multiple muscle insertions and the effects of ligaments should be included into the ATB Model.

A very important application for a completely muscularized ATB Model, besides the Air Force pilot simulations, is the simulation of manual material handling tasks in industrial jobs. The prediction of work strengths during dynamic job activities is a very desirable employee placement technique and has been strongly recommended by the National Institute of Occupational Safety and Health (Chaffin, et.al., 1977). Present results indicate the muscularized ATB Model to be a very feasible approach with good future potential.

REFERENCES

An, K. N., F. C. Hui, B. F. Morrey, R. L. Linscheid, and E. Y. Chao, "Muscles Across the Elbow Joint: A Biomechanical Analysis," J. Biom., 14:659-669, 1981.

Bawa, P., A. Mannard, and R. B. Stein, "Predictions and Experimental Tests of a Viscoelastic Muscle Model Using Elastic and Inertial Loads," Biol. Cybernetics, 22:139-145, 1976.

Butler, F. E. and J. T. Fleck, Advanced Restraint System Modeling, AFAMRL-TR-80-14, Wright-Patterson AFB, OH, 1980.

Chaffin, D. B., G. D. Herrin, W. M. Keyserling and J. A. Foulke, Preemployment Strength Testing, U.S. Dept. of HEW, NIOSH, Pub. #77-163, 1977.

Close, R. I. Dynamic Properties of Mammalian Skeletal Muscles. Physiol. Rev., 52:129-196, 1972.

Dempster, W. T. Space Requirements of the Seated Operator, WADC Technical Report 55-159, Wright-Patterson AFB, OH, 1955.

Fleck, J. T., F. E. Butler, and S. L. Vogel, "An Improved Three Dimensional Computer Simulation of Motor Vehicle Crash Victims," Final Technical Report No. ZQ-5180-L-1, Calspan Corp., 1974, 4 Vols.

Fleck, J. T. "Calspan Three-Dimensional Crash Victim Simulation Program", Aircraft Crashworthiness, University Press of Virginia, 1975.

Fleck, J. T. and F. E. Butler, Development of an Improved Computer Model of the Human Body and Extremity Dynamics, AFAMRL-TR-75-14, Wright-Patterson AFB, OH, 1975.

Fleck, J. T. and F. E. Butler, "Validation of the Crash Victim Simulator, Vol. 3, User's Manual, Final Report, ZS-5881,V-3, Calspan Corp., 1982.

Fung, Y. C., Biomechanics, Mechanical Properties of Living Tissues, Springer-Verlag, NY, 1981.

Gordon, A. M., A. F. Huxley and F. J. Julian, "The Variation in Isometric Tension with Sarcomere Length in Vertebrate Muscle Fibers," J. Physiol., 225:237-253, 1972.

Hatze, H. Myocybernetic Control Models of Skeletal Muscle, University of South Africa, Pretoria, 1981.

[illegible] of the Organization of the Filaments in Striated Muscle," Biophys. Biochim. Acta, 41:367, 1980.

McMinn, R. M. H. and Hutchings, R. T., Color Atlas of Human Anatomy, Yearbook Medical Publisher, Chicago, 1977.

McNeill, T. D. Warwick, G. Anderson and A. Schultz, "Trunk Strengths in Attempted Flexion, Extension and Lateral Bending in Healthy Subjects and Patients with Low-Back Disorders, Spine, 5:529-538, 1980.

Nachemson, G. T., "Muscle Forces in the Posterior Thoracic Spine," Clin. Orthoped., 139:28-32, 1979.

Nachemson, G. T., E. Y. S. Chao and R. N. Stauffer, "Muscle Force Analysis of the Lumbar Spine," Orthoped. Clinics of North Amer., 8:193-199, 1977.

Takeshima, S. T., S. P. Singh, K. A. Harderspeck and A. B. Schultz, "A Model for Semi-Quantitative Studies of Muscle Actions," J. Biom., 12:929-939, 1979.

Wilkie, D. R., "The Relation Between Force and Velocity in Human Muscle," J. Physiol., 110:249-280, 1950.

Williams, J. and T. Belytschko, A Dynamic Model of the Cervical Spine and Head, AFAMRL-TR-81-5, Wright-Patterson AFB, OH, 1981.

Yamada, H., Strength of Biological Materials, Baltimore: Williams & Wilkins, 1970.

1982 USAF-SCEEE GRADUATE STUDENT SUMMER SUPPORT PROGRAM

Sponsored by the

AIR FORCE OFFICE OF SCIENTIFIC RESEARCH

Conducted by the

SOUTHEASTERN CENTER FOR ELECTRICAL ENGINEERING EDUCATION

FINAL REPORT

STATIC AND DYNAMIC RESPONSE OF AIRCRAFT SHELTERS

Prepared by:	David L. Israel
Academic Department:	Civil Engineering
University:	University of Florida
Research Location:	U.S. Air Force Engineering and Services Center, Engineering and Services Laboratory, Airbase Survivability Branch, Tyndall AFB, FL
USAF Research Contact:	Lt. Cmdr. James W. Carl
SFRP Supervising Faculty Member:	Dr. Fernando E. Fagundo, Jr.
Date:	July 23, 1982
Contract No.:	F49620-82-C-0035

ACKNOWLEDGEMENTS

The author would like to thank the Air Force Systems Command, the Air Force Office of Scientific Research, the Southeastern Center for Electrical Engineering Education, and the Air Force Engineering and Services Center for providing the opportunity to participate in the 1982 USAF-SCEEE Graduate Student Summer Support Program. He would like to acknowledge LCDR James W. Carl and Captain Paul Rosengren of the Airbase Survivability Branch for their hospitality and support throughout the project. Thanks are also due to the staff of the computer facilities for their help and cooperation.

The author would like to extend special thanks to Dr Fernando Fagundo for suggesting this area of research and for his collaboration and guidance through the entirity of the project.

Static and Dynamic Response of Aircraft Shelters

by

David L. Israel

ABSTRACT

The feasibility of a fourth generation aircraft shelter is investigated. The development of mathematical models, simulating a double-radius cylindrical shelter are presented. The models are analyzed both statically and dynamically with the use of SAP IV (Structural Analysis Program).

Investigations of various loading conditions were performed to determine the effect of assumed threats on the structure. Structural response under each of the loading cases is studied in an attempt to determine which parts of the shelter will be subjected to the most severe stresses. Suggestions are offered as to which type of model and loading configuration would be the most representative and realsitic for any future development in this area.

1982 USAF-SCEEE SUMMER FACULTY RESEARCH PROGRAM

and

1982 USAF-SCEEE GRADUATE STUDENT SUMMER SUPPORT PROGRAM

Sponsored by the

AIR FORCE OFFICE OF SCIENTIFIC RESEARCH

Conducted by the

SOUTHEASTERN CENTER FOR ELECTRICAL ENGINEERING EDUCATION

FINAL REPORT

TRIALS AND TRIBULATIONS AT THE HELMET MOUNTED OCULOMOTOR FACILITY

Prepared by:	A. Terry Bahill & Jeffrey S. Kallman
Academic Rank:	Associate Professor & Graduate Student
Academic Department:	Electrical Engineering
University:	Carnegie-Mellon University Pittsburgh, PA 15213
Research Location:	Air Force Aerospace Medical Research Laboratory, Human Engineering Division Wright-Patterson AFB, Ohio
USAF Research Contact:	Dr. Ken Boff

Date:	August 27, 1982
Contract No:	F49620-82-C-0035

Acknowledgement

We thank the Air Force Office of Scientific Research and the Southeastern Center for Electrical Engineering for providing us with the opportunity to spend the summer at Wright-Patterson AFB and Yellow Springs, Ohio. We thank the many people from SRL who helped us and Dena Brooks for processing our letters and reports. Tom Furness's support and Ken Boff's enthusiam were appreciated. We are also grateful to Mike Haas for his efforts at making the oculometer work so that we could collect our data.

TRIALS AND TRIBULATIONS AT THE HELMET MOUNTED OCULOMOTOR FACILITY

by

A. Terry Bahill & Jeffrey S. Kallman

ABSTRACT

We spent most of the summer debugging the Helmet Mounted Oculometer Facility (HMOF) equipment. On our last day we were finally able to gather data on human head and eye coordination. We brought this data back to Carnegie-Mellon University; we were able to put it on our computer system and analyze it with our programs.

I. INTRODUCTION

At the beginning of the summer I stated that my objectives were

1 To present seminars to the Wright-Patterson AFB community. I presented the five seminars listed in Appendix A. The average attendance was 20.

2 To learn to use the Helmet Mounted Oculometer Facility (HMOF). The proceedures of operation that I wrote are included in Appendix B.

3 To record human head and eye movement data under a variety of target movement conditions. We have filled up a computer disk with data. It is presently in my Laboratory at Carnegie-Mellon University. I will analyze this data during the period of my minigrant.

The following narative written by Jeffrey S. Kallman summarizes our activity directly related to the Helment Mounted Oculometer Facility (HMOF).

The virtual cockpit is an idea that has existed for many years. In essence, the idea is to present a processed view of the world to a pilot. This view presents information to the pilot in the most usable form possible. Threats are emphasised, HUD information is available, displays can be task dependent, etc.. Unfortunatly, until recently, the technology and basic science needed to develop such a virtual cockpit was nonexistant. Not any longer. Currently, investigations are being made into artificial intelligence systems for threat evaluation, experiments are being performed in optimal display symbologys, and many other pieces of the virtual cockpit idea are being worked on.

One major piece of the virtual cockpit is the display system. Image

a helmet mounted oculometer (HMO), a helmet mounted sight (HMS), a Data General Eclipse minicomputer, a Network Systems HYPERchannel adapter, and a DEC PDP-11/34. This is a large, expensive and complex system.

The HMS provides a TV image of the subject's right eye illuminated by infrared light. The oculometer consists of an infrared light source, a CCD television camera, and associated optics. The light source is directed at the eye via beamsplitters and an infrared mirror. The TV camera sees the infrared light reflected from the eye. Ideally there are only two sources of infrared reflection from the eye: the corneal reflex and the bright pupil. The corneal reflex is the reflection of a bright light source off of the front surface of the cornea. The bright pupil is the effect caused by light entering the eye, bouncing off the retina and reemerging from the eye, lighting up the pupil. The corneal reflex and the bright pupil are picked up by the TV camera and then passed to the Eclipse computer.

The HMS provides head position and orientation data to the Eclipse. It works by using a transmitter to set up a magnetic field in the area the helmet will occupy. A receiver in the helmet senses the magnetic field and determines where the head is and how it is oriented.

The Eclipse computer collects the TV images from the HMO and the head position and orientation data from the HMS, computes direction of gaze, and sends it all to the HYPERchannel. The TV images are first processed to generate eye position (angular) in the helmet reference frame. Then eye position is 'added' to the head position and orientation to yield gaze angle (in universal coordinates). Finally, the Eclipse sends all of the data and the results of its computations to the HYPERchannel.

The HYPERchannel allows the transfer of data from the Eclipse

minicomputer to the PDP-11/34 minicomputer. It is questionable whether this piece of equipment has helped or hindered the development of the HMOS facility.

The PDP-11/34 minicomputer is used for a variety of purposes in the HMOF. The PDP-11/34 generates targets, drives the target display system, takes data from the HYPERchannel adapter, and formats and stores the data on disk.

Software

This section of the report will cover the software that we either developed or helped to develop. All of our programs were written on the PDP-11/34. The Eclipse minicomputer was programmed by Honeywell and the HYPERchannel was programmed by its manufacturer. In the course of the work at the HMOF several programs were written for the 11/34. These programs were written for a variety of purposes: target generation, target presentation, data collection, error calculation, and demonstration. The programs were written in FORTRAN and assembly language. Some of the programs were designed to stand alone, while others were designed to fit into existing software. I'll discuss the programs that stand alone first.

DEMO

The demonstration program DEMO stands alone. It outputs a series of two dimensional target waveforms to a target generator (in our case, either an x-y scope or mirrors deflecting a laser beam). The targets presented are: a horizontal sinusoid, horizontal parabolic sections, horizontal cubic sections, circles, horizontal parabolic sections vs vertical sinusoids, and horizontal cubic sections vs vertical sinusoids. DEMO is a static program. Each time it is run, the same targets are presented at the same speed, and in the same order. The ordering, speed, and targets presented are the responsibility of

generation and display are among the most computer intensive tasks of the virtual cockpit. To use the virtual cockpit efficiently and, with present computer speeds, effectively, requires a minimization of image generation and display. The computers should only work on the virtual areas that the pilot is looking at.

Determining where a pilot is looking is an involved process. The direction of the eye in the head must be determined and the position and orientation of the head in space must also be determined. Given these, it is possible to determine where a person is looking, but in the case of a pilot, there are additional factors that must be taken into account. Neither the oculometer (device for determining eye direction in the head) or the sight (device for determining head position and orientation) can be either intrusive or obtrusive. This presents difficulties.

Oculometer and sight systems exist that are neither unacceptably intrusive or obtrusive. One such system is the Honeywell Helmet Mounted Oculometer and Sight (HMOS). The HMOS was delivered to the AFAMRL/HEA Helmet Mounted Oculometer Facility (HMOF) in November 1981. Unfortunatly, the HMOS was still not fully integrated into the HMOF in June 1982. In addition, the HMOS's performance characteristics were an unknown factor.

II. HMOF

This discussion of the Helmet Mounted Oculometer Facility comes in three parts: the hardware, the software, and the operation of the system.

Hardware

HMOF hardware can measure, record, and (if desired) can act upon the position and orientation of the human head and eyes. It has five main parts:

the FORTRAN part of the program. Acting on the ordering, speed, and target is the responsibility of the assembly language part of the program. The assembly langage subroutine accepts the number of ten thousands of a second between target updates as an argument. The subroutine takes the target from a buffer in a FORTRAN common block filled by the FORTRAN part of DEMO. As the FORTRAN program has no interaction with the outside world, the program is static.

TARGET

TARGET is a more dynamic stand alone program for horizontal target generation and display. It allows the user to pick up to thirty targets for display from a menu of five waveforms. In addition to waveform, the user also picks target frequency and duration. After the user's targets are displayed, the program allow the user to specify a new set of target waveforms.

The five waveforms are generated and stored in buffers when the FORTRAN part of TARGET is first started up. The program then asks the user to generate a target by picking waveforms, frequencies, and durations. After the target generation is finished, the target is displayed. The assembly language display subroutines are different from the single display routine in DEMO. Whereas in DEMO the display routine's buffers had to be refilled with each change in waveform, TARGET assigns one subroutine to each buffer, and has the buffers prefilled. Thus, while DEMO has delays between output of waveforms, TARGET displays waveforms continuously.

TARTTB

TARTTB is a flexible stand alone program for horizontal and vertical target generation and display. It is similar to TARGET in that it allows the user to specify the target, and it is similar to DEMO in that between displays of the target waveform it has to refill the display buffers. TARTTB is the

last of the stand alone programs.

SSCAN

SSCAN was designed to fit into the existing data collection program COLECT (sic). COLECT is the program that run on the PDP-11/34 which is responsible for collecting data from the HYPERchannel adapter, formatting it, and storing it on disk. SSCAN allows the user of COLECT to read the analog to digital (A/D) converters in the PDP-11/34. The user can select the number of A/D converter channels that are to be read.

MSE

MSE is a group of subroutines that fits into COLECT which computes and displays a short term mean square error of the form

$$mse = \frac{1}{T} \int_{t-T}^{t} (e_{EL}^2 + e_{AZ}^2) dt \qquad (1)$$

where t is time, T is a period of time, e_{EL} is elevation error, e_{AZ} is azimuth error, and mse is mean square error. There are three parts to MSE: MSESET which sets things up, MTSER which computes mse, and MSEOUT which outputs the mse.

HMOF Operation

By far the most difficult part of using the HMOF is operating the HMOS. The HMOS operation proceedures are also the most difficult to describe. As a good description of the operating proceedures for the HMOS part of HMOF has been written by Dr. A. J. Bahill; they are included in Appendix B.

III. HMOS Evaluation

One of the most HMOS dependent developments in the virtual cockpit concept is the generic switch. Basically, the generic switch is a single switch on the stick that can represent any of a number of switches in the cockpit. In use, the generic switch represents which ever switch the pilot is currently looking at. The usefulness of the generic switch is dependent upon three HMOS parameters: resolution, drift, and noise. The resolution is the minimum angular separation that the HMOS can distinguish. In terms of the generic switch, this tells how far apart the switches the generic switch can represent must be. Drift is a measure of how incorrect HMOS determination of gaze can become over time. If the HMOS has a large drift, looking at a the same cockpit switch may not mean the same thing after an hour (i.e. the pilot looks at the radar switch, and the generic switch fires a rocket). Noise acts to degrade HMOS resolution. If the resolution of the HMOS allows switches to be separated by as little as three degrees of solid angle, but there is a jitter of five degrees, the generic switch will represent unexpected things at inconvenient times.

It turned out that we were unable to determine any of the aformentioned parameters. Because the HMOF was unable to collect and store data for ninty-nine percent of our time at WPAFB/AFAMRL-HEA, we collected approximately ten seconds of usable data. This allowed us to determine only one HMOS operating parameter; the noise in the HMOF system. This noise is large. Calculations based on the raw gaze angle data (see figure 1) yield mean square errors of 32.08 deg^2. When the data is filtered [illegible] mean square error is 27.01 deg^2. Of our own experience in the Neurological Control Systems Laboratory (NCSL) at Carnegie-Mellon University in Pittsburgh, we know that people are capable of tracking with mean squared errors of less than 0.2 deg^2.

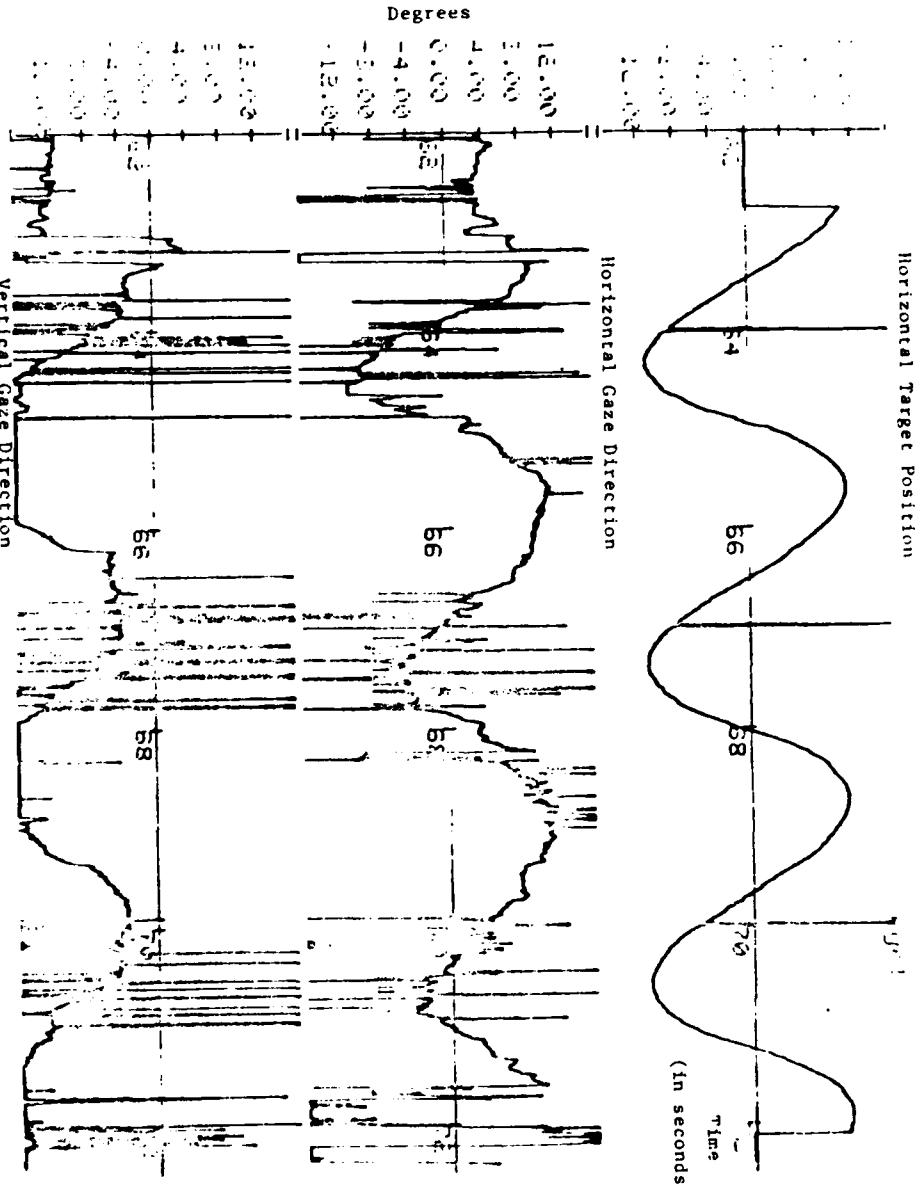

Figure 1. Target and Gaze directions as a subject tracked a target moving in a circle. Raw data.

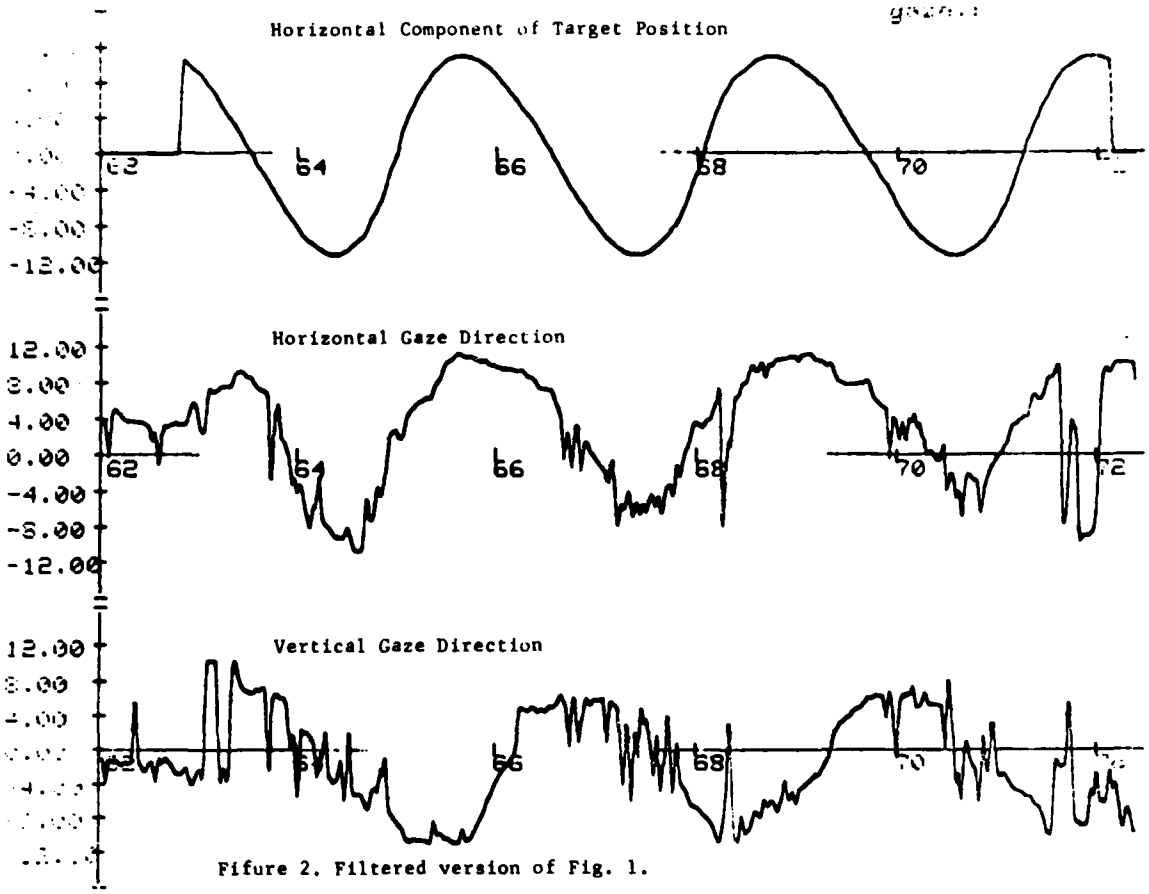

Fifure 2. Filtered version of Fig. 1.

IV. Experiments Performed With HMOF.

As mentioned in the previous section, during 99% of the time we had at the HMOF we were unable to collect and store data. This severely cramped our style. We have ten seconds of usable data. This data needed to be processed a great deal to become usable (as figures 1 and 2, data before and after filtering, attest).

The filtering was done in two stages. The first stage of the filtering was performed when the data was transformed from the HMOF format to NCSL format. During the conversion, any data that passed a size threshold was dealt with by inserting in its place the value of the previous data point. The filtering was completed by running a simple digital lowpass filter over the NCSL format data.

Analysis of the data was performed using the Carnegie-Mellon University NCSL analysis programs ANA and SPA. ANA provided the graphic output of figures 1 and 2, and SPA provided the mean squared error numbers.

V. Summary and Conclusions

There is not a whole lot that we can say about the capabilities of the HMOF or the results of our head and eye coordination experiments. The HMOF's inoperability made it impossible to get data with which to work. In the the last four hours at HMOF we were able to get ten seconds of usable data. Even so, this snippet of data shows some of the possibilities inherent in a Helmet [illegible] Facility. As far as we know, there is no other facility where gaze can be monitored with as free a head with the types of targets we've used.

Appendix A

Seminars of Dr. A. Terry Bahill

ALL YOU EVER WANTED TO KNOW ABOUT EYE MOVEMENTS BUT WERE AFRAID TO ASK

by

A. Terry Bahill
Associate Professor of Electrical
and Biomedical Engineering
Carnegie-Mellon University

Building 33 Vault - 1330-1445

THURSDAY, JUNE 24, 1982 FOUR TYPES OF EYE MOVEMENTS	A general discussion of the saccadic, smooth pursuit, vergence and vestibulo-ocular eye movement control systems. We will discuss anatomical, dynamic and behavioral differences and the interactions between these systems.

****

TUESDAY, JULY 6, 1982 THE SACCADIC EYE MOVEMENT SYSTEM	A lecture based on the Scientific American paper by Bahill & Stark, January 1979. Two tools, the main sequence diagrams and the reciprocal innervation model, will be used to explain the origin of dynamic overshoot, glissades, overlapping saccades and the curvature of oblique saccades.

****

THURSDAY, JULY 8, 1982 ZERO-LATENCY TRACKING OF PREDICTABLE TARGET WAVEFORMS BY THE HUMAN SMOOTH PURSUIT EYE MOVEMENT SYSTEM	This exciting lecture will show that the human can overcome an inherent time delay and track targets with no latency. An engineering model is developed that can do the same. Tracking of baseball players will also be shown.

****

THURSDAY, JULY 15, 1982 HEAD AND EYE MOVEMENTS WHILE WALKING	A human with a head rest and bite bar can track a target with a mean square error (mse) of 0.05 deg^2. As more freedom of movement is given to the subject the mse increases to 0.5 deg^2 for a subject standing with free head, and to 1.0 deg^2 for a subject who is walking.

****

THURSDAY, JULY 22, 1982 ADVANTAGES AND LIMITATIONS OF THE TWO-POINT CENTRAL DIFFERENCE DERIVATIVE ALGORITHM	This mathematical lecture will show the frequency limitations of this algorithm and it will show how noise and accuracy of the data influence the choice of the optimal sampling rate.

****

PLEASE RESERVE SPACE EARLY - CALL DR. KENNETH BOFF ON EXT. 54820/54693

****

HMOS OPERATING PROCEDURES

by A. Terry Bahill

July 1982

Based on Sections 4.2 to 4.4, Volume III of Honeywell's HMOS system manual

4.2 Power-Up

1. Turn on circuit breakers #3 and #30 on Circuit Panel CPP-1.

2. Turn on power to instruments. There are 4 power switches: the CRT, the Eclipse, the Link tape, and the Electrohome panel (the Remote Electronics PWR switch and the Remote Electronics Breaker that turn the lamp on will be discussed later).

3. Mount the Linc Tape on the tape drive. Thread the tape through the tape head and put on adjacent spindle. Alternate between LOAD and REWIND positions on switch so that the tape load mark (the one-inch long silver strip) is to the right of the tape head. You may have to press the LOAD switch momentarily so that the tape is tensioned.

4. On the Eclipse front panel, depress the left most switch to the STOP position then raise to the RESET position. Set switches 10, 11, 12, and 13 to up position. Momentarily raise PR LOAD switch. After a short time delay, the computer will type -EXEC? on the CRT. If computer power has just been turned on, press Alpha lock key on CRT terminal. Now tell the computer which program you want to run, e.g. "HMOS", "TERRY", or "JEFF" as shown in the following line. Underlined items are things you type. Your response should be followed by a carriage return (CR).

EXEC? HMOS (CR)

When the tape stops spinning, you will be talking to the debugger. In many of the following examples you will be asked to press the ESC key on the CRT terminal. This key will be indicated as (ESC). Set the computer to decimal mode by typing:

(ESC)N 00000 1 (CR)
or, depending upon the computer's mode, perhaps
(ESC)N +1.1 (CR)

Set lamp brightness with

EGR4+22/-xxx.-yyy. (CR)

where -xxx. represents the old brightness level and -yyy. represents the new brightness level. The brightest possible value is -512. and the dimmest possible value is -0. A good range is -100. to -150.

Raise switches 0, 1, and 14 on the Eclipse front panel to their up positions, (lower switches 10, 11, 12, and 13 if they are still up). Start software with

RUN(ESC)R

(The first time you start the program HMOS you will have to type ZZZZ(ESC)R rather than RUN(ESC)R.)

You may verify that the software is working by observing that the ION light on the Eclipse is ON and that the tracking bars on the video screen are at the bottom and at the right side.

Turn on Remote Electronics breaker on video monitor panel. Push Remote Electronics PWR button to turn on lamp power. (If you did something wrong, the red overbrightness LED on the back of the HMOS control box may be on and it may be necessary to reset the adjacent circuit breaker.)

If at any time you wish to interrupt the program and get back to the debugger (BIDEB), raise, then lower switch 15 on the Eclipse. For example, to change bulb brightness, raise, then lower switch 15 and type

EGR4+22/-xxx.-yyy. (CR)

where -xxx. is the old brightness and -yyy. is the new brightness. Then type

RUN(ESC)R

4.4.1 Linearization

To determine the size and shape of each subject's eye, run the linearization program that collects data from 51 fixation points. Raise switch 12 on the Eclipse. The computer will tell you where the subject or artificial eye should be looking in terms of the coordinates described in the figure in Appendix D.

When the "eye" is at the correct location and the video monitor shows that it is locked on, raise switch 8. The machine will now take data. After 5 or 10 seconds check to see if it has taken enough data by lowering switch 8. If it is happy, it will now ask for the eye to be aimed at the next point, otherwise it will say nothing and you should return switch 8 to the raised position. If after 30 seconds of data taking, it still has not received a preset number of successive good fields of data it will give up, label the point BAD, and instruct you to proceed to the next point. If the computer will not give up, then you should move the eye slightly until tracking gate bars become stationary. At the end of the first pass, the computer will initiate a second pass where it tries to get data for all of the BAD points. The computer will ask you to aim the eye at the designated point; when this is completed, raise switch 8 as before. When it is through, it will rapidly list out a bunch of numbers.

To speed up the linearization data collection, you may want to force it to accept noisy data, by reducing the number of times the fixation data is averaged and by increasing the maximum acceptable variance. To accomplish this, enter the debugger, and type

FIXTST+441/+10. 3. (CR)

VARLMT+4/+1000. 32700. (CR)

VAR_MT+5/+9000. 32700 (CR)

(Caution: Turning on the oscilloscope [or some other piece of equipment] may cause the program to quit.)

4.4.2 Calibration

Linearization is done only once for each subject. Calibration is done at the start of each run for each subject. To collect the calibration data, raise switch 13 and follow the computer's directions. Calibration only uses 7 fixation points and there is no second pass - if you blow a single point, do the entire calibration over again.

Creating a Version of HMOS Containing Linearization Data
by A. Terry Bahill
July 1982

1. To make room on the tape, you will probably have to delete some file using RUBOUT, SQUASH and TAPES.

2. Run HMOS and collect linearization data.

3. Enter debugger by momentarily raising switch 15 on Eclipse switch register.

4. On Eclipse front panel momentarily depress switch to STOP position, then momentarily raise it to RESET position. Set switches to 077377 and push "START" switch. LTOS should now be running, check to verify that LTOS prompt (EXEC?) is written on the TTY.

5. Put core image of HMOS into temporary file as follows:

```
EXEC-? SAVE
Filename TEMP, Ø
Addresses Ø, 74377, 44751
```

The above numbers represent the starting address and ending address of memory and the starting address of the program. This process takes approximately 3 minutes.

6. Run the program TAPES

7. Mak room on the tape by running RUBOUT, SQUASH and TAPES.

8. Run QSAVE as shown below.

```
EXEC-? QSAVE
Input file: TEMP
Output file: ARTEYE, Ø
```

This process takes approximately 10 minutes.

9. Run TAPES.

10. RUBOUT TEMP. Run the programs SQUASH and TAPES

11. The file ARTEYE can now be run just like HMOS. It contains linearization data.

12. If the file is valuable, [illegible] a backup [illegible] MOVER.

Collecting Data
by A. Terry Bahill
August 1982

1. Turn off room lights.

2. Turn on HMS power supplies (on the rear table).

3. Turn on PDP 11/34 computer and boot it.

4. Turn on Network Adapter (on the table) by pushing PWR switch on front panel.

5. Clear Network Adapter by pushing red M.C. button behind locked door on rear panel.

6. Have subject don helmet and sit in seat.

7. Turn on HMS (switch is on small 4x4x2 inch box).

8. Turn on circuit breaker #4 if laser is to be used. Do not let laser beam shine in your eyes.

9. Turn on HMOS equipment and run HMOS software as described on previous pages (keep switches 0, 1 and 14 up).

10. Run 7-point calibration routine.

11. Run collect program on 11/34. (Type RUN COLECT.)

12. Lower switch 1 on Eclipse front panel.

13. Lower switch 0 on Eclipse.

6-30-82

HMOS PROGRAMS AND OPTIONS

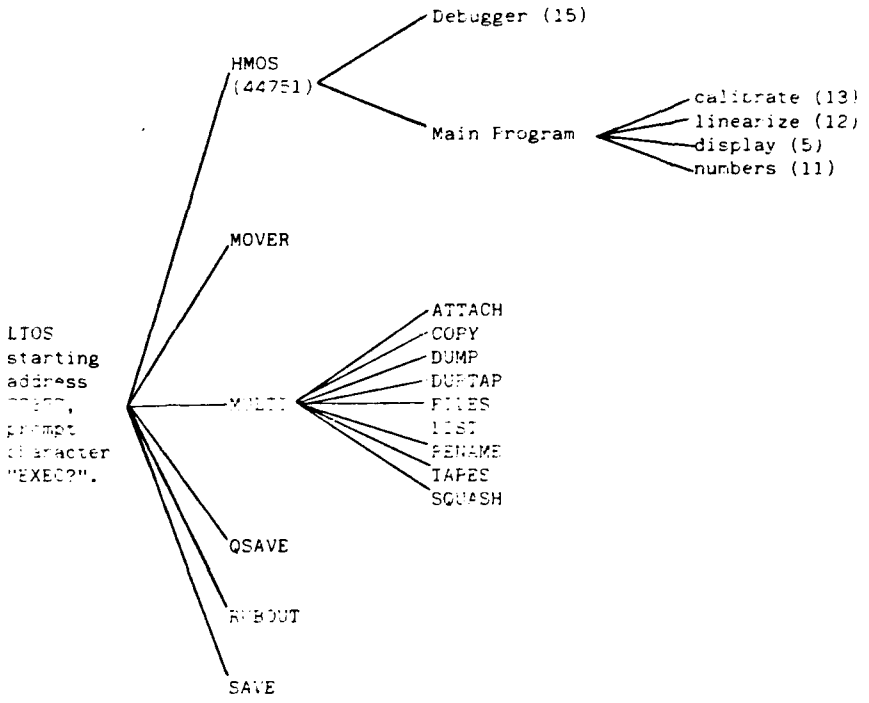

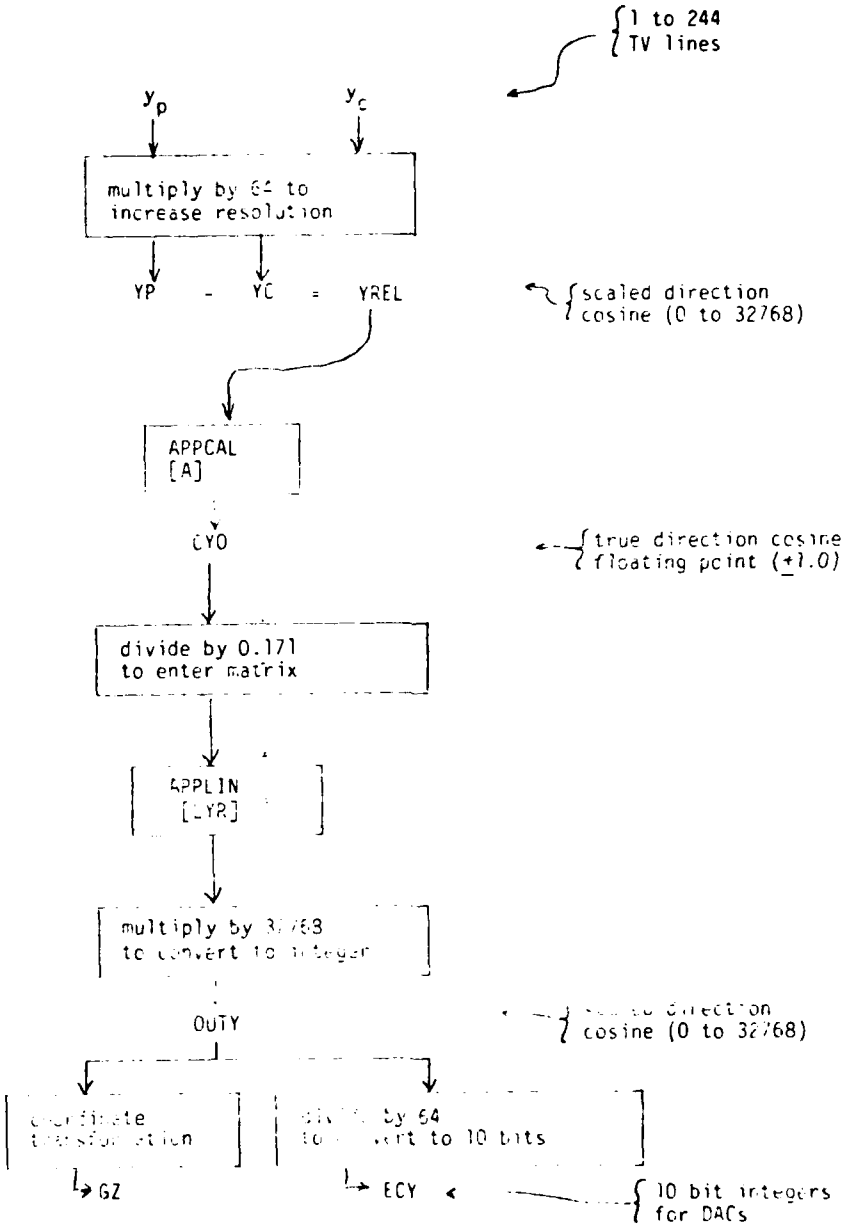
1 to 244
TV lines
y_p
y_c
multiply by 64 to
increase resolution
YP - YC = YREL
scaled direction
cosine (0 to 32768)
APPCAL
[A]
CYO
true direction cosine
floating point (±1.0)
divide by 0.171
to enter matrix
APPLIN
[CYR]
multiply by 32768
to convert to integer
OUTY
cosine (0 to 32768)
GZ
ECY
10 bit integers
for DACs

Appendix C

A History Of HMOF From June 1982 To September 1982

by J. S. Kallman

How do you solve a problem involving multiple computer interactions when you aren't familiar with two of the three computers comprising the system? With great difficulty. With ten weeks of great difficulty.

Step 1: Learn about the computers.
Step 2: Learn about the software running on the computers.
Step 3: Deduce the problem from data provided by altering software.

Debugging operations started with the Eclipse computer. The Eclipse refused to take a complete set of human linearization data. It was hoped that an artificial eye could be used to successfully model what the HMO wanted to see in a human eye (bright pupil and corneal reflex). This didn't work immediately. We though that perhaps the 'retina' of the artificial eye might be either reflecting too much light, or not enough light. We colored retinas, for a time, in search of a color that more closely approximated what the HMO was looking for. We never found such a color. Finally, knowing that the HMO wanted a bright pupil, we put a light bulb behind an artificial eye with a clear retina. By varying the voltage going to the eye, we could control the brightness of the pupil. We were able to make this work, and managed to get linearization tables. Soon thereafter we were able to obtain human linearization data. This was accomplished by turning down the room lights and moving the helmet to a new position on the human head. We then determined that human data yielded better HMOS responses with human linearization than [illegible] our hopes of being able to linearize an artificial eye and use that for everyone rather than putting all of our subjects through the linearization [illegible] (a long, boring, and painful [illegible]).

At this point we were ready to try sending data to the PDP-11/34 via the HYPERchannel. This yielded no results what so ever. The COLECT program would stop recording data for no apparent reason, the Eclipse computer would stop running the HMSC program for no apparent reason, and the whole system was fouled up. For no apparent reason. We got nowhere with resolving these problems until we made a small addition to the COLECT main program. This addition was a typical programmer's trick: add a print statement (in our case a bell ring). We set the program up to ring a bell each time it had received sixty pieces of data. This yielded some bizarre results. When the HMS data was 'added' to the HMO data, the system stopped dead after thirteen bells. When the HMS data wasn't 'added', the system stopped after thirteen bells, waited for a few seconds, and then restarted. Sometimes. Occasionally, the system died after only one or two bells. Every once in a while it wouldn't start at all.

After chasing bugs from the Eclipse to the 11/34 and back to the Eclipse, we determined that the Eclipse stack pointer had two words left behind on the stack after each data delivery. The stack was long enough to last for thirteen second. In addition we found that if HMS data is to be added to HMO data, the Eclipse cannot recover from a stack overflow, while if HMS data is not added, the Eclipse can recover. At this point we thought we had it licked. All we had to do was find a bad stack recovery. We found it and fixed it, but there was very little effect. The system still died after thirteen bells.

Two weeks were spent trying to get the system to work with little effect except a certainty that the problem was now resident in the 11/34. This was determined by inserting a [illegible] start mechanism into the COLECT program. Once the system was started, the Eclipse put out data and didn't

stop. If the bells stopped, the HYPERchannel restart would get them going again. Unfortunately, the HYPERchannel was a sealed black box to us, so we couldn't attack it and see what gave.

In a fit of desperation, we decided to go over the software and manuals one last time. This is when we noticed that the COLECT program was instructing the HYPERchannel adapter to send data in burst mode. Burst mode allows the HYPERchannel adapter to grab hold of the PDP-11/34 UNIBUS and send a burst of data without being interrupted. Reading the HYPERchannel adapter manuals indicated that the burst length (the number of words sent per burst) was set by hardware switches. Looking at the HYPERchannel adapter card in the PDP-11/34 indicated that data was being sent and received in fourteen word bursts. Now, the Eclipse sends 32 words to the HYPERchannel adapter. If the HYPERchannel adapter wants to send them to the PDP-11/34 fourteen at a time, it's going to run into trouble on the third burst. We decided to pull out the HYPERchannel board in the 11/34 and switch select a burst length of eight words. The system worked. Or at least it seemed to work.

At this point we were forced to deal with a new and different type of problem. The bulb that supplied the infrared light used in the HMO blew out. Replacing this bulb turned out to be a difficult proposition because it was epoxyed into a special bulb holder, only one such bulb holder exists at the HMOF, and to replace the bulb you have to get a special solvent to eat the old epoxy so you can epoxy a new bulb into place. In addition we had to use a special epoxy. Getting the materials and replacing the bulb in the special fixture took two days. Fortunately, this only had blown two weeks before we thought of the burst length fix.

At this point we tried to put it all together. We put a subject in the helmet, set the targets going, were all set to take data, and didn't get any.

The system was completely intolerant of human data. We put the helmet on the artificial eye stand and tried to figure out what was wrong.

The next day the bulb blew. This was a particularly bad time for this to happen, as it takes a minimum of 48 hours to replace a bulb, and we were running out of time. In addition, the debugging was made more difficult because we didn't have real data to send over the HYPERchannel adapter.

On Wednesday of our last week at the HMOF we were once again prepared to try to take data. We started the system on the artificial eye, and within ten seconds, the bulb blew. We were in the ridiculous position of having ten weeks of work go down the tubes because some 50 cent light bulbs wouldn't last. It was too late to expoxy up a new bulb. We were at the end of our collective ropes. So what did we do? We performed several experiments in the following manner: The subject sat in the target presentation chair holding a bulb into the HMO with one hand and holding the HMS switch in the other hand. The 11/34 operator sat at the 11/34 console. The Eclipse operator sat at the Eclipse front panel. The Eclipse operator guided the subject in the placement of the HMO bulb. When the bulb was in an acceptable position, the Eclipse operator guided the subject through a calibration. Then the 11/34 operator started the target and data collection program. When the 11/34 was ready, the Eclipse operator opened the data passing gate and the data collection began. At several times during the data collection the HMOS would go into a "sight death" mode, at which time the Eclipse operator flipped two front panel switches and instructed the subject to hit the sight switch. The other major [illegible] hitting a HYPERchannel init from the 11/34.

We filled [illegible] with data. When analyzing the data at Carnegie-Mellon University we found that only ten seconds were valid and usable.

1982 USAF-SCEEE GRADUATE STUDENT SUMMER SUPPORT PROGRAM

Sponsored by the

AIR FORCE OFFICE OF SCIENTIFIC RESEARCH

Conducted by the

SOUTHEASTERN CENTER FOR ELECTRICAL ENGINEERING EDUCATION

FINAL REPORT

OXYGEN IMPLANTATION OF GALLIUM ARSENIDE

Prepared by:	James R. Kempton
Academic Department:	Physics
University:	Wittenberg University
Research Location:	Air Force Avionics Laboratory, Wright-Patterson AFB
USAF Research Contact:	Dr. Yoon Soo Park
SFRP Supervising Faculty Member:	Dr. Albert J. Frasca
Date:	August 20, 1982
Contract No:	F49620-82-C-0035

Acknowledgement

The author would like to thank the Air Force Systems Command, the Air Force Office of Scientific Research, and the Southeastern Center for Electrical Engineering Education for providing him with the opportunity to spend an educational and interesting summer researching an area of vital importance to the electronics industry. He would also like to acknowledge the Avionics Laboratory, Wright-Patterson AFB, OH for its excellant equipment and environment for research.

The author wishes to thank J. E. Ehret for implanting the samples, C. R. Geesner for preparing the samples, and A. Ezis for performing the C-V measurements. He would also like to acknowledge P. P. Pronko and R. S. Bhattacharya for many helpful discussions and Y. S. Park for his guidance. Finally, the author would like to thank A. J. Frasca for his assistance.

OXYGEN IMPLANTATION OF GALLIUM ARSENIDE

by

James R. Kempton

ABSTRACT

The development of a stable semi-insulating layer in ion-implanted gallium arsenide is investigated. Analysis of samples, implanted with oxygen-18, by Rutherford backscattering and Capacitance-Voltage techniques discloses thick compensating layers with a low amount of damage after an 800^{o}C anneal. Suggestions for further research on this material are offered.

I. INTRODUCTION:

During the early 1970's oxygen was implanted to compensate n-type gallium arsenide(GaAs). Typical implant energies ranged from 50 to 1000 KeV with the dose ranging from 10^9 O^+/cm^2 to 10^{15} O^+/cm^2. C-V, C-f, and Hall techniques were used for electrical measurements, while photoluminescence was used to study the optical spectrum. In the mid-1970's the use of SIMS for studying oxygen profiles became popular. The fact that oxygen could compensate conductive layers and produce highly resistive layers made it a prime candidate for device production and isolation purposes. Favennec and Rao[1] deduced that oxygen compensates by two techniques: the first is due to defects induced by implantation, while the second is the presence of oxygen in the lattice acting as a double electron trap or dopant. It was also found that the compensation due to implant damage could be annealed away as it is with electron, proton, and deuteron compensating layers. However, the dopant contribution was thermally stable to at least 800°C provided the implant was beyond a threshold dose of approximately 10^{13} O^+/cm^2.

In a later article, Favennec[2] further studied the oxygen implant problem in n-type GaAs. He found that before annealing the oxygen formed highly resistive layers centered at the mean range for defects and at the mean range for ions. The fact that two regions exist explained the earlier results of two separate resistivity regions.

The chemical interaction of implanted oxygen with other dopants in a lattice is discussed by Favennec et. al.[3] where oxygen is implanted into a Cr-doped GaAs crystal. The results are quite interesting since both chromium and oxygen are quite mobile during the annealing process.

It has been known that oxygen and chromium would escape the GaAs lattice unless a cap of Si_3N_4 or SiO_2 was sputtered on prior to annealing at high temperature. The presence of the cap introduces irregularities on the surface of the Cr-doped GaAs which causes a reduction in the Cr mobility near the surface or a Cr pile-up near the surface(.02 to .1 um)followed by a depletion zone which extends from one to three micrometers below the surface. To further investigate Cr-doped GaAs, oxygen ions were implanted at high doses(10^{14} O^+/cm^2) at 400 and 800 KeV into the same lattice. After annealing, the following results were obtained: the Cr migrated to the surface as before, while some Cr clustered at the projected ranges of both implanted energies. Repeating the experiment using neon at 400 and 800 KeV gave no indication of clustering at the two projected ranges. Therefore, chromium trapping can be caused by the chemistry of the implant and by surface irregularities which are independent of material. Clustering of Cr was found to occur with oxygen and iron implants but not with neon or copper.

In a recent article, a study of the redistribution of oxygen (after anneal) was done. It was found that oxygen doses lower than 10^{14} O^+/cm^2 would not cluster and trap chromium. However, for doses above 10^{14} O^+/cm^2 it would cluster around the mean range for ions and trap chromium.[4] With this clustering, a narrow, highly resistive layer with a high oxygen concentration occurs which is desirable for utilization of very thin planar devices.

II. OBJECTIVES:

The present project is concerned with the implantation of GaAs with oxygen-18. Oxygen-18 was used with the intention of profiling by a nuclear reaction technique. Our specific objectives are:

(1) To determine the depth of carrier compensation using Capacitance-Voltage measurements.

(2) To determine the amount of damage caused by implantation of oxygen and the effects of 400 and 800°C anneals upon it with Rutherford backscattering.

III. CAPACITANCE-VOLTAGE MEASUREMENTS:

Capacitance-Voltage(C-V) measurements are a means of profiling the implanted material to determine the carrier concentration. This method makes use of a reverse-biased Schottky barrier. This barrier creates a depletion layer of thickness, x, below the surface with a capacitance, C, for a fixed voltage. The capacitance of this region is inversely proportional to the thickness as the equation below illustrates-

$$C = \epsilon A/x \qquad (1)$$

where A is the area of the surface and ϵ is the dielectric constant. As the voltage is augmented, the thickness of the depletion layer increases causing the capacitance to decrease while uncovering an additional charge of $eN(x)\Delta x$. Using Poisson's equation, one can show that the local carrier concentration, N, at x is given by[5]

$$N(x) = \frac{-C^3}{\epsilon eA}\left(\frac{dC}{dV}\right)^{-1} \qquad (2)$$

However, this technique is limited to analysis of carrier concentrations in GaAs of approximately 10^{16} to $10^{18}/cm^3$, which will govern

the thickness of the depletion layer. If the depletion layer is too thick($N<10^{16}/cm^3$), analysis of the doped region will not be possible due to the low electric field. If the depletion layer is thin ($N>10^{18}/cm^3$), analysis of the doped region will not be possible due to breakdown of the barrier.

The results of the C-V measurements are shown below:

TABLE 1 - DEPTH OF COMPENSATION

Anneals(20 Minutes)	10^{14} O^+/cm^2	10^{15} O^+/cm^2
As implanted	0.30 um	0.30 um
400°C	0.34 um	0.31 um
800°C	0.45 um	0.75 um

Upon performing a range calculation, one finds that the mean range for the oxygen-18 ion at 120 KeV is 0.16 um. According to table 1 oxygen will compensate and will migrate deeper into the lattice upon an 800°C anneal. From this, one can conclude that a semi-insulating layer is created.

IV. RUTHERFORD BACKSCATTERING:

Rutherford backscattering is the coulombic repulsion of an incident particle, such as a proton, by heavy target nuclei. As the particle enters and exits the target lattice, it loses energy. The amount of energy lost is dependent upon the particle's incident energy, the distance traveled, and the stopping power of the target lattice. When an ion is implanted into material of a different atomic number, the backscattering spectrum consists of two scattering spectrums, one from the implanted ion and one from the host lattice, superimposed

upon one another. With this data, one can determine the dose of the ion. The equation is as follows:

$$(Nt)_I = \frac{A_I \sigma_L(E_o) \xi}{H_L \sigma_I(E_o) [\epsilon_o]_L} \qquad (3)$$

where $(Nt)_I$: dose of the ion in ions/cm^2

A_I: total number of counts in the backscattered spectrum from the presence of the ion

H_L: the number of counts in a channel of the backscattered spectrum corresponding to the surface region

$\sigma_L(E_o), \sigma_I(E_o)$: the scattering cross section for incident particles of energy, E_o, for the lattice and the ions, respectively

ξ: the energy interval corresponding to one channel

$[\epsilon_o]_L$ the stopping cross section factor evaluated at the surface.[6]

This equation permitted us to confirm the dose calibration of the ion implanter by using a graphite sample bombarded with argon. However, no analysis of the ion dosage in GaAs could be performed due to low energy backscattered spectrum, from the oxygen, residing in a high background count region.

Rutherford backscattering also allows one to examine the amount of damage caused by implantation. Examination of spectrums of virgin GaAs and oxygen-implanted GaAs with various anneals or with no anneal yields the amount of damage caused by implantation and the temperature needed to remove it. Past experiments indicate that the $\langle 100 \rangle$ in GaAs allows the amount of damage to be observed. When the spectra

from the ⟨100⟩ and from a random scatter are compared, one can calculate the amount of disorder. The relative measure of disorder is the ratio of channeled to random at high proton energy. This ratio(χ_{MIN}) becomes larger as the amount of damage increases. For this work a 330 KeV proton beam from a Van de Graaff bombarded the targets. The ⟨100⟩ was obtained with a goniometer system capable of 0.01° increments.

Rutherford backscattering yielded the following relative measures of disorder-

TABLE 2 - RELATIVE MEASURE OF DISORDER(χ_{MIN})

Anneals(20 Minutes)	10^{14} O^{+}/cm^{2}	10^{15} O^{+}/cm^{2}
As implanted	.081	.113
$400^{\circ}C$	.059	.067
$800^{\circ}C$	.049	.050

The small relative measures of disorder for the as implanted samples indicate that the damage is dispersed throughout the crystal in the form of point defects which is a characteristic of light ion implantation. Comparing the relative measure of disorder for the $800^{\circ}C$ anneal with that of a virgin crystal, $\chi_{MIN} = .050$, implies that most of the damage caused by implantation has been removed. This agrees with the results obtained by Favennec.[2]

V. RECOMMENDATIONS:

The Rutherford backscattering data indicates that the damage is present in the form of point defects which can be removed with an $800^{\circ}C$ anneal. One can infer that the damage is either caused by the bombardment of the crystal or by the presence of off-lattice site

oxygen which either migrates out of the crystal or to a substitutional site during anneal. Upon examining the C-V data one notices a thick compensated layer for 800°C anneals which means that the oxygen has probably not migrated to the surface, but one still does not know the oxygen site before anneal. In order to verify the presence of oxygen-18, one should use a nuclear reaction technique for profiling. $^{18}O(p,\alpha)^{15}N$ has a resonance at 630 KeV which is 2.6 KeV at FWHM yielding a depth resolution of .038 um.[7] This reaction will reveal the depth and the concentration of the oxygen-18 in the crystal. A second recommendation is that this method be used in conjunction with channeling in order to determine the lattice location of the oxygen.

REFERENCES

1. Favennec, P. N. and E. V. K. Rao, "Compensating Layers in GaAs by Ion Implantation: Application to Integrated Optics," Proceedings from the Fourth International Conference on Ion Implantation in Semiconductors and Other Materials, Osada, 1974, pp. 65-71.

2. Favennec, P. N., "Semi-Insulating Layers of GaAs by Oxygen Implantation," Journal of Applied Physics, Vol. 47, 1976, pp. 2532-2536.

3. Favennec, P. N., M. Gauneau, H. L'Haridon, B. Deveaud, C. A. Evans, Jr., and R. J. Blattner, "Chromium Gettering in GaAs by Oxygen Implantation," Applied Physics Letters, Vol. 38, 1981, pp. 271-273.

4. Favennec, P. N., B. Deveaud, M. Salvi, A. Martinez, and C. Armand, "Redistribution of Implanted Oxygen in GaAs," Electronics Letters, Vol. 18, 1982, pp. 202-203.

5. Blood, P. and J. W. Orton, "The Electrical Characteristics of Semiconductors," Reports on Progress in Physics, Vol. 41, 1978, pp. 158-257.

6. Chu, Wei-Kan, James W. Mayer, and Marc A. Nicolet, Backscattering Spectrometry, (New York, Academic Press, 1978), p. 139.

7. Butler, J. W. and H. D. Holmgren, "Radiative Proton Capture by O^{18}," Physical Review, Vol. 116, 1959, pp. 1485-1489.

1982 USAF-SCEEE SUMMER FACULTY RESEARCH PROGRAM

Sponsored by the

AIR FORCE OFFICE OF SCIENTIFIC RESEARCH

Conducted by the

SOUTHEASTERN CENTER FOR ELECTRICAL ENGINEERING EDUCATION

FINAL REPORT

ELECTRICALLY COMPENSATED CONSTANT SPEED DRIVE

Prepared by:	Tim W. Krimm
Academic Department:	Electrical Engineering
University:	University of Kentucky
Research Location:	Air Force Wright Aeronautical Laboratories Aero Propulsion Laboratory
USAF Research Contact:	Dr. William U. Borger
SFRP Supervising Faculty Member	Dr. Jimmie J. Cathey
Date:	August 6, 1982
Contract No:	F49620-82-C-0035

ACKNOWLEDGMENTS

The authors extend thanks to the Air Force Systems Command, the Air Force Office of Scientific Research, and the Southeastern Center for Electrical Engineering Education for providing the opportunity to conduct research at the Air Force Wright Aeronautical Laboratories, Wright Patterson AFB, OH. A particular expression of gratitude is offered to the Power Systems Branch of the Aerospace Power Division of the Aero Propulsion Laboratory for provision of an excellent set of working conditions and facilities.

Further, the authors offer appreciative acknowledgment to Dr. William U. Borger for suggesting, encouraging, and guiding the work of this study.

ELECTRICALLY COMPENSATED CONSTANT SPEED DRIVE

by

Tim W. Krimm

and

Jimmie J. Cathey

ABSTRACT

The feasibility of designing a constant speed drive utilizing a mechanical differential in conjunction with a parallel electric drive speed compensation link is examined. Bidirectional power flow in the electric compensation link uses two high-speed, permanent-magnet, three-phase machines interconnected by a power conditioning network. One machine is operated as a brushless dc machine, while the other functions as a variable speed synchronous machine. Steady-state performance of two types of power conditioning are studied--a dc link inverter and a cycloconverter link.

The dc link inverter with bidirectional power flow is found to require excessive values of current to allow full range reverse power flow. A mode switch to synchronous inversion is necessary to reduce current values, but it adds the penalty of increase in power electronic devices and control complexity. The cycloconverter link is found to offer the better full range bidirectional power flow. In addition, a dc link system is examined for a method of operation with unidirectional power flow through the compensation link at the expense of increased size of electrical machines, but offering simpler controls.

Suggestions are made for further research on this system concept.

I. INTRODUCTION

The need for a highly efficient link, capable of bilateral power flow, connecting a variable speed shaft to a constant speed shaft is manyfold. A particular Air Force need is to drive an onboard aircraft alternator at constant speed while the turbine engine speed varies. Presently, two methods are employed to provide a constant frequency on Air Force aircraft:

1. Constant Speed Drive (CSD)
2. Variable-Speed, Constant-Frequency (VSCF)

The VSCF system allows the alternator shaft speed to vary directly with turbine speed. The variable frequency alternator output is then conditioned by a cycloconverter to obtain a constant frequency. The VSCF system is not sensitive to attitude changes, and thus, functions well on highly maneuverable aircraft. However, total output power of the alternator must pass through the cycloconverter, leading to bulky and expensive power conditioning and filter circuitry.

The CSD scheme utilizes a mechanical differential to link the turbine engine and alternator. A constant alternator shaft speed is maintained by proper clockwise or counterclockwise rotation of the differential carrier housing through use of a reversible hydraulic pump-motor drive. For a 1.7:1 turbine speed range and a lossless system, a maximum of 21.5% of the alternator shaft power must pass through the compensating hydraulic drive, while 78.5% to 100% of the power is transmitted directly through the differential gearing. The CSD has been successful in flight operation except during maneuvers that produce negative gravity. In such cases, fluid level shifts can cause the hydraulic system to momentarily malfunction, creating an out of frequency range condition and leading to loss of electrical power.

Regardless of the above described potential failure mode, the concept of the CSD system has a quite desirable feature in that a large percentage of its output power is transmitted only through a low-order-mesh gear train which by nature is highly efficient. Replacement of the hydraulic compensation drive with an electric compensation drive can yield a CSD concept that is insensitive to aircraft attitude changes while preserving

the desirable feature. Further, a properly designed electric drive should offer an increase in overall efficiency, due to reduction in losses through the speed compensation path. Also, the potential exists for a greater interval between maintenance than for the compensating hydraulic drive system.

II. OBJECTIVES

The principal goal of this research was to study the feasibility of designing an electrically-compensated, constant-speed drive (ECCSD) that has potential for application as a drive link between a turbine engine and an aircraft alternator. Objectives were established to study the nature of ECCSD systems in the steady-state. Transient characteristics and parameter sensitivity evaluations were not possible within the research period time frame, and thus, were left for future investigation. The specific objectives that were pursued are enumerated below:

1. Define candidate electrical machinery and power conditioning circuitry arrangements suitable for use with an ECCSD system.
2. Determine nature of torques, currents, and voltages for each candidate system operating as an ECCSD.
3. Identify special requirements on machines, controls, and power electronic devices that result from the ECCSD application.

III. BASIC REQUIREMENTS AND CHARACTERISTICS OF ECCSD

An understanding of the power flow and torque requirements of the ECCSD concept underlies any study as these characteristics must serve as a basis for selection of candidate electric machine and power conditioning systems.

A. Nature of Power Flow. A physical arrangement of the ECCSD power level components is shown in Figure 1(a) where variable input speed n_1, constant output speed n_0, and differential carrier speed n_2 are related by:

$$n_2 = 1/2\ (n_1 - n_0) \qquad (1)$$

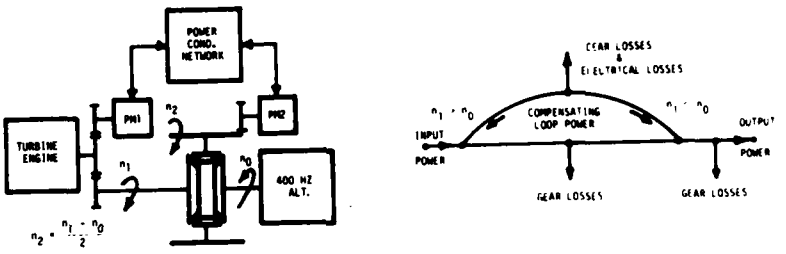

(a) (b)

Figure 1 (a) Physical Arrangement of ECSD
(b) Power Flow Diagram of ECCSD

Speed compensation to maintain n_0 constant can be accomplished by two basically different control approaches:

1. Reversing differential operation. Ratios are selected so that n_0 lies between the extremes of n_1. Thus, from equation (1) it is apparent that n_2 can range from negative to positive values or that the differential carrier must be reversed to maintain a constant n_0 over the range of n_1 excursion.

2. Unidirectional differential operation. Ratios can be selected so that n_1 is always greater than (or always less than) n_0, leading to the conclusion from equation (1) that n_2 does not change sign as n_1 varies; or, the differential carrier is always rotated in the same direction for speed compensation.

For study of basic characteristics, a typical turbine speed range of 1.7:1 (10,588 to 18,000 rpm) was used. The 400 Hz alternator was modelled as a 44.444 KW load at a constant 12,000 rpm (40 kVA output at unity power factor operating at 90% efficiency). Constant efficiencies were assumed as follows:

1. Electric machines - 90%
2. Power conditioning units - 95%
3. Gear mesh - 99%

Energy balance equations were written for the arrangement of Figure 1(a) and turbine speed was incremented across its speed range to examine both the case of reversing differential carrier and the case of unidirectional differential carrier operations. A power flow diagram of the ECCSD system is shown by Figure 1(b) where the flow direction of compensating loop power (P_c) depends upon the polarity of ($n_1 - n_0$) as indicated on the diagram.

The reversing differential carrier results in minimum torque requirements for PM2 if the midrange speed of n_1 is set to equal n_0, which also gives a symmetric range on n_2 about the zero speed point. Figure 2 displays the performance results of this system. It is observed that the torque requirements of PM2 are nearly constant across the range of operation. However, the torque requirements of PM1 range from zero at the midrange speed point to a maximum value at the point of minimum turbine speed. It is further noted that the maximum torque requirement of PM1 is greater than that of PM2. The two maximum torque requirements could be made equal by an unsymmetric shift of the differential carrier zero speed point with a net result of increasing the torque requirement of PM2 while decreasing the requirement of PM1. The ratio of power flowing into the speed compensation loop to power delivered to the 400 Hz alternator (P_c/P_o) is plotted to use as an indication of power apportionment between that transmitted by the compensation loop and that transmitted in mechanical form through the ECCSD.

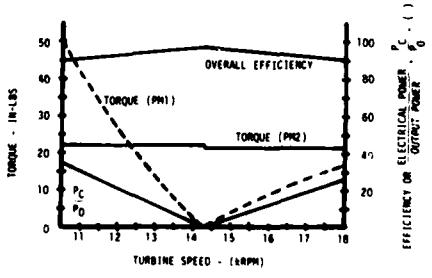

Figure 2 Calculated Performance Of Reversing Differential

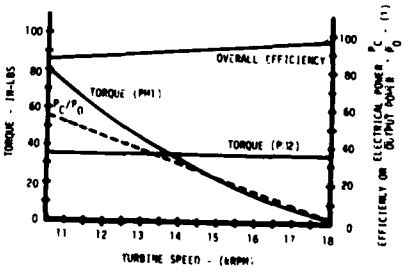

Figure 3 Calculated Performance Of Unidirectional Differential

Calculated torque requirements and performance results for unidirectional differential operation, if $n_1 < n_0$, are depicted by Figure 3. System gear ratios were selected so that n_2 ranges from 2% to 100% of PM2 base speed circumventing the necessity of dealing with low frequency torque pulsations at near zero speed.

B. Electric Machines. The wide speed range, constant torque requirements suggested for PM2 by the above work is the characteristic of a shunt dc machine; but, due to the brush-commutator maintenance requirement and poor adaptability to liquid cooling, the commutator dc machine is not suitable for aircraft application. However, the brushless dc motor offers the same desired speed-torque characteristics as the dc machine without the disadvantages of the commutator dc machine.[1-10] Further, use of a machine with a permanent magnet rotor offers two additional advantages:

1. Field excitation is eliminated which removes the complexity of supplying power to a rotating member. Also, machine efficiency is increased due to absence of field excitation losses.

2. Higher speed design is possible for permanent magnet rotors than is feasible with wound rotors permitting increased gear ratios and substantial reduction in electric machine size.

Some of the brushless dc motor performance reported in the literature is experimental data [1,3,5]. Others have presented calculations based on formulas derived using approximations of sinusoidal waveforms or neglecting commutation intervals giving results with some degree of correlation to test data but with appreciable error [2,8,9]. However, the nonlinearities introduced by the circuit switching leads to equations that are best solved by numerical techniques, and the reported performance data calculated by numerical solution of network differential equations show the least error between theoretical prediction and test results [4,10,11]. When analyzing PM machines with rare earth magnets and stainless steel retaining rings for rotor construction, Demerdash has reported [11] that rotor eddy current effects, armature reaction, and position dependence of inductances can be neglected leading to a simple third-order system of equations to describe a balanced, three-phase,

wye-connected PM machine:

$$\underline{v} = [R]\,\underline{i} + [L]\,p\underline{i} + \underline{e} \qquad (2)$$

where $\underline{v}$ is a vector of terminal phase voltages (v_1, v_2, v_3),
$\underline{i}$ is a vector of phase current (i_1, i_2, i_3),
$\underline{e}$ is a vector of phase generated voltages (e_1, e_2, e_3),
[R] is a diagonal matrix with each entry being phase resistance,
[L] is a diagonal matrix with each entry being half of line-to-line inductance, and
$p(\ )$ is understood to mean $\frac{d}{dt}(\ )$.

Since the equations given by (2) are decoupled, each can be used in networks formed by addition of the power conditioning circuitry with minimum difficulty.

C. Power Electronics. Obviously, the power conditioning circuitry of this application must be capable of bidirectional power flow when utilized in conjunction with the electric machinery. No reporting in the literature is available of an ac PM machine-to-brushless dc PM machine drive system. However, two basically different power conditioning links are candidates for use with this ECCSD under study:

1. A dc link inverter using a phase-controlled converter for rectification and synchronous inversion.
2. A cycloconverter link to perform ac-to-ac conversion.

Either of these power conditioning links can use thyristor or transistors as switching elements, but the practicality of transistors depends on values of voltage and current ratings dictated by the final system design. Much of the logic and signal manipulation of either power conditioning link will lend itself to digital processing and microprocessor control giving a finished product in which a large percentage of the signal level electronics is integrated circuits.

IV. DC LINK INVERTER WITH REVERSING DIFFERENTIAL

A. System Description. Power level components of a dc link drive system for use with the reversing differential are shown in Figure 4 where PM2 is operated as a brushless dc machine while PM1 functions as a variable speed synchronous machine.

In order to simplify the analysis, the phase-controlled converter and PM1 of Figure 4 are modelled as a dc source which, when coupled to the inverter and PM2, forms a nonplanar network. In this resulting network, the various SCRs (or transistors) and diodes are represented by nonlinear resistors the resistance of which are assigned small values

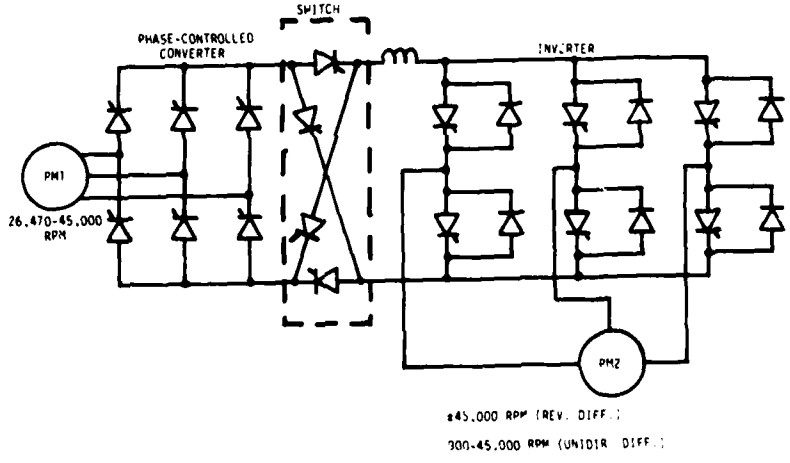

Figure 4 Power Components of DC Link Drive System

when forward conducting and large values when reverse biased. For a wye-connected PM2, the constraint that the phase currents must add to zero exists; thus, a system of two first-order differential equations is sufficient to describe the network. These equations have nonlinear coefficients due to the values of SCR (or transistor) and diode resistances being functions of the dependent variables (phase currents). Further, each 60° (electrical), a switching operation transpires in the inverter circuitry requiring a revised set of differential equations to describe the system; therefore, the differential equation coefficients

are also functions of the position (θ_2) and speed (ω_2) of PM2 rotor. In matrix notation, the network equations can be written as

$$\underline{pi} = [A(\underline{i},\theta_2)]\ \underline{i} + [B(\omega_2)]\ \underline{u} \tag{3}$$

where $\underline{i}$ is a vector of two independent phase currents (i_1, i_2), and $\underline{u}$ is a vector the entries of which are phase generated voltages and the dc source which models the phase-controlled converter and PM1 combination.

B. Control Approach. A block diagram of a control approach that can be applied to this dc link drive system is displayed by Figure 5.

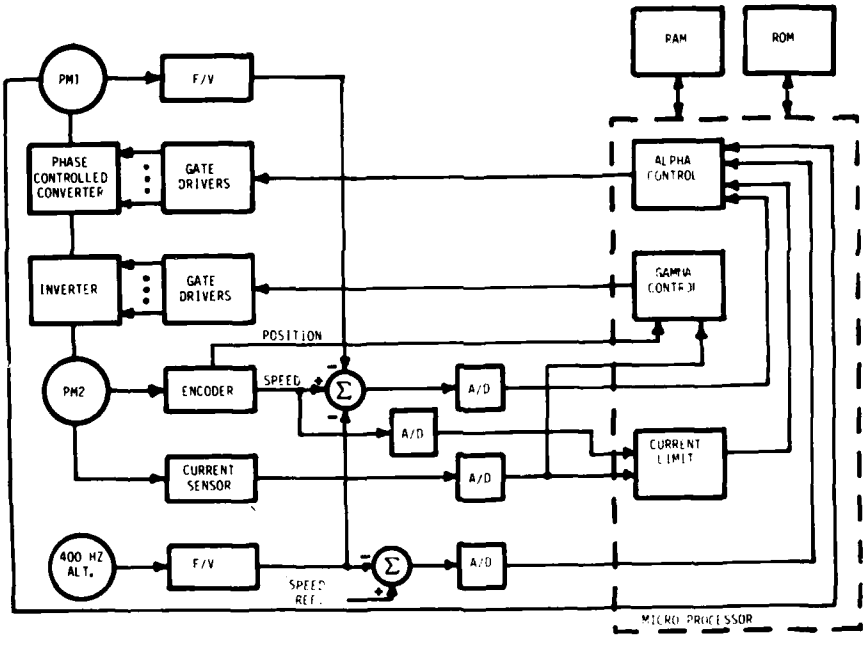

Figure 5 Block Diagram of DC Link Drive System

A primary control loop is established with a speed reference signal to assure that the 400 Hz alternator maintains rated speed. A secondary control loop is present to guarantee that equation (2) is satisfied. The SCRs (or transistors) of the inverter are fired in a manner to maintain a constant commutation angle γ, related to the angle between the mmf wave of the rotor and the no-load mmf wave of the stator. The delay angle of the phase-controlled converter is varied to regulate the value of dc link voltage applied to the inverter terminals. Steady-state characteristics of this drive are quite similar to those of a dc machine system [1-10] except for the extra degree of freedom that exists in selecting γ.

The block diagram of Figure 5 is shown with a microprocessor based control on current limit and SCR firing. It is likely that summing functions of the primary and secondary speed loops can also be handled as microprocessor operations if timing and sample rates do not become limiting factors.

C. Performance Results. Values were selected for motor and choke coil parameters as $R_a = 0.006\Omega$, $L_a = 25 \times 10^{-6}$H, $R_o = 0.003\,\Omega$, and $L_o = 43 \times 10^{-6}$H. A numerical solution of the equations represented by (3) was implemented using a fixed increment, fourth-order Runge-Kutta procedure to find performance of the dc link drive for various values of constant speed. A trial-and-error search was made for the average values of PM2 shaft torque (T_{sav}) to satisfy the requirements established by Figure 2. Results of points calculated across the speed range for forward flow of compensating loop power and partial range values for reverse flow of compensating loop power are shown in Table 1.

TABLE 1. PERFORMANCE OF DC LINK WITH REVERSING DIFFERENTIAL

Speed (rpm)	T_{sav} (N-m)	α (degrees)	γ (degrees)	I_{ave} (A)	I_{rms} (A)
45,000	2.46	18.2	45	56.4	69.5
22,000	2.48	61.6	45	56.2	69.2
5,000	2.51	82.8	45	56.4	69.8
500	2.24	88.2	45	55.2	66.3
50	2.53	88.5	45		
-500	-2.45	89.3	165	47.0	56.8
-5,000	-2.36	91.3	150	81.9	92.9
-10,000	-2.46	90.3	140	115.2	130.6

It can be observed that the values of average and RMS current required to produce the needed torque when PM2 is in the regeneration mode (reverse flow of compensating power) increase as speed becomes more negative. This increase in current values is attributable to a marked increase in the magnitude and time that current flows through the inverter shunting diodes. At some point for speed more negative than -22,000 rpm, the shunting diode current reaches a conduction angle equal to 60° at which point commutation failure occurs. A full range regenerative range operation with PM2 acting as a brushless dc machine is not possible. At some negative value of speed, it would be necessary to change modes of operation; PM2 would be allowed to operate as a variable frequency synchronous generator with the inverter shunting diodes acting as a three-phase, full-wave bridge rectifier and the phase-controlled converter could be controlled for synchronous inversion. However, use of a bridge switch as shown in Figure 4 would be necessary to establish proper polarity of dc voltage to the phase-controlled converter for synchronous inversion. Calculations show that the average values of current can be reduced to acceptable levels with the synchronous inversion operation; however, the mode change creates control complexities. Further, with addition of the bridge switch, the number (16) of power level switching devices has closely approached the quantity (18) necessary for the cycloconverter link which is capable of full speed range regenerative operation without a control mode change.

V. CYCLOCONVERTER LINK WITH REVERSING DIFFERENTIAL

A. System Description. Power level components of a cycloconverter drive system for use with the reversing differential are shown in Figure 6. As in the dc link case previously discussed, PM2 operates as a brushless dc machine while PM1 functions as a variable speed synchronous machine.

It is permissible to model PM1 as seen from the terminals of PM2 as a dc source that is magnitude dependent on both the speed of PM1 and an SCR firing delay angle α. However, since the response of PM2 due to the frequency of PM1 is desired it is necessary to describe V_d, the instantaneous waveform of PM1 generated voltage as seen from the terminals of PM2, in 60° increments of the PM1 voltage waveform giving the expression

$$V_d = V_m \sin(\omega_1 t - \phi + \frac{\pi}{3} + \alpha) \qquad (4)$$

where V_m depends on the speed of PM1, ω_1, is the electrical angular frequency of PM1 and ϕ is a phase shift angle that depends upon the

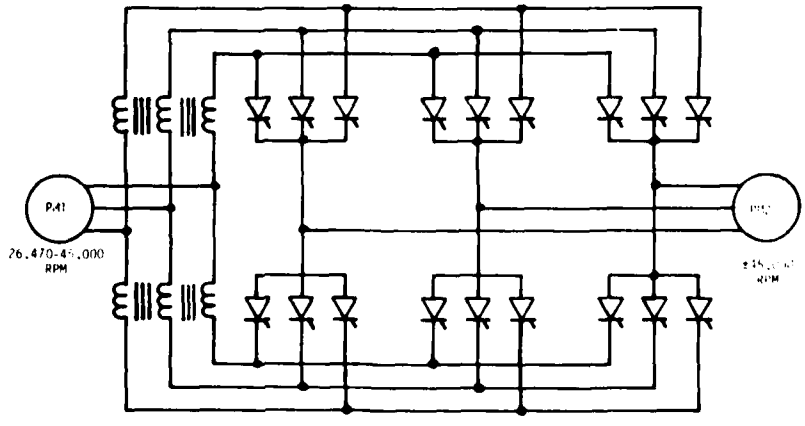

Figure 6 Power Components of Cycloconverter Link Drive

particular 60° increment of the PM1 waveform that is applicable at the instant of solution. The nonplanar network that results when V_d is coupled to PM2 through the cycloconverter is described by a set of two differential equations with nonlinear coefficients as discussed in section IV except that now the forcing function coefficient matrix has entries that depend on the electrical angular frequency of PM1:

$$\underline{pi} = [A(\underline{i},\theta_2)]\underline{i} + [B(\omega_1,\omega_2)]\underline{u} \qquad (5)$$

B. Control Approach. A control approach is suggested by the block diagram of Figure 7. The philosophy is basically that of the dc link system given by Figure 5 (discussed in Section IV) except that gating of the SCRs must be handled in such a manner to assure that both the commutation angle γ and delay angle are both simultaneously satisfied.

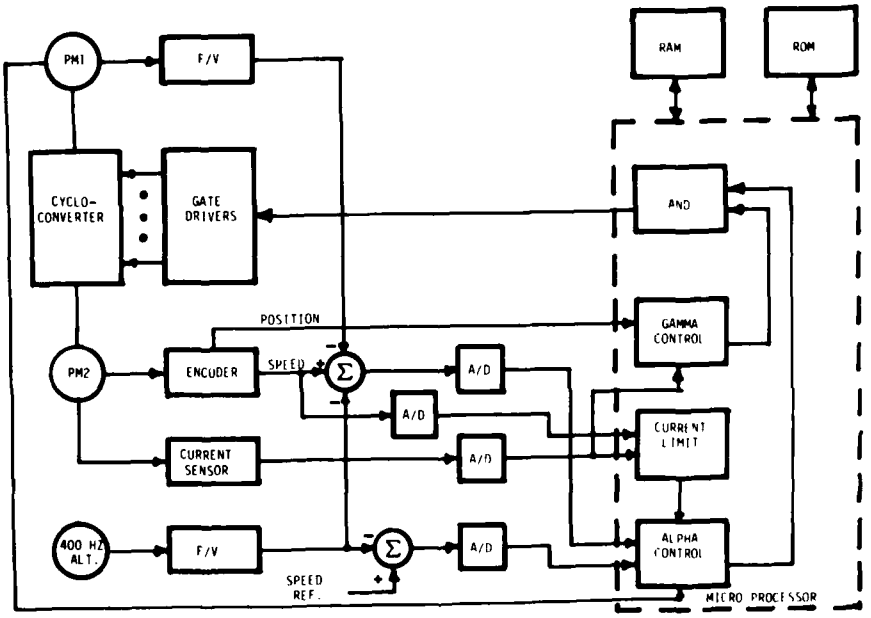

Figure 7 Block Diagram of Cycloconverter Drive System

C. Performance Results. The PM machine constants were unchanged from the dc link study. Values for the choke coil parameters were selected as $R_0 = 0.003\Omega$ and $L_0 = 150 \times 10^{-6}$ H. A numerical solution of the equations represented by (5) was implemented and a trial-and-error search made for average values of PM2 shaft torque (T_{sav}) to satisfy the requirements established in Figure 2.

Performance points across the speed range for forward and reverse flow of compensating power are tabulated in Table 2. It is observed that control across the region of reverse compensating power flow is nicely accomplished by shift of delay angle α greater than 90° and an additional forward shift of γ by 120°. No increase in PM2 phase current occurs as in the case of dc link when PM2 is regeneratively operated.

TABLE 2. PERFORMANCE OF CYCLOCONVERTER LINK WITH REVERSING DIFFERENTIAL

Speed (rpm)	T_{sav} (N-m)	α (degrees)	γ (degrees)	I_{ave} (A)	I_{rms} (A)
45,000	2.59	33.0	45	55.6	66.9
22,000	2.48	68.6	45	54.3	65.6
5,000	2.53	84.7	45	58.2	62.6
500	2.48	88.8	45	53.7	58.8
50	2.49	86.6	45		
0	2.49	89.1	45		
-5,000	-2.45	92.6	165	47.4	58.0
-22,000	-2.45	103.2	165	50.7	58.8
-45,000	-2.53	116.1	165	48.0	58.2
45,000	3.76	0	47	73.7	87.1

The last entry of Table 2 presents a set of control conditions and results for meeting a 150% load case (short time overload). Operation at such a point is automatically permitted by the control system unless prohibited by limits. Since current is monitored, the microprocessor can allow a timed interval of operation at any point above rated value before initiation of a limit action creating a quite flexible approach to overload management.

Figure 8 displays the steady-state instantaneous PM2 torque at a forward and a reverse compensating power flow point. There is inherently a pulsating torque component present in the brushless dc motor operation of a frequency that is six times the electrical angular frequency of PM2. At low speeds, this pulsation frequency can decrease to within a range at which the mechanical components respond. The control system will have a feature to assure that at low mechanical speeds, the gate drives are cyclically enabled and disabled at a frequency above that at which mechanical response is possible.

VI. DC LINK INVERTER WITH UNIDIRECTIONAL DIFFERENTIAL

A. System Description and Control. Power level component arrangement of a dc link drive system for use with a unidirectional differential is the same as shown in Figure 4 except that the bridge switch is not needed. The system equations are formulated as discussed in section IV and are given by (3). The block diagram of Figure 5 is applicable in describing a control system for this unidirectional differential drive.

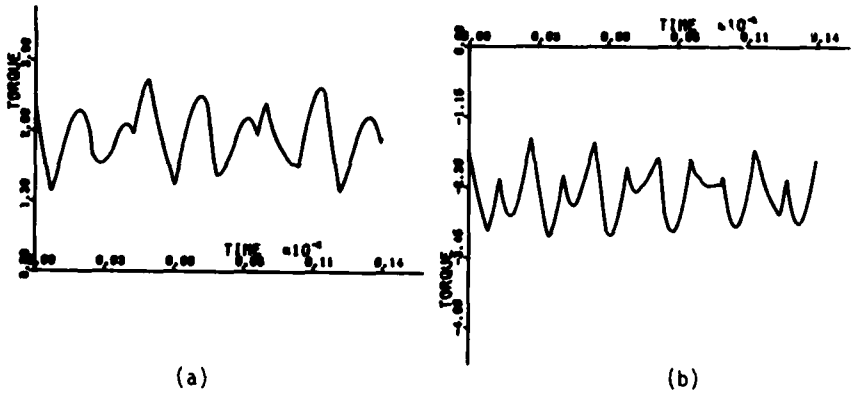

(a) (b)

Figure 8 Calculated Torque For Cycloconverter Link with Reversing Differential
(a) Forward Compensating Power Flow (+22,000 RPM)
(b) Reverse Compensating Power Flow (-22,000 RPM)

B. Performance Result. The drive system must meet the performance criteria of Figure 3. Since the torques required are approximately 50% greater than for the reversing differential case, the PM machines will

necessarily be about 50% larger in size. The parameters for PM2 and the choke coil values are adjusted accordingly to give $R_a = 0.004\Omega$, $L_a = 15 \times 10^{-6}$ H, $R_0 = 0.003\Omega$, and $L_0 = 25 \times 10^{-6}$ H. A numerical solution for values of average torque to satisfy the requirements of Figure 3 and the results are presented in Table 3.

TABLE 3. PERFORMANCE OF DC LINK WITH UNIDIRECTIONAL DIFFERENTIAL

Speed (rpm)	T_{sav} (N-m)	α (degrees)	γ (degrees)	I_{ave} (A)	I_{rms} (A)
45,000	4.09	22.7	45	92.7	114.2
22,000	3.98	62.5	45	89.6	110.7
5,000	3.98	82.6	45	91.0	111.5
900	4.12	86.9	45	100.6	120.9

Inspection of Table 3 shows that average current values are approximately 60% greater than for the reversing differential case (See Table 1). Although this unidirectionally operated differential offers control simplification in that only one direction of compensating power flow is required and the necessity of dealing with torque pulsations at near zero speed is eliminated, the increased size requirements on the PM machines (to deliver approximately 50% more torque) and the increased current ratings on the SCRs or transistors (to conduct approximately 60% more current) are considered sufficient weight and cost penalties to abandon further study of this concept.

VII. RECOMMENDATIONS

Although this feasibility study uses specific examples, it is only possible to examine nonlinear systems of this complexity by numerical methods. The values of constants and parameters selected are believed to be sufficiently typical to identify problem areas and to allow formulation of general conclusions with reasonable confidence. The work leads to the conclusion that an ECCSD system is feasible and practical if PM machines are used in conjunction with a cycloconverter link and a reversing differential. Additional study is recommended in the areas enumerated below prior to and as an aid in forming specific guidelines for any prototype design.

A. Control system. Design and breadboard a microprocessor based control system to identify problems with timing and sampling rates.

B. PM Machines. Rough design PM machines of appropriate voltage rating and torque capability to verify that the needed parameters are practical and to establish approximate weights and sizes. Study the advantages and disadvantages of using identical machine sizes for both PM machines. Predict the approximate effects of magnetic saturation on performance.

C. Parameter Variation. Study the sensitivity of system performance to variation of design parameters.

D. Transient Performance. After a control system model has been formed and machine parameters and mechanical sizes determined, study the nature of response to step load changes and rapid turbine speed changes.

E. Operational Model. Fabricate a test bed model to further verify operational characteristics.

F. Transistor Switching Elements. Examine the increase in electrical machine utilization gained by transistor switching elements which allow operation at unity power factor without the danger of commutation failure that exists when SCRs are used.

G. Dual Function of PM1. Examine the feasibility of designing PM1 large enough to also serve as either a pilot exciter or primary exciter for the 400 Hz alternator.

REFERENCES

1. E. Ohno, T. Kishimoto, and M. Akamatsu, "The Thyristor Commutatorless Motor," IEEE Trans. Mag., vol. MAG-3, Sept. 1967, pp. 236 -240.

2. T. Tsachiya, "Basic Characteristics of Cycloconverter-Type Commutatorless Motors," IEEE Trans. IGA, Vol. IGA-7, No. 4, July-Aug. 1970, pp. 349 - 356.

3. N. Sato and V.V. Semenos, "Adjustable Speed Drive with a Brushless DC Motor," IEEE Trans IGA, Vol. IGA-7, No. 4, July - Aug. 1971, pp. 539 - 543.

4. E.P. Cornell and D.W. Novotny, "Commutation by Armature Induced Voltage in Self-Controlled Synchronous Machines," IEEE Trans. PAS, Vol. PAS-93, 1974, pp. 760 - 766.

5. N. Sato, "A Brushless DC Motor with Armature Induced Voltage Commutation," IEEE Trans. PAS, Vol. PAS-91, July - Aug. 1972, pp. 1485 - 1492.

6. J.M.D. Murphy, Thyristor Control of AC Motors, (Pergamon Press, Oxford, 1973), pp. 140 - 149.

7. F.J. Bourbeau, "Synchronous Motor Railcar Propulsion," IEEE Trans. IAS, Vol. IA-13 No. 1, Jan -Feb. 1977, pp. 8 - 17.

8. T. Maeno and M. Kobata, "AC Commutatorless and Brushless Motor," IEEE Trans. PAS, Vol. PAS-91, July - Aug. 1972, pp. 1476 - 1484.

9. Y. Shrinryo, I. Hosono, and K. Syoji, "Commutatorless DC Drive for Steel Rolling Mill", IEEE-IGA Conference Record, 1977 Annual Meeting, pp. 263 - 271.

10. A.C. Williamson, N.A.H. Issa, and A.R.A.M. Makky, "Variable-Speed Inverter-Fed Synchronous Motor Employing Natural Commutation," Proc. IEE, Vol. 125, No. 2, Feb. 1978, pp. 118 - 120.

11. N.A. Demerdash, T.W. Nehl, and E. Maslowski, "Dynamic Modeling of Brushless DC Motors in Electric Propulsion and Electromechanical Actuation by Digital Techniques," IEEE-IAS Conference Record, 1980 Annual Meeting, Sept. 28 - Oct. 3. 1980, pp. 570 - 579.

1982 USAF - SCEEE SUMMER FACULTY RESEARCH PROGRAM

Sponsored by the

AIR FORCE OFFICE OF SCIENTIFIC RESEARCH

Conducted by the

SOUTHEASTERN CENTER FOR ELECTRICAL ENGINEERING EDUCATION

FINAL REPORT

PHOTOIONIZATION OF IODINE MOLECULES AND CLUSTERS IN A SUPERSONIC MOLECULAR BEAM

Prepared by:	Dr. Edward A. Walters and J. Kent Newman
Academic Rank:	Associate Professor
Department and University	Department of Chemistry University of New Mexico
Research Location:	Air Force Weapons Laboratory, ARAP, Kirtland AFB, NM 87115
UASF Research	Capt. David Ellis
Date:	September 10, 1982
Contract No.	F49620-80-C-0035

ACKNOWLEDGEMENT

The authors are pleased to extend their thanks to the Air Force Systems Command, the Air Force Office of Scientific Research and the Southeastern Center for Electrical Engineering Research for providing them with the opportunity to spend 10 weeks this summer closely affiliated with the personnel and programs of the Air Force Weapons Laboratory, Kirtland AFB, NM. We are particularly grateful to the personnel in ARAP branch for their assistance and interest in this project. We especially wish to recognize Lt. Col. William E. McDermott for interesting and fruitful discussions leading to the identification and Captain David E. Ellis for continued and faithful support during this effort. We also acknowledge helpful discussions with Dr. R. Shea and assistance in locating a variety of pieces of equipment and hardware from Mr. R. Rathge.

PHOTOIONIZATION OF IODINE MOLECULES AND CLUSTERS IN A SUPERSONIC MOLECULAR BEAM

by

Edward A. Walters

and

J. Kent Newman

ABSTRACT

In preparation for a study of the photoionization of I_2, I_3, I_4, etc. a photoionization mass spectrometer employing a supersonic molecular beam emerging from a small nozzle was relocated from Los Alamos National Laboratory. Much of the effort described here has to do with moving and critical alignment of the mass spectrometer. Also described are the results of a literature survey of the photoionization and photoelectron spectroscopy literature on the important iodine molecules and clusters. Design of a nozzle for the generation of I_3 is discussed. Work done in interfacing a PDP 11/23 computer to the mass spectrometer and initial results of software development for controlling the experiments are described.

I. INTRODUCTION

The iodine laser depends upon the production of electronically excited iodine atoms. Any channel for chemical reaction or energy transfer for which the velocity exceeds the stimulation of emitted radiation will reduce the laser efficiency. It is possible that the reaction

$$I + I_2 \dashrightarrow I_3$$

is such a chemical reaction since I_3 has been calculated to be bound. If I_3 survives for more than even a few collisions, the laser efficiency will be affected. Thus, it is important to know and understand the properties of I_3. We report here the initial efforts in the direction of preparing and studying I_3 by photoionization mass spectrometry.

II. THE IODINE LASER

The means of generating excited iodine, I*, is a crucial step. There are two methods that have been examined rather extensively: flash photolysis of organic iodides (RI), and energy transfer from singlet oxygen ($O_2^1\Delta$). Both of these methods will be discussed briefly.

A. Flash Photolysis.

The iodine photochemical laser operates by flashlamp photolysis of an organic compound to produce iodine atoms in the upper state of the ground state multiplet, $I(5^2P_{1/2})$. The effective iodide has been perfluoroisopropyl iodide, i-C_3F_7I, though others may be used. A flashlamp emitting light in the range of 35,000 to 45,000 cm^{-1} excites i-C_3F_7I to a dissociative upper level which leads almost exclusively to $I(5^2P_{1/2})$.

$$i\text{-}C_3F_7I + h\nu \rightarrow i\text{-}C_3F_7 + I^*$$

The net result is the conversion of the absorbed uv photon with an energy of ~4.5 eV into an ir photon at an energy of ~1 eV in the process

$$I(5^2P_{1/2}) \rightarrow I(5^2P_{3/2}) + h\nu(\lambda = 1.351\ \mu m)$$

The ground state iodine, $I(5^2P_{3/2})$, recombines very efficiently with $i\text{-}C_3F_7$ to regenerate the parent compound (1).

$$i\text{-}C_3F_7 + I(5^2P_{3/2}) \rightarrow i\text{-}C_3F_7I.$$

There are a large number of secondary processes which affect the concentrations of atomic iodine and the radical C_3F_7. These include collisional deactivation of I*, radical recombinations of R•+R and R•+RI, radical-molecule reactions such as R•+RI and R•+I_2, and the three-body recombinations I*+I+M and I*+I+RI. Although many of the rate coefficients for these reactions are not known for R = C_3F_7, there are enough rate coefficients available for the closely related compound with R = CF_3 to permit reliable kinetic modeling. From a computed time development of concentrations based on these rate coefficients it has been shown that under typical operating conditions collisional deactivation of I* is not expected at times less than 10 μs.

Although the method of generating I* is different for the chemical iodine laser, the photophysics is nearly the same. Hence it is instructive to consider the levels involved in the laser in more detail.

The laser transition from $I(5^2P_{1/2})$ to $I(5^2P_{3/2})$ is a magnetic dipole transition for which the radiative lifetime is ~130 ms. For ^{127}I the degeneracy of both the upper and lower levels is removed by the magnetic dipole and the electric quadrupole moments of the nucleus which has a nuclear spin of 5/2. Consider first the upper level; the angular momentum can be parallel or opposed to the nuclear spin so the total angular momentum will be $F = 5/2 + 1/2 = 3$ or $F = 5/2 - 1/2 = 2$. For the lower level however there are four hyperfine states: $F = 5/2 + 3/2 = 4$, $F = 5/2 + 1/2 = 3$, $F = 5/2 - 1/2 = 2$, $F = 5/2 - 3/2 = 1$. The selection rule governing allowed transitions between these levels is $\Delta F = F_u - F_\ell = 0, \pm 1$. There are consequently six transitions allowed: $F_u - F_\ell = F_3 \rightarrow F_3$, $F_2 \rightarrow F_2$, $F_2 \rightarrow F_1$. The splitting of the upper levels F_2 and F_3 is larger than the splitting in the lower levels, so the six transitions cluster into two sets of three closely spaced transitions. The transitions center around 7603.15 cm^{-1} with a total frequency spread of 0.7 $cm^{-1} \simeq 2 \times 10^{10} s^{-1} = 20$ GHz.

The Einstein coefficients A for stimulated emission have been reported for the six laser lines (2). These values are reproduced in Table I along with

Table I. Einstein coefficients and line center cross sections of the iodine laser lines.

$F_u \rightarrow F_\ell$	3→4	3→3	3→2	2→3	2→2	2→1
$A_{u\rightarrow\ell}, (s^{-1})$	5.0	2.1	0.6	2.4	3.0	2.3
$\sigma_{u\rightarrow\ell}(\nu_o)$, $(10^{-18} cm^2)$	6.0	2.4	0.66	2.67	3.3	2.55

the line-center cross sections, $\sigma_{u\to\ell}(\nu_0)$, for photolysis of i-C_3F_7I at 20 Torr. The net spontaneous emission rate for the process

$$I^* \longrightarrow I + h\nu$$

is given by

$$\text{rate} = A[I^*]$$

Here A is the effective Einstein A coefficient which is obtained by averaging individual A values over the initial (upper) states and summing over the final (lower) levels. The average over initial states is done by computing the degeneracies of the upper levels. Since degeneracy is 2F + 1 we get for $F_u = 3$ and $F_u = 2$ that $g_3 = 7$ and $g_2 = 5$, respectively. Thus the statistical weights are 7/12 for $F_u = 3$ and 5/12 for $F_u = 2$. These considerations give

$$A = \left(\frac{g_3}{g_2+g_3}\right)\left(A_{3\to4} + A_{3\to3} + A_{3\to2}\right)$$

$$+ \left(\frac{g_2}{g_2+g_3}\right)\left(A_{2\to3} + A_{2\to2} + A_{2\to1}\right)$$

Using the degeneracies calculated above and the $A_{u\to\ell}$ values from Table I, we get $A = 7.7\ s^{-1}$.

A parallel argument can be used to derive an expression for a net stimulated emission cross section $\sigma(\nu)$ as a function of frequency:

$$\sigma(\nu) = \left(\frac{g_3}{g_2+g_3}\right)[\sigma_{3\to4}(\nu) + \sigma_{3\to3}(\nu) + \sigma_{3\to2}(\nu)]$$

$$+ \left(\frac{g_2}{g_2+g_3}\right)[\sigma_{2\to3}(\nu) + \sigma_{2\to2}(\nu) + \sigma_{2\to1}(\nu)].$$

This is a very interesting result since the frequency dependence of $\sigma(\nu)$ and therefore the gain depends upon the extent of overlap and linewidths of the individual transitions. The linewidths can be manipulated by changing pressure and gas mixture in the laser cavity. This ability to control the frequency and intensity of stimulated emission is a remarkable and powerful feature of the iodine laser.

B. The Oxygen-Iodine Laser.

Excited iodine atoms can also be produced by energy transfer from molecular oxygen in the singlet state, $O_2(^1\Delta)$. There are two common ways of generating $O_2(^1\Delta)$. First, excited oxygen is produced in usable concentrations when a mixture of O_2 in He is passed through a microwave discharge at 2450 MHz. Alternatively, it is the product of the reaction between Cl_2 and a mixture of NaOH and H_2O_2. This later route provides a chemical pathway to pumping the iodine laser and consequently presents many attractive possibilities.

The lasers that have been constructed to date have been almost exclusively small-scale devices in which I_2 is injected into a cavity containing $O_2(^1\Delta)$. The net result of this interaction is the generation of I*, but the mechanism by which this occurs is unknown. It is generally believed that the reaction consists of at least two steps, the dissociation of I_2 by $O_2(^1\Delta)$ to give I*. This however is not at all clear. Nevertheless,

if the laser is to be scaled from a "bench-top" model to something larger, the order and mechanism of the reactions must be understood to assure proper scaling.

The first reported work on I_2 dissociation by $O_2(^1\Delta)$ was by Derwent, Kearns, and Thrush (3). In addition to the evidence of emission from atomic iodine they noticed a yellow glow which was attributed to the I_2 transition $B^3\pi_{0^+u} \rightarrow X^1\Sigma$. The mechanism they suggested to be compatible with their results was

$$O_2(^1\Sigma) + I_2(X^1\Sigma) \rightarrow O_2(^3\Sigma) + 2I$$

$$O_2(^1\Sigma) + I_2(X^1\Sigma) \rightarrow O_2(^3\Sigma) + I_2(A^3\pi_{1u})$$

$$I_2(A^3\pi_{1u}) + O_2(^1\Delta) \rightarrow O_2(^3\Sigma) + I_2(B^3\pi_{0^+u})$$

The serious flaw with this mechanism is that I* atoms are produced in the chemically pumped reaction and that under these conditions sufficient H_2O is present to quench all $O_2(^1\Sigma)$ before reaction with I_2 is possible. This was confirmed by experiments in which I* was produced in the absence of $O_3(^1\Sigma)$ (4). Thus the only other excited species, $O_2(^1\Delta)$, must be responsible for the dissociation and energetics requires at least two of these molecules. A number of possible mechanisms are currently under investigation, but they are all still quite speculative and very little information is available which even favors such a mechanism as, say, one involving vibrationally excited $O_2(^1\Delta)$ or the theoretically predicted but experimentally unknown dark state of $I_2(A'^3\pi_{2u})$.

In order to minimize the quenching effects of all the compounds found in the chemically pumped laser and thereby produce efficient cw operation of the oxygen-iodine laser, it is important to remove the products as quickly as possible from the active volume. This is accomplished by rapid mixing of the reactants $O_2(^1\Delta)$ and I_2. In order to obtain high cw power levels it is necessary that the gas flow velocities be supersonic. In the case of the HF/DF laser this is done by injecting H_2 or D_2 through nozzles into an expanding flow of F atoms in an appropriate carrier gas. Unlike the HF/DF system, for which a large amount of practical data are at hand, the problems of mixing a very massive molecule like I_2 into a relatively light gas of O_2 molecules have not been resolved. The low cross section for stimulated emission also dictates that the mole fraction of iodine be high. It is evident therefore that supersonic mixing introduces a number of other unanswered questions into the operation of the oxygen-iodine laser.

There are more questions related to the basic chemistry of the laser. For example, in a clean system of I atoms and $O_2(^1\Delta)$ molecules only the four following reactions are needed to describe the observed kinetics (5);

$$O_2(^1\Delta) + I \quad <==> \quad O_2(^3\Sigma) + I^*$$

$$I^* + O_2(^1\Delta) \dashrightarrow I + O_2(^1\Sigma)$$

$$I^* + O_2(^3\Sigma) \dashrightarrow I + O_2(^3\Sigma)$$

$$O_2(^1\Delta) + O_2(^1\Delta) \dashrightarrow O_2(^3\Sigma) + O_2(^1\Sigma)$$

Although there does exist data on all of these reactions, it is relatively

incomplete and, in fact, there is considerable uncertainty about the $I^* + O_2(^3\Sigma)$ reaction.

In a real system there will be contaminants in the flow, principally H_2O and Cl_2; rates of reactions of these species with I^* and $O_2(^1\Delta)$ are not well known .

Iodine recombination rates are also critical (5). The reaction rates are known for the three-body process

$$I + I + I_2 \rightarrow 2I_2$$

at room temperature to 1000°K and atmospheric pressure. Extrapolation to temperatures of 100-200 K, as encountered in supersonic nozzle expansions, is very uncertain except for the knowledge that the three-body rate increases as the temperature decreases.

Finally, cluster formation is a well-known phenomenon in supersonic nozzle expansions. The possibility of the formation of small metastable clusters in reactions like

$$I + I_2 \rightarrow I_3$$

need to be explored. It has been predicted that I_3 is bound (6); if so, the reaction resulting in its formation will be a channel for depletion of the I atoms needed for producing high energy laser emission. This is but one of several broader questions related to cluster formation and nucleation phenomena in a supersonic oxygen-iodine laser (7).

a) How readily does nucleation occur?

b) What is the time scale for nucleation and what implications does this have for the O_2I^* laser?

c) Will wall or nozzle conditions influence nucleation?

D. Purpose of this Work.

In light of the preceding discussion, it was agreed that a better understanding of I_3 is important. This species has not been observed experimentally, so a somewhat exotic approach is needed. We decided to try to generate I_3 in a supersonic nozzle source and to study it by photoionization mass spectrometry. A photoionization mass spectrometer with a supersonic nozzle was available for loan from Los Alamos National Laboratory, so the goal of this effort was (a) to move the apparatus from Los Alamos National Laboratory, (b) to design nozzles for the generation of I_2 and I_3, and (c) to automate the data collection and reduction steps by interfacing the apparatus with a PDP 11/23 computer. We report the results of the effort.

III. I_2 PHOTOIONIZATION

The absorption spectrum of the iodine molecule has been studied extensively over a period of many years. The great majority of this work has concentrated on tne region above 1700 Å and surprisingly little has been done in the vacuum-UV region below this value. There are several reasons for this. First, autoionization features are dominant from threshold into the far UV thereby making identification of vibrational progressions and ionization to excited states difficult. In addition, the close spacing of the vibrational levels of I_2, 214 cm^{-1}, means that at 300 K there is considerable population of the v=2 and v=3 levels, so hot bands obscure the ionization threshold and other vibrational sequences. The ionization potential has been

determined by vuv spectroscopy (8), electron impact ionization (9), photoelectron spectroscopy (10-12), photoionization without mass selection (13-15) and photoionization with mass analysis (15,16). Photoion yield curves for the region of 1050 to 1410 Å (13,16) have been published. In the first instance (13) only total ion current was measured, so the rather prominent structures at lower energy than the spectroscopic ionization potential of 9.400 eV (8) were attributed to the ion-pair formation

$$I_2 + h\nu \longrightarrow I_2^* \longrightarrow I^+ + I^-.$$

The threshold for this process was measured as 8.84 eV. This corresponds well with the earlier results of Morrison et al. (15) and Watanabe (17) who give 8.85 ± 0.1 eV and 8.93 ± 9.02 eV, respectively, as the onsets for ion-pair production. Ionization potentials for I_2 have been established from these reports as being close to 9.38 eV.

The photoion yield curves are characterized by extensive autoionization features which largely obscure ionization to the higher electronic states of I_2^+ that have been identified by PES. In addition, spin-orbit splittings and vibrational transitions cannot be clearly identified. Because of the relatively low vapor pressure of I_2 (0.35 Torr at 300 K), no effort was made to examine the photoion yield curve close to threshold as a function of temperature for the purpose of clarifying which of the observed peaks are due to hot bands.

On the basis of our experience with supersonic nozzles, however, it is reasonable to expect the cooling of the gases during expansion to be sufficient to reduce or even eliminate the problem of hot bands (18-20). With the resolution of our apparatus, 0.006 meV for monomers, and the spectral

range accessible, 960-1250 Å, a detailed exploration of the photoion yield behavior of I_2 is worthwhile. The autoionization behavior should be resolvable into Rydberg series that can be identified through convergence to the second and higher ionization limits. The photoion yield curve for the ion pair production partner I^+ should also provide very interesting results for detailed analysis. These thoughts are the incentive for some of the photoionization studies we have initiated this summer. A thorough survey of the literature revealed nothing pertaining to the cluster species $I \cdot I_2 = I_3$. Consequently, any information that can be supplied from photoionization will be a useful contribution.

IV. APPARATUS RELOCATION AND RECONSTRUCTION

The primary objective of the summer work was to relocate a molecular beam photoionization mass spectrometer from Los Alamos National Laboratory to a permanent location at the University of New Mexico. In preparation for the move, a large number of detailed photographs of the assemoled apparatus were taken to assure ease of reassembly and relocation of wiring, flanges, fittings, forepumps, diffusion pumps, etc. These were printed as 8" x 10" glossies which have subsequently been used extensively. Figures 1-3 are photographs of the assembled apparatus at LANL. Disconnection of the electrical components and labeling of the wires were completed in early June. At this time all parts of the apparatus were checked for possible radioactive contamination by H Division personnel. Direct counting was done where possible, smears were taken of less accessible portions, and water lines were flushed with dilute acids which were then monitored. No evidence of any residual radioactive material was found. Next, the mass spectrometer was carefully disassembled and all critical parts -- nozzle source, ionizer, grating, channeltron -- were

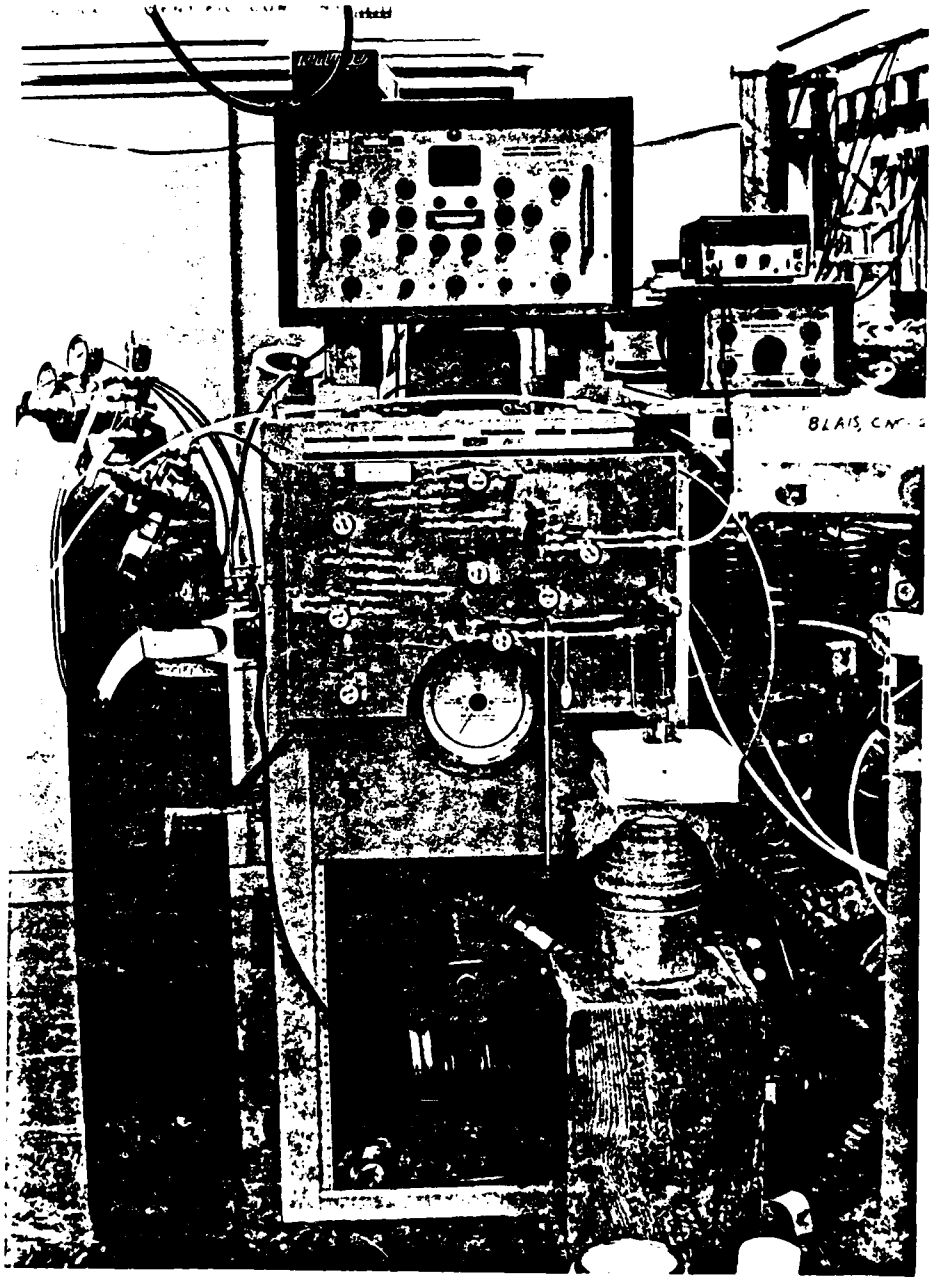

Figure 1. Gas inlet manifold and [illegible] on photoionization mass spectrometer.

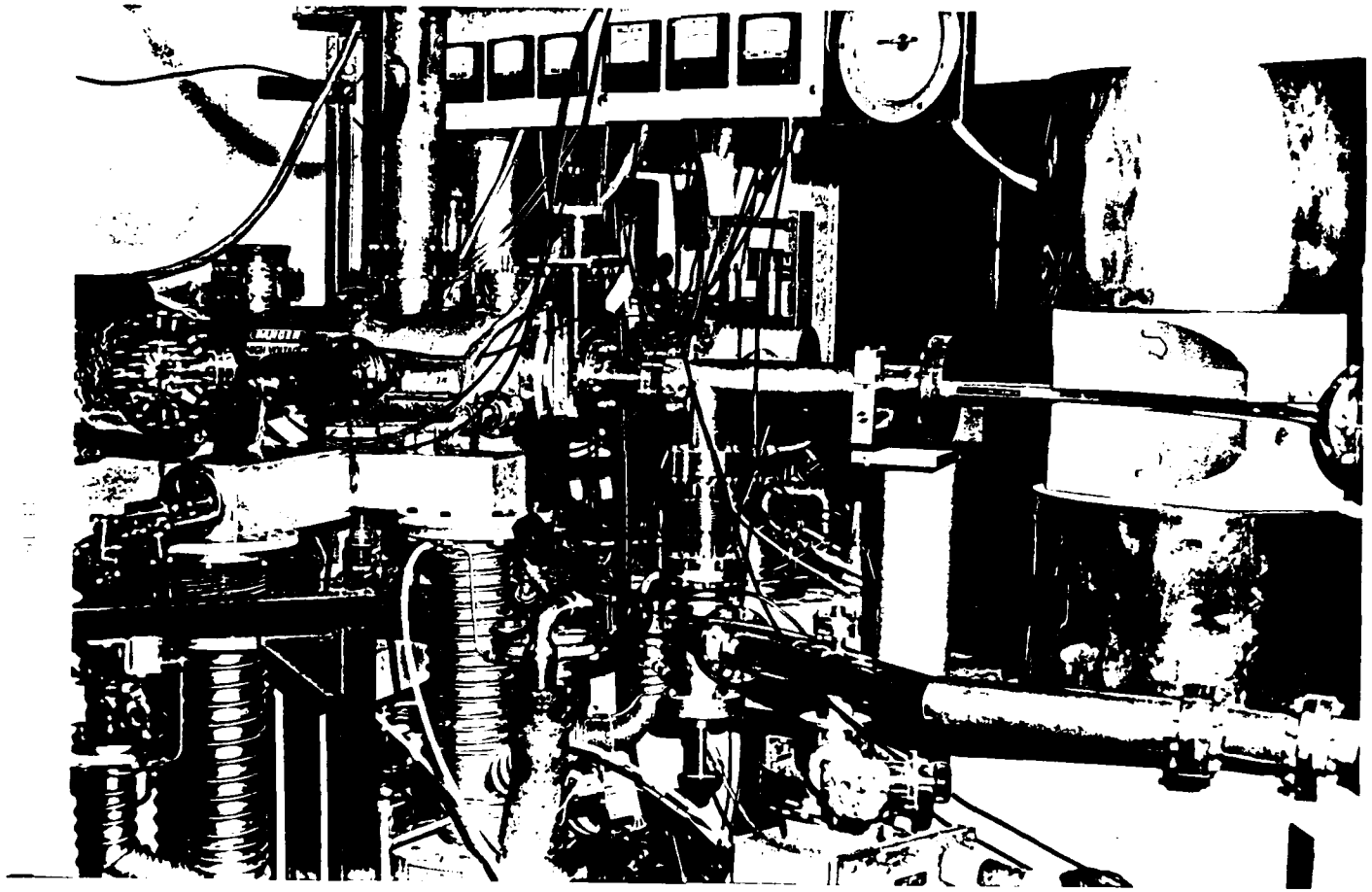

Figure 2. Source region of the photoionization mass spectrometer. The electromagnet is on the right hand side of the photograph.

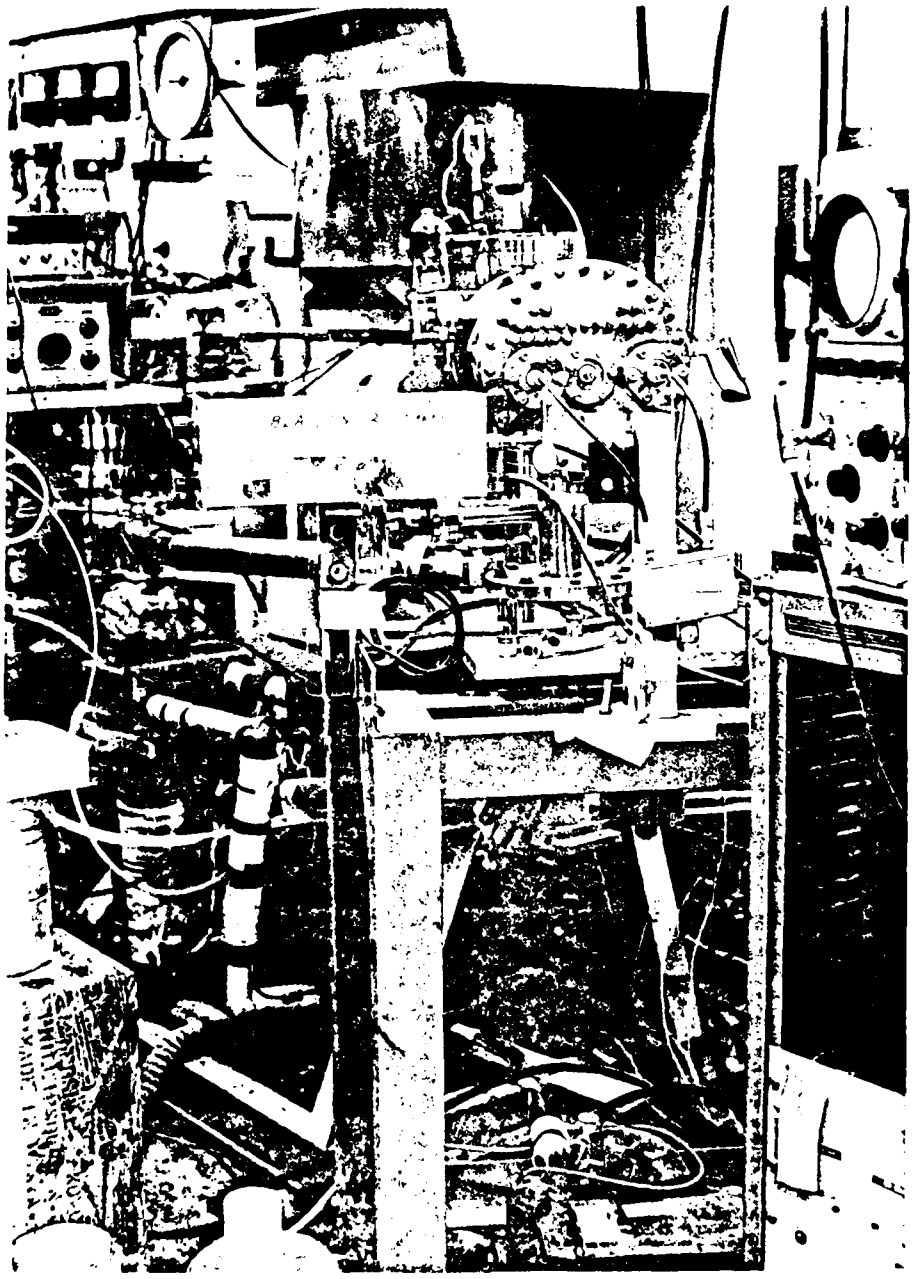

Figure 3. The detector and [illegible] of the [illegible] mass spectrometer.

packed with extreme care. This was then moved to UNM by U-Haul truck. This was accomplished by early July.

The heart of the apparatus is the electromagnet which weighs about 6,000 lbs. Special provisions and coordination of effort was required for moving the magnet. For removing the magnet and stand from the CMR Building at LANL, Zia Corporation provided a crew of riggers; they placed the magnet on a truck from UNM which was used to transport it to Albuquerque. The UNM Physical Plant service lifted the magnet from the truck and set it on the ground next to the Chemistry Building. The magnet is too heavy for the freight elevator in the building so Crane Services, Inc. was hired to move the magnet into the lab and mount it on the stand. Because of the awkward location of the balance point on the magnet, it was necessary to fix a set of I-beams to the top of the magnet for lowering it into a doorway with direct access to the basement. Once in the lab another arrangement of I-beams was needed to lift the magnet into position so the stand could be moved under it. This was accomplished by using a set of short (8") hydraulic jacks mounted on cribbing of large timbers. This last stage of getting the magnet into the building and mounted properly took about 1 week of full-time effort.

While this was being done the source chamber was reassembled, leak-checked, and pumped down. With very little effort besides closing all the flanges, the source chamber was pumped down to a pressure of 5×10^{-7} Torr. This assures us that the apparatus is tight enough to begin experiments, that is, it suffered no major damage in the move. A beam of He atoms was run through the nozzle and routine checks were performed on the beam flag, ion gauges, power supplies, etc. which showed that all are in working order.

We also performed some checks with the monochromator. Since the monochromator as originally designed does not fit into the available space around the ion source compartment, it was necessary to reverse the entrance and exit arms. This means that the grating must be turned so the blazed grooves point in the correct direction. It also means however that to scan into the +1 order, the scan must be in the opposite direction from the zero-order reflection than the readout drive on the monochromator. Some simple experiments confirmed this expectation. Slight modification of the monochromator will be required when it is being mounted to assure maximum recovery of light from the H_2 discharge lamp.

Magnet Alignment Considerations. The first, and extremely critical, job is proper alignment of the source and detector chambers. This is essential if adequate resolution is to be achieved. The resolution R is given by

$$R = \frac{r}{2(s_1 + \psi(r))}$$

where r is the radius of curvature of the magnet (17.750") in this case) and s_1 is the source exit slit width. $\psi(r)$ is the error term which can be 0.004", expressed as

$$\psi(r) = r\alpha^2 + E$$

where α is the half angle of the lateral divergence out of the source slit. In this apparatus α is determined by the quadrupole focusing lens system and is 0.015 radians. E is the sum total of errors which arise from misorientation of the magnet, anomalies in the magnet field, etc. For our

apparatus r_α^2, = 0.004", so that if a resolution R = 1000 is desired, E cannot exceed 0.0018". We are confident that this maximum value for E has been achieved with this mass spectrometer since the mass spectrometer equation

$$m/e = \frac{B^2 r^2}{2V}$$

has been previously satisfied. In this equation m is the mass of the particle, e is the electrical charge, B is the magnetic field strength, V is the accelerating potential, and r is the particle orbit radius. Figure 4 shows the relationships of the slits and the magnet with respect to one another. The desired resolution (R = 1000) will be obtained when the following conditions are satisfied:

a) The distance between the slits if 71.000±0.005".

b) $X_1 = X_2 \pm 0.005$".

c) The ions enter the magnetic field at an angle of 90° ±0.001 rad.

d) The mass spectrometer equation is satisfied.

The cross-hatched area in Figure 4 indicates the location of the virtual magnet. By rule-of-thumb, the outer edge of the fringing field is one pole gap away from the side of the magnet. The pole gap in our magnet is 7/8". Although the radius of curvature of the real magnet is 16", when the fringing field is taken into account the radius of curvature of the virtual magnet is r = 17.750". The geometry of the system then requires that $X_1 = X_2 = r\sqrt{3}$ + 0.875" = 31.618". This condition must be met in the first-order alignment, second-order alignment will later be done by moving the magnet just enough so that mass spectrometer equation is satisfied.

Alignment Procedure. In order to accomplish the alignment several special pieces of equipment were made. These were:

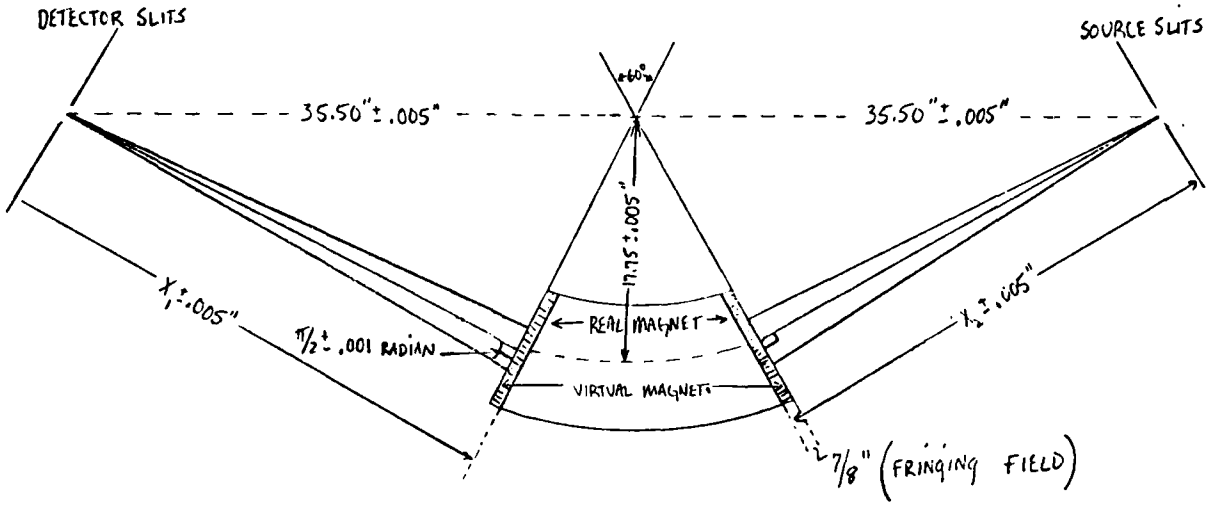

Figure 4. A schematic diagram at the magnet and the required orientations with respect to the source and detector slits.

a) An aluminum bar whose total length is 71.000±0.010". The center is clearly marked and the ends are oriented at an angle so the tips fit into the slits of the source and detector.

b) Two pieces of aluminum angle were fit with threaded rods to hold them against the sides of the magnet. The center of curvature of the virtual magnet was precisely located near the intersection of these bars.

c) A block of aluminum was machined to fit between the pole faces of the magnet. A long rod was calibrated so the distance between the magnet sides and the slits could be determined to ±0.005".

d) A second aluminum block was manufactured to fit between the magnet pole faces. This one was cut so the side facing the slit is perpendicular to the lower magnet pole face to ±0.001 rad. A first surface mirror was attached to this face.

e) A surveyor's transit.

These tools were then used to complete the alignment. First, the center of curvature of the virtual magnet was located near the intersection of the two aluminum angles mounted on the magnet sides. Second, the long aluminum bar was centered over this point so that it was perpendicular to the symmetry axis of the magnet. The source and detector chambers were then moved until the tips of the bar touched the slits. Third, the distances from the magnet sides to the slits were measured and the chambers were adjusted to get these distances (X_1 and X_2) nearly identical. Fourth, the block with a mirror was placed between the poles faces of the magnet and viewed through the slits at both the source and detector ends with the surveyor's transit. These units were then oriented carefully and cautiously until they were symmetrically disposed about the line of sight through the telescope and the reflection of the slit was also symmetric about the line of sight. These steps were

repeated in this sequence until self-consistency of all the measurements was obtained. In the final configuration $X_1 = X_2 = 31.581 \pm 0.005$".

Reassembly. After the first-order alignment was obtained, the channeltron was fit into the detector chamber and entrance and exit slits were set at 0.004". The vacuum system of the analyzer was assembled and leak checking commenced. It appears that everything is in reasonably good order and that only a few O-rings and new pump oil will be needed before the desired pressure of $\sim 1 \times 10^{-7}$ Torr will be achieved.

V. I_3 NOZZLE DESIGN

The production of the possible intermediate I_3 is of critical importance to this experiment. The goal is to be able to generate a sufficient amount of I_3 in a supersonic molecular beam to be able to study it by photoionization. The most convenient way to do this would be to generate the I_3 in the nozzle itself, so the first attempt at constructing an I_3 nozzle is based on mixing I_2 and I immediately prior to expansion through the nozzle. The nozzle designed is being constructed according to the drawing given in Figure 5. It consists of a pair of concentric nozzles; I_2 will pass through the inner nozzle into a buffer region between the nozzles where the process $I + I \dashrightarrow I_3$ can occur. The I_2 will be mixed with a carrier gas, probably helium or argon, and the entire nozzle and inlet system can be heated.

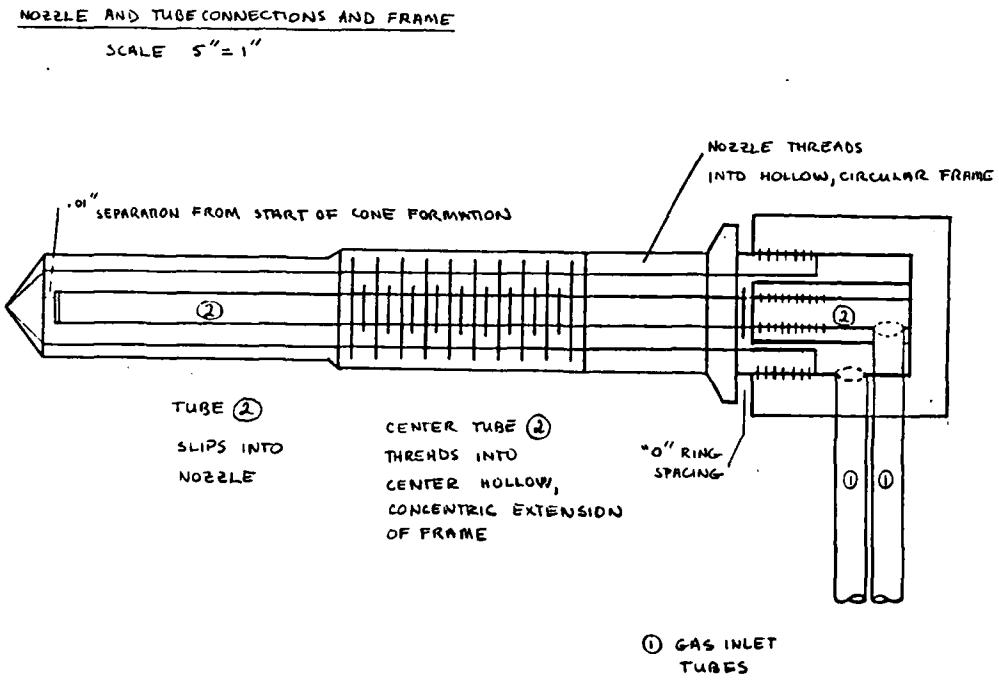

Figure 5. Schematic drawing of the nozzle for I_3 generation.

The outer portion is where I atoms are transported to the interaction region. The plan is to prepare I by the reaction

$$I_2 + O_2\ (^1\Delta) \rightarrow 2I + O_2(^3\Sigma)$$

Singlet oxygen $O_2(^1\Delta)$ will be prepared by a microwave discharge through a flowing stream of O_2 in He. This will intersect the I_2 in an interaction region immediately prior to expansion. This nozzle design can be employed in a variety of ways to dissociate iodine. Much work will be required to characterize the nozzle and to establish optimum operating conditions. A preferred characterization technique is laser induced fluorescence.

If a satisfactory I atom concentration cannot be achieved by this approach, it may be necessary to revert to the standard nozzle design and to generate I atoms from photodissociation of I_2 or $(I_2)_2$. This possibility is suggested by the work of Valentini and Cross (21) who have reported substantial cage effects in I_2 Ar clusters when photodissociated at 488 nm with a cw argon ion laser.

VI. COMPUTER INTERFACING

The photoionization mass spectrometer was operating at Los Alamos National Laboratory required manual data collection and wavelength positioning in addition to manual data manipulation to correct for background, pressure drift, magnet drift, and normalization of day-to-day data. All of this is rather tedious and inefficient when the instrument is fully operational since the data reduction may require considerably more time than the data collection and the possibility of error from manual treatment of the data increases substantially. Consequently, we have proceeded with efforts to interface the equipment to a computer which will be used to do much of the routine work.

To this end we have acquired a PDP-11/23 computer with 32 K of memory. It uses the RT 11 operating system for data acquisition. The mass storage medium is a TU-58 cassette tape system. We expect to have access to either an RX01 or RX02 disc drive in the near future to use for software development, but these have not been available to us yet.

We have developed a parallel digital I/O to the photon counting system. This channel reads the total number of counts collected on a PAR Model 1112 digital synchronous computer in a preset period of time and resets the time to zero and initiates counting. This much of the code is currently working. We plan to include an option in which it is possible to choose between a predetermined counting time; a total number of counts such that the counting errors reach some selected percentage error given by $1/\sqrt{N}$, where N is the number of pulses collected; or the choice between $1/\sqrt{N}$ and some maximum count time if N is small. To write the software for these options, it is most useful to be able to connect the computer directly to the apparatus. We expect to be able to do this very shortly -- we need only to find all the leaks in the analyzer section of the machine and then we can apply power to the detector and receive counts.

The computer has eight double-ended A to D channels which can be used for data collection. For example, it is important to monitor the intensity of light from the H_2 source as measured by the photomultiplier tube. The ideal situation is to, in fact, integrate the light over the counting period so that the number of ions produced per photon intersecting the molecular beam can be determined. This can be done easily with the computer. Also, it will be useful to monitor the various pressure gauges to be able to normalize the count rate to some pressure. This is important since the concentration of clusters in the beam is related to pressure by a function like $p_2 = p_T^n$ where n is some number greater than unity, p_T is the total pressure and p_2 is the partial pressure of dimers.

The computer system supports D-to-A channels which can be used to drive a stepping motor which will be attached to the monochromator drive system. This will allow us to advance the monochromator automatically by punching the desired wavelength increment into the computer console. This capability will also be used to display the final adjusted results on an XY plotter.

In preparation for writing our own software we have reviewed the code used on the photoionization apparatus at the National Synchrotron Light Source at Brookhaven National Laboratory, which was graciously loaned to us by J. R. Grover (22).

VII. RECOMMENDATIONS

It is quite evident that many uncertainties exist with respect to the operation of the oxygen-iodine laser. A large number of these questions pertain to the basic science of the reaction mechanism while a collection of others are related to the operation of the device itself. We have chosen to address some of the questions about nucleation or condensation phenomena in the oxygen-iodine laser. The experiments initiated are difficult because the species we wish to investigate, most notably I_3 and I_4, are short lived and transient. We have made considerable progress in constructing an apparatus which can supply information about these species. however in the 10 week period of this project we were not able to actually come up with answers. In view of the potential importance of these answers to the supersonic oxygen- iodine laser, we recommend that the photoionization and I_3 nozzle work be pursued. The limited experiments done on the photoionization of I_2 point to the need to clarify these results, particularly in supersonic beams. Clusters can be identified and examined by electron impact ionization is a rather crude way, and in much more detail with photoionization. Particular emphasis should be placed on obtaining thermodynamic parameters for the clusters and cluster ions. Development of an I_3 nozzle should be pursued.

REFERENCES

1. A. Ben-Shaul, Y. Haas, K. L. Kompa and R. D. Levine, "Lasers and Chemical Change", (Springer-Verlag, Berlin) 1981, 305-314.
2. K. Hohla and K. L. Kompa in "Handbook of Chemical Lasers", R.W.F. Gross and J. F. Bott (eds.) Wiley, New York) 1976, 667.
3. R. G. Derwent, D. R. Kearns and B. A. Thrush, Chem. Phys. Lett. 6, 115 (1970).
4. P. D. Whitefield and S. J. Davis, Laser Digest, AFWL-TR-80-4, 175 (1980).
5. R. F. Shea, personal communication.
6. H. Michaels, personal communication.
7. Lt. Col. W. McDermott, personal communication.
8. P. Venkateswarlu, Can. J. Phys. 48, 1055 (1970).
9. D. C. Frost and C. A. McDowell, Can. J. Chem. 38, 407 (1960).
10. D. C. Frost, C. A. McDowell and D. A. Vroom, J. Chem. Phys. 46, 4255 (1967).
11. A. B. Cornford, D. C. Frost, C. A. McDowell, J. L. Ragle and I. A. Stenhouse, J. Chem. Phys. 54, 2651 (1971).
12. S. Evans and A. F. Orchard, Inorg. Chem. Acta 5, 81 (1971).
13. K. Watanabe, T. Nakayama and J. Mottl, J. Quant. Spectrosc. Radiat. Transfer 2, 369 (1962).
14. J. A. Mayer and J.A.R. Samson, J. Chem. Phys. 52, 716 (1970).
15. J. D. Morrison, H. Hurzeler, M. G. Inghram and H. E. Stanton, J. Chem. Phys. 33, 821 (1960).
16. V. H. Dibeler, J. A. Walker, K. E. McCulloh and H. M. Rosenstock, Int. J. Mass Spectrom. Ion Phys. 7, 209 (1971).
17. K. Watanabe, J. Chem. Phys. 26, 542 (1957).

18. W. M. Trott, N. C. Blais and E. A. Walters, J. Chem. Phys. 69, 3150 (1978).

19. W. M. Trott, N. C. Blais and E. A. Walters, J. Chem. Phys. 71, 1692 (1979).

20. E. A. Walters and N. C. Blais, J. Chem. Phys. 75, 4208 (1981)

21. J. J. Valentini and J. B. Cross, J. Chem. Phys. 77, 572 (1982).

22. J. R. Grover, personal communication.

1982 USAF-SCEEE GRADUATE STUDENT SUMMER SUPPORT PROGRAM

Sponsored by the

AIR FORCE OFFICE OF SCIENTIFIC RESEARCH

Conducted by the

SOUTHEASTERN CENTER FOR ELECTRICAL ENGINEERING EDUCATION

FINAL REPORT

SIMPLIFIED USERS GUIDE FOR THE ICSSM COMMUNICATIONS SIMULATION PACKAGE

Prepared by:	Craig A. Paul
Academic Department:	Electrical Engineering
University:	University of Kansas
Research Location:	Rome Air Developement Center, Digital Communications Telecommunications Facility
USAF Research Contact:	Mr. Peter K. Leong
SFRP Supervising Faculty Member:	Dr. Kumaraswamy "Sam" Shanmugan Professor

Date:	July 6, 1982
Contract No.:	F49620-82-C-0035

ACKNOWLEDGMENTS

I wish to thank my RADC sponsor, Dr. Peter K. Leong, for his support in dealing with the computation personnel, and his general good nature and wonderful hospitality. Words cannot express my gratitude to Professor Shanmugan for his help in making this summer research possible; thanks alot, Sam. Others who helped smooth the way for a fast start-up on the RADC Multics system were Dave Schmitt, Dan Kupiak, and Honeywell software maintainance personel Keith Loepere, and the man with the important answers quickly amongst the software people Mr. Joseph M. Weiner.

A SIMPLIFIED USERS GUIDE FOR THE ICSSM COMMUNICATIONS PACKAGE

by

Craig A. Paul

ABSTRACT

The Interactive Communications System Simulation Model (ICSSM) was presented to RADC by Hazeltine Corporation on June 16, 1982. The accompanying users manual, while presenting some information for running the ICSSM package and programming to add simulation capabilities to ICSSM was far too detailed in some cases, lacked important information in other cases, and required too much knowledge of the internal workings of the package for the manual to make much sense to the user and potential programmer.

Hazeltine presented a half-day briefing for potential ICSSM users and left a users manual behind. After two and a half weeks of reading the users manual, some conversations with Hazeltine, and examination of the ICSSM FORTRAN coding I could implement my own ICSSM modules and explain to others via a seminar and a short users guide how to really use ICSSM to simulate communication systems

and install their own ICSSM modules into the package.

Included in this report is a half-page users guide and an ICSSM programmers guide. The programmers guide is intended as a supplement to be referred to concurrently while examining certain sections of the ICSSM users manual.

AD-A130 767 USAF/SCEEE GRADUATE STUDENT SUMMER SUPPORT PROGRAM (1982) MANAGEMENT AND..(U) SOUTHEASTERN CENTER FOR ELECTRICAL ENGINEERING EDUCATION INC S..

UNCLASSIFIED W D PEELE ET AL. OCT 82 AFOSR-TR-83-0611 F/G 5/9 NL

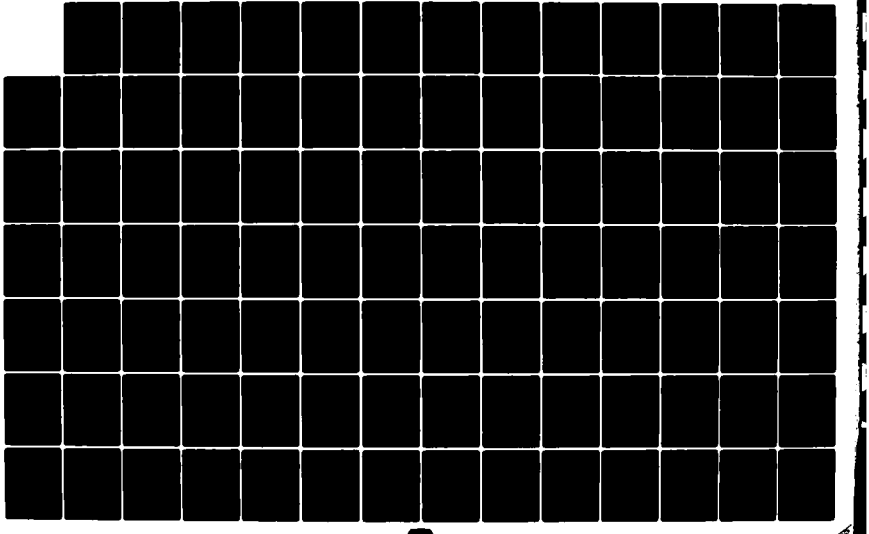

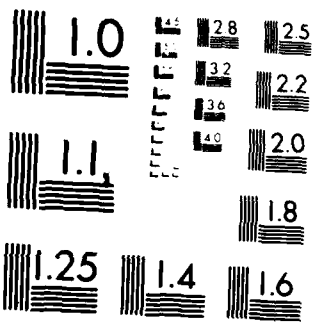

I. INTRODUCTION: At the University of Kansas I have been engaged for the last eighteen months implimenting a digital communications system simulation package authored by Hughes Aircraft Space Communicatiions Division called SYSTID. The FORTRAN code for SYSTID included a source language compiler, FORTRAN communication component models, and post-processor routines. Having converted SYSTID from a PRIME machine to a Harris machine at Kansas University and with ten years of experience with Operating Systems Design and Implimentation I was selected to help RADC understand and use ICSSM.

II. OBJECTIVES OF THE RESEARCH EFFORT: Our research goals were to impliment our own modules into ICSSM to see how difficult that task would be, condense and supplement information in the ICSSM users guide for users and programmers here at RADC, and to advise RADC as to what additional modeling elements they would need to make ICSSM a flexible and easy to use package to model communications systems including anti-jamming, spread spectrum, combat RF environment simulations, and other C cubed communication systems.

III. HOW TO USE ICSSM

First get permissions to access the ICSSM directory on the MULTICS system through Peter Leong, RADC/DICEF, 4567. Next, go to a Tektronix 4014 terminal, and log in. ICSSM screen formatting was designed only for use on Tektronix equipment and can be most easily used on a 4014. After logging in and getting to the correct directory the user can run all of ICSSM by simple one line commands.

TO CONFIGURE A SYSTEM FOR MODELING PURPOSES TYPE

ec sel

AFTER CONFIGURING THE SYSTEM YOU NEED TO RUN THE PRECOMPILER, SO TYPE

ec pc

TO ACTUALLY RUN THE MODEL TYPE

ec exxer

IF YOU NEED TO POST-PROCESS ANY MODEL OUTPUT FIRST TYPE

ec run_pps

This is the post-processor selection package.

TO RUN THE SELECTED POST-PROCESSING SOFTWARE TYPE

ec run_ppe

During the system model configuration phase (ec sel) you will be prompted as to what is available to run and certain module (model) specific parameter values to set.

"Checkpoint" values are set at this time. During model execution, when checkpointed variables reach their specified values ICSSM will tell you how long the system has run, give an estimate of how much longer it will take, and occasionally give reassurances that the system is indeed running. These "reassurances" will, of course, take place during the system "exerciser" phase (ec exxer).

During the system model configurator, when you have finished specifying the system and have told ICSSM to finish, ICSSM will notify you that there is no post-processor port. Let ICSSM go ahead and put a default post-processor port in the system. This post-processor port dumps the signals from the entire simulation to a file called "exer9_dat" in ASCII floating point numbers.

ICSSM has enough memory space to run systems with 25 modules. If your system has more modules you will want to consider splitting it into two or more separate systems. Or, if you want to reduce MULTICS run times on two similar systems that only differ in the last few modules ,for example, you may want to run the system once and output data that will feed into the dissimilar sections. In these cases you will want to put an "output driver" at the end of each system that provides the common signals. Later, when you run the second segment(s) of your systems you can choose the appropriate "input driver" to recover the "output driver"'s data file so as to continue your system simulation.

IV. FOR ICSSM PROGRAMMERS

This section assumes that those of you interested in programming for ICSSM have access to parts of or the entire manual entitled "Report 6390R1, USER MANUAL FOR INTERACTIVE COMMUNICATIONS SYSTEM SIMULATION MODEL (ICSSM) EXTENSION". This section is intended as a supplement. While the ICSSM manual tells what each variable means, it does not tell you what it is used for. This section will hopefully provide that information for you.

Section A in the ICSSM manual covers programming requirements for ICSSM modules. Various labelled common areas and other FORTRAN statements are highlighted as needing to be contained in ICSSM modules. Commentary and page references are provided for elements that I think need further explanation. Refer to page A-2, Figure A-1, for the "APPLICATION MODULE DESIGN ELEMENTS" needed for different "generic types" of ICSSM modules.

(On page A-3)

```
COMMON /EXEC/ TNOW,MODUL,IPORT,NDCD,KEVNT,AUX,IOK,VNOIS
```

TNOW Given

MODUL An ICSSM assigned number uniquely identifying this module (Given)

IPORT The data streams this module is currently getting data from (initially set to 1) or putting data to (you set it) or the last data stream port that the module immediately upstream from this module just output (Given) This will be covered more during the discussion

of "KEVNT" below.

NDCD Given.

KEVNT Check this to see what the module immediately upstream is doing. See discussion below for details.

AUX This variable needs to be an integer. Otherwise, don't worry about it.

IOK Set it to 1 as the first executable statement of your module, then forget about it.

VNOIS Unimplemented.

(On page A-3)

COMMON /PARAM/ (User-settable real parameters), (hidden real parameters)

The settable parameters are those that the user should set during system configuration (ec sel). As an example, a transmitter module (called a "self-updating module" in ICSSM nomenclature) should allow the user to set the total amount of time that the transmitter will transmit signal.

Hidden parameters are those that should be saved so that their values remain valid from previous invocations of this module, for example, a sum of an input signal accumulated over many module invocations needs to be saved as a hidden parameter.

(On page A-4)

COMMON /IPARAM/ (User-settable integer parameters), (Hidden integer parameters)

This corresponds to COMMON /PARAM/ except that this area is for integers.

For further commentary about these design elements see paragraph A.2.5, pages A-4 and A-5.

NOTE: Before a module is invoked its /PARAM/ and /IPARAM/ commons are restored from large arrays in the ICSSM exerciser mainline and saved back into those large arrays after the module has finished executing. This means that each module can have its "own" /PARAM/ and /IPARAM/ areas regardless of values inserted in /PARAM/ and /IPARAM/ by any other modules.

(On page A-5)

COMMON /XBLOCK/

Any variables that you want to put here that have the meanings in /XBLOCK/ can be accessed by any other module with COMMON /XBLOCK/ in it. Any other variables that you want all modules to have access to can be put into REAL1X, REAL2X, INT1X, INT2X, INT3X as needed. A word of caution: other ICSSM modules may already use these for their own purposes. Also note that TON and TOFF are already set.

(On page A-7)

COMMON /UBLOCK/ U(4096)

This array is filled with signal by the module immediately upstream. ICSSM nomenclature for signal samples is unfortunate. Contiguous samples from a signal stream is

called a "coefficient list".

(On page A-7)

```
COMMON /EVENT/ ION,IOFF,IDEL,ICON,IUP,ISTOP,ICHK,IEND
```

IUP Used by self-updating modules to let ICSSM know to run them first during the current simulation time "chunk" TDUR. Every time an IUP is encountered by the ICSSM exerciser the screen status information will be updated.

ION Tell ICSSM that this module is ready to run only after all modules who have values IUP in KEVNT have been run. This is also used in ICSSM routine "SIGOUT" to let downstream modules know that this module has put out an output signal.

ICON This "event" can be used for feedback. A further explanation of how to accomplish feedback is presented later in this paper.

IOFF ICSSM programmers will generate this event only for feedback purposes.
An ION event, when passed through "SIGOUT", will change the downstream state to IOFF.

The remaining states should not be issued by ICSSM programmers.

(On page A-8)

```
IOK=1
```

This lets ICSSM know that a module is currently running.

(On page A-8)

IF(KEVNT.EQ.(logical expression)) or
IF(KEVNT.NE.(logical expression)

Example: For a module with one input port

IF(KEVNT.NE.ION) RETURN

This means that if there is no input signal to process don't execute the module.

The following are equivalent statements for their applications:

IF(KEVNT.EQ.ION.AND.IPORT.EQ.N) (process data)
(for an example of this see page A-19)

or

IF(KEVNT.EQ.IOFF.AND.IPORT.EQ.1) (process data)
(for an example of this see page A-42)

In the first form the module(s) immediately upstream indicate(s) that valid input signals are available at input ports up to and including port N. Since all input ports now have valid data this module's processing can proceed.

The second form is independent of the number of input ports in that the IOFF event is checked for. IOFF means that all modules immediately upstream have finished and that they have called "SIGOUT" to put signals into their

output ports. The IPORT.EQ.1 check indicates that the port number has been reset to 1; this module's COMMON /UBLOCK/ has been filled with signal for input port 1 of this module.

(On page A-9)

CALL DUPXY

This routine transfers data in COMMON /XBLOCK/ to COMMON /YBLOCK/. Before a module is invoked its COMMON /XBLOCK/ is retrieved from a disk area. Any modifications to /XBLOCK/ are then transferred to /YBLOCK/ by DUPXY. After the module has finished executing during this invocation the /YBLOCK/ area is output to a disk area. This way, a time history can be kept of these areas *(called the "signal list" in ICSSM nomenclature)*.

(On page A-9)

CALL DUPUV

This routine copies /UBLOCK/ to /VBLOCK/ and also copies their associated disk records associated with the input port (/UBLOCK/) to the output port (/VBLOCK/).

(On page A-9)

CALL FETCHX(INPORT,ISTATUS)

INPORT Data associated with this input port
is brought from disk into /UBLOCK/.
A call to FETCHX is unnecessary for
input port 1 upon initial entry into

a module.

ISTATUS ICSSM code never checks this variable.
Hazeltine programmers appear to rely
totally on KEVNT and port numbers.

(On page A-10)

CALL CKTRIG(MODUL)

This allows the ICSSM mainline to suspend execution of the model at this module and look to see whether any of the user specified variables for this module (MODUL) has reached a value indicated as a checkpoint value. If any of the variables has reached a checkpoint value data files will be written containing system state. In case the system run gets interrupted and execution is prematurely terminated the system can be restarted at the last checkpoint and proceed as if no interruption had occured.

(On page A-10)

CALL YSET(TIME,TDUR,SINGTM,MODUL,ICUMUL,NPTINV,RBASIS)

TIME Use TNOW in common /EXEC/

TDUR Amount of simulation time that this module
will be active for this invocation.
Usually TDUR is set by a self-updating
module and is made available in common /YBLOCK/
and therefore equivalently in common /XBLOCK/.
For examples see page A-18 and TDURP on page
A-26.

MODUL Provided in common /EXEC/ as discussed above.

ICUMUL Cumulative number of samples. This is updated

by YSET but should be stored as a hidden parameter in common /IPARAM/. This value is incremented by NCOF in common /XBLOCK/ usually set by a self-updating module.

NCOF Number of samples processed during the time TDUR, number of samples generated per invocation.

RBASIS Usually set to 1. This variable is put into common /XBLOCK/ variable SPACX by routine YSET.

(On page A-11)

SIGOUT(TNOW,IPORT,1,IEVNT)

TNOW Current simulation time, available from common /EXEC/.

IPORT Note: This port number takes into account also the number of input ports present for this module. Given a module with 1 input port and 1 output port the output port number to be used here would be 2. If the module has 3 input ports and 3 output ports and I wanted to output signal on the second port the SIGOUT port number would be 5.

IEVNT ION means send the ION event to all modules immediately downstream and run this module next time only after modules with IUP event codes have been run.
ICON means that this module will be let run after

all modules with IUP and ION event codes have been run. ICON is used for feedback processing. More about this later.

(On page A-11)

```
TNEXT=TNOW+TDUR    (See if this module should run again.)
IF(TNEXT.GT.TSTOP) GO TO xxx  (Wrap up processing.)
CALL SCHDL(0,TNEXT)    (Run this module again.)
       .
       .
(optional FORTRAN code)
       .
       .
xxx  (wrap up code)    (Special wrap up code may be needed
                        for the last invocation or all
                        invocations.)
```

(On page A-12)

COMMON /YBLOCK/

This common block is similar to /XBLOCK/ except that it is associated with output ports. The contents of this common are written to the signal list file, SW, by SIGOUT.

(On page A-13)

COMMON /VBLOCK/

This common block contains signal samples to be output to the coefficient work file, CW, by SIGOUT. SIGOUT needs to be called once per output port.

FEEDBACK PROCESSING

In certain applications feedback of signals is desirable. There are two easy ways to do feedback supported by ICSSM.

1) If there is enough room in common /PARAM/ you can store data there to be fed back at the next invocation of the module. *Remember, common* /PARAM/ including settable and hidden parameters can be at most 2100 real locations.

2) Compute TNEXT and use it as the first variable to SIGOUT. Use ICON as the last variable for SIGOUT. Use SIGOUT with these variables to output the data to be fed back. Call SCHDL with an IOFF event. The next time the module is invoked the proper data will be available at the feedback input port.

UPDATING THE LIBRARY

Definition: For ICSSM purposes the "library" comprises only ASCII documentation files to be used during system configuration (ec sel). The ASCII file is needed so that the user configuring a system can see values needed for user-settable parameters and explanations of what modules in the library do.

Edit file "filea_dat" so that all the number of models per chapter, the numbers appearing at the end of the chapter descriptions, are set to 0 (zero). You are now finished updating that file, close it. See page G-4 for its format. Append your module specifications to "filed_dat" in "filed_dat"'s format (see pages G-2 and

G-3). Update the first line in "filed_dat" to reflect the total number of modules in the library, now including your new modules. Close that file. When you are ready to update the library type "util". You'll get the entire library file listed to your terminal ordered by chapter. If you look at "filea_dat" after "util" is finished you will note that the chapter entry numbers have been properly updated. Ignore the "open statement" section in the "filea dat" and "filed dat" layout specifications. They are not needed.

Output files produced by "util" are "fileb_dat" and "filec_dat". In the ICSSM manual these files are referred to by the names "b_dat" and "c_dat". Next, put object code from your module and all the functions and subroutines your module calls in the ICSSM directory. This will allow all your routines to be available to ICSSM during the execution of your system during the exerciser (ec exxer).

Some final observations: While ICSSM is running the screen is filled with status information. This makes output to the screen by user modules somewhat obliterated. The best thing to do is to output to a file by using the fortran "WRITE" statement. For example, WRITE(66,...) will output to a file named "file66". No FORTRAN open statements are necessary and the file will be closed when ICSSM stops. To see your data simply "print" it to your terminal or use "dprint" to get hardcopy to the main MULTICS line-printer.

After sucessfully programming an ICSSM module you will find that programming for ICSSM is fairly easy, there is just alot of tedious insertion of design elements. Use caution, especially making sure that your entries in "filed dat" are in the correct format and have correct entries.

V. RECOMMENDATIONS: The Hazeltine ICSSM documentation should incorporate information provided in this report as users and programmers really only need part of the information presented in the ICSSM users manual to get their own models running in ICSSM and to run ICSSM itself.

Many more communications system components need to be modeled for use in ICSSM. These include generalized low-pass, band-pass, band-reject, and high-pass filters, modulation schemes, other encoding schemes, spread-spectrum schemes, and transmission media simulators.

REFERENCES

1. Saul Ginsberg, Mary Mammone, Irene Gerry, and William Griese,: Report 6390R1, USER MANUAL FOR INTERACTIVE COMMUNICATIONS SYSTEM SIMULATION MODEL (ICSSM) EXTENSION, February, 1982, Hazeltine Corporation, Greenlawn, New York.

1982 USAF-SCEEE GRADUATE STUDENT SUMMER SUPPORT PROGRAM

Sponsored by the

AIR FORCE OFFICE OF SCIENTIFIC RESEARCH

Conducted by the

SOUTHEASTERN CENTER FOR ELECTRICAL ENGINEERING EDUCATION

FINAL REPORT

A MODEL FOR PULSED LASER ANNEALING OF SILICON

Prepared by:	Gregory D. Punkar
Academic Department:	Department of Physics
University:	Kent State University
Research Location:	Air Force Wright Aeronautical Laboratories, Materials Laboratory, Electromagnetic Materials Division, Laser and Optical Materials Branch, Building 651, Wright Patterson Air Force Base, Ohio
USAF Research Contacts:	Dr. Patrick M. Hemenger, Capt. Kenneth R. Bradley
SFRP Supervising Faculty Member:	Dr. David S. Moroi, Professor
Date:	August 11, 1982
Contract No:	F49620-82-C-0035

Acknowledgements

The author would like to thank the people at the Materials Laboratory of Wright-Patterson Air Force Base, particularly those in the Laser and Optical Materials Branch, for their generous hospitality during his stay there. He would also like to thank the Air Force Office of Scientific Research and the Southeastern Center for Electrical Engineering Education for providing him with this valuable research opportunity.

Finally, special thanks go to Dr. David S. Moroi for introducing the author to this program, and for erdless support and encouragement.

A MODEL FOR PULSED LASER ANNEALING OF SILICON

by

Gregory D. Punkar

ABSTRACT

In this paper we seek a solution of the thermal diffusion equation, which describes pulsed laser annealing of silicon. This equation is a non-linear differential equation with temperature-dependent parameters; functional forms are fitted to these parameters using empirical data. For the non-homogeneous case (including the incident laser source term), the equation is solved numerically, using an adiabatic approximation to incorporate the temperature dependences of thermal and optical properties. Melt depths and evaporation losses are also tabulated numerically using energy balance equations.

An analytical method for solving the homogeneous equation is introduced, applicable for certain functional forms of temperature-dependent thermal properties. This method is not incorporated into the above-mentioned model; however, we include it as it may be useful in other contexts.

GLOSSARY OF SYMBOLS USED

Symbol	Meaning	Units	Value used
T	Temperature	see text	
t	Time	sec	
τ_p	Time of laser pulse	sec	15×10^{-9}
d_L	Diameter of laser pulse	cm	
λ	Laser wavelength	$\mu = 10^{-4}$ cm	.53, 1.06
I_o	Incident laser intensity	Watts/cm^2	
E	Laser energy density ($=I_o\tau_p$)	Joules/cm^2	1-2, steps of .25
τ	Melt time after pulse	sec	
x	Depth	cm	
x_M	Melt depth at pulse termination	cm	
Δx_M	Melt depth after pulse (additional)	cm	
x_B	Depth which reaches boiling temperature	cm	
Δx_V	Evaporation loss	cm	
K	Thermal conductivity	Watts/cm-°K	
K_S	Thermal conductivity of solid Si at room temp.	Watts/cm-°K	.25
C	Specific heat	Joules/g-°K	see text
C_L	Specific heat of liquid Si	Joules/g-°K	1.05
ρ	Density	g/cm^3	2.33
D	Thermal diffusivity $= K/c\rho$	cm^2/s	see text
D_L	Thermal diff. of liquid Si	cm^2/s	.28
R_S	Reflectivity of solid Si		.35
R_L	Reflectivity of liquid Si		.7
α	Absorption coefficient	cm^{-1}	
T_R	Room temperature	°K	298
T_M	Melting point of Si	°K	1683

GLOSSARY OF SYMBOLS USED (continued)

Symbol	Meaning	Units	Value used
T_B	Boiling point of Si	°K	2950
v	Melt front velocity	cm/sec	
L_M	Latent heat of melting	Joules/g	1800
L_V	Latent heat of vaporization	Joules/g	11000

I. INTRODUCTION:

Laser annealing of semiconductors is a process which restores the crystalline quality of the solid by repairing the damage done by ion-implantation. A field of study which is less than a decade old, laser annealing currently stimulates some of the most intense interest at the frontiers of research in materials processing. Production of high-quality semiconductors is essential to the improvement of highly technical electronics in modern aircraft.

Ion-implantation of impurities in semiconductors produces a disordered (amorphous) surface layer in the solid. This layer can be anywhere from a few hundred to a few thousand angstroms thick. Two schools of thought have dominated the study of the process by which crystallinity is restored during pulsed laser annealing. One theory states that the surface region of the semiconductor melts, after which epitaxial crystal regrowth occurs.[1] The other states that damage is repaired by the formation of an electron-hole plasma.[2] Most recent experimental evidence is in favor of the melting model;[3,4] some recent treatments of the problem have incorporated both melting and plasma effects.[5] In this project we assume that melting takes place; we thus try to predict the effects of various incident laser energies.

At the Materials Laboratory of Wright Patterson Air Force Base, experimental laser annealing research has recently been initiated using a single 15-nanosecond Nd:YAG laser pulse. The incident laser actually consists of two beams: a fundamental with wavelength 1.06μ, and simultaneously, a frequency-doubled beam at $\lambda = .53\mu$. The optical absorption coefficient of Si varies strongly with wavelength. Since it is much higher for the .53μ beam than for the 1.06μ beam,[6] we consider only the absorption of the former.

II. OBJECTIVES:

At the Materials Laboratory, total time of surface melting is measured by monitoring the reflectivity of the semiconductor surface during annealing. The time during which the reflectivity is that of liquid Si (as opposed to that of solid Si) is taken to be the total time of melting. Unfortunately, the time frame of this project (ten weeks) has not allowed us to make cogent predictions concerning the regrowth velocity (that is, the rate of recrystallization after annealing), which, of course, is crucial to a prediction of total melting time. However, we have devised a model that, in addition to predicting maximum melt depths and evaporation losses as functions of incident laser energy, has the flexibility of varying the initial substrate temperature and thickness of the surface amorphous layer. Annealing of other materials, such as GaAs and Ge, could also be investigated with this model without too much difficulty (functional forms of temperature-dependent parameters for these materials would have to be obtained). Further study of the problem could result in predictions about the rate of crystal regrowth, which would enable extensive comparison with experiment.

III. THEORETICAL BACKGROUND:

Heat transport in materials obeys the continuity equation,

$$\frac{\partial \eta}{\partial t} + \nabla \cdot \vec{J} = S(\vec{r},t) \qquad (1)$$

Here η, the volume energy density, is cT. $\vec{J}$, power per unit area, is $-k\nabla T$ (minus sign because the temperature gradient must be negative for energy to flow). S(r,t) is the source intensity which is given by

$$S(\vec{r},t) = (1-R_s)\alpha I_0 e^{-\alpha \vec{r}}$$

The criterion for treating the problem as one-dimensional[3] is that

$\sqrt{DT_p} \ll d_L$; here $\sqrt{DT_p}$ represents an approximation of a "lateral diffusion length." Since d_L is of the order of 1 centimeter for our case, T_p =15 nanoseconds, and D varies from about .8 to .1 from room temperature to melting point, the inequality is satisfied. Thus the diffusion equation reduces to

$$\frac{\partial T}{\partial t} - \frac{\partial}{\partial x} D \frac{\partial T}{\partial x} = \frac{\alpha (1-R_s)}{cp} I_0 e^{-\alpha x} \qquad (2)$$

It becomes convenient to work in a temperature scale in which the initial substrate temperature (for our case, 298 K) is the zero of temperature. Then, if we treat the material as semi-infinite, the initial and boundary conditions are:

$$T(t=0) = 0 \; ; \; T(x=\infty) = 0 \; , \; \frac{\partial T}{\partial x}(x=0) = 0 \qquad (3)$$

The problem is greatly complicated by the fact that D and α are strong functions of temperature. For the solid phase D can be fitted well[3,9] by

$$D = D_0 T^{-\varphi} \quad \begin{array}{l} D_0 = 2078.26, \; \varphi = 1.3876, \text{ for } 298\,^\circ K < T < 1200\,^\circ K \\ D_0 = 13.7037, \; \varphi = .67934, \text{ for } 1200\,^\circ K < T < 1683\,^\circ K \end{array} \qquad (4)$$

(Here T is in Kelvins).

The temperature behavior of the absorption coefficient of solid Si is not well known. It is known to be $\sim 10^4 cm^{-1}$ at room temperature[7] for $\lambda = .53\mu$. The liquid value at that wavelength is known[7] to be $\sim 10^6 cm^{-1}$. As one approximation, we treat $\log_{10}\alpha$ as being linear with T. However, recent data from Oak Ridge National Laboratories[10] indicates an exponential dependence of with T up to 1000 °K. We can extrapolate this to the melting point. Thus we investigate the effects of using two different functional dependences of the absorption coefficient:

$$\begin{array}{l} \alpha = \alpha_0 \, 10^{(2(T-T_0)/T_c)}, \; \alpha_0 = 10000, \; T_0 = 1385 \\ \alpha = \alpha_0 \exp(T/T_c), \; \alpha_0 = 5020, \; T_0 = 430 \end{array} \qquad (5)$$

where again T is in Kelvins.

Thus, equations (2)-(5) descibe the heat transport process

for pulsed laser annealing of Si with $\lambda = .53\mu$. Purely analytical attempts to solve this differential equation have not met with success; thus approximations must be made. We investigate these in a later section.

IV. AMORPHOUS LAYER:

We take the thickness of the amorphous layer to be 1000 Å. (This value can easily be changed; it is an input to the computer program). Temperature-dependent parameters for amorphous Si are not well known; however, it is believed that the thermal conductivity is lower than that of solid Si (at least at low temperatures), and that the absorption coefficient is higher. For the latter, we use eqs. (5), with $\alpha_0 = 30000$ and 2 replaced by 1.53 in the first equation; $\alpha_0 = 30465$ and $T = 601.5$ in the second. For the former, we follow the predictions of Wood[11] and set the thermal diffusivity at .1 cm^2/s. (It may be still slightly higher at low temperatures, but the high-temperature data is more important to our analysis. Test runs of the computer program have indicated that, regardless of the thickness, the amorphous layer does not make a great deal of difference concerning melting and evaporation. This is probably due to the fact that our high-temperature predictions for the diffusivity and absorption of amorphous Si do not differ greatly from those for solid Si).

V. ADIABATIC APPROXIMATION:

For constant D and α, equations (2-3) can be solved using the Green's function technique. The result[12] is

$$T(x,t) = \frac{(1-R)}{\kappa\rho} I_0 F(D,\alpha,x,t), \text{ where}$$

$$F(D,\alpha,x,t) = \frac{1}{\alpha D}\left\{-\alpha x \operatorname{erfc}\left(\frac{x}{2\sqrt{Dt}}\right) + 2\alpha\sqrt{\frac{Dt}{\pi}}\exp\left(\frac{-x^2}{4Dt}\right)\right. \quad (6)$$

$$\left. - e^{-\alpha x} + \frac{1}{2}\exp(\alpha^2 Dt)\left[e^{-\alpha x}\operatorname{erfc}\left(\alpha\sqrt{Dt} - \frac{x}{2\sqrt{Dt}}\right) + e^{\alpha x}\operatorname{erfc}\left(\alpha\sqrt{Dt} + \frac{x}{2\sqrt{Dt}}\right)\right]\right\}$$

We now incorporate the temperature dependence of D and α in the following manner[12]: the incident laser pulse is divided into many subpulses of infinitesimal time duration Δt. During each subpulse the temperature rise is assumed to be small enough that D and α can be treated as adiabatically constant. The value of D and α at the beginning of each subpulse is determined by the temperature due to incremental increases from all previous subpulses. In other words, from eq. (6), the temperature rise during the first subpulse is given by (using the Oak Ridge absorption function for the sake of illustration):

$$\Delta T_1 = \Delta t \frac{(1-R_s)}{c\rho} I_0 \left\{ \frac{\partial}{\partial t} F\left(D_0 T_R^{-\beta}, \alpha_0, x, t\right)\Big|_{\Delta t} \right\} \tag{7}$$

The temperature rise during the n subpulse is given by

$$\Delta T_n = \Delta t \frac{(1-R_s)}{c\rho} I_0 \left\{ \frac{\partial}{\partial t} F\left(D_0 \left(T_R + \sum_{s=1}^{n-1} \Delta T_s\right)^{-\beta}, \alpha_0 \exp\left(\frac{\sum_{s=1}^{n-1} \Delta T_s - T_c}{T_0}\right), x, t\right)\Big|_{n\Delta t} \right\}$$

To evaluate the temperature distribution at any time t, we sum over all the incremental rises, then take the limt as $\Delta t \to 0$:

$$T(x,t) = \frac{(1-R_s)I_0}{c\rho} \int_0^t dt' \frac{\partial}{\partial t'} F\left(D_0 T^{-\beta}, \alpha_0 e^{T/T_c}, x, t'\right) \tag{8}$$

The specific heat c is a weak function of temperature in the range of interest[9]:

$$c(T) = c_0 T^{\gamma} \tag{9}$$

where $c_0 = .27867$, $\gamma = .17734$. It can be treated, without great error, as constant; we choose, however, to incorporate its temperature dependence into the solution by the method described earlier in this section.

Since one of the boundary conditions of the problem is that T(t=0)=0 (this can be checked by evaluating F(t=0), remembering that erfc(ξ)=1-erf(ξ); erf($-\xi$)=-erf(ξ); and erf(∞)=1), equations (6), (8), and (9) lead to (again using the Oak

Ridge absorption function),

$$T(x,t)=\frac{(1-R_s)I_0\tau^{-\beta-\frac{1}{2}}}{\sqrt{\pi}\alpha_0 D_c \exp(T/T_c)}\left\{-\alpha_0\exp(T/T_c)\operatorname{erfc}\left(\frac{xT^{\beta/2}}{2\sqrt{D_c\tau}}\right)\right. \quad (10$$

$$+2\alpha_0\exp(T/T_c)\sqrt{D_c t/\pi}\;T^{-\beta/2}\exp\left(\frac{-x^2T^{\beta}}{4tD_c}\right)-\exp(-\alpha_0 x\exp(T/T_c))$$

$$+\frac{1}{2}\exp\left(\alpha_0^2 D_c\tau T^{-\beta}\exp\left(\frac{2T}{T_c}\right)\right)\left[\exp\left(-\alpha_0 x\exp(T/T_c)\right)\operatorname{erfc}\left(\alpha_0\exp(T/T_c)\sqrt{D_c\tau}\,T^{-\beta/2}\right.\right.$$

$$\left.\left.-\frac{xT^{\beta/2}}{2\sqrt{D_c\tau}}\right)+\exp\left(\alpha_0 x\exp(T/T_c)\right)\operatorname{erfc}\left(\alpha_0\exp(T/T_c)\sqrt{D_c\tau}\,T^{-\beta/2}+\frac{xT^{\beta/2}}{2\sqrt{D_c\tau}}\right)\right]\Bigg\}$$

This implicit function of T must, of course, be solved numerically. This is done for both of the aforementioned functional forms of $\alpha(T)$.

VI. MELTING DURING LASER PULSE:

By conservation of energy at the melt front, the melting velocity is determined by[7]

$$L_M v_p=(1-R_L)I_0-K_s\left|\frac{\partial T}{\partial x}\right|_{\text{melt front}} \quad (11)$$

The first term on the right hand side of equation (11) represents the energy incident upon the liquid layer at the semiconductor surface; the second term represents the energy lost to the solid beyond the melt front. Due to the latent heat L_M, it is probable (and is verified by our data for most energies) that, during the pulse, a greater depth will have reached the melting temperature than will have melted. This suggests the presence of a transition or "slush" zone[11]. We thus evaluate the temperature gradient at the end of the slush zone, since the entire zone is assumed to be at the melting point. As is mirrored by the discussion in the last few sentences, an upper limit on the melting depth is the depth which has reached the melting temperature. For high energies (1.75-2 J/cm^2), it is found that, near the end of the pulse, the melt depth reaches

this upper limit. In other words, there is no slush zone for these energies at the end of the pulse.

VII. HEATING OF LIQUID DURING PULSE:

For liquid Si, the thermal and optical parameters are treated as constant (see Glossary). We thus assume that, once a given depth has melted, it heats according to eq. (6), with the zero of temperature now being T_M, and the zero of time being the melting time for that depth, determined by eqs. (10) and (11).

VIII. SURFACE EVAPORATION:

According to the preceding section, at the end of the pulse there will be a certain temperature distribution in the liquid (arbitrarily shown in fig. 1). A certain depth, X_B, will be calculated to have exceeded the boiling point. However, assuming the liquid does not heat above T_B, we can assume that calculated temperatures above T_B contribute to surface evaporation.[13] We can thus calculate the amount lost to evaporation by the following energy balance equation:

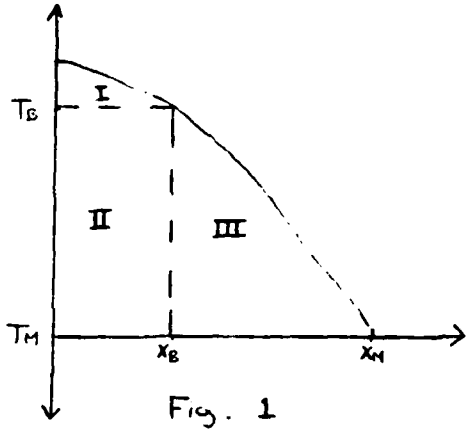

Fig. 1

$$L_V \Delta x_V = C_L \int_0^{X_B} T(x)\, dx \qquad (12)$$

Here the integral represents region I in fig. 1.

We should mention here that doubts exist as to what the boiling point of Si is. Estimates in the literature range from 2500-3500°K.[11,14] Variations in this will alter the predicted value of evaporation loss as well as the total melt depth (see

next section). Further, some evaporation will occur before the boiling point is reached; however, since the temperature rise from T_M to T_B near the surface is found to occur in a much quicker time than τ_p, we neglect evaporation before the boiling point is reached.

IX. MELTING AFTER PULSE:

Using a similar method we can calculate the additional depth to which the solid melts after pulse termination. Using a similar argument to that of the last section we can write (see fig. 1)

$$L_M \Delta x_M = C_L \left[\int_{x_B}^{x_M} T(x)\,dx + (T_C - T_M)(x_B - \Delta x_V) \right] \qquad (13)$$

Here the integral represents region III in fig. 1; the second term on the right represents region II corrected for evaporation loss.

The time of melting after the pulse can be approximated by $\tau = \bar{x}^2/D_L$, where $\bar{x} = x_M + \Delta x_M - \Delta x_V$. This estimates the time it takes for heat to diffuse from the front surface of the liquid (corrected for evaporation) to the maximum melt depth.

This approach assumes that, at the end of the pulse, the solid is at the melt temperature to at least a depth Δx_M beyond the pulse-termination melt depth, x_M. However, recall from section VI that, for energies of 1.75-2 J/cm^2, no such transition zone is found to exist. Although it is logical to assume that further heating of the solid takes place for these energies (since the upper limit melt velocity is reached), it is not safe to assume that a transition zone exists to a depth $x_M + \Delta x_M$. For this reason, in fig. 2 we plot the melt depth reached <u>during</u> the pulse, x_M. This can be regarded as a lower limit to the actual melt depth reached, while $x_M + \Delta x_M$ can be regarded as the corresponding upper limit.

X. SOME COMMENTS CONCERNING RECRYSTALLIZATION VELOCITY

As mentioned before, we were unable to make any good predictions of recrystallization velocities. However, some qualitative comments may be helpful:

We have assumed that once the total melt depth has been reached, the entire liquid layer is at T_M, all "excess" heat having been exhausted by the process described in eq. (13). Then the recrystallization velocity can be determined by

$$L_M v_p = K_S \left.\frac{\partial T}{\partial x}\right|_{\text{melt front}}$$

The melt velocity (eq. (11)) at the end of the pulse is found to almost triple when the energy density is doubled. This suggests shallower temperature gradients in the solid for increasing energy density. If we assume that this same trend holds true by the time total melt depth is reached, then recrystallization velocity will decrease with increasing energy density.

For further discussion of recrystallization, consult references 15 and 16.

XI. RESULTS AND FURTHER DISCUSSION:

In figs. 2 and 3 we plot melt depths and evaporation losses, respectively, as functions of incident energy density. This is done for both previously mentioned functional forms of α. It is seen that which functional form of α is used is not crucial, even though the value of α for solid Si at the melting point differs by a factor of 4 for the two cases. The reason for this can be seen upon examination of equation (6): for $\alpha^{-1} << \sqrt{Dt}$, which is the case at melting point for either functional form, the terms that dominate F are

$$-\frac{x}{D}\,\text{erfc}\left(\frac{x}{2\sqrt{Dt}}\right) + 2\sqrt{tD/\pi}\,\exp\left(-x^2/4tD\right),$$

independent of α.

Examination of the melt depth graph reveals that the depth of melting appears to approach a saturation value. This is

due, in part, to the fact that at higher energies the melt depth reaches its upper limit prior to pulse termination. As energy density is increased, this occurs sooner and sooner in the pulse. The melt depth is then limited to the depth which has reached melt temperature. Inspection of the dominant terms of eq. (6) reveals that the temperature will fall off with depth faster than it will rise with increasing intensity, suggesting a threshold on the depth to which melt temperature is reached.

Further study of this problem could determine whether or not melting can occur to a total depth of $x_M + \Delta x_M$ for the energies at which the melt velocity reaches its upper limit during the pulse. If we were to predict that this cannot occur, then a maximum total melt depth threshold of ~8000 Å would be predicted (indicated by the dashed line in fig. 2). Otherwise, surface ablation damage, which is known to occur if the melt depth reaches ~1 micron[7], is predicted for energies at or above 1.75 J/cm^2.

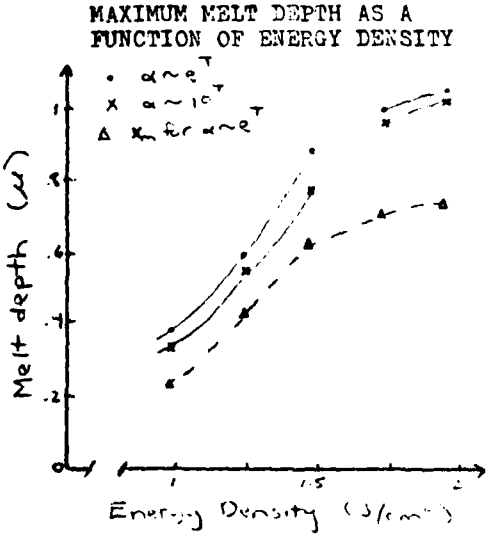

Fig 2

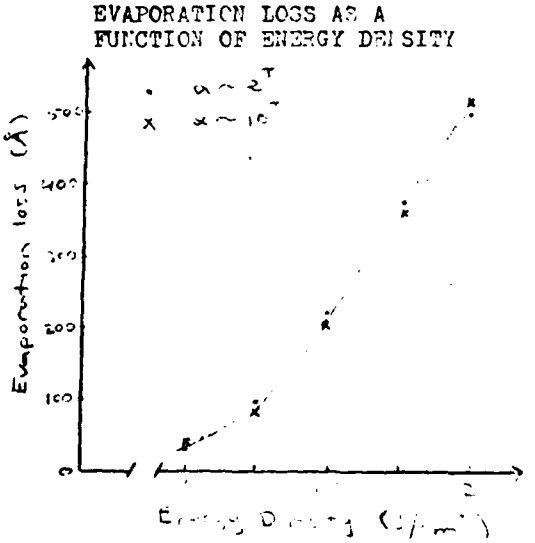

Fig 3

XII. RECOMMENDATIONS:

A detailed description of the computer program which models the processes described in this paper is being provided to the people at the Materials Laboratory. The programmer inputs three quantities into the program: laser energy density, initial substrate temperature, and amorphous layer thickness. It was found in this paper that amorphous layer thickness is not crucial to this model; however, if more reliable information is obtained concerning the characteristics of amorphous Si, it could be found that the amorphous layer thickness is a more crucial quantity. One possibility that was not investigated in this model was that of a lowered melting temperature and/or latent heat of melting in the amorphous layer; it might be instructive to modify the program to include these possibilities.

Based on the findings of this model, energies of the order of 1 to 1.5 J/cm^2 should be used for desired melt depths; higher energies could result in damage to the silicon wafer. The melting threshold is predicted to be about .5 J/cm^2: this is one suggested way to test the accuracy of the model.

The references cited in section X are a good starting point for further investigation of regrowth velocity. If we predict a regrowth velocity of 5m/sec, which is comparable to experimental findings, the resulting predictions of total surface melting time are $\sim$250 nanoseconds for $2J/cm^2$ pulse, and about 100 nanoseconds for $1J/cm^2$ pulse.

Acquisition of better data, especially at high temperatures for absorption and diffusivity of Si, would improve the accuracy of this model. So would more efficient and precise computing techniques.

APPENDIX: TREATMENT OF THE NONLINEAR HOMOGENEOUS DIFFUSION EQUATION[17]

In the absence of a source term, equation (2) reduces to

$$\frac{\partial T}{\partial t} - \frac{\partial}{\partial x} D(T) \frac{\partial T}{\partial x} = 0 \tag{A-1}$$

Suppose $D(T) = D_0 T^{-(1+\beta)}$, where $0 < \beta < 1$. Then

$$D(T) \frac{\partial T}{\partial x} = D_0 T^{-(1+\beta)} \frac{\partial T}{\partial x} = -\frac{D_0}{\beta} \frac{\partial}{\partial x} T^{-\beta} \tag{A-2}$$

thus

$$\frac{\partial T}{\partial t} = -\frac{D_0}{\beta} \frac{\partial^2}{\partial x^2} T^{-\beta} \tag{A-3}$$

We now employ separation of variables: let $T = Y(x)\Theta(t)$. Then

$$Y \frac{d\Theta}{dt} = -\frac{D_0}{\beta} \Theta^{-\beta} \frac{d^2}{dx^2} Y^{-\beta}, \text{ or}$$

$$\Theta^{\beta} \frac{d\Theta}{dt} = -\frac{D_0}{\beta Y} \frac{d^2}{dx^2} Y^{-\beta} = -\lambda, \quad \lambda > 0. \tag{A-4}$$

(We have chosen the negative sign on λ for convenience; treatment is just as straightforward for the positive case). Solving the time-dependent part,

$$\Theta(t) = \left[(1+\beta)\lambda(\tau - t)\right]^{1/1+\beta} \tag{A-5}$$

where τ is a constant of integration.

Turning now to the spatially-dependent part of eq. (A-4), we make the transformation $\xi = Y^{-\beta}$. Then

$$\frac{d^2\xi}{dx^2} = \frac{\beta\lambda}{D_0 \xi^{1/\beta}} \tag{A-6}$$

The left-hand side can be written as $\frac{1}{2}\frac{d}{d\xi}\left(\frac{d\xi}{dx}\right)^2$. Then

$$\left(\frac{d\xi}{dx}\right)^2 = \frac{2\beta\lambda}{D_0} \int \frac{d\xi}{\xi^{1/\beta}} = \frac{2\beta^2\lambda}{D_0(1-\beta)} \left[\xi_0^{1-1/\beta} - \xi^{1-1/\beta}\right], \tag{A-7}$$

and $$\frac{d\xi}{\left(\xi_0^{1-1/\beta} - \xi^{1-1/\beta}\right)^{1/2}} = \pm\sqrt{\frac{2\beta^2\lambda}{D_0(1-\beta)}}\,(x \pm x_0)$$

Let $\gamma=\frac{1}{\beta}-1$. Since $0<\beta<1$, $\gamma>0$. Then

$$\frac{d\xi}{\left(\xi_0^{-\gamma}-\xi^{-\gamma}\right)^{1/2}} = \pm\sqrt{\frac{2\beta^2\eta}{D_0(1-\beta)}}\,(x\pm x_0) = \frac{\xi^{\gamma/2}\,\xi_0^{\gamma/2}\,d\xi}{\left(\xi^{\gamma}-\xi_0^{\gamma}\right)^{1/2}} \qquad \text{(A-8)}$$

For even powers of γ (corresponding to β =1/3, 1/5, 1/7, etc.) solutions to the left-hand side of (A-8) can be found in standard integral tables. (Solutions may also be found for certain negative values of β). For instance, for Si the thermal diffusivity can be fitted quite well, in the solid phase, by $D(T)=1414\,T^{-4/3}$; for this case $\beta=1/3$, $\gamma=2$ and eq. (A-5) becomes

$$\theta(+) = \left[\frac{4}{3}\eta(T-t)\right]^{3/4} \qquad \text{(A-9)}$$

Eq. (A-8) becomes

$$\frac{\xi\xi_0\,d\xi}{\left(\xi^2-\xi_0^2\right)^{1/2}} = \pm\sqrt{\eta/3D_0}\,(x\pm x_0)^2, \text{ or}$$
$$\xi^2 = \xi_0^2\left[1+\frac{\eta}{3D_0\xi_0^4}(x\pm x_0)^2\right] \qquad \text{(A-10)}$$

But $\xi=\gamma^{-1/3}$, so

$$\gamma=\gamma_0\left[1+\frac{\eta\gamma_0^{4/3}}{3D_0}(x\pm x_0)^2\right]^{-3/2}$$

$$\text{and}\quad T=T_0\left[1+\frac{T_0^{4/3}}{3D_0}(x+x_0)^2\right]^{-3/2}(T-t)^{3/4} \qquad \text{(A-11)}$$

where $T_0=\left(\frac{4}{3}\eta\right)^{3/4}\gamma_0$. Thus, if T_0, x_0, and T can be fitted to boundary and/or initial conditions of a homogeneous diffusion problem for Si, equation (A-11) is a complete analytical solution for the temperature as a function of depth and time.

REFERENCES

1. C. M. Surko, A. L. Simons, D. H. Auston, J. A. Golovchenko, and R. E. Slusher, "Calculation of the Dynamics of Surface Melting During Laser Annealing," Appl. Phys. Lett., Vol. 34, No. 10, pp.635-637, 1979.

2. J. A. Van Vechten, R. Tsu, F. W. Saris, "Nonthermal Pulsed Laser Annealing of Si: Plasma Annealing," Phys. Lett., Vol. 74-A, pp.422-431, 1979.

3. B. Stritzker, A. Pospieszczyk, and J. A. Tagle, "Measurement of Lattice Temperature of Silicon During Pulsed Laser Annealing," Phys. Rev. Lett., Vol. 47, No. 5, pp.356-358, 1981.

4. J. Narayan, J. Fletcher, C.W. White, and W. H. Christie, "Melting Phenomena and Pulsed-Laser Annealing in Semiconductors," J. Appl. Phys., Vol. 52, No. 12, pp.7121-7128, 1981.

5. A. Lietoila and J. F. Gibbons, "Computer Modeling of the Temperature Rise and Carrier Concentration Induced in Silicon by Nanosecond Laser Pulses," J. Appl. Phys., Vol. 53, No. 4, pp.3207-3213, 1981.

6. M Neuberger and S. J. Welles, Silicon, Electronic Properties Information Center, Culver City, California, October 1969, pp. 110-111.

7. K. R. Bradley, Laser Annealing of and Laser Interactions with Ion Implanted Semiconducting Materials, Thesis, Air Force Institute of Technology, 1979: and references therein.

8. A. E. Bell, "Review and Analysis of Laser Annealing ," RCA Review, Vol. 40, pp. 295-338, 1979.

9. Thermophysical Properties of Matter, Vol. 4, pp.204-207, and Vol. 10, pp.160-165, IFI/Plenum, New York, 1970.

10. G. E. Jellison, Jr., and F. A. Modine, "Optical Absorption of Silicon Between 1.6 and 4.7 eV at Elevated Temperatures," Appl. Phys. Lett., Vol. 41, No. 2, pp. 180-182, 1982.

11. R. F. Wood and G. E. Giles, "Macroscopic Theory of Pulsed-Laser Annealing I: Thermal Transport and Melting," Phys. Rev. B, Vol. 23, No. 6, pp.2923-2942, 1980.

REFERENCES (continued)

12. D. M. Kim, "Adiabatic Approach to Transport Processes: A General Analytic Technique for Nonlinear Dynamic Heat and Mass Diffusion," Laser and Electron Beam Processing of Materials, Materials Research Society, pp. 83-88, 1980.

13. A. K. Jain, V. N. Kulkarni, and D. K. Sood, "Pulsed Laser Heating Calculations Incorporating Vaporization," Appl. Phys., Vol. 25, pp.127-133, 1981.

14. R. Yen, J. M. Liu, H. Kurz, and N. Bloembergen, "Space-Time Resolved Reflectivity Measurements of Picosecond Laser-Pulse Induced Phase Transitions in (111) Silicon Layers," Appl. Phys. A, Vol. 27, pp.153-160, 1982.

15. P. Baeri, "Computer Modeling of Laser Annealing," Laser and Electron-Beam Interactions with Solids, Materials Research Society, Vol. 4, pp.151-160, 1982.

16. J. M. Poate, "The Recrystallization and Amorphization of Si from the Melt at Interface Velocities Approaching 20 m/sec," Laser and Electron-Beam Interactions with Solids, Materials Research Society, Vol. 4, pp.121-130, 1982.

17. K. R. Bradley, private communication.

18. D. S. Moroi, private communication.

1982 USAF-SCEEE GRADUATE STUDENT SUMMER SUPPORT PROGRAM

Sponsored by the

AIR FORCE OFFICE OF SCIENTIFIC RESEARCH

Conducted by the

SOUTHEASTERN CENTER FOR ELECTRICAL ENGINEERING EDUCATION

FINAL REPORT

ANALYSIS AND MODELING OF A REAL-TIME HOLOGRAPHY SYSTEM

Prepared by:	Jeffrey M. Swindle
Academic Department:	Electrical Engineering
University:	University of Missouri-Rolla
Research Location:	Rome Air Development Center, Surveillance Division, Strategic Surveillance Branch, Electro-Optics Section
USAF Research:	Dr. Donald W. Hanson
SFRP Supervising Faculty Member:	Dr. Jerome Knopp Associate Professor
Date:	August 13, 1982
Contract No:	F49620-82-C-0035

ACKNOWLEDGEMENT

The authors would like to thank the Air Force Systems Command, the Air Force Office of Scientific Research and the Southeastern Center for Electrical Engineering Education for providing them with the opportunity to spend a very worthwhile and interesting summer at Rome Air Development Center, Griffiss AFB, NY. They would like to acknowledge Dr. Don Hanson and the Electro-Optics Section for their hospitality and excellent working conditions.

ANALYSIS AND MODELING OF A REAL-TIME HOLOGRAPHY SYSTEM

by

Jerome Knopp

and

Jeffrey M. Swindle

ABSTRACT

The real-time holography system was studied in some detail using a generic model. It is shown that aberrations are introduced by wavelength rescaling. Further errors are generated by the very nature of phase recording a hologram plus the non-linearities in the recording media. Resolution requirements and MTF limitations show that present day phase recording devices are just barely adequate to correct low level turbulence.

A study of the system using dimensional analysis showed that the Fresnel approximation may be used to construct a scale model based on Arkadiew's Law.

I. INTRODUCTION

At the present, DARPA has considerable interest in the application of optical phase conjugation techniques to visible laser communication. In principle, phase conjugation can be used to compensate for most of the optical phase distortions along the beam path of a propagating laser. In cases of practical interest, the aberrations are due primarily to the atmosphere; however, phase conjugation can be used to correct other aberrations such as those due to errors in optical components or within a laser cavity.

At the present there are several different methods of phase conjugation which are being considered including adaptive mirrors, nonlinear optics and real-time holography.

Adaptive mirrors represent conventional technology and have been under active development for more than 14 years. In order to employ mirrors for phase conjugation, a wavefront sensor is required that can determine the aberrated wave profile and then apply a best estimate of the profile conjugate to the adaptive mirror surface by distorting the surface with an array of actuators. The practical problems of constructing such systems are considerable. In order to apply these mirrors to total atmospheric compensation would require mirrors better than those presently available off the shelf. Atmospheric compensation requires a fast time response (i.e., in the millisecond range) and large numbers of actuators (on the order of 10^3 to 10^4). While it is possible to build adaptive mirrors meeting the required performance criteria, the costs are hign. For this reason, other approaches to phase conjugation are being investigated.

Nonlinear optics refers to a collection of methods that use wavefront reversal (i.e., phase conjugation) caused by elastic photon scattering or stimulated interactions of inelastic photon scattering. Both three wave and four wave mixing techniques are described in the literature.[1,2] It appears that these techniques are the leading technologies for future work in phase conjugation; however, they are not

available in the near term because most mixing schemes are very inefficient. In most practical schemes that implement phase conjugation, the conjugate must be produced from a very weak aberration sensing beacon that is not strong enough to produce a clean conjugate wave.

The most promising near term prospect for phase conjugation is real-time holography. A hologram is made of the aberrated wavefront from which a conjugate wavefront is produced. Real-time holography requires a fast recording medium in which to form the phase correcting holograms. Devices, such as the Ediphor, Ruticons, photo-TITUS and the PROM which employ fast (real-time) media, are possible candidates for real-time holography[3]. The cost versus risks for developing a workable phase conjugation system based on real-time holography appear reasonable; it is this particular approach which is the subject of this report.

The fundamental propagation problem to be analyzed is shown in Fig 1. It is desired to direct the energy from a laser source of wavelength λ_1 to a target aperture of diameter D_T from a telescope with a diameter D_S. It is assumed that a pointing and tracking system keeps the beam boresighted on the target aperture. Mounted at the center of the target aperture is a beacon source of wavelength λ_2. The beacon propagates a wave from the target. The wave travels through the aberrated atmosphere and is used to form a hologram of an aberrated wavefront at the source. The hologram is used to produce a conjugate wavefront that is propagated back through the atmosphere. In principle, this conjugate would precisely cancel the wavefront aberrations of the atmosphere. This corrected wavefront could deliver energy very efficiently from the source to the target provided the target aperture was large enough to collect the energy from an ideal diffraction limited spot. In practice, the implementation of a real-time holography system presents many problems that will prevent ideal correction of a wavefront. An attempt will be made here to analyze some of these problems and to examine the possibility of studying a real-time

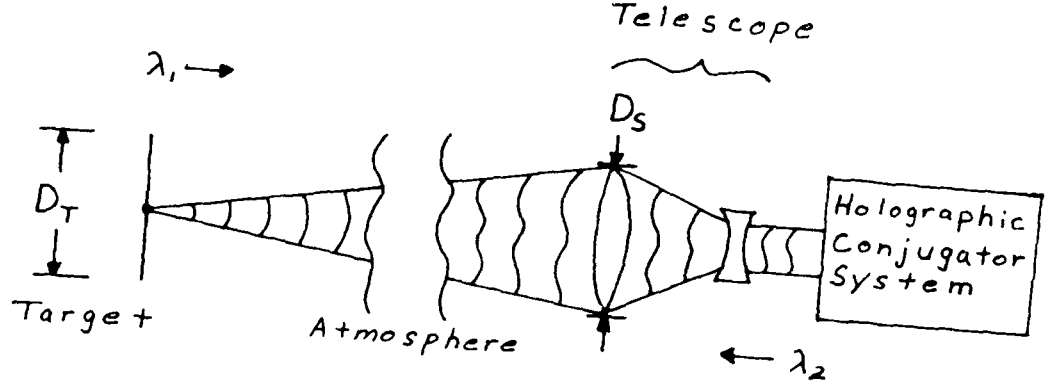

Figure 1 The Problem to be Analyzed

holography system using a scale model.

II. OBJECTIVES AND OUTLINE OF THE APPROACH

The objectives of this report are to conduct a systems level study of the real-time holographic approach and to discuss the possibility of constructing scale model experiments. The systems study will be conducted by defining a generic model and applying scalar diffraction theory to examine certain problems associated with a working system. Scale modeling will be discussed using dimensional analysis to construct a group of dimensionless parameters to model a working system. Using this group, certain scaling effects will be examined.

III. GENERIC MODEL OF A REAL-TIME HOLOGRAPHY SYSTEM

The system model for real-time holography will be broken into two parts: hologram formation as shown in Fig 2(a) and conjugate playback as shown in Fig 2(b). In Fig 2(a) a hologram is formed of an aberrating atmosphere using a beacon wavefront at wavelength λ_1. The beacon is received by the pointer telescope and the received beam cross section is reduced by the telescope expansion ratio M. The reduced beam is directed to a beam splitter from which a reference wave is derived. In general, the reference may be formed in one of several ways; no generally accepted scheme is available yet. (Some comments on this issue are included in the conclusions.) For the purpose of the model, it will be assumed that a spherical or plane reference wave is produced. The interference of the reference wave with the aberrated beam produces a hologram of the aberration. The hologram will be assumed to be a phase hologram, since most of the materials being considered at present for real-time holography depend on index changes, surface relief or birefringence to encode the wavefront. In the model, the material is assumed non-linear, with a band limited modulation transfer function.

The playback system used in Fig 2(b) produces a conjugate wavefront that would in principle be perfect; however, in most practical systems the conjugate would be reconstructed at a different wavelength, λ_2,

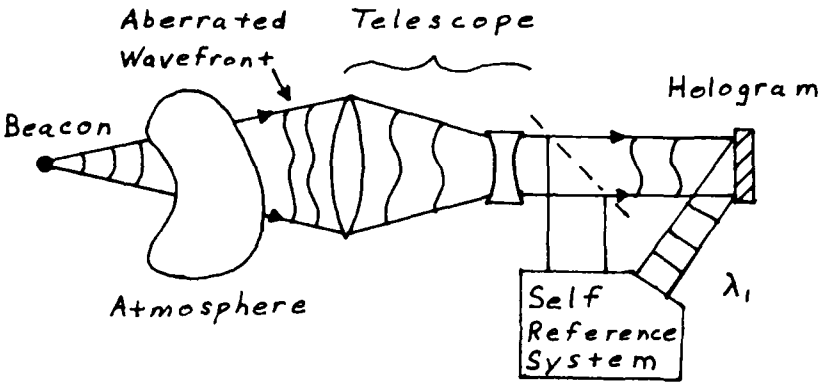

(a) Hologram Formation

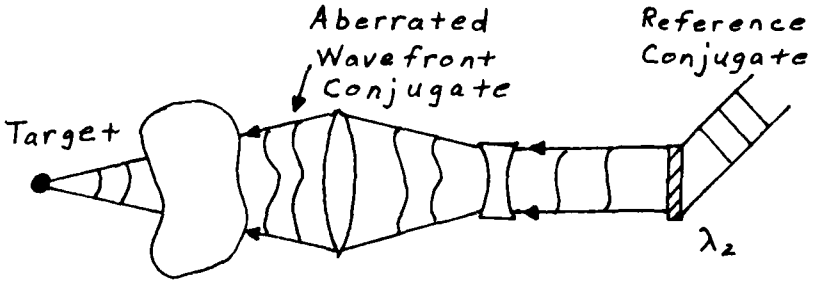

(b) Conjugate Playback

Figure 2 Generic Model

than the beacon wavelength. (This is done in part to assure good separation between outgoing scatter and the weaker beacon.) The "laser power amplifier" is used to strengthen the reconstructed conjugate. Strictly speaking, the power amplifier may in practice upshift or downshift the conjugate wavelength; however, this model will not include that effect. It will also ignore atmospheric effects due to wavelength differences between the beacon and the conjugate wave as well as the pointing and stationkeeping problems of a beacon in geosynchronous orbit. These issues are addressed elsewhere.[4]

IV. ANALYSIS OF THE GENERIC MODEL

In the analysis that follows, the generic model will be used to examine the following issues:

i) Aberrations introduced by the rescaling of wavelengths between the beacon and conjugate waves.

ii) Reconstruction errors in phase recording the aberrated wavefront.

iii) The effects of non-linearities in the recording media.

iv) Resolution requirements and MTF limitations.

A. Wavelength Rescaling

The problem of reconstructing holograms with a reference wave different from the reference used in forming the hologram has been studied extensively in the past; however, most of these studies are concerned primarily with image aberrations rather than wavefront reconstruction. The concern here is with reproduction of an exact conjugate.[5] Consider the most general situation, a beacon wavefront $\underline{U}_B(x,y,z)$ to be recorded with a reference $\underline{U}_R(x,y,z)$. Note that underlined quantities represent clockwise phasors. Assume that a hologram is formed with an exposure range that is in a linear region of

the field amplitude transmittance-exposure curve for the recording media that encodes the hologram. Then the following field amplitude transmittance will result:

$$\tau(x,y) = C_o (\underline{U}_B + \underline{U}_R)(\underline{U}_B + \underline{U}_R)^* \qquad (1)$$

where C_o is a constant and the asterick indicates conjugation.

Expanding Eq. (1)

$$\tau(x,y) = C_o (U_B^2 + U_R^2 + \underline{U}_B \underline{U}_R^* + \underline{U}_B^* \underline{U}_R). \quad (2)$$

Rewriting the phasor quantities explicitly gives

$$\underline{U}_B = U_B \; e^{-j \phi_B(x,y)}$$

and

$$\underline{U}_R = U_R \; e^{-j \phi_R(x,y)}.$$

Substituting into Eq. (2) and using Euler's identity gives

$$\tau = C_o (U_B^2 + U_R^2 + 2 U_R U_B \cos(\phi_B - \phi_R)). \quad (3)$$

In equation (3) the first two terms represents the intensities of the waves used to record the hologram while the last term encodes the phase difference in a fringe structure. From a communication viewpoint the last term represents encoding of the beacon information on a reference carrier. In order to retrieve the information the carrier must be known. In order to accurately retrieve the conjugate wave, the conjugate of the reference must be used to reconstruct the hologram. If the reconstructed field is designated as $\underline{U}_H$, then

$$\underline{U}_H = \tau \underline{U}_R^*$$

or from (2)

$$\underline{U}_H = C_o (\underline{U}_R^* U_B^2 + \underline{U}_R^* U_R^2 + \underline{U}_R^{*2} \underline{U}_B + U_R^2 \underline{U}_B^*). \quad (4)$$

The last term in equation (4) represents the reconstructed conjugate provided that $\underline{U}_R^2$ is relatively uniform in amplitude. This term is of special interest and will be designated as $\underline{U}_c$, therefore

$$\underline{U}_c = U_R^2 \, \underline{U}_B^* . \tag{5}$$

The first two terms represent low frequency bias terms due to the intensities associated with $\underline{U}_B$ and $\underline{U}_R$. They are a source of noise in the reconstruction. The third term in general, $\underline{U}_R^{*2} \underline{U}_B$ represents a distorted version of $\underline{U}_B$ since $\underline{U}_R^{*2}$ is not necessarily a constant phasor. Usually $\underline{U}_R$ is chosen as an easily reproducible wavefront. Failure to accurately reproduce $\underline{U}_R$ results in errors.

For the applications of interest here, a plane wave or a spherical reference wave is of interest. For the case of a plane wave the reference can be defined as:

$$\underline{U}_R = C_p \; e^{-j k_1 (\alpha x + \beta y + \gamma z)}$$

where α, β, γ are direction cosines with respect to the x, y and z axes, respectively. If a wavelength of λ_1 is used in recording the hologram then $k_1 = 2\pi/\lambda_1$. The only term of interest in reconstruction is $\underline{U}_c$. Assuming the conjugate is used in reconstruction, then, substituting the plane wave conjugate into (5) gives $\underline{U}_c = C_p^2 \, \underline{U}_B^*$ and an exact duplicate of the beacon is produced; however, if a different wavelength, λ_2, is used in the reconstruction then

$$\underline{U}_c = C_p^2 \; e^{-j (k_1 - k_2)(\alpha x + \beta y + \gamma z)} \underline{U}_B^* \tag{6}$$

where $k_2 = 2\pi/\lambda_2$. Equation (6) shows two types of error; one is a tilt term represented by the exponential, the second error is an error in the optical path. The tilt term is not a problem since it is a fixed pointing error. The path error is more of a problem. The $\underline{U}_B^*$ term is the correct phase at the wrong wavelength. Therefore, a path error of $(1 - \lambda_2/\lambda_1)\phi_B$ is produced. The path error can not be eliminated easily. It could be approximately corrected using an Arnulf lens,[6] a device that approximately multiplies the phase at each point by a

constant without changing the lateral dimensions of the beam. Since the resolution requirements for atmospheric correction are quite low (to be discussed later) such a lens is workable if the wavelength ratio between λ_1, and λ_2 becomes a significant problem.

If a spherical reference is used and a change in wavelength is involved, then for an off-axis reference point located at (x_c, y_c, z_c) then

$$\underline{U}_R = C_S \frac{e^{-j k_1 r}}{r}$$

where C_S is a constant and

$$r = \sqrt{(z - z_c)^2 + (x - x_c)^2 + (y - y_c)^2} \; .$$

Reconstructing the conjugate at a different wavelength gives

$$\underline{U}_c = C_s^2 \frac{e^{-j(k_1 - k_2) r}}{r} \underline{U}_B^* . \qquad (7)$$

Equation (7) shows that a spherical error is introduced that presents no problems since it can be corrected with a fixed lens and the path length error is identical to the one previously discussed.

Therefore provided a plane or spherical reference is used, reconstruction phase errors should be determined by $(1 - \lambda_2/\lambda_1)\, \phi_B$.

B. Reconstruction Error in Phase Holograms

As previously mentioned, real-time holography is based primarily on phase holograms. Phase holograms encode the holographic fringe structure as a phase change that is directly proportional to exposure. Unfortunately, they are inherently more noisy than amplitude transmission holograms. This can be seen by rewriting the exposure, E, directly in terms of a phase shift and using a second order approximation to the phasor exponential to describe the field amplitude transmittance $\underline{\tau}$. In phasor form

$$\underline{\tau} = T_o \, e^{-j \mu E(x, y)} \qquad (8)$$

where μ is a constant. Now expanding the exponential term gives

$$\underline{\tau} = T_o \left(1 + j\mu E - \frac{\mu^2}{2} E^2 + \cdots\right). \qquad (9)$$

If

$$E(x,y) = U_R^2 + U_B^2 + \underline{U}_R \underline{U}_B^* + \underline{U}_R^* \underline{U}_B$$

Then equation (9) describes a phase hologram for the beacon. The only terms of interest in reconstructing the phase hologram are the ones containing $\underline{U}_B^*$, all other terms are ignored. It will be assumed that the angle between the beacon wave and the reference wave is large enough to provide adequate angular separation between these other terms and $\underline{U}_B^*$. Therefore

$$\underline{\tau} = T_o \left[1 - (\mu^2 U_R^2 - j\mu)\underline{U}_R \underline{U}_B^* - (\mu^2 U_B^2)\underline{U}_R \underline{U}_B^* + \text{other terms}\right] \qquad (10)$$

Since U_R^2 is assumed uniform, the first set of parentheses in Eq (10) yields only a quadrature component. The second set of parentheses contains U_B^2 which is not uniform and is in fact highly speckled in the case of atmospheric recordings. This term is intermodulation noise and is referred to as "flare light" or "halo". This halo, in general, may not be easily removed. Therefore, by its very nature a phase hologram will have noise. The only way to reduce the noise is to keep μ small and accept very low diffraction efficiencies.

It should be pointed out that in devices used for real-time holography, the intermodulation will be worse than that normally observed in bleached photographic emulsions. In emulsions, both relief and index changes occur at low frequencies and they tend to cancel out and compensate for the low frequency speckle.

C. The Effects of Non-Linearities in the Recording Media

In the previous section, only linear phase recording was considered. The recording media in general will not record the phase in a linear fashion. Therefore, this section will concern itself to the effect of a quadratic approximation to the non-linear recording. The previous hologram transmittance Eq (8) now becomes:

$$\underline{\tau} = T_o \, e^{-j(\mu E + \Delta E^2)} \tag{11}$$

where μ and Δ are constants and E(x,y) is as previously described. Expanding the exponential yields:

$$\underline{\tau} = T_o [1 + j\mu E - (\tfrac{1}{2}\mu^2 - j\Delta)E^2 - \mu\Delta E^3 - \tfrac{\Delta^2}{2} E^4 + \cdots] . \tag{12}$$

Considering, as before, only terms containing $\underline{U}_B^*$:

$$\tau = T_o \{ 1 - [\mu^2 U_R^2 + 6\mu\Delta U_R^4 + 2\Delta^2 U_R^6 - j(\mu - 2\Delta U_R^2)] \underline{U}_R \underline{U}_B^* - U_B^2 [\mu^2 + 6\mu\Delta (U_B^2 + U_R^2) + 2\Delta^2 (U_B^4 + 6U_B^2 U_R^2 + 6U_R^4) - j2\Delta] \underline{U}_R \underline{U}_B^* + \text{other terms} \} . \tag{13}$$

Comparing Eq. (13) to Eq. (10), it is seen that the non-linear recording makes matters worse; it increases the number of intermodulation terms. These terms cannot be filtered out by angular separation like the terms that are not shown. Therefore, maintaining linearity is very important since there is no way to compensate for the non-linearities. It might be hoped that nonlinearities in the media could be played against the inherent non-linearity of phase recording; unfortunately, if equation (13) is examined closely, it will be observed these non-linearities terms are at quadrature with respect to one another.

C. Resolution Requirements and MTF Limitations

The best of the present devices being considered for real-time holography use a crystalline material that have modulation transfer functions that roll off at spatial frequencies on the order of the crystal thickness. Typically, these devices depend on materials that are difficult to fabricate much thinner than about 100 microns. This suggests that, at present, spatial frequencies are limited to about 10 lines/mm. For correction of atmospheric disturbances in "good" seeing the angular spectrum extends to about 10 μrads. Under the best turbulence conditions, given a receiving telescope with a beam expansion ratio of M, the received angular spectrum at the hologram will extend to about 10M μrads. Since the angular spectrum interprets the aberrated wavefront in terms of plane waves, it is only necessary to determine the highest spatial frequency needed for an off-axis recording of the plane wave making the largest angle with respect to the reference. For two plane waves at angles θ_1 and θ_2 on either side of a normal to a thin hologram, the spatial frequency S of the recording is given by

$$S = \frac{\sin\theta_1 + \sin\theta_2}{\lambda} \qquad (14)$$

where λ is the recording wavelength. For small angles

$$S \simeq \frac{\theta_1 + \theta_2}{\lambda} .$$

Since the minimum reference angle for adequate separation of the conjugate must be at least three times the atmospheric bandwidth[7] then the minimum spatial frequency S_{min} is given by

$$S_{min} = \frac{40 \times 10^{-6} M}{\lambda} \quad \text{cycles/meter.}$$

For an expected demagnification on the order of 100 this means resolution requirements of about $S_{min} = 8$ lines/mm which is just about the state-of-the-art. Therefore, we may expect that there is

adequate resolution in presently available materials to make turbulence corrections in good seeing. For extreme levels of high turbulence, it will be necessary to reduce M and increase the hologram surface. This would require growing fairly large crystals to record the holograms, it is not clear what the limitations are here, but such devices are not off-the-shelf.

V. SCALE MODELING OF THE REAL-TIME HOLOGRAPHY SYSTEM

The only exact way to evaluate any real system is to construct a prototype to make measurements on; however, for system development it is often reasonable to consider building a scale model in cases where the model is economical. Unfortunately, it is not always possible to fabricate a scale model in such a way that useful information can be extracted from it. In order to be of value, a direct relationship must be established between measurements made on the model and measurements made on the prototype. If a scale model is possible, a set of linear scales can be used to establish a correspondence or "similarity" between the systems. In what follows, the theoretical question of a scale model will be examined using techniques from dimensional analysis. From this analysis certain dimensionless groups will be established. These groups will define a set of dimensionless variables and parameters through which model and prototype measurements can be related. It will also provide a complete system description using a minimum number of variables and parameters. This is useful in reducing the amount of data and the number of experiments needed by a considerable amount.

Consider rescaling the generic model. In practice the beacon will be essentially at infinity. Therefore, the fundamental problem is that of a plane wave on an atmospheric "slab" that has an index of refraction, $n(x,y,z,t)$, that varies randomly from point to point. For the purposes of this analysis, the atmosphere will be examined at a specific instant of time; all of the index variations will be frozen in place. If index variations are small then it can be rewritten as

$$n(x,y,z) = n_0 + \Delta n(x,y,z)$$

where n_o is an average value and $\tilde{n}(x,y,z)$ is a perturbation about the average. If the perturbation is small, then the diffracted field from the slab can be approximated by examining only first order diffraction.

Consider a plane wave <u>propagating</u> in the z direction impinging normally on the atmospheric slab at $z=0$ and through the randomly varying index until it reaches a receiving aperture at $z = z_o$. The problem is to model accurately the field in the $z = z_o$ plane using a three dimensional scale model of the atmosphere. This can be done for the first order diffracted part of the field. The first order effects are estimated by dividing the slab into a thin stack of lamina; each thick, then the field from a single lamina at z is given approximately by

$$A e^{jk n_o z} e^{jk \tilde{n} \Delta z} \simeq A e^{jk n_o z} (1 - jk \tilde{n} \Delta z) .$$

Here A represents the amplitude of a plane wave that passes through the slab with negligible loss. The diffracted field from each lamina is assumed to reach z without further diffraction by other laminae. This represents first order effects only and ignores the "diffraction of the diffraction". Using the Fresnel approximation[7] and ignoring the undiffracted part of the field, the diffracted field $\underline{U}_D$ at z_o is given by integrating over all laminae:

$$\underline{U}_D = \frac{A e^{jk n_o z_o}}{\lambda n_o} \int_0^{z_o} \int_{-\infty}^{\infty} \frac{\tilde{n}}{z_o - z} e^{j \frac{k n_o}{2(z_o - z)} [(x_o - x)^2 + (y_o - y)^2]} dx\, dy\, dz \quad (15)$$

By defining a set of dimensionless variables equation (15) can be redefined in dimensionless form.[8] One particularly useful set is:

$$\overline{\underline{U}}_D = \frac{\lambda n_o}{k A} e^{-jk n_o z_o} \underline{U}_D \quad (16)$$

$$\overline{x} = \frac{x}{\sqrt{\lambda z_o}} \quad (17)$$

$$\overline{y} = \frac{y}{\sqrt{\lambda z_o}} \quad (18)$$

$$\bar{x}_o = \frac{x_o}{\sqrt{\lambda z_o}} \qquad (19)$$

$$\bar{y}_o = \frac{y_o}{\sqrt{\lambda z_o}} \qquad (20)$$

$$\bar{z} = z/z_o \quad . \qquad (21)$$

Rewriting (15) gives the normalized diffracted field at = 1 as

$$\underline{U}_D = \int_o^1 \int_{-\infty}^{\infty} \frac{\tilde{n}}{n_o(1-\bar{z})} e^{j\frac{\pi n_o}{(1-\bar{z})}[(\bar{x}_o-\bar{x})^2+(\bar{y}_o-\bar{y})^2]} d\bar{x}\, d\bar{y}\, d\bar{z} \quad . \qquad (22)$$

The normalized equation represents a generalized form through which a relationship can be established between model and prototype variables since this equation represents both systems. Letting primed and double primed variables represent model and prototype systems respectively the scale relations between the model and prototype can be derived directly from equations (16) through (21). They are

$$\underline{U}_D = \frac{U_D' \lambda' n_o}{k' A_p'} e^{-jk' n_o z_o'} = \frac{U_o'' \lambda'' n_o}{k'' A_p''} e^{-jk'' n_o z_o''} \qquad (23)$$

$$\bar{x} = \frac{x'}{\sqrt{\lambda' z_o'}} = \frac{x''}{\sqrt{\lambda'' z_o''}} \qquad (24)$$

$$\bar{y} = \frac{y'}{\sqrt{\lambda' z_o'}} = \frac{y''}{\sqrt{\lambda'' z_o''}} \qquad (25)$$

$$\bar{x}_o = \frac{x_o'}{\sqrt{\lambda' z_o'}} = \frac{x_o''}{\sqrt{\lambda'' z_o''}} \qquad (26)$$

$$\bar{y}_o = \frac{y_o'}{\sqrt{\lambda' z_o'}} = \frac{y_o''}{\sqrt{\lambda'' z_o''}} \qquad (27)$$

$$\bar{z} = \frac{z'}{z_o'} = \frac{z''}{z_o''} \qquad (28)$$

These relations establish a linear scale between the diffracted fields in the model and prototype systems, hence, measurements of the diffracted field from the model can be directly related to those in the prototype. Therefore a scale model is possible at least as far as first order diffraction effects.

These equations also determine how the scale model is to be constructed in order to keep a linear relation between the diffracted fields in the model and prototype systems. The scaling of refractive index coordinates is a key point in the modeling. The index coordinates in equation (22) must be scaled in normalized coordinates. Index coordinates will follow the scale relations given by equation (23) through (28). This means that if the thickness z_o is reduced by a factor p in the model, then the lateral index variations in x and y are scaled by the $\sqrt{p}$ provided the wavelength remains unchanged. This scale relation is not new, it was discussed by Arkadiew[9] in 1913; however, his presentation was highly intuitive, based on Fresnel zone construction, while the results given are rigorous. It should also be pointed out that only the diffracted field was discussed here. In general, it is not possible to scale the total field including the undiffracted part. It can be shown that the ratio of the diffracted to the undiffracted part of the field does not scale linearly. Fortunately, the effect is not critical since the net effect is to lower the contrast in the intensity variations. This effect is easy to account for since the undiffracted part is an additive constant.

It should be pointed out that the non-dimensional parameters given in equations (16) through (21) are the most compact representation of the atmospheric slab possible. They are ideal for minimizing parameters needed for either experimental or computer simulation. If two particular parameters such (e.g., wavelength and thickness) are in the same dimensionless group, then varying one is equivalent to varying the other as far as making measurements are concerned. Therefore, using non-dimensional variables and parameters reduces the number of parameter changes needed for investigation. This often means orders of magnitude

reduction in the amount of effort needed in experimental or computer simulation.

VI. CONCLUSIONS

From the results of the analysis using the generic model the following conclusions have been reached:

1. Phase aberrations introduced by rescaling the wavelengths will depend only on the ratio of the wavelengths used in forming and playing back the hologram if spherical aberration and tilt are accounted for. This assumes that a perfectly plane or spherical reference can be derived from a beam split off from the beacon wave. This is highly debateable. Since adequate filtering of the reference means that a small portion of the angular spectrum from the derived beam is used and therefore a small portion of the energy from it. This means a weak reference beam and requires a weak or attenuated object wave to form a proper hologram. This represents a great waste of photons. Furthermore, some suggested schemes for deriving a reference, filter out the reference using a pinhole filter in conjunction with a lens to carry out optical Fourier transform filtering. Considering the very speckled nature of the return wave impulse repsonse, the pinhole filter will be a very hit and miss operation that will provide a reference with large dynamic variations. This issue definitely needs more thought.

2. The problems of phase reconstruction errors in phase holograms are two fold,

   i. Inherent errors due to the non-linearities in phase recording
   ii. Additional errors due to non-linearities in the mapping of intensity into phase.

These problems are inescapable and lead to intermodulation noise in the reconstructed wave. The first is avoided by accepting low diffraction efficiency, the second by making sure the phase recording have adequate

dynamic range, this may be a difficult problem considering the intensity variations inherent in the speckled beacon return.

3. The resolution requirements of present materials appears adequate for correction in loss turbulence. Correction in high turbulence may require devices with larger surface areas than are presently available off-the-shelf to accomodate the higher space bandwidth product required.

4. Modeling the effects of the atmosphere appears to be practical. It is possible in principle to construct a small model atmosphere, if the index variations can be properly scaled using Arkadiew's scaling laws for the diffracted field.

VII. RECOMMENDATIONS

In order to further reduce risks in developing a working real-time holography system it is recommended that in future work the following issues be examined:

1. The effects of speckle on a reference wave derived from the incoming beam.
2. Alternate techniques for deriving a reference wave to avoid wasting photons.
3. Dynamic range effects of present real-time media and trade-offs that can be made between dynamic range and signal-to-noise ratios.
4. Applications of scale modeling to reducing development cost and improving laboratory simulations, presently being considered.

REFERENCES

1. Pepper, D. M., "Nonlinear Optical Phase Conjugation," Optical Engineering, Vol. 21, No. 2, p156, March-April, 1982.

2. White, J. O. and Amnon Yariv, "Spatial Information Processing and Distortion Correction Via Four-Wave Mixing," Optical Engineering, Vol. 21, No. 2, p224, March-April, 1982.

3. Lipson, G. G., "Recyclable Incoherent-to-Coherent Image Converters," in Advances in Holography, Vol. 2, ed. by N. H. Farhat, p69, Marcel-Dekker Inc., NY, 1976.

4. Strategic Laser Communications Uplink Analysis, (Volumes 1 and 2), RADC-TR-341 V. 1, RADC-TR-81-186 V. 2, Rome Air Development Center, Griffiss AFB, NY, Dec and July, 1981.

5. Smith, H. M., Principles of Holography, Wiley Interscience, NY, 1975.

6. Gabor, D., "Summary and Directions for Future Progress," in Acoustical Holography V 1, ed. by Methrell, A. F., H. M. A. El-Sum and L. Larmore, p267, Plenum Press, NY, 1969.

7. Goodman, J. W., Introduction to Fourier Optics, McGraw-Hill, NY, 1968.

8. Kline, S. J., Similitude and Approximation Theory, McGraw-Hill, NY, 1965

9. Sommerfield, A., Optics, Academic Press, NY, 1954.

1982 USAF-SCEEE SUMMER FACULTY RESEARCH PROGRAM

Sponsored by the

AIR FORCE OFFICE OF SCIENTIFIC RESEARCH

Conducted by the

SOUTHEASTERN CENTER FOR ELECTRICAL ENGINEERING EDUCATION

FINAL REPORT

THE MEASUREMENT OF ION-MOLECULE REACTION RATE COEFFICIENTS

Prepared by:	Dr. Thomas M. Miller
Academic Rank:	Associate Professor
Department and University:	Department of Physics and Astronomy University of Oklahoma
Research Location:	Air Force Geophysics Laboratory, Aeronomy Division
USAF Research Colleague:	Dr. John F. Paulson
Date:	August 9, 1982
Contract No:	F49620-82-C-0035

This report was prepared with Rodney E. Wetterskog, graduate student, University of Oklahoma.

THE MEASUREMENT OF ION-MOLECULE REACTION RATE COEFFICIENTS

by

Thomas M. Miller and Rodney E. Wetterskog

ABSTRACT

Rate coefficients have been measured for C^+, CO^+, and CO_2^+ reactions with O_2 over a temperature range of 90-450 K using a selected-ion flow-tube (SIFT) apparatus at the Air Force Geophysics Laboratory. Charge transfer is observed to take place for $CO^+ + O_2$ and $CO_2^+ + O_2$, but is not allowed energetically for $C^+ + O_2$. Instead, we observe $C^+ + O_2 \rightarrow O^+ + CO$ and $C^+ + O_2 \rightarrow CO^+ + O$ occurring. The $C^+ + O_2$ reaction is found to proceed at its gas kinetic rate of about 9×10^{-10} cm^3/s, independent of temperature for 90-450 K. The rate coefficients for both the $CO^+ + O_2$ and $CO_2^+ + O_2$ reactions are decreasing functions of temperature in this range. The ion flow velocity in the SIFT apparatus has been determined versus gas pressure and temperature using a time-of-flight technique. These results, combined with our helium flow measurements, have significant implications for low-temperature reaction experiments with flow-tube reactors.

I. INTRODUCTION:

The Aeronomy Division at the Air Force Geophysics Laboratory has long been active in research on the composition and chemistry of the earth's upper atmosphere. This research involves both atmospheric sampling and laboratory studies of atmospheric reactions. The laboratory research centers on charged-particle interactions primarily because of the importance of military communications through (or reflected by) the partially ionized gas of the earth's atmosphere. The particular laboratory we were working with (AFGL/LKB) is currently studying atmospheric ion reactions with neutral constituents, and the photodissociation of ionic molecules.

The main interest at present in the AFGL ion-molecule reaction research concerns ion clusters which have been found to dominate the stratospheric ion population. Since there has been very little work done on negative ion reactions the emphasis has been in that direction. (The negative ion reactions tend to be more difficult to study because generally speaking it is easier to make large densities of positive ions than negative ions.) The neutral reactants chosen for these experiments are of course observed (or suspected) atmospheric molecules which may be present in the atmosphere in very small fractional concentrations (mixing ratios $\leq 10^{-6}$) but nevertheless play an important role because of their large dipole moments or low ionization potentials.

At AFGL/LKB a selected-ion flow-tube (SIFT) apparatus was constructed about two years ago to study ion-molecule reactions. An essential feature of the design of the AFGL SIFT apparatus is its ability to operate over a temperature range of 80-500 K, which allows the determination of ion-molecule reaction rate coefficients for

atmospheric temperatures (180-300 K) as well as providing for a wider range necessary for insight into the reaction mechanisms. Much of the work we were involved in during the summer of 1982 was in taking the SIFT apparatus to low and high temperatures for the first time and the solution of various problems encountered. For this purpose relatively straightforward ion-moleucle reactions were chosen, $C^+ + O_2$, $CO^+ + O_2$, and $CO_2^+ + O_2$. Our objective was to study the fate of these reactions over a wide temperature range.

One of us (TMM) has had experience with ion-molecule reaction research at the University of Birmingham (UK) on the original SIFT apparatus and at Georgia Tech with a drift tube apparatus. Both of us have worked with a flow tube reactor at our home institution, the University of Oklahoma.

II. APPARATUS AND EXPERIMENTAL METHOD:

The selected-ion flow-tube method was developed by Adams and Smith[1] at the University of Birmingham (UK) around 1975 and represented a significant improvement over the already quite successful flowing afterglow technique. The SIFT method is still being improved upon as its use spreads.

Briefly, the AFGL SIFT apparatus consists of a 108-cm long, 7.3-cm i.d. tube through which a helium carrier gas is flowed at low pressure (~0.3 torr) and high speed ($\sim 10^4$ cm/s). Ions are created in an electron-impact ion source, mass analyzed, and a current of $\sim 10^{-10}$ A of a single desired ion species is injected into the flow tube at low energies in the center of a supersonic jet of the helium carrier gas. The ions quickly thermalize in collisions with the helium gas and flow

with the gas down the tube. The trip requires approximately 10 ms. At the end of this trip some of the ions pass through a small (0.03 mm) aperture leading into a second mass spectrometer maintained at high vacuum. The detected ion count rate is proportional to the original injected current.

In order to determine ion-molecule reaction rate coefficients, a very small concentration of reactant gas is titrated into the flow tube at a point sufficiently downstream from the ion and helium injector that equilibrium flow has been reached. If the primary ions react with the titrated gas, producing a product ion of different e/m, the detected primary ion current I_o is attenuated exponentially by the reaction according to Beers' Law:

$$I = I_o e^{-knt}. \tag{1}$$

The reaction rate coefficient k is calculated from measurement of the fractional decrease I/I_o in the primary ion current by a known concentration of reactant gas n, in a time t:

$$k = \frac{\ln(I_o/I)}{nt}. \tag{2}$$

Experimentally, the small fractional concentration n of the reactant gas is determined from the measured helium density N and the throughput Q_R of the reactant gas compared to the helium throughput Q_{He}. The reaction time t is determined from a direct measurement of the ion velocity v_i and of the distance d over which the reactant gas flows. Thus,

$$k = \frac{\ln(I_o/I)}{(Q_R N/ Q_{He})(d/v_i)}. \tag{3}$$

A computer program, SIFT82, has been written to handle the SIFT data on the laboratory's Hewlett-Packard 2112 computer. The program plots the data, calculates the reaction rate coefficient and related quantities, and calculates and plots the ion product percentages.

An example of the raw data is given in Fig. 1 for the reaction $C^+ + O_2$ at 196 K. The reaction time in this case is 3.84 ms and the reaction distance is 43.5 cm. The direct ionic products of the reaction are O^+ or CO^+ ions. The O_2^+ ions observed are secondary products from the subsequent reactions $O^+ + O_2$ and $CO^+ + O_2$. The reaction rate coefficient is 8.8×10^{-10} cm^3/s.

Three different titrant ports are available to enter reactant gases, at three different distances, permitting any end effects to be accounted for.

Ion-molecule reactions are examined for temperatures other than room temperature by cooling or heating the flow tube and the helium gas.

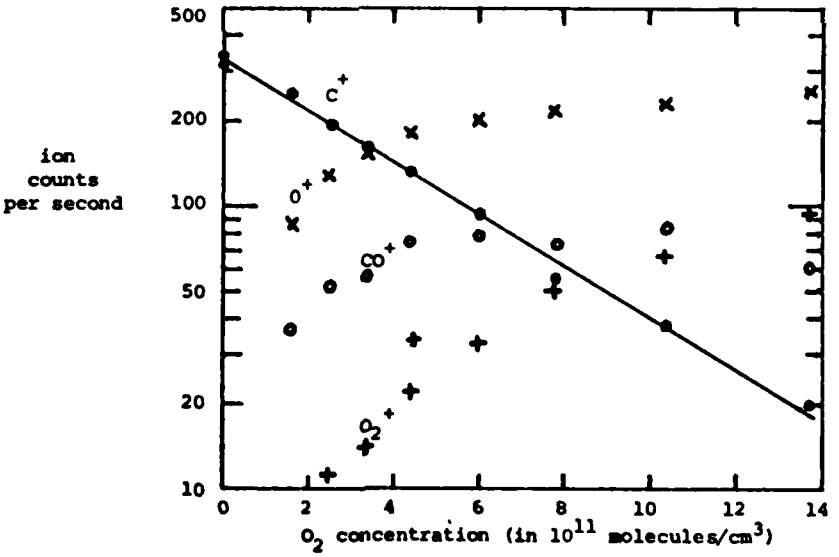

FIG. 1. DATA FOR THE REACTION $C^+ + O_2$ AT 196 K.

III. RESULTS:

A. Ion-Molecule Reactions. The reactions $C^+ + O_2$, $CO^+ + O_2$, and $CO_2^+ + O_2$ have been studied over the temperature range 90-450 K. The results are shown in Figs. 2-4, compared to previous work.

The interaction $C^+ + O_2$ proved to be independent of temperature over the range 90-450 K and essentially equal to the calculated gas kinetic (Langevin) rate coefficient of 1.0×10^{-9} cm^3/s. Simple charge transfer is endoergic in this case. Two reaction channels were observed, however. The first, $C^+ + O_2 \rightarrow O^+ + CO$ is exoergic by 3.635 eV, and is favored (62%) at all temperatures used. Although the neutral CO product is not observed directly, the energetics of the reaction require that it be bound. The second channel observed is $C^+ + O_2 \rightarrow CO^+ + O$, which is exoergic by 3.240 eV.

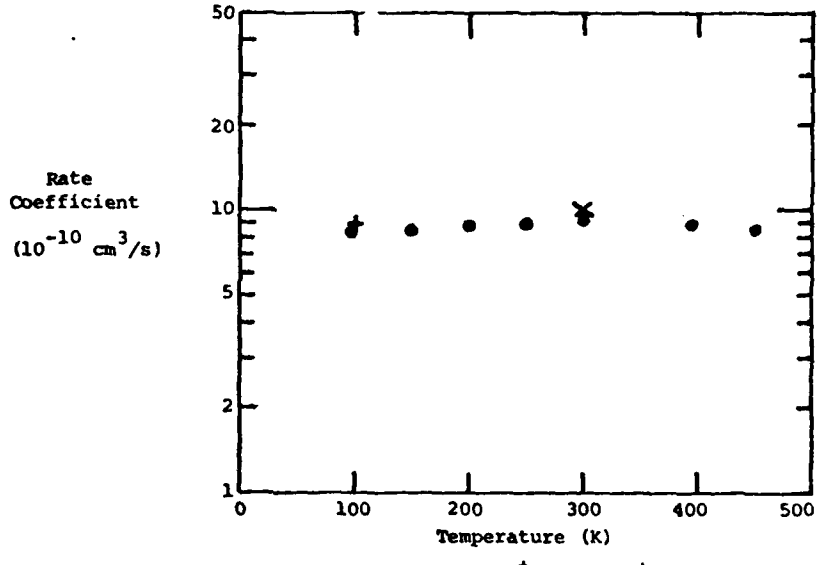

FIG. 2. REACTION RATE COEFFICIENT FOR $C^+ + O_2 \rightarrow O^+ + CO$. The data point ✕ is that of Adams and Smith,[2] and of Rakshit et al.[3] The point + is that of Rakshit et al.[3]

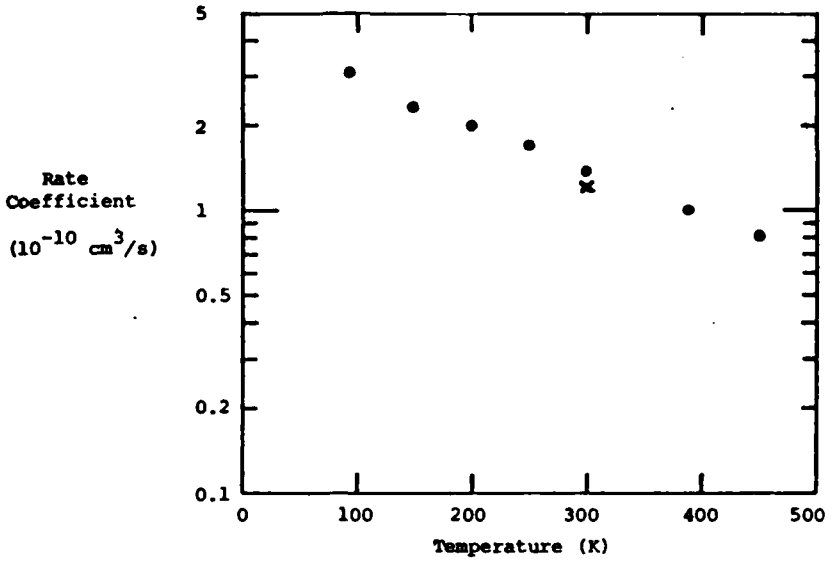

FIG. 3. REACTION RATE COEFFICIENT FOR $CO_4^+ + O_2 \rightarrow CO + O_2^+$. The data point X is that of Adams et al.[4]

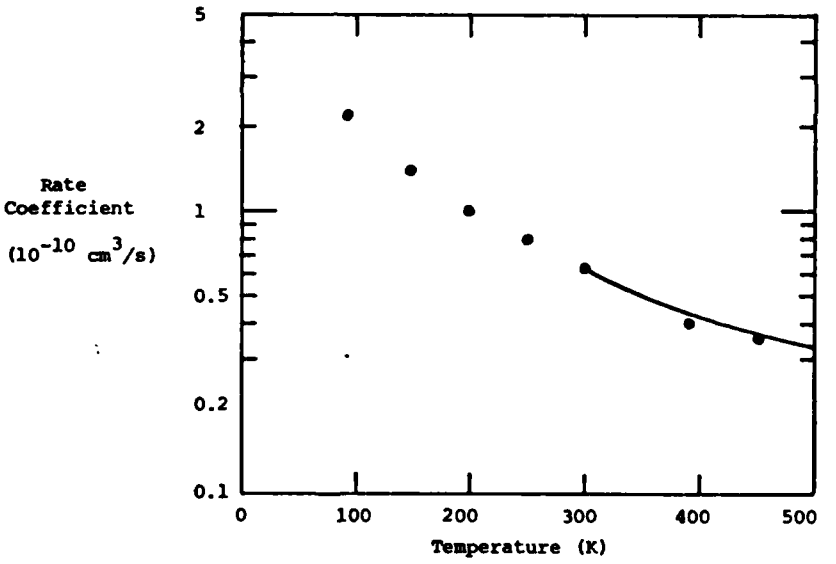

FIG. 4. REACTION RATE COEFFICIENT FOR $CO_2^+ + O_2 \rightarrow CO_2 + O_2^+$. The solid line is an average of various data reported by Lindinger et al.[5]

The rate coefficient for the charge transfer reaction $CO^+ + O_2 \rightarrow CO + O_2^+$ was found to increase with decreasing temperature, approaching the calculated gas kinetic rate of 7.7×10^{-10} cm^3/s at very low temperatures. This reaction is exoergic by 1.950 eV.

The rate coefficient for the charge transfer reaction $CO_2^+ + O_2 \rightarrow CO_2 + O_2^+$ was likewise found to increase with decreasing temperature, approaching the calculated gas kinetic rate of 6.9×10^{-10} cm^3/s at very low temperatures. Our data join smoothly onto the high temperature data of Lindinger et al.,[5] which extend to 900 K and show that the rate coefficient passes through a minimum in the neighborhood of 680 K, implying that a second reaction mechanism becomes effective at higher temperatures. The charge transfer reaction is exoergic by 1.706 eV. All rearrangement reaction channels are forbidden energetically.

The reaction rate coefficients presented above are estimated to be accurate to ±30%. The reaction temperatures are estimated to be correct within 5 K, which is the greatest variation observed among five platinum resistance thermometers mounted along the flow tube. However, at high temperatures this variation was as large as 20 K and hence the temperatures above room temperature are much less certain.

B. Ion Flow Velocities and Injection Shock Effects. As a part of our studies of the behavior of the flowing ion swarms at different temperatures we measured the time-of-flight of the ion swarms. These data are of interest to others using SIFT or flowing afterglow apparatuses for two reasons. First, the ion velocity is needed in order to determine the reaction rate coefficient in Eq. (3), and we are not aware of any work done on this matter other than at room temperature.

Second, the results give evidence for undesirable effects of a shock wave in the flow tube associated with the supersonic helium injector. The SIFT injection shock was brought to general attention by Dupeyrat et al.[6] who studied various injector designs in a flow tube and a wind tunnel. The shock apparently carries ions downstream in the flow tube much faster than they would otherwise travel. The shock presents no problem provided (a) the flow has reached equilibrium by the time the ions arrive at the reactant gas titrant port, and (b) the ion velocity is measured entirely in the equilibrium flow region.

Dupeyrat et al.[6] find that the persistence of the shock downstream in the flow tube depends on the ratio of the gas pressures on either side of the injector. A large pressure drop across the injector means that a greater distance must be allowed for the flow to reach equilibrium. (In the AFGL SIFT apparatus the first titrant port is 34 cm downstream of the helium injector.) We have measured the average ion velocity over the first half of the flow tube and over the second half of the flow tube under widely varying conditions. Some of these data are presented in Table I and have been used by us as a diagnostic to indicate safe conditions for ion-molecule reaction studies.

Also calculated for Table I is the ratio of the average equilibrium ion velocity v_i to the bulk helium velocity v_{He} (determined from the helium throughput and pressure). The ion swarm could be pulsed for time-of-flight data either in the ion source or at an electrode midway down the flow tube. We found that the measured time-of-flight is independent of the precise pulsing scheme (turning the ion current on or off with the pulse, partly or fully) and independent of the mass of the ions (from 12 to 44 amu), within about 1%. The less massive ions

TABLE I. A SAMPLE OF ION VELOCITY RESULTS VERSUS FLOW TUBE PRESSURE AND TEMPERATURE.

Temperature (K)	Pressure (torr)	$v_i^{(1)}$ for first half of flow tube	$v_i^{(1)}$ for second half of flow tube	$\frac{v_i^{(1)}}{v_i^{(2)}}$	$\frac{v_i^{(2)}}{v_{He}}$
92	0.160	5864 cm/s	4909 cm/s	1.19	2.18
	0.200	7687	5385	1.43	2.08
	0.230	8402	5579	1.51	2.10
	0.299	13677	6015	2.27	2.10
	0.372	25293	6608	3.83	2.16
250	0.240	15263	13230	1.15	1.72
	0.320	18689	14040	1.33	1.71
	0.372	21046	14637	1.44	1.71
450	0.460	28649	25141	1.14	1.64
	0.550	32971	26296	1.25	1.68
	0.600	34266	26705	1.28	1.68

clearly diffused more in the pulse, however, as evidenced by the greater width of the arrival time spectra.

Considering only the results for v_i from the equilibrated flow, we find (a) the ratio v_i/v_{He} is independent of pressure at a given temperature, and (b) the ratio v_i/v_{He} is constant for temperatures

above about 270 K but increases at decreasing temperatures below 270 K. The ratio v_i/v_{He} is expected to be greater than unity since the ion density is greatest along the axis of the flow tube where the helium velocity is the greatest.[1,7] However, it has heretofore been assumed that the parabolic velocity profile across the diameter of the flow tube was essentially the same at all temperatures, and therefore the ratio v_i/v_{He} would be independent of temperature. Our data indicate that the helium velocity profile across the flow tube becomes more sharply peaked at low temperatures, leading to a larger value of v_i and hence of v_i/v_{He}. This conclusion is supported by viscous flow measurements we have made which imply that a molecular slip contribution is more important at low temperatures. Sufficient molecular slip would decrease the radius of the region of viscous flow and modify the helium velocity profile across the tube.[8] Further analysis of the flow problem is needed at this point before we can offer a quantitative explanation of our results.

C. Other Ion-Molecule Reaction Data. We have obtained a few preliminary results for N^+ and N_2^+ ions reacting with O_2, CO, and NO and for C^+ + NO. These studies are in too early a stage to report on here. Data for C^+ + NO and N^+ + CO are needed for comparison to recent atomic beam results.[9]

IV. RECOMMENDATIONS:

An abstract for a paper on this research has been submitted for presentation at the Gaseous Electronics Conference in Dallas in

October 1982,[10] and we anticipate that one journal article will be prepared on the ion-molecule reaction results and a second article will be written on the implications of the SIFT ion velocity data we have obtained.

We still need to carry out some analytic work in regard to the helium flow problem, as discussed in Sect. III-B, with the goal of supporting our ion velocity data with calculations. These results are important for research with flow-tube reactors (SIFT and flowing afterglow). Very little work has been done at low temperatures, but as the number of flow-tube reactors in use around the world grows, the flow problem must be worked out.

ACKNOWLEDGMENTS

We wish to thank our colleagues at AFGL, John Paulson, Fred Dale, and Tim Thomas, for making our summer exciting and scientifically rewarding; for trusting us with the SIFT apparatus; and for their help minimizing the problems of settling into a new environment. We also thank the Air Force Systems Command, the Air Force Office of Scientific Research, and the Air Force Geophysics Laboratory for making our participation in this research possible.

REFERENCES

1. N. G. Adams and D. Smith, "The Selected Ion Flow Tube (SIFT): A Technique for Studying Ion-Neutral Reactions," Int. J. Mass Spectrom. Ion Phys., Vol. 21, pp. 349-359 (1976).

2. N. G. Adams and D. Smith, "Product-Ion Distributions for Some Ion-Molecule Reactions," J. Phys. B, Vol. 9, pp. 1439-1451 (1976).

3. A. B. Rakshit, H. M. P. Stock, D. P. Wareing, and N. D. Twiddy, "Ion-Molecule Reaction Rates at 100 and 300 K," J. Phys. B, Vol. 11, pp. 4237-4247 (1978).

4. N. G. Adams, D. Smith, and D. Grief, "Reactions of H_nCO^+ Ions with Molecules at 300 K," Int. J. Mass Spectrom. Ion Phys., Vol. 26, pp. 405-415 (1978).

5. W. Lindinger, F. C. Fehsenfeld, A. L. Schmeltekopf, and E. E. Ferguson, "Temperature Dependence of Some Ionospheric Ion-Neutral Reactions from 300-900 K," J. Geophys. Res., Vol. 79, pp. 4753-4756 (1974).

6. G. Dupeyrat, B. R. Rowe, D. W. Fahey, and D. L. Albritton, "Diagnostic Studies of Venturi-Inlets for Flow Reactors," Int. J. Mass Spectrom. Ion Phys., in press.

7. E. E. Ferguson, F. C. Fehsenfeld, and A. L. Schmeltekopf, "Flowing Afterglow Measurements of Ion-Neutral Reactions," Adv. At. Mol. Phys., Vol. 5, pp. 1-56 (1969).

8. E. H. Kennard, Kinetic Theory of Gases (New York, McGraw-Hill,

1938), p. 294.

9. W. Frobin, Ch. Schlier, K. Strein, and E. Teloy, "Ion-Molecule Reactions of N^+ with CO: Integral Reactive Cross Sections in the Collision Energy Range 0.2-13 eV," J. Chem. Phys., Vol. 67, pp. 5505-5516 (1978); also, private communication.

10. T. M. Miller, R. E. Wetterskog, and J. F. Paulson, "Reaction Rate Coefficients for C^+, CO^+, and $CO_2^+ + O_2$," Bull. Am. Phys. Soc., to be published.

1982 USAF-SCEEE SUMMER FACULTY RESEARCH PROGRAM

Sponsored by the

AIR FORCE OFFICE OF SCIENTIFIC RESEARCH

Conducted by the

SOUTHEASTERN CENTER FOR ELECTRICAL ENGINEERING EDUCATION

FINAL REPORT

ANALYSIS AND COMMENTS ON THE THEORY OF THE CAPACITANCE-RATIO TEST

Prepared by:	Dr. R. L. Remke Kevin Wilson
Academic Rank:	Assistant Professor Graduate Student
Department and University:	Dept of Electrical and Electronic Systems, Univ. of South Florida
Research Location:	Rome Air Development Center, Rome, NY Reliability Branch, Product Evaluation Section, Reliability and Compatibility Division
USAF Research Colleague:	Dr. Robert W. Thomas
Date:	September 10, 1982
Contract No:	F49620-82-C-0035

ACKNOWLEDGEMENTS

The authors would like to gratefully acknowledge the invaluable assistance and gracious hospitality rendered by the Product Evaluation Section of the Reliability Branch at Rome Air Development Center (RADC) in Rome, NY, and in particular the Section Chief, Dr. Robert Thomas. A special thanks to Charles Windisch of RADC/RBRE for his daily assistance and cooperation, and to Dr. Mike Kovac of the University of South Florida for providing the link to make this effort possible.

Finally, the authors would like to acknowledge the sponsorship of the Air Force Systems Command, Air Force Office of Scientific Research (AFOSR) and the Southeastern Center for Electrical Engineering Education (SCEEE).

ANALYSIS AND COMMENTS ON THE THEORY OF THE CAPACITANCE-RATIO TEST

BY

R. L. REMKE

K. WILSON

University of South Florida

ABSTRACT

A detailed analysis is given on the theory of the capacitance-ratio test used in the detection of moisture in hermetically sealed microelectronic packages. The model for the moisture-induced frequency-dependent capacitance observed between pins of an integrated circuit is developed. This model is then extended to describe its use in the capacitance-ratio test. Also included are some observations and comments concerning the implementation and use of the capacitance-ratio test.

1. INTRODUCTION

The capacitance-ratio test is presently being evaluated and tested by Rome Air Development Center (RADC) as a non-destructive method for determining the moisture-induced capacitance between two metallization lines in an integrated circuit package. This capacitance is compared with a known reference to determine if the moisture content of the package is less than or greater than the reference.

The theory and practice of the capacitance-ratio test was originally postulated and developed by R. Merrett[1,2], and has been proposed as an alternative to the existing standard moisture content tests. However, to properly implement and interpret the data of the capacitance-ratio test, an understanding of the theory of the measurement technique is essential. In addition, an acute understanding of the mechanisms influencing the measurement, provides insight into additional potential applications for the technique.

In this document, the theory of the capacitance ratio-test is analyzed in detail, beginning with Section 2, which outlines the objectives of the project. Section 3 describes the derivation of the characteristic impedance and propagation constant in the distributed element model of adsorbed water, above a metal track in an integrated circuit package. Section 4 then uses the general transmission line equation to convert the distributed parameters into a representative lumped-element network. The T-network is simplified in Section 5 on the basis of appropriate approximations, as presented in a numerical example. The equivalent circuit model is given in Section 6 for the most general case of multiple parallel metallization tracks. From this equivalent circuit model, the frequency dependent and independent capacitances, used in the capacitance-ratio, are defined in Section 7. Section 8 discusses the relation used in the measurement of the capacitance-ratio. Section 9 outlines the derivation of the failure criterion based on the results of the calibration procedure. Results of the initial measurements, and recommendations for further testing and applications of the technique are given in Sections 10 and 11, respectively.

2. OBJECTIVES

The primary objectives of this project were to analyze the theory and give further empirical evidence on the capacitance-ratio test as a means for determining the relative moisture content of integrated circuit packages. While a comprehensive study of the measurement technique was beyond the scope of this project, the following were project objectives:

(1) Analyze in detail the model for moisture-induced and frequency-dependent capacitance observed between two metallization tracks.

(2) Analyze the application of the model in the capacitance-ratio test.

(3) Assist in the implementation of the capacitance-ratio test system as a viable moisture detection system, through establishment of a data base.

(4) Correlate the test results in the capacitance-ratio data base with those from the mass spectrometer.

(5) Investigate the use of the capacitance-ratio test as a leak detection technique.

3. THE CHARACTERISTIC IMPEDANCE AND PROPAGATION CONSTANT OF A LAYER OF ADSORBED WATER ABOVE A METALLIZATION TRACK

The theory of the capacitance-ratio test is based on a distributed element analysis similar to that used in transmission line analysis. For convenience, a brief review of distributed element theory is presented in Appendix A.

The characteristic impedance, Zo^*, and the propagation constant, γ^*, of the cell shown in Fig. 1(a), (see also Fig. 2) which represents the region above a single metal track, can be found by considering the following:

a. the resistance per unit length between edges aa' and bb', and

b. the capacitance per unit length between the adsorbed water and the metal track.

3.1 DISTRIBUTED SERIES IMPEDANCE

For a layer of adsorbed water of thickness, t, the resistance per unit length is given by

$$R \text{ (ohms/m)} = 1/(\sigma' A)$$

where σ' is the conductivity in mhos/m. For a cross-sectional area, $A = Lt$,

$$R = 1/(\sigma' Lt)$$

Since the surface conductivity is defined as $\sigma \text{ (mhos)} = \sigma' t$, the distributed series impedance per unit length, Z, is

$$Z = R = 1/(\sigma L) \qquad (1)$$

3.2 DISTRIBUTED SHUNT ADMITTANCE

The capacitance between the adsorbed water and the metal track is

$$C = \varepsilon A'/d$$

where A' is the cross-sectional area LW, ε is the permittivity of the material, and the depth of the dielectric spacing is d .

If c_o^* is defined as the capacitance per unit area,

$$c_o^* = C/A' = \varepsilon/d \qquad (2)$$

and the capacitance per unit length in the x direction is

$$C' \text{ (farads/m)} = (C/A')\, L = c_o^* L$$

then the distributed shunt admittance per unit length, Y, is

$$Y = j\omega(c_o^* L) \tag{3}$$

3.3 CHARACTERISTIC IMPEDANCE

The characteristic impedance is defined (Reference Appendix A) as

$$Z_o^* = \sqrt{Z/Y} = Z/\gamma^* \tag{4}$$

where γ^* is the propagation constant.

Substituting eqns. (1) and (3) into eqn. (4),

$$Z_o^* = \sqrt{\frac{1/\sigma L}{j\omega c_o^* L}} = (1\angle -90^\circ)^{1/2}\left(\frac{1}{L}\right)\sqrt{\frac{1}{\omega c_o^* \sigma}}$$

$$= (1-j)\frac{1}{L}\sqrt{\frac{1}{2\omega c_o^* \sigma}} \tag{5}$$

From eqn. (4), $\gamma^* = \sqrt{ZY}$, therefore,

$$\gamma^* = \sqrt{\left(\frac{1}{\sigma L}\right)(j\omega c_o^* L)} = \sqrt{\frac{j\omega c_o^*}{\sigma}}$$

$$= (1\angle 90^\circ)^{1/2}\sqrt{\frac{\omega c_o^*}{\sigma}}$$

or, $$\gamma^* = (1+j)\sqrt{\frac{\omega c_o^*}{2\sigma}} \tag{6}$$

4. LUMPED ELEMENT T-NETWORK MODEL

Having determined the characteristic impedance, Z_o^*, and the propagation constant, γ^*, the lumped elements in the representative network, as shown in Fig. 1(b), can be determined.

Given (see Appendix B , noting the change in notation)

$$Z_2^* = \sqrt{Z_{2oc}\left(Z_{1oc} - Z_{1sc}\right)} \tag{7a}$$

$$Z_1^* = Z_{1oc} - Z_2^* \tag{7b}$$

and the general transmission line equation (see Appendix A)

$$Z_i = Z_o^*\left(\frac{Z_L \cosh\gamma^*\ell + Z_o^* \sinh\gamma^*\ell}{Z_o^* \cosh\gamma^*\ell + Z_L \sinh\gamma^*\ell}\right) \tag{8}$$

then,

$$Z_{1oc} = Z_i\Big|_{Z_L\to\infty} = \lim_{Z_L\to\infty}\left[Z_o^*\,\frac{\cosh\gamma^*\ell + \left(\frac{Z_o^*}{Z_L}\right)\sinh\gamma^*\ell}{\left(\frac{Z_o^*}{Z_L}\right)\cosh\gamma^*\ell + \sinh\gamma^*\ell}\right]$$

$$Z_{1oc} = Z_o^*\left(\frac{\cosh\gamma^*\ell}{\sinh\gamma^*\ell}\right) = Z_o^* \coth\gamma^*\ell \tag{9}$$

and,

$$Z_{1sc} = Z_i\Big|_{Z_L\to 0} = Z_o^*\,\frac{\sinh\gamma^*\ell}{\cosh\gamma^*\ell}$$

$$= Z_o^* \tanh\gamma^*\ell \tag{10}$$

Since the transmission line is a reciprocal, or bilateral network[3],

$$Z_{2oc} = Z_{1oc} = Z_o^* \coth \gamma^* \ell \tag{11}$$

So, from eqn. (7a) $Z_2^* = \sqrt{(Z_o^* \coth \gamma^* \ell)(Z_o^* \coth \gamma^* \ell - Z_o^* \tanh \gamma^* \ell)}$

$$= Z_o^* \sqrt{\coth^2 \gamma^* \ell - \coth \gamma^* \ell \tanh \gamma^* \ell}$$

But $\coth x \tanh x = 1$

then $Z_2^* = Z_o^* \sqrt{\coth^2 \gamma^* \ell - 1}$

Using the hyperbolic trigonometric identity

$$\coth^2 x - 1 = \operatorname{csch}^2 x = \frac{1}{\sinh^2 x}$$

then

$$Z_2^* = Z_o^* \sqrt{\operatorname{csch}^2 \gamma^* \ell} = Z_o^* \operatorname{csch} \gamma^* \ell \tag{12}$$

From eqn. (7b) $Z_1^* = Z_{1oc} - Z_2^*$

so, $Z_1^* = Z_o^* \coth \gamma^* \ell - \frac{Z_o^*}{\sinh \gamma^* \ell}$

$$Z_1^* = Z_o^* \left(\frac{\cosh \gamma^* \ell - 1}{\sinh \gamma^* \ell} \right)$$

Using the hyperbolic trigonometric identity

$$\tanh \frac{x}{2} = \frac{\cosh x - 1}{\sinh x}$$

then $Z_1^* = Z_o^* \tanh \left(\frac{\gamma^* \ell}{2} \right)$ (13)

Noting that the "length of the transmission line", $\ell = W$, then

$$Z_1^* = Z_o^* \tanh \left(\frac{\gamma^* W}{2} \right) \tag{14}$$

and $$Z_2^* = Z_c^* \operatorname{csch}(\gamma^* W) \qquad (15)$$

5. SIMPLIFIED T-NETWORK

From the general relations in eqns. (14) and (15) defining the lumped elements in the representative network, a simplified network model can be obtained under certain approximation conditions. These approximation conditions place a limitation on the lower test frequency to be used in the capacitance ratio test.

Considering the following representative values:

ϵ (overglaze -SiO_2) = 3.9

d (thickness of overglaze) = 6000Å

σ (surface conductivity of adsorbed water) = 10^{-14} mho

W (width of metal track) = 6μm

F_L (lower test requency) = 83Hz

These approximate values for the parameters in the equation for the propagation constant can be used to calculate the magnitude of this term. Thus,

$$C_o^* = \frac{\epsilon}{d} = \frac{3.9(8.854\times10^{-12}\ F/m)}{(6000\text{Å})(1\times10^{-10}\ m/\text{Å})}$$

$$C_o^* = 57.6\ \mu F/m^2$$

and therefore $\gamma'' = (1+j)\sqrt{\frac{\omega C_0''}{2\sigma}}$

$$|\gamma''| = \left(\frac{\omega C_0''}{\sigma}\right)^{1/2} = \left(\frac{2\pi F_L C_0''}{\sigma}\right)^{1/2}$$

$$= \left(\frac{2\pi(83\,Hz)(576\times10^{-6}\,F/m)}{10^{-14}\,mhos}\right)^{1/2}$$

$$= 1.73\times10^{6}\ nepers/m$$

Then $|\gamma''|W = (1.73\times10^{6}\ nepers/m)(6\times10^{-6}m) = 10.4\ nepers$

From the plot of the hyperbolic tangent function, shown in Fig. 3, it can be seen that if the argument of the hyperbolic tangent function is greater than 3, the functional value is approximately equal to unity. Thus,

$$\tanh\left(\frac{|\gamma''|W}{2}\right) \cong 1 \quad \text{for} \quad |\gamma''|W >> 1$$

and as a result, since $Z_1'' = Z_0'' \tanh\left(\frac{\gamma''W}{2}\right)$

then $Z_1'' \cong Z_0'' \quad \text{for} \quad |\gamma''|W >> 1$

Similiar ly, from the plot of the hyperbolic cosecant function shown in Fig. 4, it can be seen that if the argument of the hyperbolic cosecant is greater than 6, the functional value is approximately equal to zero. That is,

$$\operatorname{csch}(|\gamma''|W) \cong 0 \quad \text{for} \quad |\gamma''|W >> 1$$

and as a result, since $Z_2^* = Z_o^* \operatorname{csch}(\gamma^* W)$

then $Z_2^* \cong 0 \quad \text{for } |\gamma^*|W >> 1$

5.1 MODEL FOR THE REGION BETWEEN THE TRACKS

From this model of the region above a single metal track, a similar model can be developed for the region between the metallization tracks, as shown in Fig. 2. The parameters Z_1 and Z_2 in the lumped element T-network model of this region, are derived in a similar fashion as the derivation for Z_1^* and Z_2^*. For a spacing between the metallization tracks of width S, and under the approximation that $|\gamma|S >> 1$

$$Z_1 \cong Z_o \quad \text{and} \quad Z_2 \cong 0$$

where $$Z_o = (1-j)\frac{1}{L}\sqrt{\frac{1}{2\omega C_o \sigma}} \tag{16}$$

and c_o is the capacitance per unit area between the film of adsorbed water and the substrate.

6. EQUIVALENT CIRCUIT MODEL

For the case of an interdigitated structure, that is, for multiple parallel tracks, the representative network is shown in Fig. 5. Z_1^*, Z_2^*, Z_1, and Z_2 are as previously defined, and C_T is the capacitance between the metal track and the substrate. This is defined as

$$C_T = c_T L W$$

where c_T is the capacitance per unit area between the metal track and the substrate.

Under the appropriate approximation conditions, $|\gamma^*|W >> 1$ and $|\gamma|S >> 1$, the simplified multiple track network model is shown in Fig. 6. Reduction of this

network into an equivalent circuit model can be done by first reducing a single section from node A to node B, as shown in Figs (6) and (7). The resulting equivalent impedance is

$$Z_{EQ} = Z_c /\!/ Z_s + Z_c /\!/ Z_s$$

$$Z_{EQ} = 2\left(\frac{1}{\frac{1}{(Z_o + Z_o^*)} + j\omega C_T}\right) \tag{17}$$

So, $$Y_{EQ} = 1/Z_{EQ} = \frac{1}{2}\left(\frac{1}{Z_o + Z_o^*} + j\omega C_T\right)$$

and since $$C_T = c_r L W$$

$$Y_{EQ} = \frac{1}{2}\left(\frac{1}{Z_o + Z_o^*} + j\omega c_r L W\right) \tag{18}$$

For n tracks, there are n-1 networks of this form in parallel, therefore the overall admittance is

$$Y = (n-1)\, Y_{EQ} = \frac{n-1}{2}\left(\frac{1}{Z_o + Z_o^*} + j\omega c_r L W\right)$$

7. DEFINITION OF CAPACITANCE TERMS

For the case of only two tracks, as expressed in eqn. (18), the equivalent admittance is,

$$Y_{EQ} = \frac{1}{2}\left\{\frac{1}{(1-j)\frac{1}{L}\frac{1}{\sqrt{2\omega x_o^* \sigma}} + (1-j)\frac{1}{L}\frac{1}{\sqrt{2\omega c_o \sigma}}} + j\omega c_r L W\right\}$$

$$= \frac{1}{2}\left\{\frac{L\sqrt{2\omega\sigma}}{(1-j)\left(\frac{1}{\sqrt{c_o}} + \frac{1}{\sqrt{c_o^*}}\right)} + j\omega c_r L W\right\}$$

$$= \frac{1}{2}\left\{\frac{L\sqrt{2\omega c_o \sigma}}{(1-j)\left(1 + \sqrt{c_o/c_o^*}\right)} + j\omega c_r L W\right\} \tag{20}$$

Let $$\frac{1}{K_1} = \frac{L\sqrt{2\omega c_o \sigma}}{1 + \sqrt{c_o/c_o^*}} \tag{21}$$

and $$K_2 = \omega C_T L W \tag{22}$$

so $$Y_{EQ} = \frac{1}{2}\left\{\frac{1}{(1-j)K_1} + jK_2\right\}$$

$$= \frac{1}{2}\left\{\frac{(1+j)}{2K_1} + jK_2\right\}$$

$$= \frac{1}{4K_1} + j\left(\frac{1}{4K_1} + \frac{K_2}{2}\right)$$

$$= \frac{1}{4K_1} + j\omega\left(\frac{1}{4\omega K_1} + \frac{K_2}{2\omega}\right)$$

$$= G + j\omega C \tag{23}$$

Thus, $\left(\frac{1}{4\omega K_1} + \frac{K_2}{2\omega}\right)$ represents the capacitive term, C, in the equivalent admittance model as shown in Fig. 8. Defining,

$$C_W = \frac{1}{4\omega K_1} = \frac{1}{4\omega}\left(\frac{L\sqrt{2\omega C_0 \sigma}}{1+\sqrt{C_0/C_0''}}\right)$$

$$C_W = \frac{L}{2}\sqrt{\frac{C_0\sigma}{2\omega}}\ \frac{1}{1+\sqrt{C_0/C_0''}} \tag{24}$$

and $$C_i = \frac{K_2}{2\omega} = \frac{\omega C_T L W}{2\omega}$$

$$C_i = \frac{1}{2} C_T L W \tag{25}$$

From these two capacitance terms, given in eqns. (24) and (25), the capacitance ratio, ϕ, can be defined as

$$\phi = \frac{C_W}{C_i} = \frac{\frac{L}{2}\sqrt{\frac{C_0\sigma}{2\omega}}\left(\frac{1}{1+\sqrt{C_0/C_0''}}\right)}{\frac{1}{2} C_T L W}$$

$$\phi = \frac{1}{C_T W}\sqrt{\frac{C_0\sigma}{2\omega}}\left(\frac{1}{1+\sqrt{C_0/C_0'}}\right) \tag{26}$$

8. MEASUREMENT OF THE CAPACITANCE RATIO

The capacitance, C, is given by

$$C = C_i + C_W \tag{27}$$

From eqn. (25) it can be seen that Ci is a frequency independent term, and represents the INHERENT CAPACITANCE, and from eqn (24), it can be seen that Cw is the FREQUENCY DEPENDENT CAPACITANCE, representing the partial capacitance contribution due to the adsorbed water.

Thus, since $\phi(\omega) = \frac{C_W}{C_i} = \frac{1}{C_T W}\sqrt{\frac{C_0\sigma}{2\omega}}\left(\frac{1}{1+\sqrt{C_0/C_0'}}\right)$

$$\phi(\omega) = \frac{k_0}{\sqrt{\omega}} \tag{28}$$

and $$\frac{\phi(\omega_2)}{\phi(\omega_1)} = \frac{k_0/\sqrt{\omega_2}}{k_0/\sqrt{\omega_1}} = \sqrt{\frac{\omega_1}{\omega_2}}$$

or $$\phi(\omega_2) = \phi(\omega_1)\left(\frac{\omega_1}{\omega_2}\right)^{1/2} \tag{29}$$

From eqns. (26) and (27), $\phi(\omega) = \frac{C_W}{C_i}$ and $C(\omega) = C_i + C_W(\omega)$

so, $$C_W(\omega) = C(\omega) - C_i$$

then $$\phi(\omega) = \frac{C(\omega) - C_i}{C_i} = \frac{C(\omega)}{C_i} - 1$$

so, $$C_i = \frac{C(\omega)}{\phi(\omega) + 1}$$

Since Ci is frequency independent,

$$C_i = \frac{C(\omega_1)}{\phi(\omega_1) + 1} = \frac{C(\omega_2)}{\phi(\omega_2) + 1}$$

So, $$C(\omega_1)\left[\phi(\omega_2)+1\right] = C(\omega_2)\left[\phi(\omega_1)+1\right]$$

and then $$\phi(\omega_2) = \frac{C(\omega_2)\phi(\omega_1) + C(\omega_2) - C(\omega_1)}{C(\omega_1)}$$

but, $$\phi(\omega_2) = \left(\frac{\omega_1}{\omega_2}\right)^{1/2}\phi(\omega_1)$$

then $$\left(\frac{\omega_1}{\omega_2}\right)^{1/2}\phi(\omega_1) = \frac{C(\omega_2)\phi(\omega_1) + C(\omega_2) - C(\omega_1)}{C(\omega_1)}$$

$$\left(\frac{\omega_1}{\omega_2}\right)^{1/2}\phi(\omega_1) = \frac{C(\omega_2)}{C(\omega_1)}\phi(\omega_1) + \frac{C(\omega_2) - C(\omega_1)}{C(\omega_1)}$$

$$\phi(\omega_1)\left[\left(\frac{\omega_1}{\omega_2}\right)^{1/2} - \frac{C(\omega_2)}{C(\omega_1)}\right] = \frac{C(\omega_2) - C(\omega_1)}{C(\omega_1)}$$

$$\phi(\omega_1)\left[C(\omega_1)\left(\frac{\omega_1}{\omega_2}\right)^{1/2} - C(\omega_2)\right] = C(\omega_2) - C(\omega_1)$$

$$\phi(\omega_1) = \frac{C(\omega_2) - C(\omega_1)}{C(\omega_1)\left(\frac{\omega_1}{\omega_2}\right)^{1/2} - C(\omega_2)} \qquad (30)$$

Where $\omega_2 >> \omega_1$, and $C(\omega_1)$ and $C(\omega_2)$ are comparable in magnitude, eqn. (30) reduces to

$$\phi(\omega_1) = \frac{C(\omega_1) - C(\omega_2)}{C(\omega_2)} \qquad (31)$$

9. DERIVATION OF THE FAILURE CRITERION

For experimental convenience, the calibration procedure is performed at room temperature. Since the capacitance-ratio test is performed at a lower temperature, the failure criterion as deduced from the calibration procedure, must be extrapolated to the testing temperature. The fundamentals of this extrapolation are given below, prefaced by a brief summary of the terminology used.

9.1 TERMINOLOGY

In general, the capacitance (C) measured across two pins of an IC is a function of temperature (T), frequency (F), and relative humidity (RH). Where the previous analysis has assumed ideal isolated metallization strips, actual strips are connected to circuit elements. These circuit elements may exhibit a frequency and temperature dependent capacitance, Cp (T, F).

If Δ is defined as the difference in capacitance at the two test frequencies (F_H, F_L indicate the higher and lower test frequencies, respectively), then

$$\Delta(T, RH) = C(T, F_L, RH) - C(T, F_H, RH) \tag{32}$$

but, since each of the capacitances above has a frequency dependent and independent component as discussed previously, and a circuit element component, then

$$C(T, F, RH) = C_W(T, F, RH) + C_L(T) + C_P(T, F) \tag{33}$$

and

$$\Delta(T, RH) = C_W(T, F_L, RH) + C_L(T) + C_P(T, F_L) - C_W(T, F_H, RH) - C_L(T) - C_P(T, F_H)$$

$$\Delta(T, RH) = C_W(T, F_L, RH) - C_W(T, F_H, RH) + C_P(T, F_L) - C_P(T, F_H) \quad (34)$$

If we define a moisture-induced capacitance difference, Δ_m (T, RH), and the circuit element capacitance difference, Δ_p(T), then

$$\Delta(T, RH) = \Delta_m(T, RH) + \Delta_p(T) \quad (35)$$

where $$\Delta_m(T, RH) = C_W(T, F_L, RH) - C_W(T, F_H, RH)$$

and $$\Delta_p(T) = C_P(T, F_L) - C_P(T, F_H)$$

Defining δ as the difference in capacitance due to moisture in the two calibration environments,

$$\delta = C(T_c, F_H, RH_W) - C(T_c, F_H, RH_D) \quad (36)$$

where T_C - calibration temperature (room temperature)

RH_D - relative humidity of dry nitrogen gas (< 5%)

RH_W - relative humidity of wet environment (75% RH)

Substituting eqn. (33) into eqn. (36),

$$\delta = C_W(T_c, F_H, RH_W) + C_i(T_c) + C_P(T_c, F_H) - C_W(T_c, F_H, RH_D) - C_i(T_c) - C_P(T_c, F_H)$$

$$\delta = C_W(T_c, F_H, RH_W) - C_W(T_c, F_H, RH_D)$$

However, since there is no moisture present in a dry environment to produce the capacitive effect,

$$C_W(T_c, F_H, RH_0) \cong 0$$

and as a result,

$$\delta = C_W(T_c, F_H, RH_W) \tag{37}$$

9.2 THE FAILURE CRITERION

The parameter of primary interest in the capacitance-ratio test is the $\Delta_m(T, RH)$ term of eqn. (35). For the calibration temperature, T_c, and test temperature, T_t, the moisture-indiced capacitance difference may be written,

$$\Delta_m(T_c, RH) = C_W(T_c, F_L, RH) - C_W(T_c, F_H, RH) \tag{38}$$

and

$$\Delta_m(T_t, RH) = C_W(T_t, F_L, RH) - C_W(T_t, F_H, RH) \tag{39}$$

From eqn. (24)

$$C_W(T, F, RH) = \frac{\frac{L}{2}\sqrt{\frac{C_0\sigma}{2\omega}}}{1+\sqrt{C_0/C_0''}} = k\sqrt{\frac{\sigma}{f}} \tag{40}$$

where surface conductivity is given by[4]

$$\sigma(T) = \sigma_0 \exp\left(\frac{-\varepsilon}{kT}\right)$$

and the associated activation energy has been experimentally determined [2] to be 0.4 eV.

Then,

$$\frac{\Delta m\,(T_t, RH)}{\Delta m\,(T_c, RH)} = \frac{k\sqrt{\frac{\sigma(T_t)}{F_L}} - k\sqrt{\frac{\sigma(T_t)}{F_H}}}{k\sqrt{\frac{\sigma(T_c)}{F_L}} - k\sqrt{\frac{\sigma(T_c)}{F_H}}} \tag{41}$$

$$\frac{\Delta m\,(T_t, RH)}{\Delta m\,(T_c, RH)} = \frac{\sqrt{\sigma(T_t)}\left(\frac{1}{\sqrt{F_L}} - \frac{1}{\sqrt{F_H}}\right)}{\sqrt{\sigma(T_c)}\left(\frac{1}{\sqrt{F_L}} - \frac{1}{\sqrt{F_H}}\right)}$$

so, $$\Delta m\,(T_t, RH) = \Delta m\,(T_c, RH)\sqrt{\frac{\sigma(T_t)}{\sigma(T_c)}}$$

$$= \Delta m\,(T_c, RH)\left(\frac{\sigma_0\, exp\,(-\mathcal{E}/kT_t)}{\sigma_0\, exp\,(-\mathcal{E}/kT_c)}\right)^{1/2}$$

$$= \Delta m\,(T_c, RH)\; exp\left[\frac{\mathcal{E}}{2k}\left(\frac{1}{T_c} - \frac{1}{T_t}\right)\right] \tag{42}$$

where $$\frac{\mathcal{E}}{2k} = \frac{0.4\,eV}{2(8.62\times10^{-5}\,eV/{}^{\circ}K)} = 2.32\times10^{3}\,{}^{\circ}K$$

Then $$\Delta m\,(T_t, RH) = \Delta m\,(T_c, RH)\,exp\left[2.32\times10^{3}\left(\frac{1}{T_c} - \frac{1}{T_t}\right)\right] \tag{43}$$

This equation can be expressed in alternate form by considering the expressions in eqns. (35) and (37).

where $$\Delta m\,(T_c, RH_W) = C_W\,(T_c, F_L, RH_W) - C_W\,(T_c, F_H, RH_W)$$

and $$\delta = C_W\,(T_c, F_H, RH_W)$$

then $$\Delta m\,(T_c, RH_W) = C_W\,(T_c, F_L, RH_W) - \delta \tag{44}$$

Refering again to eqn. (43), $$C_W\,(T_c, F_L, RH_W) = k\sqrt{\frac{\sigma(T_c)}{F_L}}$$

and $$\delta = C_W\,(T_c, F_H, RH_W) = k\sqrt{\frac{\sigma(T_c)}{F_H}}$$

so, $$\frac{C_W\,(T_c, F_L, RH_W)}{\delta} = \frac{k\sqrt{\frac{\sigma(T_c)}{F_L}}}{k\sqrt{\frac{\sigma(T_c)}{F_H}}} = \sqrt{\frac{F_H}{F_L}}$$

$$C_W\,(T_c, F_L, RH_W) = \delta\sqrt{\frac{F_H}{F_L}} \tag{45}$$

but where $$F_H = 10F_L$$

then $$C_W\,(T_c, F_L, RH_W) = 3.16\,\delta \tag{46}$$

and substituting back into eqn. (44) yields

$$\Delta_m(T_c, RH_W) = 3.16\,\delta - \delta = 2.16\,\delta \tag{47}$$

Thus, from this relation and eqn. (43),

$$\Delta m\,(T_t, RH_W) = 2.16\,\delta\,\exp\left[2.32\times10^3\left(\frac{1}{T_c} - \frac{1}{T_t}\right)\right] \tag{48}$$

We define Δ_m' as the failure criterion given by

$$\Delta_m' = \Delta m\,(T_t, RH_W)$$

$$\Delta_m' = 2.16\,\delta\,\exp\left[2.32\times10^3\left(\frac{1}{T_c} - \frac{1}{T_t}\right)\right] \tag{49}$$

where $\bar{\delta}$ is the average δ over the calibration samples.

9.3 THE TEST APPROXIMATION

Recalling from eqn. (34) that

$$\Delta(T, RH) = C_W(T, F_L, RH) - C_W(T, F_H, RH) + C_P(T, F_L) - C_P(T, F_H)$$

Then if the capacitance due to the circuit elements is generally frequency independent, the capacitance difference may be written at the test temperature

$$\Delta(T_t, RH) \cong C_W(T_t, F_L, RH) - C_W(T_t, F_H, RH) = \Delta m$$

This approximation has been discussed by Merrett[2] and is used in the test procedure discussed in the following sections.

10. CAPACITANCE-RATIO TEST PROCEDURES AND INITIAL RESULTS

The apparatus and procedure for performing the capacitance-ratio test was implemented according to the description by Merrett[1,2]. A block diagram summary of the procedure is given in Figure 9. Initially, the relation between junction voltage and temperature for a forward biased pn junction on the die is determined. This junction is used in the test to monitor the die temperature. Two pins are then chosen for the capacitance-ratio test using the selection criteria as described by Merrett[2]. The response of the die to moisture is determined in the calibration procedure. The change in capacitance between the pins is measured as the relative humidity is varied from $<$ 5% RH to 75% RH. This change in capacitance is then used to calculate the moisture induced capacitance at the test temperature (T_t). Several samples are used in the calibration procedure and the average change in capacitance is used. The final step in the capacitance-ratio test involves cooling the die down to the test temperature while maintaining the lid temperature at $\geq 15^{\circ}C$. The change in capacitance between the two pins at the high and low frequencies is measured and compared with the previously calculated value obtained from the calibration procedure. If for each sample, the change in capacitance measured in the test is greater than that determined from the calibration procedure, the CERDIP tested has an unacceptable moisture content. In making this comparison, the reader is referred to the comments of Merrett[1,2] concerning the sensitivity and sources of error involved.

The capacitance-ratio test was performed on several linear and digital integrated circuits. Temperature calibration was obtained using diodes within the circuits, yielding a change in the forward biased junction voltage with temperature of, typically two to three $mv/^{\circ}C$ for 50 microamperes constant current. The calibration procedure was performed at 830 Hz as the relative humidity was varied from $<$ 5% RH to 75% RH. As the relative humidity increased, the capacitance between the pins increased. Typical values of ζ ranged from 0.1 pF to 0.8 pF and some variation was observed from die to die in the

AD-A130 767 USAF/SCEEE GRADUATE STUDENT SUMMER SUPPORT PROGRAM (1982) MANAGEMENT AND..(U) SOUTHEASTERN CENTER FOR ELECTRICAL ENGINEERING EDUCATION INC S..

5/6

UNCLASSIFIED W D PEELE ET AL. OCT 82 AFOSR-TR-83-0611 F/G 5/9 NL

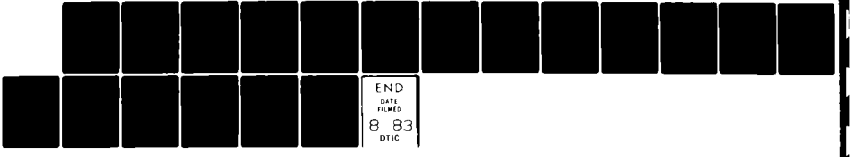

END
DATE FILMED
8 83
DTIC

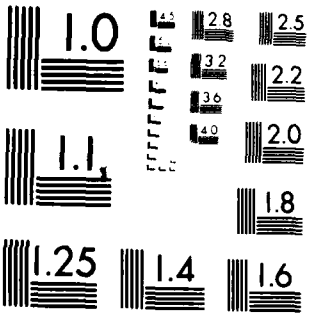

magnitude of δ. This variation has been previously discussed by Merrett.[1] The capacitance-ratio test was performed at 83 Hz and 830 Hz using a die temperature of -5.5°C and a lid temperature of 15°C. Initial results indicate the test is performing as expected with the experimental results to be compared with those of the mass spectrometer. It is recommended that this initial work be continued and a comprehensive data base on capacitance-ratio test results be established, with correlation from the mass spectrometer.

An interesting phenomena was observed when certain CERDIP packages (unopened) were exposed to the ambients used in the calibration procedure. In several cases, a change in capacitance at 83 Hz was noted when the ambient was varied from $<$ 5% RH to 75% RH. This change ranged from .1 pF to 0.4 pF and the time constants were approximately those observed in the die calibration procedure. This change in capacitance is believed to be due to the preferential adsorption of moisture in cracks in the sealing glass of the integrated circuit. Further study of this phenomena is recommended to evaluate its potential as a crack detection technique.

Since the capacitance-ratio test measures the relative amount of moisture in a package, the test offers potential as a leak detection technique. To test for package leaks, the capacitance-ratio test could be used to measure the increase in the moisture content of packages after they have been "bombed" in a humid environment. Leaky packages should exhibit an increase in moisture content after "bombing", whereas hermetically sealed packages should show no change. This use of the capacitance-ratio test is recommended for further study.

In addition to the previously described uses of the capacitance-ratio test, the change in capacitance at low frequencies between metallization strips offers a sensitive technique for investigating the adsorption-desorption of water on SiO_2. This technique could be used to study the fundamental processes involved in the

adsorption and desorption of moisture on insulating substrates and is recommended for future work.

11. RECOMMENDATIONS

On the basis of analysis of test results and associated experimental observations, the following recommendations are extended with regard to further testing of the capacitance-ratio test:

(1) Establish a comprehensive data base on the behavior of different kinds of integrated circuit packages to the capacitance-ratio test.

(2) In this data base, establish a repeatable correlation of test results with those obtained from the mass spectrometer.

(3) Invesitgate the use of the capacitance-ratio test as a leak detection technique.

(4) Investigate the use of the capacitance-ratio test as a technique for locating the presence of cracks in the sealing glass of integrated circuit packages.

(5) Investigate the adsorption of water on SiO_2 using the change in capacitance between metallization strips at low frequencies (from the capacitance-ratio test).

REFERENCES

1. Merrett, R., Sim, S.P., Bryant, J.P., "A Simple Method of Using the Die of an Integrated Circuit to Measure the Relative Humidity Inside its Encapsulation", Proceedings of the IEEE Reliability Physics Symposium, March 1980.

2. Merrett, R., "Moisture Measurement by the Capacitance-Ratio Test", Rome Air Development Center (RADC) In-House Report, RADC-TM-82-2, March 1982.

3. Ryder, J., Networks, Lines and Fields, Pub. Prentice-Hall, 1955, pp. 19-20.

4. Koelmans, H., "Metallisation Corrosion in Silicon Devices by Moisture Induced Electrolysis", Proceedings of the IEEE Reliability Physics Symposium, 12, 168, 1974.

5. Ramo, Whinnery, and Van Duzer, Fields and Waves in Communications Electronics, Pub. J. Wiley and Sons, 1965, pp. 44-45.

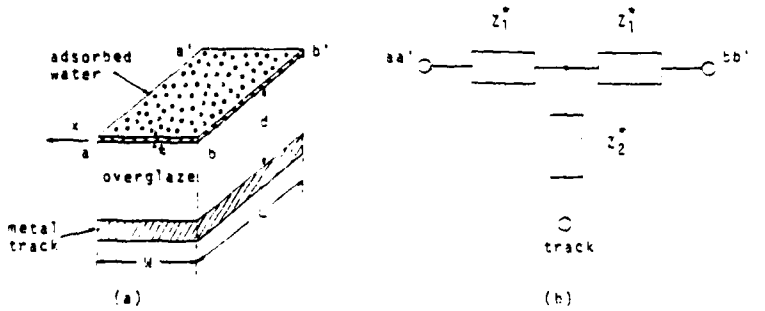

Figure 1. Equivalent circuit representation of adsorbed water above the metallisation track.

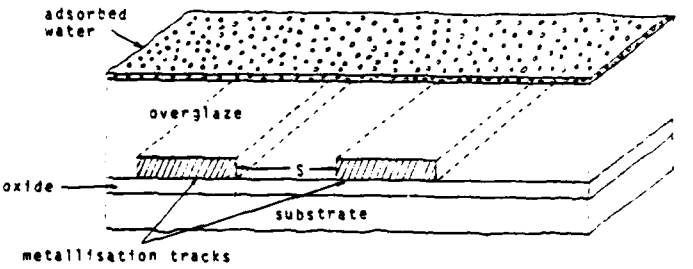

Figure 2. Schematic representation of the regions above and between the metallisation tracks.

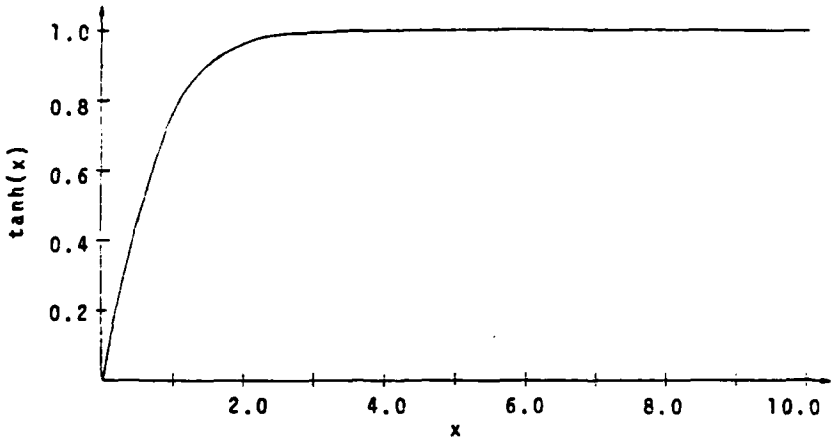

Figure 3. Hyperbolic tangent function.

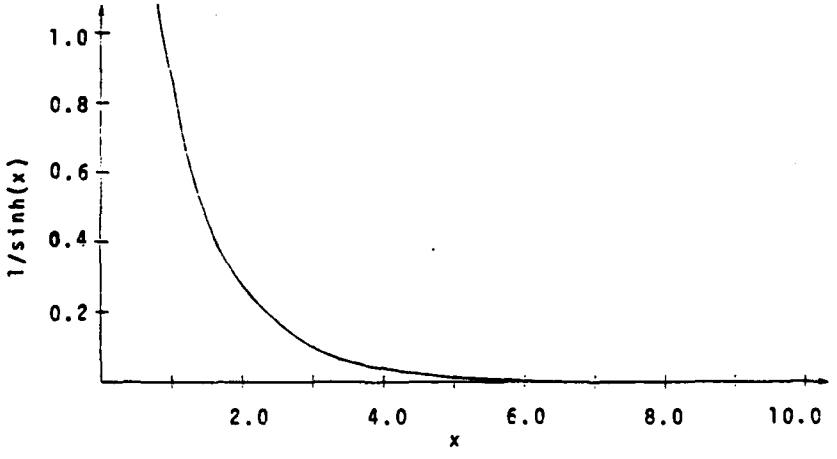

Figure 4. Hyperbolic cosecant function.

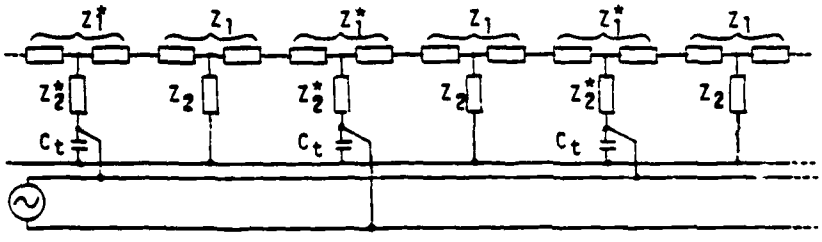

Figure 5. Lumped element network model of adsorbed water on multiple parallel metallisation tracks.

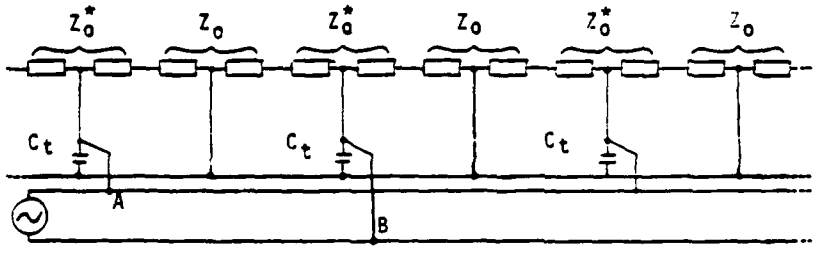

Figure 6. Simplified network model.

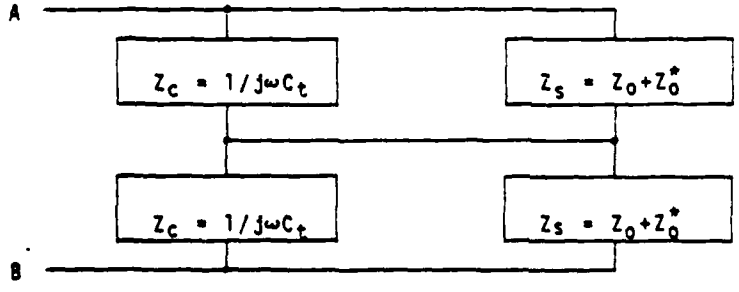

Figure 7. Impedance block diagram for a single pair of parallel metal tracks.

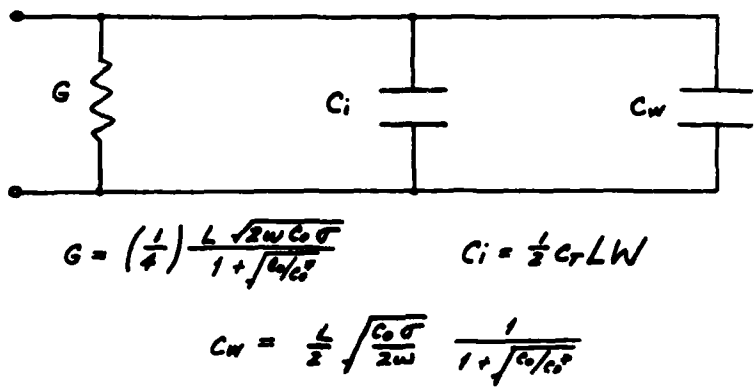

Figure 8. Equivalent admittance model.

CAPACITANCE-RATIO TEST

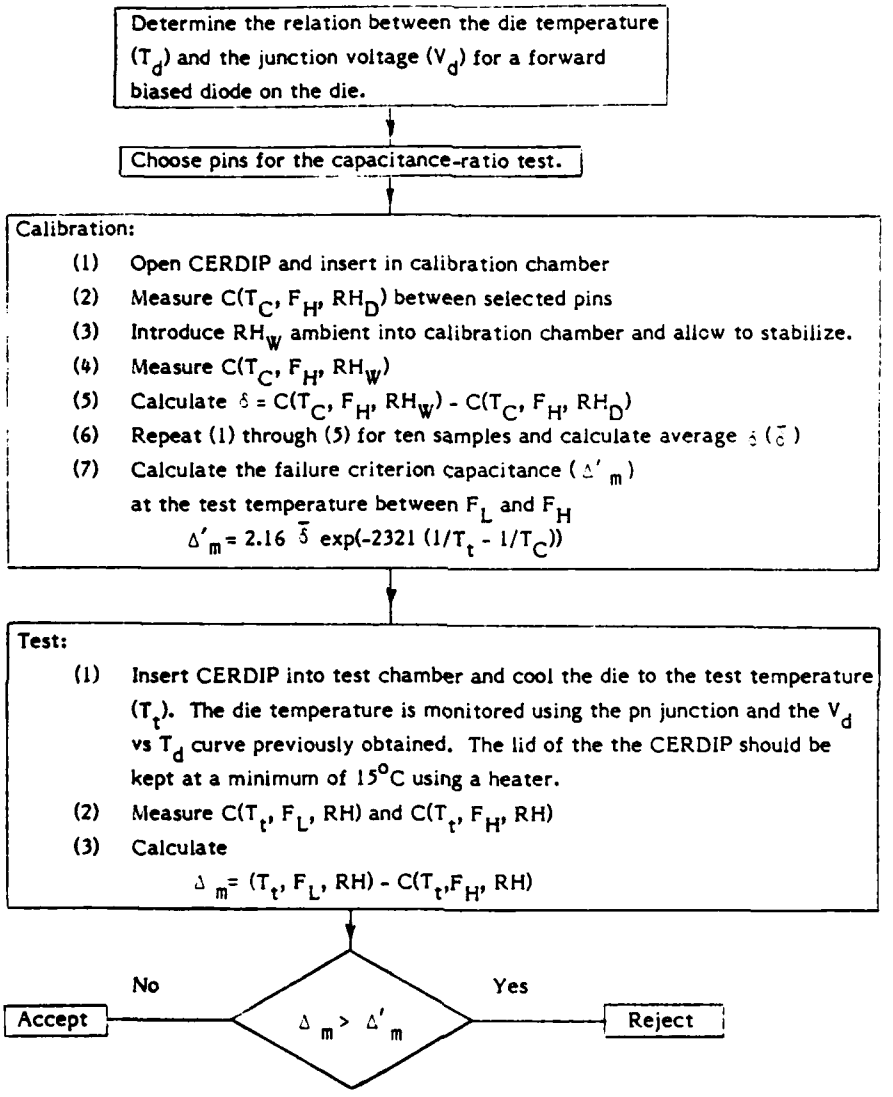

Figure 9. Block diagram summary of the capacitance-ratio test.

Terminology:

T_C = Calibration temperature (room temperature in ^oK)

T_d = Die temperature

T_t = Test temperature (267.5^oK)

V_d = Junction voltage

F_L = Low frequency (83 Hz)

F_H = High frequency (830 Hz)

RH = Relative humidity

RH_W = Relative humidity - wet (75% RH)

RH_D = Relative humidity - dry (<5% RH)

C = Capacitance between two pins of integrated circuit

δ = Change in capacitance at F_H between RH_W and RH_D. $\bar{\delta}$ is average δ.

Δ_m = Moisture induced capacitance measured from test procedure.

Δ'_m = Failure criterion capacitance determined from calibration procedure

Figure 9 continued.

APPENDIX A. REVIEW OF NETWORKS OF DISTRIBUTED ELEMENTS[5]

Consider a network with distributed elements,

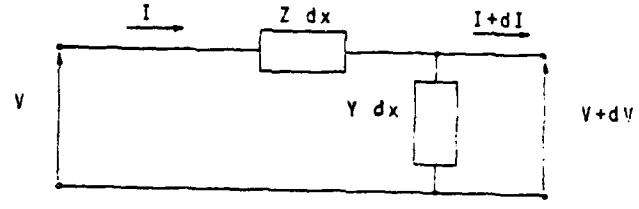

Figure A1

The change in voltage across the series element Zdx is

$$dV = -(Zdx)I$$

or,
$$\frac{dV}{dx} = -ZI \qquad \text{(A-1)}$$

Similarly, the decrease in current which flows through the shunt element Ydx is

$$dI = -(Ydx)V$$

or,
$$\frac{dI}{dx} = -YV \qquad \text{(A-2)}$$

From equations (A1) and (A2) a general wave equation for the transmission line may be written:

$$\frac{d}{dx}\left(\frac{dV}{dx}\right) = -Z\frac{dI}{dx}$$

$$\frac{d^2V}{dx^2} = -Z(-YV)$$

$$\frac{d^2V}{dx^2} = (ZY)V \qquad \text{(A-3)}$$

Defining the PROPAGATION CONSTANT, $\gamma = \sqrt{ZY}$ (A-4)

such that, $\frac{d^2V}{dx^2} = \gamma^2 V$ (A-5)

Solution of this differential equation is of the form

$$V = Ae^{-\gamma x} + Be^{\gamma x} \quad \text{(A-6)}$$

where A and B are arbitrary constants which may be solved for from the boundary conditions.

From eqn. (A1), $I = \frac{-1}{Z}\left(\frac{dV}{dx}\right)$

thus,

$$I = \left(\frac{-1}{Z}\right)\frac{d}{dx}\left(Ae^{-\gamma x} + Be^{\gamma x}\right)$$

$$= \left(\frac{-1}{Z}\right)\left(-\gamma Ae^{-\gamma x} + \gamma Be^{\gamma x}\right)$$

$$= \frac{\gamma}{Z}\left(Ae^{-\gamma x} - Be^{\gamma x}\right)$$

$$= \frac{\sqrt{ZY}}{Z}\left(Ae^{-\gamma x} - Be^{\gamma x}\right)$$

$$= \frac{1}{\sqrt{\frac{Z}{Y}}}\left(Ae^{-\gamma x} - Be^{\gamma x}\right)$$

Defining the CHARACTERISTIC IMPEDANCE of the transmission line, Z_o,

$$Z_o = \sqrt{\frac{Z}{Y}} \quad \text{(A-7)}$$

thus,

$$I = \frac{1}{Z_o}\left(Ae^{-\gamma x} - Be^{\gamma x}\right) \quad \text{(A-8)}$$

Now, consider a transmission line terminated by a load Zl, as shown in Fig A-2.

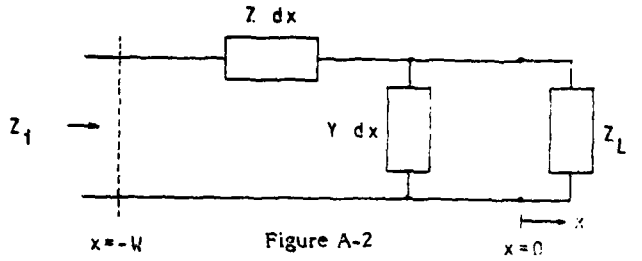

Figure A-2

The input impedance at any point on the transmission line is given by

$$Z_i(x) = \frac{V(x)}{I(x)} = \frac{Ae^{-\gamma x} + Be^{\gamma x}}{\frac{1}{Z_0}(Ae^{-\gamma x} - Be^{\gamma x})}$$

$$Z_i(x) = Z_0 \frac{(A/B)e^{-\gamma x} + e^{\gamma x}}{(A/B)e^{-\gamma x} - e^{\gamma x}}$$

$$Z_i(x) = Z_0 \frac{Ce^{-\gamma x} + e^{\gamma x}}{Ce^{-\gamma x} - e^{\gamma x}} \qquad \text{(A-9)}$$

Applying the boundary condition that at x = 0, the input impedance is merely Z_L the constant C can be solved for.

$$Z_i(0) = Z_L = \frac{C+1}{C-1} Z_0$$

$$Z_L(C-1) = Z_0(C+1)$$

$$C = \frac{Z_L + Z_0}{Z_L - Z_0}$$

Substituting this back into equation (A-9),

$$Z_i(x) = Z_0 \frac{\left(\frac{Z_L+Z_0}{Z_L-Z_0}\right)e^{-\gamma x} + e^{\gamma x}}{\left(\frac{Z_L+Z_0}{Z_L-Z_0}\right)e^{-\gamma x} - e^{\gamma x}}$$

$$= Z_0 \frac{(Z_L+Z_0)e^{-\gamma x} + (Z_L-Z_0)e^{\gamma x}}{(Z_L+Z_0)e^{-\gamma x} - (Z_L-Z_0)e^{\gamma x}}$$

The input impedance on the transmission line at some point x = -l is given by

$$Z_i(-l) = Z_0 \frac{(Z_L+Z_0)e^{\gamma l} + (Z_L-Z_0)e^{-\gamma l}}{(Z_L+Z_0)e^{\gamma l} - (Z_L-Z_0)e^{-\gamma l}}$$

$$Z_i = Z_o \frac{Z_L(e^{\gamma l} + e^{-\gamma l}) + Z_o(e^{\gamma l} - e^{-\gamma l})}{Z_o(e^{\gamma l} + e^{-\gamma l}) + Z_L(e^{\gamma l} - e^{-\gamma l})}$$

where $\frac{1}{2}(e^{\gamma l} + e^{-\gamma l}) = \cosh \gamma l$

and $\frac{1}{2}(e^{\gamma l} - e^{-\gamma l}) = \sinh \gamma l$

Then,

$$Z_i = Z_o \frac{Z_L \cosh \gamma l + Z_o \sinh \gamma l}{Z_o \cosh \gamma l + Z_L \sinh \gamma l} \qquad \text{(A-10)}$$

which is the general equation for the impedance on a transmission line.

APPENDIX B. REVIEW OF NETWORK ELEMENT DETERMINATION [3]

Consider the following 2-port T-network,

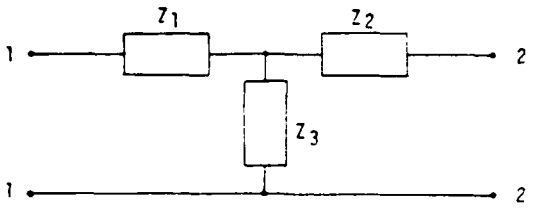

Figure B1

The following parameters can be obtained,

(a) open circuit port 2: $Z_{1oc} = Z_1 + Z_3$ (B-1)

(b) open circuit port 1: $Z_{2oc} = Z_2 + Z_3$ (B-2)

(c) short circuit port 2:
$$Z_{1sc} = Z_1 + Z_2 // Z_3 = Z_1 + \frac{Z_2 Z_3}{Z_2 + Z_3} \quad \text{(B-3)}$$

(d) Short circuit port 1:
$$Z_{2sc} = Z_2 + Z_1 // Z_3 = Z_2 + \frac{Z_1 Z_3}{Z_1 + Z_3} \quad \text{(B-4)}$$

Substracting equation (B3) from (B1),

$$Z_{1oc} - Z_{1sc} = Z_3 - \frac{Z_2 Z_3}{Z_2 + Z_3}$$

$$Z_{1oc} - Z_{1sc} = \frac{Z_3^2}{Z_2 + Z_3}$$

$$Z_3^2 = (Z_{1oc} - Z_{1sc})(Z_2 + Z_3)$$

where from equation (B2), $Z_3 + Z_B = Z_{20c}$

Then, $Z_B^2 = (Z_{10c} - Z_{15c}) Z_{20c}$

$$Z_B = \sqrt{(Z_{10c} - Z_{15c}) Z_{20c}} \qquad \text{(B-5)}$$

from equation (B2), $Z_2 = Z_{20c} - Z_B$ (B-6)

and from equation (B1) $Z_1 = Z_{10c} - Z_3$ (B-7)

1982 USAF-SCEEE GRADUATE STUDENT SUMMER SUPPORT PROGRAM

Sponsored by the

AIR FORCE OFFICE OF SCIENTIFIC RESEARCH

Conducted by the

SOUTHEASTERN CENTER FOR ELECTRICAL ENGINEERING EDUCATION

FINAL REPORT

THE MANUFACTURING CONTROL LANGUAGE FOR ROBOTIC WORK CELLS

Prepared by:	Brian O. Wood
Academic Department:	Industrial Engineering
University:	Penn State
Research Location:	Air Force Wright Aeronautical Laboratories Materials Laboratory Wright-Patterson AFB, Ohio
USAF Research Contact:	Lt. Gordon Mayer
SFRP Supervising Faculty Member:	Dr. Mark A. Fugelso, Assistant Professor
Date:	August 10, 1982
Contract No:	F49620-82-C-0035

ACKNOWLEDGEMENTS

The authors would like to thank the Air Force Systems Command, the Air Force Office of Scientific Research, and the Southeastern Center for Electrical Engineering Education for providing us the opportunity to spend a worthwhile and interesting summer at the Air Force Wright Aeronautical Laboratories, Wright-Patterson AFB, Ohio. In particular, we would like to thank Lt. Gordon Mayer and everyone else at the Materials Laboratory for their hospitality.

Additionally, we would like to extend a special thank you to Glenn Houston and David Clare of the McDonnell Douglas Corporation in St. Louis for information they have provided during the course of our research period.

THE MANUFACTURING CONTROL LANGUAGE FOR ROBOTIC WORK CELLS

by

Mark A. Fugelso and Brian O. Wood

ABSTRACT

Under contract F33615-78-C-5189 within the United States Air Force ICAM program, the McDonnell Douglas Corporation has developed the Manufacturing Control Language (MCL) for use with robotic work cells. An extension of the numerical control language APT, MCL contains control words for real time decision making and vision processing. These facilities, along with several other features, make this language a versatile off-line programming tool. This paper gives a basic overview of MCL's capabilities. Suggestions for further research in this area are offered.


ATE
LME